

Imperial College
London

Transient Optical Characterisation of Donor-Acceptor Block Copolymers for Use in Solar Cells

Imperial College London
Department of Chemistry

Simon P. King

A thesis submitted in fulfilment of the requirements for the degree of
Doctor of Philosophy

June 2010

My Dear Reader,

Congratulations! Having made it thus far into the document, my first vote of thanks must be to your kind self. I hope you find the following pages useful if needs be and stimulating if not.

Acknowledgements

Writing this beast has been a lonely pastime, but I have been very fortunate to have family, friends and colleagues who have made the process and preceding years particularly enlightening, enjoyable and worthwhile. The following sets of people by no means encompass all those who have added to my 'PhD experience' over the last few years, and those who I do not mention by name, know that you have my thanks none the less.

Foremost in the list must be the people without whom I simply could not have started. These are without doubt, Dr. Ana Morandeira-Lopez and Dr. Tracey Clarke, who between them have made a chemist out of me (albeit a physical chemist ;). While it was these two who fielded what seem to me now to be an obtuse number of questions, others did come under more occasional fire and I must thank: Li Xiaoe, Sara Koops, Siva K, Chris Shuttle, Ric Hamilton, Matthias Eng, Piers Barnes, Brian O'Regan, James Durrant and Jenny Nelson for their input. Thanks also to John de Mello for his help in examining my first year report. On a practical note, thanks must go to Prof. Thelakkat, Dr. Michael Sommer and Dr. David Jones for providing the excellent sample sets with which I have had the opportunity to work.

Then there are the people who have made coming in to 'work' every day something to look forward to. These are mainly those in the basement offices including especially: Chris S, Sara K, Fi, Luke, Siva, Adrian, Harry, Safa, Assaf, Andrea and Nurlan, although more recently, George, Alice, Annalisa, Dan, Steph and Simon D have also joined the happy clan. Special mention must also go to Clare D-S as an honorary basement member. Finally among these is one fellow who has shared my time at Imperial more closely, and with whom I have sipped more beers than any other, thank you Henry.

From a more active perspective, there have been three people who really stood out in beating me into shape. Thanks goes to Chris Shuttle for the runs, 100 km walks and 240 km cycle rides, to Allan Peterson for being an ever-present spot, and finally to Adrian Nightingale for super fun runs! Also, nets buddies and swimming buddies.

Of course, at home, my family have been a rock and I would not be at this point, in any sense, if it weren't for them. A very affectionate thanks to Dom, Tim, Mum and thanks especially to Dad for numerous edits and discussions! And then thanks to Charlie. It is Charlie who has had to put up with me on a day-to-day basis and given me the love and support that are such an essential part of everything one does. For that, words are not enough.

Finally, I would like to thank Dr. Saif Haque for being a most excellent supervisor! It is he who has given me the opportunity, the impetus, the guidance and importantly the freedom to complete this work and still be hungry for more. Thank you Saif.

Declaration of Originality

Except where specific reference is made to the work of others, this work is original and has not been already submitted either wholly or in part to satisfy any degree requirement at this or any other university.

Simon P. King

Abstract

This thesis presents a study of photo-active, semiconducting block copolymers for use in molecular solar cells. Current state-of-the-art organic devices utilise blends of two (or more) materials that are co-deposited from a common solution; the resulting structures formed are determined by material properties and deposition conditions, but often result in configurations that are detrimental to device performance. An answer to this problem comes in the form of the block copolymer; using these materials, devices can be formed from a single material active layer. In addition, the counterbalance of forces within films of block copolymer can lead to nano-scale self-assembly that allows for a strong degree of control over layer equilibrium morphology. Such control will be an important step forward in the evolution of molecular solar cells.

The main body of this work is concerned with the study of the photo-physics of photo-conductive block copolymers, especially the generation of free charge.

First, an investigation is made into the inherent structure-function relationship in block copolymers. A varying chain length is seen to drastically affect the photoluminescence quenching and yield of long-lived charges. Photovoltaic devices made using these materials show a peak efficiency of 0.11% and correlate with the spectroscopic results, subject to a trade off between charge generation and transport/collection. In a second investigation, the effects of post-fabrication annealing on block copolymer films are considered; studies on annealed samples lead to the conclusion that domain crystallinity is a significant factor in determining the yields of long-lived charge carriers. It is found that these yields are comparable with those of a standard blend (that achieve 75% photon to electron conversion efficiency). Annealing leads to increases in photovoltaic device performance over unannealed samples, although additional control over active layer morphology is necessary for these materials to attain their potential.

Following this, a comparative study is made between a block copolymer and a similarly composed blend formed from well studied polyfluorene copolymers. Further advantages of block copolymers are highlighted, including the stability of morphologies generated under different deposition conditions.

Finally, a novel tool set is introduced using a block copolymer sample to emphasise the experiments potential with regard to studying interfacial photophysical effects.

List of publications

1. Charge separation and recombination in self-organizing nanostructured donor-acceptor block copolymer films. *S. King, M. Sommer, S. Huettner, M. Thelakkat, S. Haque*, **Journal of Materials Chemistry**, 2009, *19*, 5436-5441.
2. Synthesis, Photophysical, and Device Properties of Novel Dendrimers Based on a Fluorene-Hexabenzocoronene (FHBC) Core. *W. W. H Wong, D. J. Jones, C. Yan, S. E. Watkins, S. King, S. A. Haque, X. Wen, K. P. Ghiggino and A. B. Holmes*, **Organic Letters**, 2009, *11*, 975-978.
3. Nanostructured Hybrid Polymer-Inorganic Solar Cell Active Layers Formed by Controllable in Situ Growth of Semiconducting Sulfide Networks. *H. C. Leventis, S. P. King, A. Sudlow, M. S. Hill, K. C. Molloy, S. A. Haque*, **Nano Letters**, *10*, 1253-1258.
4. The influence of post-fabrication annealing and polymer crystallinity on the morphology and interfacial charge transfer dynamics in nanostructured donor-acceptor block copolymer solar cells. *S. King, M. Sommer, S. Huettner, M. Thelakkat, S. Haque* (In preparation)
5. Benzothiadiazole-containing Pendant Polymers Prepared by RAFT and their Electro-optical Properties. *M. Häußler, P. Lok, M. Chen, J. Jasieniak, R. Adhikari, S. King, S. Haque, C. M. Forsyth, K. Winzenberg, S. E. Watkins, E. Rizzardo, G. J. Wilson* (In preparation)
6. Block Copolymers for Improved Efficiency in Bulk Heterojunction Solar Cells. *D. J. Jones, M. Heusler, A. B. Holmes, S. King, S. Haque, K. Hegedus, S. Watkins, Q. Mao and W. Tang* (In preparation)
7. Controlling Charge Transfer in Organic Photovoltaics Using Donor-Acceptor Block Copolymers. *S. King, S. Handa, S. Haque*, **Poster presentation at MC8** (Materials Chemistry Forum of the Royal Society of Chemistry, University College London, 2007)
8. Controlling Charge Transfer in Polymer Photovoltaics Using Donor-Acceptor Block Copolymers. *S. King, S. Haque*, **Oral presentation at ESC2008** (Excitonic Solar Cell conference, Warwick, 2008)
9. Controlling Charge Transfer in Polymer Photovoltaics Using Donor-Acceptor Block Copolymers. *S. King, D. J. Jones, M. Heusler, A. B. Holmes and S. A. Haque*, **Poster presentation at PPC11** (Polymer Pacific Conference 11, Cairns, Australia, 2009)

Frequently used acronyms and abbreviations

Short	Stands for
AFM	Atomic force microscopy
AM1.5	Air Mass 1.5 (see section 3.3.2)
ΔOD	Change in optical density
F8BT	polyfluorene copolymers poly(9,9'-dioctylfluorene-co-benzothiadiazole)
FF	Fill Factor
HOMO	Highest occupied molecular orbital
ITO	Indium Tin Oxide
J_{sc}	Short circuit current density (mA cm^{-2})
λ	Light wavelength (often in nanometres [nm])
LUMO	Lowest unoccupied molecular orbital
MO	Molecular orbital
N	Degree of polymerisation (ie. number of monomer units making up a polymer)
OD	Optical density
OPV	Organic photovoltaic
OSC	Organic semiconductor
P3HT	poly(3-hexylthiophene)
PCBM	[6,6]-phenyl C60-butyric acid methyl ester
PDI	Poly-dispersity index
PEDOT:PSS	Poly(3,4-ethylenedioxythiophene): poly(styrenesulphonate)
PFB	Poly(9,9'-dioctylfluorene-co-bis-N,N'-(4-butylphenyl)-bis-N,N'-phenyl-1,4-phenylenediamine)
PFM	Poly(9,9'-dioctylfluorene-co-bis-N,N'-(4-methylphenyl)-bis-N,N'-phenyl-1,4-phenylenediamine)
PL	Photoluminescence
PPerAcr	Poly(perylene bisimide acrylate)
PV	Photovoltaic
PvTPA	Poly(vinyl triphenylamine)
sccm	Standard cubic centimetres per minute
SEM	Scanning electron microscopy
TAS	Transient absorption spectroscopy
TCSPC	Time correlated single photon counting
TEM	Transmission electron microscopy
T_g	Glass transition temperature
TFB	poly(9,9'-dioctylfluorene-co-N-(4-butylphenyl)diphenylamine)
UV/Vis	Ultra-violet/Visible (normally in reference to absorption spectra in these ranges of light)
V_{oc}	Open circuit voltage (V)
X	Energetic interaction parameter

Contents

CHAPTER 1	10
INTRODUCTION	10
CHAPTER 2	14
BACKGROUND AND THEORY	14
2.1 PHOTOVOLTAICS	14
2.1.1 <i>Semiconductors and Photovoltaics</i>	14
2.1.2 <i>Organic Semiconductors (OSCs) as a Basis for Photovoltaics</i>	16
2.1.3 <i>Basic Working Principles of a Photovoltaic Device</i>	19
2.1.4 <i>Basic Working Principles of an Organic Heterojunction Device</i>	22
2.2 BLOCK COPOLYMERS	28
2.2.1 <i>Fabrication</i>	28
2.2.2 <i>Background</i>	28
2.2.3 <i>Routes to Microphase Separation</i>	31
2.2.4 <i>Diblock Copolymers in Ultra-thin Films</i>	31
2.2.5 <i>Rod-Like Block Copolymers</i>	33
2.3 BLOCK COPOLYMER PHOTOVOLTAICS	34
2.4 MOTIVATIONS AND LAYOUT OF THESIS	37
CHAPTER 3	40
EXPERIMENTAL DETAILS	40
3.1 FABRICATING ULTRA-THIN POLYMER FILMS	40
3.2 FABRICATING DEVICES	41
3.3 EXPERIMENTAL TECHNIQUES	41
3.3.1 <i>Steady State UV/Vis Absorption Spectroscopy and Emission Spectroscopy</i>	41
3.3.2 <i>Electrical Measurement of PV Devices under AM1.5 Solar Simulation</i>	41
3.3.3 <i>Time Resolved Photoluminescence Spectroscopy</i>	42
3.3.4 <i>Transient Absorption Spectroscopy</i>	43
3.3.5 <i>Atomic Force Microscopy</i>	46
3.3.6 <i>Transmission Electron Microscopy</i>	47
3.4 SOLVENT ANNEALING	47
CHAPTER 4	49

RESULTS: CHARGE SEPARATION AND RECOMBINATION IN SELF-ORGANIZING NANOSTRUCTURED DONOR-ACCEPTOR BLOCK COPOLYMER FILMS	49
4.1 ABSTRACT	49
4.2 INTRODUCTION	49
4.3 EXPERIMENTAL	50
4.4 RESULTS AND DISCUSSION	51
4.5 CONCLUSION	59
CHAPTER 5	60
RESULTS: THE INFLUENCE OF POST-FABRICATION ANNEALING AND POLYMER CRYSTALLINITY ON THE MORPHOLOGY AND INTERFACIAL CHARGE TRANSFER DYNAMICS IN NANOSTRUCTURED DONOR-ACCEPTOR BLOCK COPOLYMER SOLAR CELLS	60
5.1 ABSTRACT	60
5.2 INTRODUCTION	60
5.3 EXPERIMENTAL	61
5.4 RESULTS	62
5.5 DISCUSSION	71
5.6 CONCLUSION	76
CHAPTER 6	77
RESULTS: A STUDY OF AN ALL CONJUGATED DONOR-ACCEPTOR-DONOR TRIBLOCK COPOLYMER	77
6.1 ABSTRACT	77
6.2 INTRODUCTION	77
6.3 RESULTS	81
6.4 RESULTS: ANNEALING STUDIES	91
6.5 CONCLUSIONS	96
CHAPTER 7	98
RESULTS: SPECTROSCOPIC STUDIES ON SWOLLEN BLOCK COPOLYMER FILMS	98
7.1 ABSTRACT	98
7.2 INTRODUCTION	98
7.3 EXPERIMENTAL	100
7.4 RESULTS	101
7.5 CONCLUSIONS	113
CHAPTER 8	114
CONCLUSIONS AND FURTHER WORK	114

8.1	CONCLUSIONS	114
8.2	SUGGESTIONS FOR FURTHER WORK	116
APPENDIX A		117
	HÜCKEL MOLECULAR ORBITAL THEORY AND THE BAND GAP OF POLYMERS.....	117
APPENDIX B		123
	FLORY-HUGGINS THEORY OF POLYMER-SOLUTION AND POLYMER-POLYMER DEMIXING	123
APPENDIX C		131
	ADDITIONAL RESEARCH ON PERYLENE DIIMIDE	131
APPENDIX D		137
	TABLE OF COLLABORATORS.....	137
BIBLIOGRAPHY.....		138

Chapter 1

Introduction

Is there an energy crisis?

Sufficient proven coal reserves exist to sustain 2006 production rates for coal for approximately 150 years; similarly natural gas for ~60 years and crude oil for ~40 years (to say nothing of shale oil, clathrates and as yet undiscovered reserves).^{1,2} However, rates of production must increase. Due to continued and increasing growth in developing countries, most notably the BRIC states (Brazil, Russia, India and China), energy requirements will increase dramatically in coming years. In quantifiable terms: energy consumption is set to increase this century from 13.5 terawatts (TW) in 2001 to a projected ~43 TW in 2100.³ 'Current fossil fuel production rates' and a threefold increase in energy consumption do not match up! A good example of this comes from our own country. In the early 19th century, British coal reserves (measured by amount of carbon) were roughly equivalent to the oil reserves in Saudi Arabia. In 1865, by quoting 'current coal production rates' estimates of how long British coal would last were of the order 1000 years; however British coal production peaked in 1910 and is effectively nil today.⁴ Exactly the same thing is happening today with fossil fuel production; this is highlighted by the exponential increase in production as shown by Figure 1-1. In order to estimate the remaining coal reserves, while factoring in increasing coal production, if we assume 150 years of coal left and use 2006 production rates with a growth in production of 2% per year (by fitting to data from 1930 to 2000), there are only 90 years of coal left.

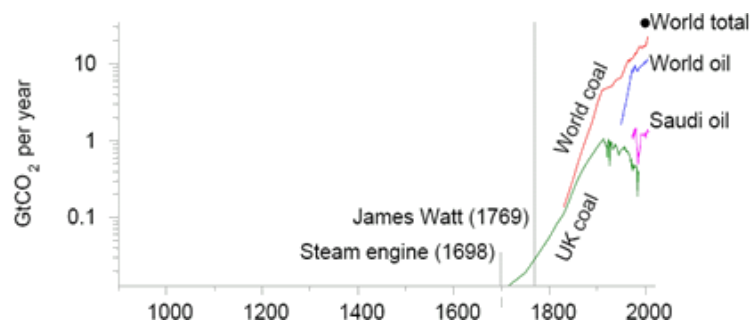


Figure 1-1

The graph shows the history of UK coal production, Saudi oil production, world coal production, world oil production and (by the point) the total of all greenhouse gas emissions in 2000. In order to directly compare these, all production rates are expressed in Gigatonnes of CO₂ emitted on burning. Reproduced from reference 4.

In addition, carbon emission as a result of using these fuels is causing major concerns with regard to climate change. Carbon dioxide (CO₂) is the most abundant 'green house gas' and a by product of burning coal, oil

or natural gas. There is very strong evidence that, since the industrial revolution of the early 19th Century, human development has caused an increase in the global concentration of airborne CO₂.⁵ This increase is believed to be increasing global temperatures, a phenomenon dubbed 'global warming'.^{6,7} So, while energy use is set to increase, carbon intensity (global carbon emission normalised by global energy use) targets are predicted to decrease from 0.49 (2001) to 0.31 Kg C/(W · yr) by 2100. [It is worth noting that 0.31 KgC/(W · yr) is a value lower than that for natural gas, the fossil fuel with lowest carbon emissions per kilowatt hour peak].

To date, few carbon-neutral energy sources are available to provide the predicted increase in energy; one source that may do is solar energy, in particular photovoltaic (PV) devices. PVs allow conversion of sunlight directly to electricity and have received much attention over the past fifty years. However it was Alexandre-Edmond Becquerel in the 19th century who first observed the photoelectric effect, arguably the scientific discovery that marked the very beginning of the technology. The modern age of solar power can be traced back to Russell Ohl's patent of the modern solar cell in 1946 [US2402662, "Light sensitive device"] (Sven Ason Berglund had a prior patent concerning methods of increasing the capacity of photosensitive cells), but realisable photovoltaic device technology arrived in 1954 when Bell Laboratories, experimenting with semiconductors, accidentally found that silicon doped with certain impurities was sensitive to light.⁸ Since then, work in the field of inorganic semiconductor based devices has led to improvements that have brought solar produced electricity to the attention of the world, from: silicon based solar panels powering industry in Germany (see Figure 1-2) to personal retail products, like the Solio® solar phone charger, or the silicon and gallium-arsenide PV modules on virtually every satellite orbiting the planet.



Figure 1-2
A massive array of single crystal silicon solar cells, covering 40,000 m² of a warehouse rooftop in Buerstadt, Germany. The plant is capable of delivering approximately 5 MW of power. [Reuters file photo]

Inroads into these technologies over the last fifty years have led to power conversion efficiencies approaching and surpassing the Shockley-Queisser theoretical limit (32%)⁹ in lab based cells, while commercially available modules typically quote efficiencies of 12 – 15% (these are almost all single crystalline silicon). Despite these advances, solar generated electricity is still too expensive to compete on a global scale with coal power at ~\$1/W. Figure 1-3 shows module efficiency against costs per m² production for three generations of PV technology.¹⁰ First generation devices consist of inorganic solar cells that are not dissimilar to those produced in 1954, while second generation are thin-film PV that are the subject of

much research at present and encompass the types of device addressed by this report; third generation technologies have yet to be dreamt up.

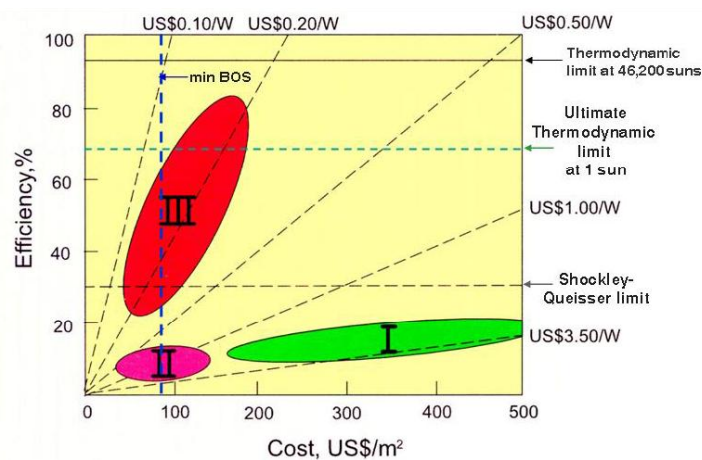


Figure 1-3
 The three generations of photovoltaic as identified by Green, reproduced from reference 10. First generation are the inorganic cells currently at market; second generation are thin-film PVs that are currently the subject of intense research and venture capital funding; third generation are future technologies yet to be addressed. Horizontal dotted lines show relevant theoretical limits to power conversion efficiency, while diagonal dotted lines show cost per Watt peak. Balance of systems costs (BOS) are estimated at just under 100\$/m².

It is first generation technologies that dominate the rapidly expanding commercial market for solar electricity. Global photovoltaic device production increased from 750 MW in 2003 to 1200 MW in 2005; approximately 90% of these devices were from monocrystalline and polycrystalline silicon solar cells.¹¹ Pure crystalline silicon is costly to make in monetary terms as well as energetically, and photovoltaics manufacturers compete with the semiconductor industry for processed materials. An unpredicted surge in demand for solar electricity in recent years, due to rocketing fossil fuel prices and increasing environmental awareness, led to a bottleneck in the production of solar grade silicon; costs per kilo rose from USD 25 in 2003 to USD 350 in 2007.^{11,12} Despite increased silicon production and an apparent letting of this pressure in 2008, other supply bottlenecks threaten to stall expansion of the market for first generation PV modules.

One technology that aims to make headway at this time is the organic semi-conductor (OSC) photovoltaic. Within the last three decades, there has been much development in this area. Initially, organic photovoltaics (OPVs) were fabricated using small organic molecules. In more recent years however, the advent of semi-conducting polymers (and soluble derivatives of C₆₀) has opened new directions for research with promising results. Semi-conducting polymers offer the chance for PV devices that are: low cost on large scale industrial manufacture, mechanically flexible, ultra-fast in opto-electronic response and chemically versatile. Despite this exciting list, there are many challenges to overcome; current state-of-the-art devices consist of blended (p-type) conjugated polymer and C₆₀ derivative and reach efficiencies of only ~ 5-7% (under AM 1.5 solar cell conditions).¹³⁻¹⁷

This thesis aims to: give the reader a general introduction to the 'solar cell', cover the main advances in the field of polymer based solar cells, introduce the reader to block copolymers and their applications in PV devices and present some novel research into block copolymers as active layers for use in photovoltaics. The more specific aims of the thesis are laid out at the end of the next chapter as they require some supporting comment prior to their inclusion; however, as with any research directed towards a specific technological application, the ultimate goal is the advancement of said technology. Progression in the field of photovoltaics is measured by record device efficiencies certified by an independent institution, although such a measure often masks the diverse threads of research that have led to this progress. The ultimate goal of the research presented herein has therefore been the advancement of organic photovoltaics based on block copolymers.

Chapter 2

Background and Theory

2.1 Photovoltaics

2.1.1 Semiconductors and Photovoltaics

In a simplistic sense, two things are required for a material or set of materials to be effective in a PV device: It has to absorb sunlight in order to facilitate the formation of free charge and it must be able to conduct that free charge to a load where it can do work. One caveat to this is that in order to make a *good* PV device, charge has to flow one way through the circuit created. This means there must be an inherent asymmetry across the device to drive current in a single direction.

Semiconductors have a number of interesting properties that fulfil the above requirements and are currently the only materials used in solar cells. It is insightful therefore, to delve a little deeper into the nature of these materials.

A semiconductor is "a substance whose conductance, due to charges of both signs, is normally in the range between that of metals and insulators and in which the electric charge carrier density can be changed by external means".¹⁸

In single atoms, electrons are distributed, according to Pauli's exclusion principle, across quantised energy levels that are eigenvalues of the quantum mechanical Schrödinger equation. The eigenfunctions corresponding to these energy levels give the probability of finding an electron in one place or other around the nucleus. The collective name for the energy/spatial distribution associated with each level is an 'atomic orbital' (AO). Putting two atoms together leads to the formation of new (molecular) orbitals that are the solution to a new Schrödinger equation describing both atoms at once (the molecule). This happens because the energy levels of the newly occupied orbitals are lower than those of the individual atoms (see Figure 2-1); these are called bonding molecular orbitals. There are also orbitals with energy higher than those of the individual atoms, these are termed anti-bonding molecular orbitals. Progressive addition of atoms leads to larger molecules with more electrons occupying more molecular orbitals; the largest

example of this is the crystal. In a crystal, there are so many molecular orbitals, that energetically the levels appear to be continuous and are called 'bands'.

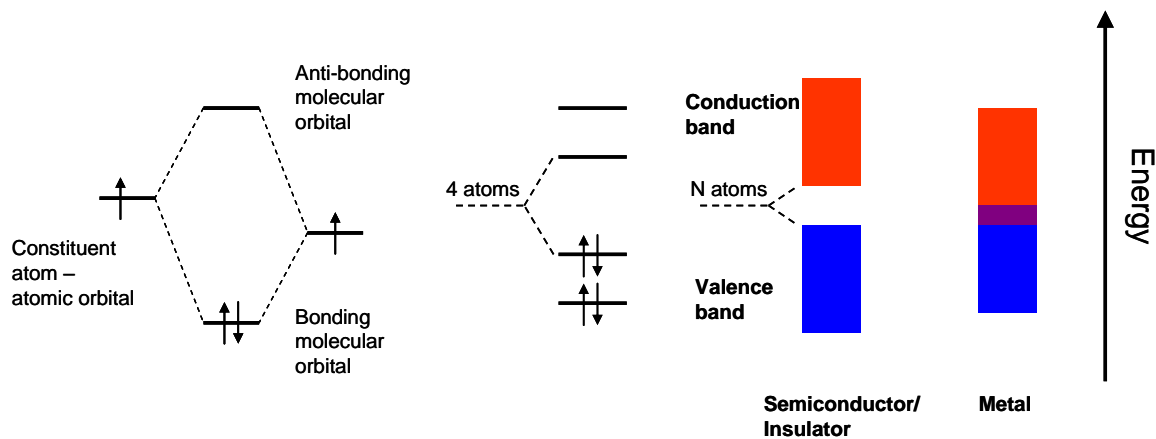


Figure 2-1

A simple description for the formation of semiconductors. In a diatomic molecule (far left), two atomic orbitals combine to give two molecular orbitals whose energy is lower (bonding MO) or higher (anti-bonding MO) than the constituent atoms AOs. Since both electrons from the atoms can occupy a single orbital, it is energetically favourable to form a molecule. For each additional atom in the molecule, another MO is added. This process is continued until the MOs are so close in energy that they form bands, the bonding MO band is called the 'valence band' and the anti-bonding MO band is called the 'conduction band'. If these bands overlap, the crystal will be metallic. If there is a 'band gap' between conduction and valence bands, then depending on the size of gap, the crystal will be either a semiconductor or an insulator.

A substance is a semiconductor when there is a gap in energy between the highest occupied molecular orbital (HOMO) and lowest unoccupied molecular orbital (LUMO) of between ~0.5 and ~4 eV (these limits are widely accepted, although arbitrarily defined). In semiconductor crystals, the filled MO band is called the valence band and the unfilled MO band is called the conduction band (see Figure 2-1) and the energy separation is called the band gap. Electrons may be promoted across the band gap by an external source of energy such as heat or light. Conductance in a semiconductor is achieved by the promotion of electrons across the band gap. Electrons in the conduction band can be thought of as free due to the continuum of empty states available to them and will drift under an applied electric field. Similarly, holes in the valence band can be thought of as positive charges free to drift when an electric potential is applied (holes drift in the opposite direction to an applied field). The electron or hole mobility (μ_e or μ_h respectively) gives a measure of the drift velocity (v) per unit electric field (see Equation 2-1); for example, the mobilities in (undoped) silicon are $\mu_e = 1350 \text{ cm}^2 \text{ V}^{-1} \text{ s}^{-1}$ and $\mu_h = 480 \text{ cm}^2 \text{ V}^{-1} \text{ s}^{-1}$.

$$\mu = \frac{|v|}{E}$$

Equation 2-1

When absorption of a photon leads to an electron being promoted across the band gap, the two requirements for solar generated free charge carriers are satisfied, since 0.5 to 4 eV is equivalent to photon wavelengths of between 310 and 2480 nm and encompasses the entire solar spectrum.

The intrinsic electrical properties of a pure semiconductor are often permanently altered by a process known as doping in which impurities are added to the material. Each atom of dopant introduces either a

hole or electron that may flow freely in the bulk; the electrical conductivity of the material is then controllable depending on the relative proportion of impurity added. With a sufficiently large proportion of doping, the semiconductor can be tuned to conduct nearly as well as a metal. A material that is doped so as to conduct holes is known as a p-type semiconductor, while one that conducts electrons is known as an n-type semiconductor. It is the juxtaposition of an n-type and p-type semiconductor that leads to the asymmetry that allows current to move only one way through the circuit. A p-n junction stops current in one direction and is an important type of electrical diode.^{20,21}

2.1.2 Organic Semiconductors (OSCs) as a Basis for Photovoltaics

It is worth describing the energy gap that gives rise to semiconductors in organic molecules in a little more detail. This may be done by considering the example of a conjugated polymer.

The simplest conjugated polymer is polyacetylene, in which each carbon is connected to two other carbons and one hydrogen atom. Due to the flat trigonal planar bonding pattern of each carbon, it is said to be sp^2 hybridised according to valence bond theory.²² There is a single electron in a p orbital (conventionally the p_z orbital) left over after hybridisation which, in molecular orbital theory, mixes with all the other p_z electrons of the other carbon atoms in the chain forming a number of delocalised π molecular orbitals (MO); a scheme to help demonstrate this is shown in Figure 2-2. Hückel's approximations allow for a semi-empirical determination of the energy level of each π orbital which are found to be split, half into 'bonding' π orbitals whose energy is lower than the p orbitals from which it was formed, half into 'antibonding' π orbitals with higher energy (see Appendix A).^{23,24} Since there is one electron per carbon in a π MO, and each MO holds only two electrons, the bonding MOs are filled completely and the anti-bonding MOs are empty. If the energy gap between the bonding and anti-bonding MOs is in the range described in section 2.1.1 above, then the polymer will be a semiconductor.

A further result of Hückel's model leads to a smaller MO separation and particularly HOMO-LUMO offset with increasing conjugated chain length. This means that for long conjugated chains, the energetically adjacent MOs can be separated by less than $k_B T$ so that they may be considered similar to crystal bands. It also means a red shift in the peak absorbance of the polymer. The absorption of an organic semiconductor is therefore tuneable and molecules can be fabricated that give a good spectral overlap with the solar spectrum. (In fact, according to Hückel's model, an infinite chain of polyacetylene will have no energy gap and be a one dimensional metal. In practice there is a gap due to an energetically favourable structural rearrangement known as Peierls' distortion. (See Appendix A). Compounds containing conjugated ring system (aromatic) molecules are often also semiconductors, whose conductivity and HOMO-LUMO offset are governed by the same factors as above.

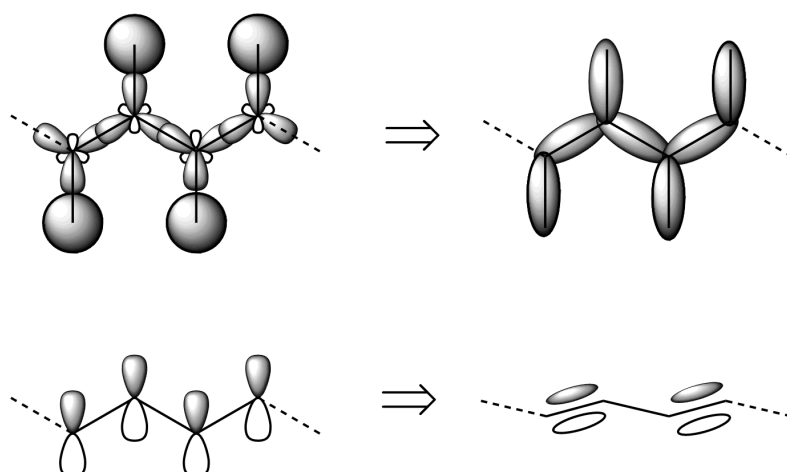


Figure 2-2

The figure shows a short section of polyacetylene with electronic orbitals displayed for each atom (the double bonds are omitted for clarity). Each carbon atom is sp^2 hybridised. In the upper portion of the figure, sp^2 hybridised carbon orbitals overlap with either each other or with 1s hydrogen orbitals to form σ bonds. In the lower portion of the figure, the remaining p_z orbitals from each carbon overlap to form alternant π bonds.

However, the situation is far more complex than that painted by Hückel's model, and there are many parameters that influence the optical gap of conjugated polymers. Designing perfect absorbing and conducting polymers for photovoltaics is the subject of substantial research effort; a good review of recent work, and a more detailed picture of how to tune a polymer's electronic parameters can be found in reference 25. One design consideration of prime importance is that for a single gap photovoltaic, energy from short wavelength light is optimally harvested at the gap energy. A schematic illustration of this is shown in Figure 2-3. Thus energy is lost in two ways: i) photons with energy less than the gap energy will not be collected at all and ii) photons with more energy than the gap will lose the extra energy as heat. The two losses are counterpoised and balancing them results in an optimal energy band gap of 1.4 eV.⁹

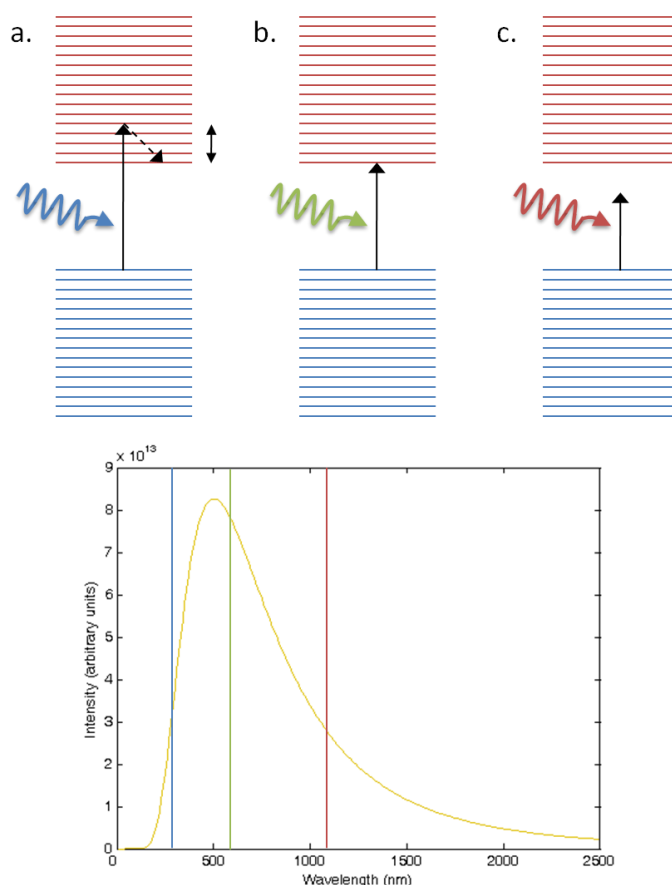


Figure 2-3

The figure demonstrates the principle of photon energy loss in a single gap semiconductor. In scheme a, more energy than the gap is delivered by an incoming photon. An electron is promoted to a state within the conduction band, but will rapidly thermalise to a low energy state with a loss of some energy as heat. In scheme b, exactly the right amount of energy is delivered to promote an electron to the conduction band with no loss to thermalisation. In scheme c, insufficient energy is delivered by the photon to promote an electron to the conduction band; all of the photons energy is lost.

The graph below shows a black body radiation spectrum of an object with temperature 5777 K, similar to that of our sun. The coloured vertical lines on the graph represent photons with energies as in the schematics above. Any photon with a wavelength longer than the green line will have insufficient energy to promote an electron to the conduction band. Any photon with a wavelength shorter than the green line will promote an electron, but some energy will be lost due to thermalisation.

In organic solids, there is a further issue to discuss when contemplating their semi-conducting nature. While a small molecule or conjugated polymer may satisfy the condition for HOMO-LUMO offset, individual molecules in the gas phase are semiconductors (or conductors) individually and charges are localised on a single molecule (these charges are ionic molecular states; eg. if an electron is removed from a neutral molecule M , the radical cation is formed M^+). In order for conduction to take place in a solid (in three dimensions), charges must move between molecules (in the previous example, this involves the movement of the defect electron from one molecule to the next). When in the solid state, charges are stabilised by the polarisation energy of the local environment as shown in Figure 2-4. This means the charge carrier transport mechanism in organic semiconductors is dependent on the degree of intermolecular order and transport mobilities can be anisotropic.^{26,27} In the case of perfect molecular crystals at low temperatures, transport is observed to be similar to inorganic semiconductors and can be described within the framework of coherent Bloch-type band states (ie. tunnelling) with mobilities in the range $1-10 \text{ cm}^2 \text{ V}^{-1} \text{ s}^{-1}$.^{28,29} In amorphous

materials (such as conjugated polymers), there will be a range of local environments with varying polarisations energies, which will lead to a broadened density of transport sites as seen in Figure 2-4. In these materials, an activated hopping transport prevails which leads to much lower mobilities (not often exceeding $10^{-3} \text{ cm}^2 \text{ V}^{-1} \text{ s}^{-1}$).^{30,31}

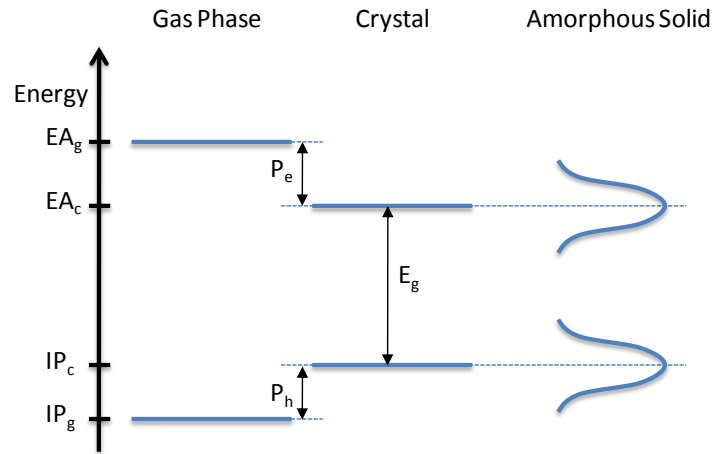


Figure 2-4
The figure shows the energy levels of an isolated molecule (left), a molecular crystal (middle) and an amorphous solid (right). The electron affinity (EA) and ionisation potential (IP) are marked for the gas phase (subscript g) and crystalline (subscript c) molecules. In a crystal, charged states are stabilised by the polarisation energies of the local environment (P_h and P_e); this gives rise to a band gap (E_g) in the crystal. Adapted from reference 32.

2.1.3 Basic Working Principles of a Photovoltaic Device

The conversion of sunlight into electricity within a photovoltaic device can be split into distinct steps:

- Absorption of a photon leads to the energetic promotion of an electron and formation of a bound electron-hole pair (known as an exciton).
- Charge separation occurs, splitting the exciton into an electron and a hole.
- The individual charges are transported to their corresponding electrodes.
- Charge carriers are collected by an appropriate electrode and are made available to do work.

The efficiencies of each of these steps have an effect on the photocurrent density of a device, for example at short circuit (J_{sc}), and are qualitatively defined by the following equation:

$$J_{sc} = q \int b_s(E) EQE(E) dE \quad \text{Equation 2-2}$$

Where q is the charge on an electron, b_s is the incident spectral photon flux density, the number of photons incident on a device per unit area per unit time, and a device's external quantum efficiency, EQE, is the probability that one incident photon is absorbed and delivers one electron to be collected at the electrodes.

The exact dependencies of EQE on the steps above and the loss mechanisms that cause low device efficiencies constitute the main threads of research in the field at present.

On applying a voltage across a device, non-photogenerated current develops and driving forces for charge separation and transport are altered leading to current densities different to that at short circuit. A simple way of understanding the rectifying behaviour of a semiconductor device is provided by a metal-insulator-metal model.

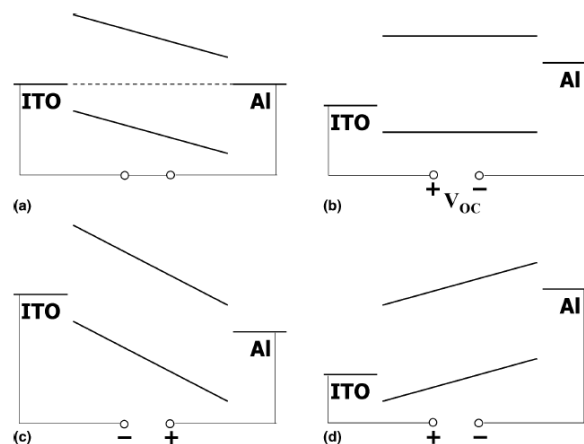


Figure 2-5
Metal insulator-metal (MIM) picture of semiconductor diode device function. (a) Short circuit condition: under illumination photogenerated charges drift toward the contacts. (b) Open circuit condition: the current becomes zero. (c) Reversed bias: photogenerated charges drift in strong electric fields, the device operates as a photodetector. (d) Forward bias larger than open circuit voltage: charges are injected from the contacts and current flows through the circuit. Reproduced from reference 33.

In Figure 2-5 a semiconductor is sandwiched between Indium Tin Oxide (ITO) and Al electrodes. Four situations are presented, each corresponding to different circuit conditions. The conductors are represented by their Fermi energy levels, whereas the semiconductor is shown by its valence and conduction bands. The gradient in the semiconductor bands represents the potential gradient felt within the layer. In Figure 2-5 (a) the device is shorted, and in the dark no current will flow. Under light however, charges are generated and pulled to separate sides of the device by a difference in electrode work functions: holes are pulled towards ITO and electrons towards Al, ie. a photocurrent is generated.

Figure 2-5 (b) shows a schematic of the illuminated device in open circuit; here, photogenerated current has initially flowed, building a potential difference (open circuit voltage, V_{oc}) that exactly opposes the inherent driving force present in Figure 2-5 (a). At this point (corresponding to schematic) there is no driving voltage and no current flows.

In Figure 2-5 (c) a reverse bias is applied against which, very little dark current may flow (the cell is working like a diode). On illumination, photogenerated charges feel a force due to the potential difference created by the electrodes and additionally the applied voltage and are accelerated towards the electrodes; the device acts as a photodiode detector.

Finally, in Figure 2-5 (d) a forward bias greater than V_{oc} is applied and charges are injected into the semiconductor. If these can recombine radiatively, the device acts as a light emitting diode (LED). A device acts as a solar cell at forward bias less than V_{oc} .

The above situations are experimentally tested in a PV device by taking a current-voltage (IV) curve. Figure 2-6 shows an IV curve for an illuminated PV device (solid line) and that same device in the dark (dashed line). Each schematic from Figure 2-5 is depicted as well as the condition of forward bias and negative current where the device produces electricity. Figure 2-6 also shows the 'voltage at maximum power point' (V_{MPP}) at which power-output of a PV is greatest. Using this quantity and the associated current at maximum power point, one can calculate maximum power conversion efficiency (η_p), for a device according to:

$$\eta_p = \frac{P_{out}}{P_{in}} = \frac{V_{MPP} \cdot I_{MPP}}{P_{in}} = \frac{FF \cdot V_{OC} \cdot I_{SC}}{P_{in}} \quad \text{Equation 2-3}$$

It is more common to see the efficiency written in terms of $V_{oc} \cdot J_{sc}$ and a 'Fill Factor', the ratio of maximum power output possible (given a set J_{sc} and V_{oc}) to the maximum power output a given device actually achieves.

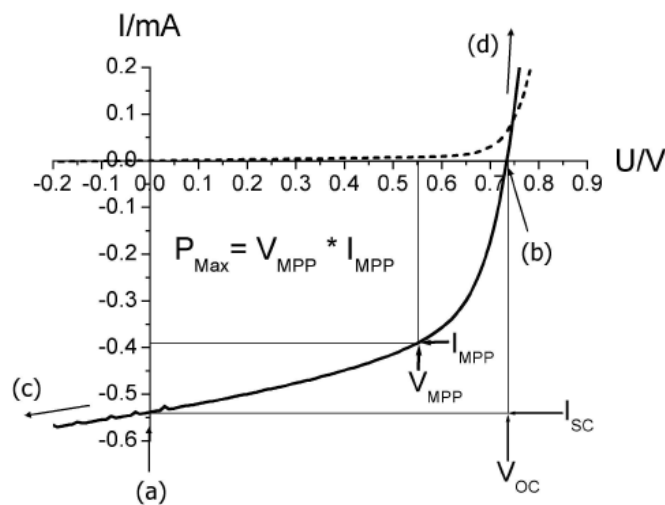


Figure 2-6 Current-Voltage (IV) curves for a photovoltaic measured in the dark (dashed line) and under illumination (full line). The letters (a-d) correspond to the situations dictated by the schematics from Figure 2-5. Maximum power output (P_{Max}) is the product of voltage and current at maximum power point (V_{MPP} and I_{MPP}). Reproduced from ref 33.

An equivalent circuit for a solar cell can be drawn that enables a better understanding of the curve in Figure 2-6; this is done assuming linearity (ie. superposition of currents) and equates the non-ideal PV device to a circuit shown in Figure 2-7. The photocurrent is represented by a current-source with current I_{photo} in parallel with a diode, which gives rise to the dark current (dashed line from Figure 2-6). The series resistance (R_s) is due to resistance of the cell material and contacts. The shunt resistance, in parallel (R_{SH}), is due to current

leakage within the cell (exciton recombination and charge carrier trapping). For an ideal device: R_{SH} is infinite, R_S is negligible and the perfect diode has an IV given by Shockley's equation:

$$I = I_0 \left(e^{\frac{qV}{k_B T}} - 1 \right) \quad \text{Equation 2-4}$$

In a real diode, an ideality factor (n) is included in the equation to account for physical effects. For a real PV, including parasitic resistances, the equation governing current becomes:

$$I = I_{SC} - I_0 \left(e^{\frac{q(V+IR_S)}{nk_B T}} - 1 \right) - \frac{V + IR_S}{R_{SH}} \quad \text{Equation 2-5}$$

The solid line of Figure 2-6 is therefore a superposition of the dark current (dashed line), the short circuit photocurrent and potential drops due to the specific resistances.

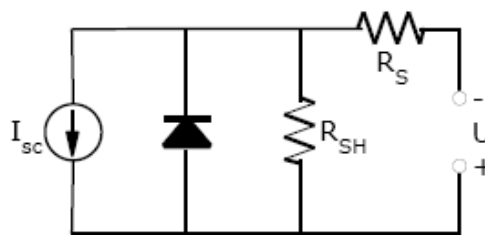


Figure 2-7
The equivalent circuit for a solar cell, consisting of: a current source (delivering current I_{sc}), diode, shunt resistor (R_{SH}) in parallel and a series resistor (R_S) and some load U .

2.1.4 Basic Working Principles of an Organic Heterojunction Device

2.1.4.1 Excitonic Solar Cells

An organic semiconductor device differs from its inorganic counterpart in several ways. In a silicon solar cell for example, an exciton formed by photo-absorption is localised at a separation larger than ten nanometres (nm) and is easily separated by thermal energy of room temperature. In an organic device, a photogenerated exciton is much more strongly bound (a so called 'Frenkel exciton'), due to its confinement on a molecule and a generally low dielectric constant of the compound it is formed in; it will not be split by energy provided by room temperature, but may live from pico- to nanoseconds and diffuse to distances of order 10 nm (in conjugated polymers) before radiatively recombining.³⁴ Excitons may be split at impurities or trap sites and OPVs have been fabricated using a single component active layer,³⁵ but this has not yet been shown to be a viable route to sustained photocurrent generation. A more commonly employed method is to fabricate devices from two (or more) compounds with an offset in their electrical band gaps; the offset provides an energetically favourable pathway for exciton dissociation. Figure 2-8 shows an example of an interface between two OSCs and relevant energy levels. The compound with smaller ionisation potential (IP) is referred to as the donor (D) while the compound with larger electron affinity (EA)

is referred to as the acceptor (A). In the case shown, absorption occurs in the acceptor, and the offset between donor and acceptor HOMOs provides the energetic offset; however, absorption could equally well occur in the donor in which case, the offset would be between LUMOs.

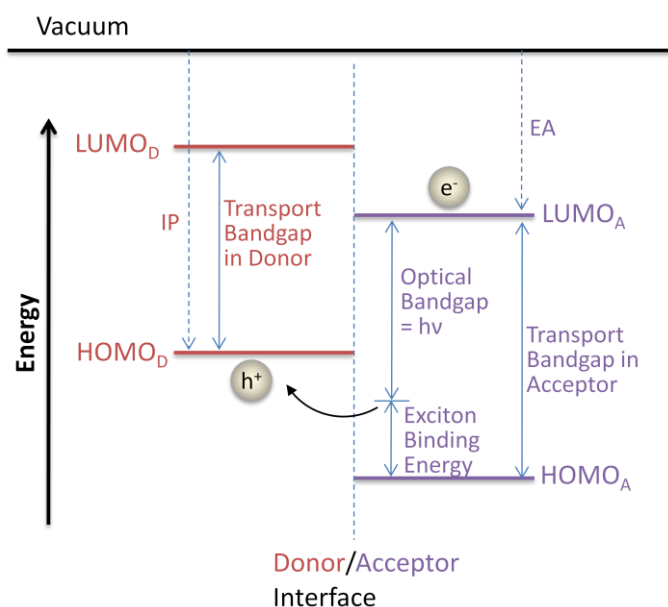


Figure 2-8

Scheme of electronic states (relative to vacuum) for an organic semiconductor heterojunction device. The compound with smaller ionisation potential (IP) is referred to as a the donor (D; donor of electrons) while the compound with larger electron affinity (EA) is referred to as the acceptor (A). In this scheme, an exciton is generated in the acceptor compound and is split by an energy difference between HOMOs such that the hole moves into the donor material.

Splitting an exciton at a D/A interface with larger band offsets than exciton binding energy corresponds to an exothermic pathway for dissociation and the kinetics of charge separation are often ultra-fast (of order femto to picoseconds).^{36,37} This is several orders of magnitude faster than the relaxation (often radiative) of the exciton (pico to nanoseconds) and can lead to high separation efficiencies. However, such a step results in a loss of energy without external work; this should be observed as a drop in the potential for work and is manifested as a drop in V_{oc} ; quantitatively, the maximum voltage obtainable with such a step corresponds to $IP_D - EA_A$. However, even this drop in energy may not be sufficient to generate fully dissociated charge carriers and the products of exciton dissociation often include charge pairs bound across the interface.

2.1.4.2 Interfacial States

There has been much work in recent years on the products of this initial charge step, due to the increasing body of evidence for interfacially bound charge pairs.³⁸⁻⁴⁴ Considering the relatively small separation of the charges across the interface (of order 5-10 Å) and the low dielectric constant of these materials, it is unsurprising that bound pairs can result. Such states are known by many terms in different material sets: exciplexes, bound-radical pair states, charge transfer excitons and geminate pairs, often dependent on the

physical manifestation that has indicated their presence. In future chapters, such states will be termed exciplexes in agreement with the bulk of literature references available on these specific material sets. For the rest of this chapter however, these shall be referred to as Charge Transfer (CT) states.

The dissociation of CT states is a necessary requirement in the generation of photocurrents. If a pair does not dissociate during the lifetime of the CT state, it will undergo recombination, often termed 'geminate recombination'. A similar balance between separation and recombination was initially quantitatively investigated by Onsager due to a break down in the theory explaining observed electrolytic dissociation in a weak electrolyte; the result was then applied, in a separate publication, to the effects of ionising radiation.^{45,46} Onsager introduced the concept of a 'capture radius' (r_c) defined (as in Equation 2-6) as the distance at which Coulombic interaction is balanced by the available thermal energy ($k_B T$):

$$r_c = \frac{e^2}{4\pi\epsilon_r\epsilon_0 k_B T} \quad \text{Equation 2-6}$$

in which e is the electric charge, ϵ_r is the relative permittivity of the surrounding medium and ϵ_0 is the permittivity of free space (*in vacuo*). In his model, generation of a bound pair (our CT state) occurs with excess energy that leads to a physical separation at a distance, a (known as the thermalisation length). If this separation is larger than the capture radius ($a > r_c$), the charges are said to be dissociated; if the separation is smaller than the capture radius ($a < r_c$), charges may still be dissociated, but do so with a reduced probability $P(E)$. Onsager determined a relationship for the rate of dissociation, dependent (in part) on the thermalisation separation and the external electric field, E . Many additional constraints and revisions have since been proposed to adapt the probability $P(E)$ to bring predictions into line with observations in solid-state organic semiconductors.⁴⁷⁻⁵⁰ While the theory has proved very successful in predicting some experimental trends, it still fails to predict absolute yields of charge photogenerated at organic donor-acceptor interfaces. In general, the overall implication of the analysis is: that unless charge separation occurs immediately on exciton dissociation, CT states will form that have a reduced probability for dissociation, thus reducing the photocurrent. This leaves two possibilities for efficiently generating photocurrent: i) to ensure that dissociation happens with sufficient energy that thermalisation results in free (non-bound) charges and ii) to increase the probability for charge dissociation from the bound state (a relaxed CT state).

- i. Since a CT state is formed on electron transfer from donor to acceptor (whether this is hole or electron transfer), the energy of the initially formed state will depend on two factors: a) the energy offset between the initially excited state (S_1) and the energy of the CT state, and b) whether transfer occurs from the lowest energy conformation of S_1 . Examples of different energy level relationships are represented in an energy diagram (Figure 2-9). Evidence for the role of excess energy in the generation of free charge carriers has been seen by Morteani et al.⁵¹ In their donor-acceptor polymer blends, the authors found that

charge was not extractable from a thermally relaxed emissive CT state (therein referred to as an exciplex), but that photocurrent was generated from an interfacial intermediate of higher energy. Ohkita et al. have monitored the yield of long-lived charges in samples formed from a number of polythiophene polymers blend with a fullerene derivative in order to find the effect of the energy offset $E_{S_1}-E_{CT}$ on free charge generation.⁵² For an increase in offset of 300 meV, the yield of dissociation is seen to increase by two orders of magnitude, attributed to the increase in energy of the 'hot' CT state. These observations imply a further relationship between the energetic potential of charge carriers and photocurrent that will result in more energy losses in a device.

- ii. The probability for dissociation from the relaxed CT state will depend on the rate of dissociation as compared to the rates for competing processes. One such process is the decay of the CT state by geminate recombination back across the interface. Another commonly observed process from this state is recombination to one half of the interface, forming a triplet excited state (T_1);^{44,53-55} although, this is only an effective route to depopulation if the triplet state is lower in energy than the CT state (see Figure 2-9d). In a further complication, work done by Morteani et al. and Benson-Smith et al. has also shown that the CT state can repopulate the singlet excited state (S_1).^{51,56} Determining the rate of dissociation however is non-trivial and likely to depend on many specific interfacial properties including: external electric fields and their relative orientation compared to the interface, the thermalisation distance (a), charge mobilities, confinement to a specific volume and the effective screening of charges. For the experimentalist distinguishing between these effects present significant challenges as the CT state is often short lived (of order nanoseconds) and the effects are often coupled.

In fact, upon photoexcitation, both free charges and charges in thermally relaxed CT states will be generated in dynamic equilibrium and so both of the dissociation pathways discussed above will be important.

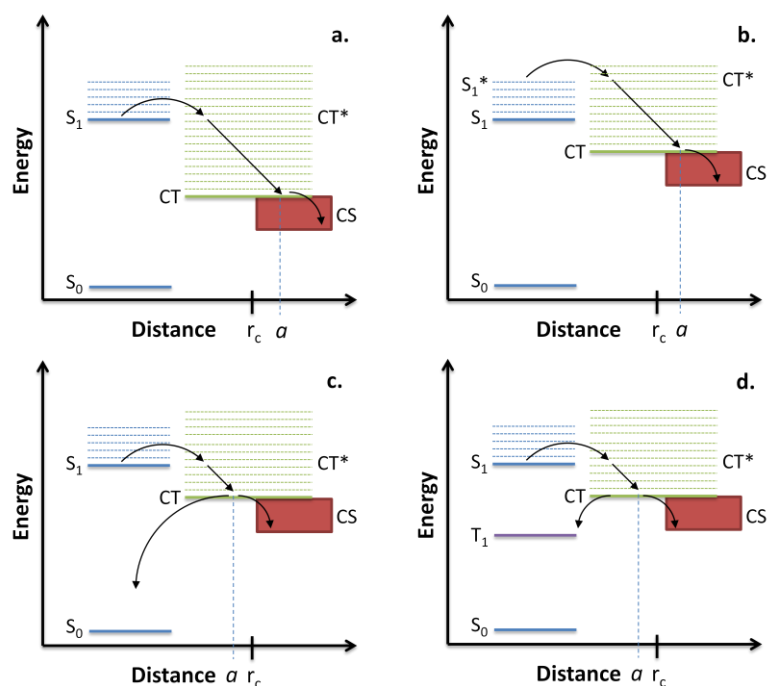


Figure 2-9

Schemes showing the pathways for an excited state near a donor-acceptor interface. The abscissa represents the separation distance between hole and electron. An initially excited state (S_2) that reaches an interface will undergo charge transfer. The fastest rate of transfer will be to an initially 'hot' charge transfer (CT^*) state. The excess energy will result in rapid thermalisation to a relaxed CT state at a thermalisation distance a . If this distance is greater than the Onsager capture radius, the charges may be instantly dissociated to charge separated states (CS) as in Figure a. If the excited state has not equilibrated before charge transfer occurs, it may be in a high energy configuration (S_1^*) that could aid charge dissociation (Figure b). If the charge thermalises at a distance less than the capture radius (Figure c), dissociation may still occur, but will do so with reduced probability and in addition, charges may undergo geminate recombination to the ground state (S_0). If a triplet exciton state (T_1) lies below the CT state, then recombination to T_1 will reduce the probability of dissociation as in Figure d. These are meant as helpful schematics and should not be over-analysed, for example the energy of the CT state will vary with separation.

2.1.4.3 Morphology as a Critical Parameter

Morphology of a two component organic photovoltaic has been found to have a significant impact on many aspects of device performance. A good yield of exciton dissociation for example, is only conducive to high separation efficiency if it is generated within ~ 10 nm of an interface. Early devices used a flat heterojunction in a bilayered device architecture as seen in Figure 2-10.⁵⁷ However, these PVs would have to be very thin in order to harvest all photogenerated excitons and hence sacrifice light absorption in the process. A more recent development was the invention of a donor-acceptor 'bulk heterojunction' (architecture shown in Figure 2-10).⁵⁸ Films with this structure are commonly formed by spin casting two components from a common solution. Inherent immiscibility leads to demixing during drying (known as phase segregation-see Appendix B) and to a chaotic heterojunction interface.⁵⁹ While this regularly results in well mixed donor-acceptor systems, there are a number of issues that arise from an essentially random mix of constituents found in films with bulk heterojunction morphology. The balance between charge separation and recombination for example is thought to be influenced by the surface area to volume ratio of domains. In addition, the size and position of domains will be critical to charge percolation and extraction. While it is possible to tailor the hetero-interface by fabrication conditions such as solvent the blend is spin coated

from^{60,61} or rate of solvent evaporation after spin coating,⁶² and/or post-fabrication processes such as thermal annealing,^{13-15,63,64} predicting the exact morphology is not yet possible. Also, the stability of the resultant morphologies over extended periods of time at operating temperatures (approximately 40-60 °C) is largely untested.⁶⁵ Despite these possible problems, current state-of-the-art organic devices utilise bulk heterojunctions in their active layers and achieve efficiencies of between 5-7%.^{13,15-17}

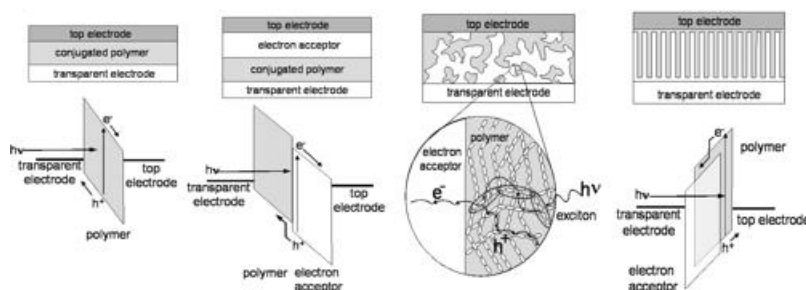


Figure 2-10
Schematics showing progressive organic PV device architectures. From left to right shows successively: a monolayer device, a bilayer device, a bulk heterojunction device and a nanostructured bulk heterojunction device. Current state of the art devices are of the third type in their architecture. It is postulated that the ideal morphology for a PV device is that shown on the far right. Reproduced from ref. 66.

Understanding the role of morphology in end device performance has been the subject of significant debate over recent years and although 'ideal' active layer morphologies have been suggested (see Figure 2-10) and are well studied for hybrid inorganic-organic devices, they have not yet been achieved in all organic materials.⁶⁶⁻⁷⁰ It has proven difficult to measure morphology-function relationships in organic photovoltaics, as structure within donor-acceptor bulk heterojunction systems is hard to measure directly. This is because length scales are often too small to use visible light, and the contrast is too poor to use electron microscopy. Surface imaging is common (for example by scanning probe microscopy), but provides only a small (and possibly unrepresentative^{71,72}) window into film morphologies. One promising measurement technique that has recently been applied to both organic bulk heterojunctions and organic-inorganic hybrid devices is electron tomography.^{73,74} In this technique, a three dimensional picture of a layer is built up from a series of flat transmission electron micrographs. Despite an issue of poor contrast between different organic materials, this method has produced, for the first time, accurate morphological data about both planar and vertical blend segregation. However, even blends with apparent large scale phase segregation will theoretically have impure domains (see Appendix B); these impurities have been seen in donor-acceptor polymer blends, leading to further problems in determining the role of morphology.⁷⁵ Additional problems are encountered when analysing materials that preferentially crystallise. Degree of crystallinity in a material (as distinct from phase segregation) can significantly alter the photo-physical properties of a conjugated polymer and thus can have a large effect on device performance.^{15,76,77} X-ray measurements are commonly employed to study crystalline polymeric materials and when combined with other techniques have provided good insight into the effects of polymer crystallinity in molecular electronics applications.^{76,78,79} Despite a significant amount of research into exerting some control over blend morphologies (for a good overview of

recent work see ref. 80), the parameter space for processing conditions is vast and will differ from material to material. Given the importance of morphology in device function, and the limited control currently available in blend heterojunctions, one elegant way around this obstacle is to synthetically control the range of possible morphological arrangements by tethering together donor and acceptor polymer components; such asymmetric molecules are known as block copolymers.

2.2 Block Copolymers

In this section a brief introduction to the field of block copolymers is presented. While most areas necessary to the understanding of relevant properties will be covered here, there is an extremely large body of theoretical and empirical work that has been carried out on a wide range of materials. For good reviews on the general topic, the reader is directed to refs. 81, 82 and 83.

2.2.1 Fabrication

The modern field of block copolymers originated in 1956 with the discovery of anionic living polymerisation by M. Szwarc.⁸⁴ Using this method, monomer units are successively added (fed) to an unterminated anion until, after a certain length of time, a terminating compound is added to 'kill' the reaction. If two different types of monomer add to two different ends of a living chain, a diblock copolymer will grow (back-to-back). This method of fabrication is one of very few that results in a monodisperse distribution of molecular weights of copolymer, necessary for ordered molecular self-assembly.

Since the advent of this technique, other forms of living polymerisation have increased the range of copolymers accessible to synthetic chemists; free radical chemistry, especially, has become important in this area. It is now possible to synthesise triblock copolymers in ABA or ABC forms as well as other linear multiblock copolymers and 'star' block copolymers (multiple different chains linked to a central 'hub' molecule).

2.2.2 Background

A copolymer is a long chain made up from at least two different types of monomer unit. When these units are found in concatenated 'blocks' of a single type of monomer, the resulting chain is known as a block copolymer. An example of this is an AB diblock copolymer, which may be thought of as two different polymers (A and B) covalently bonded together at one end. The polymerisation length of such a block copolymer, N , is the sum of the polymerisation lengths of the constituent blocks, N_A monomers of polymer A and N_B monomers of polymer B.

Most mixtures of polymers are immiscible and for the case of an AB diblock copolymer system, the two polymer constituents will phase separate into A- and B- rich domains (if they have sufficient mobility to do so); however, they are constrained to separate on a length scale of order a typical block length and hence a domain is usually between 5 and 50 nm; in the literature these are referred to as microdomains. The appearance of microdomains by self-assembly of individual block copolymer molecules is known as *microscopic phase (microphase) separation*.

The nature of a domain structure and its natural repetition length are dependent on three factors: the relative lengths of the polymers ($f_A = N_A/N$), the length of the whole polymer (N) and their mutual interaction χ_{AB} (this is often called the Flory-Huggins interaction parameter; see Appendix B). Based on these parameters, microdomains form with various geometries whose nature is determined by the balance of spontaneous mean curvature of the internal interface, which is produced by a mismatch in entropic stretching of the A and B blocks; an experimental phase diagram demonstrating these principles (reproduced from work by Khandpur et al.)⁸⁵ is shown in the top right of Figure 2-11. The ordinate axis in the phase diagram corresponds to increasingly strong segregation between the blocks. This is due to increasing enthalpic interaction between blocks (χ) and decreasing entropy for mixing (that scales with N^{-1}). Theoretically predicted structures are shown in Figure 2-11 (bottom right) and include: lamellae (LAM), hexagonally packed cylinders (HEX), a body-centered cubic array of spheres (BCC) and a bi-continuous gyroid phase (GYR). Experimentally, a further bi-continuous phase is observed that is a cross between LAM and HEX morphologies and is termed perforated lamellae (HPL or PL).

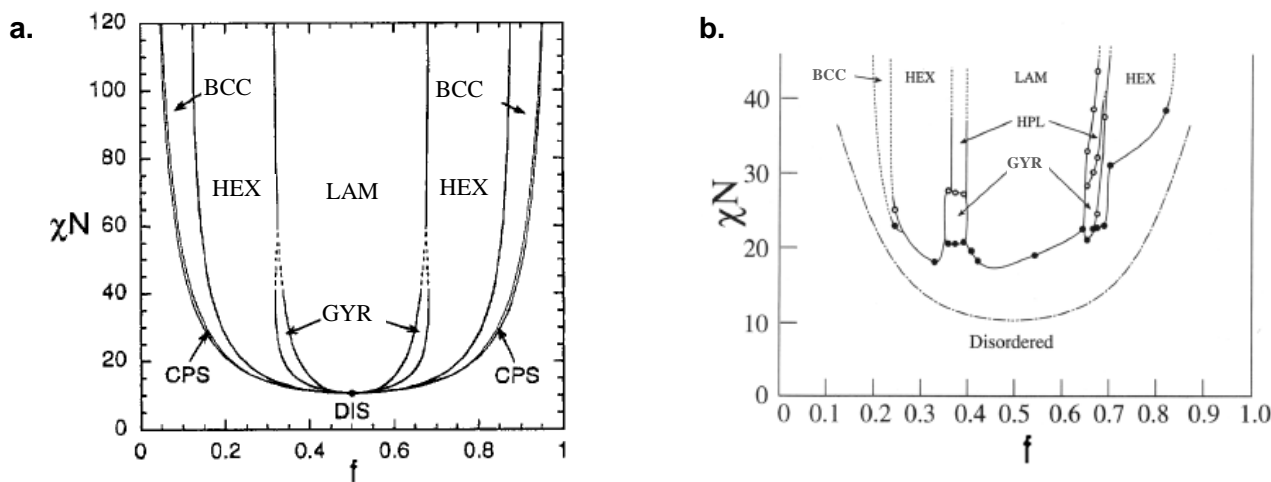
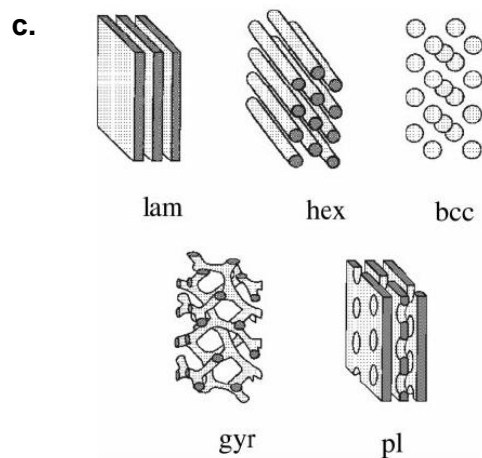


Figure 2-11
 Theoretical (figure a.) and experimental (figure b.) phase diagrams for a diblock copolymer. The graph shown in figure a. shows theoretical treatment by Matsen et al. determined by self-consistent mean field theory; image reproduced from reference 86. Self-assembly occurs for large combined interaction parameter, χN (small temperature and high degree of polymerisation), and varies with the volume fraction of segments of one block, f . Dependent on these factors, one of four morphologies are predicted to occur; these are shown bottom right, in an image reproduced from reference 87, and consist of lamellar (LAM), hexagonally packed cylinders (HEX), the bi-continuous gyroid phase (GYR) and body centered cubic packed spheres (BCC). In the image (bottom right) the shaded region corresponds to the minority component, while the majority (matrix) component is left bland. Outside of the self-assembled regime, the polymer is disordered (DIS). The theory also predicts the appearance of closely packed spheres (CPS) in a small region of the diagram.

An empirically determined phase diagram (reproduced from work by Khandpur et al. in reference 85) is shown, top right, for polystyrene-*b*-polyisoprene (PS-*b*-PI) block copolymers. It is strikingly similar to the predicted diagram. One additional morphological structure is observed, a cross between HEX and LAM structures, termed perforated lamellae (PL or HPL).



Theoretically, the first molecular description of microdomain structure in block copolymers was developed by Meier in 1969.⁸⁸ Since then, block copolymer theory has split into two directions that are categorised by regime and approach. In the self-descriptive strong segregation limit ($\chi N \gg 10$), Helfand and co-workers used a self-consistent mean-field (SCFM) approach that assumes a narrow interface between domains plays a central role.^{89,90} In the weak segregation limit ($\chi N \ll 10$), Leibler adapted de Gennes' random phase approximation to investigate the limits of ordered phase stability.^{91,92} Both theoretical approaches have been adapted and tested, although it is numerical SCFM theory in the strong segregation limit that has been improved to the point where it is considered to be almost quantitatively reliable. A good example of this is the work by Matsen et al. whose theoretical phase diagram (seen in the top left of Figure 2-11) is in good agreement with the empirically derived diagram.⁸⁶ For good reviews of the theoretical treatment of block copolymers and empirical evidence supporting it, the reader is directed to references 93 and 94.

2.2.3 Routes to Microphase Separation

Block copolymers with immiscible components microphase separate when in a mobile, generally liquid, state. Two different experimental approaches are commonly employed to shift a solid disordered copolymer into such a regime:

The first induces polymer mobility via thermally annealing above the highest glass transition temperature (T_g) of a component in the system.⁹⁵⁻⁹⁷ A small window between low thermal degradation temperatures and high T_g (typical of long chain molecules) limits the use of this technique and means that thermal annealing is not possible for some polymeric systems. In block copolymers, the system often displays a T_g for each block and in order for the whole chain to become mobile, the temperature must surpass the highest T_g .

The second technique involves forming concentrated solutions of copolymer by exposure to a solvent atmosphere. This is often known as solvent vapour (or often just solvent) annealing. Polymers in solvent atmospheres absorb a certain amount of solvent dependent, in part, on the energetic interaction between monomer and solvent, $\chi_{monomer-solvent}$. When a block copolymer sample (AB) is exposed to a solvent atmosphere, (S), each, both or neither block may absorb solvent dependent on the energetic interactions between blocks (χ_{AB}) and between the solvent and each monomer (χ_{SA} and χ_{SB}). Solvent acts as a plasticiser inducing polymer mobility without any fear of degradation; hence the number of materials that can be induced to microphase separate is substantially increased. In addition, the precise concentration of copolymer and interaction between the polymers and solvent add to the parameters available to control microdomain morphology. One such parameter is the selectivity of a solvent for a polymer. Solvents can be good, bad or θ solvent towards a given polymer (see Appendix B). In a good solvent, polymers swell whereas in a bad solvent they shrink. For a diblock copolymer, a 'selective solvent' is a better solvent for one block than another (a non-selective solvent is equally good or bad for both).

2.2.4 Diblock Copolymers in Ultra-thin Films

Polymers in films of order 10 to 200 nm (ultra-thin films) feel additional constraints that lead to further effects on a system. This is in contrast to thicker films and solids that are referred to as 'bulk' systems. One such constraint concerns the large surface area to volume ratio in thin films. Interaction of a polymer with a substrate or free surface gives rise to comparatively large surface energies under which a system equilibrates. In the case of diblock copolymers, the block with lowest interfacial energy accumulates at the substrate and that with lowest surface energy accumulates at the free surface. The attraction of a block toward a surface/interface (often termed the *surface field*) is a driving force for structure formation in both the bulk and thin films; however, limited volume in thin films results in this structure formation having a

large impact on the internal morphology of the film. A second constraint is confinement of a film to a thickness that is not compatible with the bulk micro-morphological repetition length and can also lead to deviations from microdomain structures observed in bulk samples. For a comprehensive review of both theory and experiment focussing on block copolymers in thin films see reference 98.

An observable effect of the above constraints is the formation of 'terraces' during microphase separation of an initially disordered thin-film of block copolymer. The formation is due to local adjustments in height of a film to match local minima in free energy associated with energetically favourable microdomain morphologies in a film.^{99,100} Evidence of such terraces can be seen in Figure 2-12, in which a ~150 nm thick film of poly(fluorinated)styrene-*b*-polylactic acid (PFS-*b*-PLA) has 'terraced' to form a film of two distinct thicknesses, characterised by uniform interference colours in the optical image.

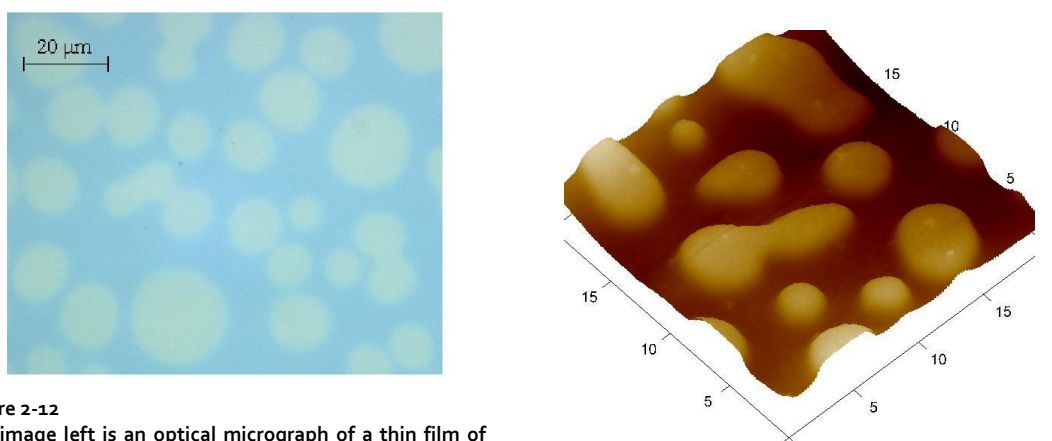
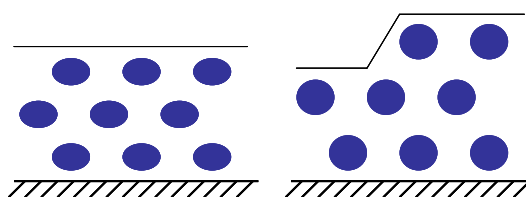


Figure 2-12

The image left is an optical micrograph of a thin film of diblock copolymer that has microphase separated to a terraced formation. The polymer is HEX forming poly(fluorinated)styrene-*b*-polylactic acid (PFS-*b*-PLA). Interference effects lead to different heights being seen as different colours; in this case light green islands correspond to an upper terrace (thicker film) and light blue corresponds to a lower terrace (thinner film). The atomic force micrograph (upper right) shows the variation in topography of a 20μm square section of the film. The schematic on the right hand side shows the reason for the formation of terraces. A BCC forming block copolymer is shown in blue and white, between a substrate and free surface. The agglomeration of the white block at the free surface and substrate leads to an energetically expensive confinement of the blue polymeric component. This is negated by the formation of a film of two thicknesses.



These additional constraints can also lead to rearrangement of microdomain morphology, known as surface reconstruction. A good example of this has been observed by Knoll et al. in cylinder-forming ABA triblock copolymers.¹⁰¹ In thin films, such triblock copolymers show interesting phase behaviour similar to that seen in diblock copolymers^{102,103}. Figure 2-13a and b show scanning force microscopy (SFM) phase images of two annealed polymer films with different initial thickness (<60 nm). Both have formed terraces as shown by the height profile in Figure 2-13c. Different heights have distinct morphologies (seen as

patterns in SFM images) ranging from a disordered wetting layer (dis) to cylinders lying parallel and perpendicular to the substrate (C_{\perp} , C_{\parallel}) as well as perforated lamellae (PL). These observed morphologies are in good agreement with those predicted by simulations shown in Figure 2-13d. Such evidence further demonstrates the interplay between confinement effects (as a result of film thickness) and surface field effects, in determining the microdomain morphology.

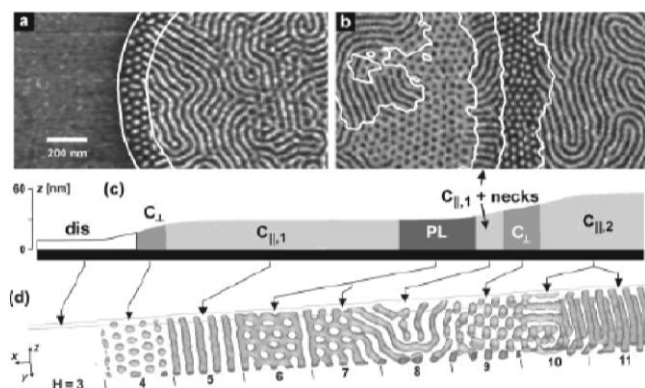


Figure 2-13

(a,b) Tapping-mode scanning force microscopy (SFM) phase images of thin ABA polystyrene-*b*-polybutadiene-*b*-polystyrene films on silicon substrates after annealing in chloroform vapour. The surface is covered with a homogeneous ~10 nm thick polybutadiene (PB) layer. Bright regions correspond to PS while dark corresponds to PB microdomains below this top PB layer. Contour lines calculated from the corresponding height images are superimposed. c) Schematic height profile of the phase image shown in (a,b). d) Simulation of an $A_3B_{12}A_3$ block copolymer film in one large simulation box with film thickness increasing from left to right. The isodensity surface $A = 0.5$ is shown. Reproduced from reference 101.

Much experimental work has been done in recent years on utilising concentrated solutions of block copolymer to alter the microdomain morphology away from a solid state equilibrium configuration. This has been achieved by altering the parameters of a polymer solution to influence surface reconstruction.^{104,105} For example, by controlling the concentration of the solution and by choosing a suitable solvent, film swelling can be directed to a film thickness that (by confinement) ensures a certain morphology or microdomain orientation.^{106,107} Further effects on microphase separated morphology are induced by choosing a selective solvent for one block over another. On swelling in a selective solvent, the relative volume fraction of one block is increased and the effective position on the phase diagram is shifted, leading to a different equilibrium morphology.^{108,109} Using a solvent atmosphere to anneal block copolymers in thin films is therefore an attractive proposition as it provides the experimenter another tool in fabricating a variety of self-assembled nano-scale structures.

2.2.5 Rod-Like Block Copolymers

Polymers that are relatively stiff and straight are often termed rod-like. These properties are inherent in many conjugated polymers due to the nature of the bonding in these molecules; that is trigonal-planar sp^2 hybrid orbitals leading to $\sim 120^\circ$ main chain bond angles and axially asymmetric π -orbitals which cause chain stiffness. Rod-like polymers cannot be treated in the same way as more flexible coil like polymers, as they

have nearly linear chain conformations and their inherent stiffness causes them to form anisotropic liquid crystalline phases above their glass transition temperature.¹¹⁰ Diblock copolymers with one or both components made up from these types of conjugated polymers are in the class rod-coil or rod-rod copolymers. Studies on these systems are limited, but the phase behaviour of some rod-coil systems has been investigated and is found to be very different from that of non-conjugated copolymers (coil-coil type).¹¹¹⁻¹¹⁶ Anisotropic rod interactions have a profound effect on block copolymer equilibrium microphase structure leading to unique self assembled morphologies such as the zig-zag,¹¹⁷ wavy lamellar, arrow-head,¹¹⁸ stripe, broken lamellar and puck phases.¹¹⁵ Modelling and theoretical treatment of these systems has only been rigorously performed relatively recently.^{112,119-121} One pertinent and accessible study is that of Pryamitsyn and Ganesan, in which the authors use self-consistent field theory to model the self-assembly of rod-coil block copolymers in the bulk.¹²¹ In the study, rod-like interactions are treated using a Maier-Saupe potential to describe the steric repulsion between rods. This leads to a phase diagram determined by four independent parameters. Apart from the interactions between different component monomers, $\chi_{AB}N$, and the coil volume fraction, f , this leads to two more parameters that define the morphological phase space: ωN is the Maier-Saupe parameter characterising alignment (where N is the polymerisation length) and ω is the relative block volume (the volume of coil phase divided by the volume of rod phase for one chain). The phase diagrams produced are complex and highly asymmetric, they are also dependent on whether rod/rod interactions or rod/coil interactions dominate, ie. whether ωN or $\chi_{AB}N$ is the dominant thermodynamic parameter.¹²⁰ The situation is further complicated if both components are rigid and crystallize; such block copolymers are often termed double crystalline or rod-rod type.¹²²

To date, the overlap between research in rod containing block copolymers and photovoltaics has been negligible. Most of the experimental work that has been performed to determine the empirical phase diagram of rod-coil block copolymers has utilised organic semiconducting conjugated polymers as the rod-like component.^{116,123} However, the work has not been directly applied to photovoltaics applications as the coil type component is often not a semiconductor. In addition, some polymers used in photovoltaics have been seen to experience anisotropic interactions such as preferential π - π stacking that has not been considered in most treatments of rod-coil block copolymers. Whether the work done in this area will have consequence in the photovoltaics field is still largely unknown. What little work has been done on block copolymer photovoltaics will be summarised in the following section.

2.3 Block Copolymer Photovoltaics

In this section, some of the work that has been published on photovoltaics utilising block copolymers will be highlighted. Donor-acceptor block copolymers have recently attracted attention in the field of organic

photovoltaics¹²⁴⁻¹³³ as they display several attractive properties including: phase separation of p-type and n-type block components restricted to length scales commensurate with exciton diffusion lengths in these materials and an ability to self assemble into a range of different morphologies; one such arrangement is hexagonally packed cylinders (HEX) that, when aligned, bear a striking resemblance to 'optimised' nanostructures proposed in the literature (see Figure 2-10, far right).^{66,134} Two numerical studies in particular have been applied to block-copolymer photovoltaics. Buxton and Clarke generated 'ideal' morphologies in asymmetric coil-coil block copolymers using numerical methods and studied the effects of morphology on simulated photovoltaic devices.⁶⁷ The authors find significant improvement in photocurrent and fill factor for the block copolymer generated ideal morphology compared to a disordered bulk heterojunction. More recently, Shah and Ganesan have investigated the effects of rod-coil block copolymer morphologies generated using self-consistent field theory (under the constraint of a thin film) on photovoltaic performance using a drift-diffusion model.¹³⁵ This detailed report includes the effects of microdomain structure, strength of segregation, domain spacing, and anisotropic charge transport on device performance. A complex balance of these properties is shown to lead to the most efficient devices. In particular, a strongly segregated lamellar morphology aligned perpendicularly to the electrodes yields the highest efficiency device as long as optimal domain spacing and charge transport anisotropy are found. In practice, the application of block copolymers in photovoltaics has only very recently been open for study due to the complex nature of developing asymmetric conjugated polymers with monodisperse molecular weights. A consequence of this is a lack of literature available on block copolymer PV devices. This is highlighted by the analysis of SciFinder searches for publications seen in Figure 2-14. While both block copolymers and photovoltaics separately constitute massive and historic research areas, they have only recently come in contact and research into block copolymer photovoltaics is a substantially less well developed field. Publications on block copolymer photovoltaics make up ~0.5% of the total publications on photovoltaics, and less than 0.3% of publications on block copolymers; although, the increasing number of publications in recent years is a good indicator that the field is beginning to receive the attention it warrants.

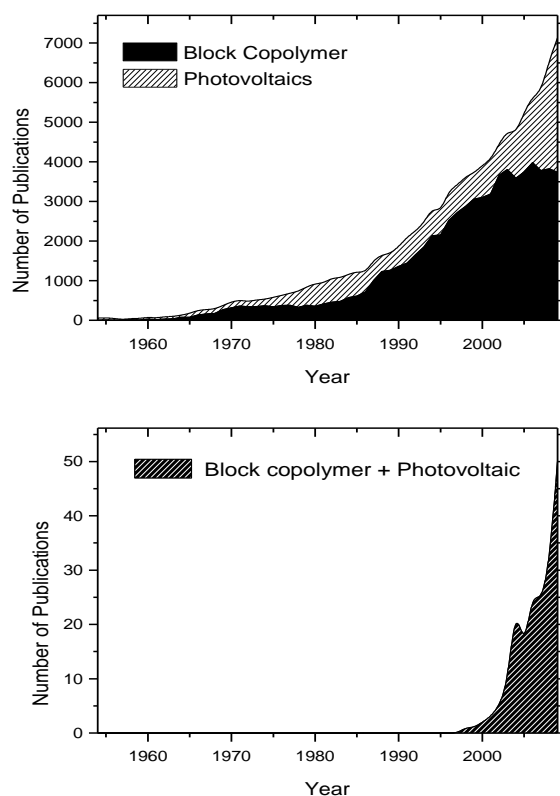


Figure 2-14

These graphs show the histogram results of analysis on the number of publications by year when a search is performed by phrase using the American Chemical Society's SciFinder Scholar™. The upper graph shows number of publications found when the phrase 'block copolymer' is entered (total area (black) amounts to 70,019 publications) or when the phrase 'photovoltaic' is entered (total area (hatched) amounts to 31,876 publications). The lower graph by comparison shows the number of publications found when both terms are searched for simultaneously (total area (black hatched) amounts to 195 publications).

Published results on block copolymer photovoltaics all show larger photocurrents and where quoted, higher power conversion efficiencies than an equivalent blend of homopolymers.^{125,129,133} This is shown to be as a result of self assembly at the nanoscale leading to higher blend dispersity which gives a higher yield for charge separation. In 2001, B. de Boer et al. published one of the earliest reports of photovoltaic action in a monolayer of donor-acceptor block copolymer making use of a diblock copolymer consisting of a poly(p-phenylene vinylene) (PPV) block and a polystyrene block with pendant C₆₀ fullerenes.¹³³ The group at the University of Bayreuth in Germany have published numerous studies into block copolymers for use in photovoltaics utilising a comb type acceptor polymer with pendant perylene diimide moieties.^{125-129,136,137} Work from these studies has clearly shown self-assembly at length scales of the order tens of nanometres compared to microns in equivalent homopolymer blends, with correspondingly better device power conversion efficiencies. Subsequent work on similar polymers has shown promising progress in morphological control.^{138,139} Sun et al. have proposed polymers with a donor-bridge-acceptor-bridge structure including in-chain conjugation in both semiconducting blocks and a flexible, wide band gap bridge.¹³⁰⁻¹³² Currently, the most efficient reported photovoltaic fabricated using a block copolymer active

layer uses a pendant perylene diimide acceptor and (poly(3-hexylthiophene (P3HT)) donor and reaches 0.49% power conversion efficiency.¹³⁸ This is unacceptably low, but leaves a lot of room for improvement. Another use of block copolymers in organic photovoltaics was first reported by Sivula et al.⁶⁵ In this paper, the authors used a diblock copolymer as a compatibiliser between P3HT and a C₆₀ derivative ([6,6]-phenyl C₆₀-butyric acid methyl ester (PCBM)), lowering the interfacial energy and preventing macroscale phase separation. The block copolymer surfactant also stabilised the device structure against destructive thermal phase segregation and may thus lead to improved device longevity. Similarly, improved efficiencies have recently been found utilising P3HT and polystyrene-pendant C₆₀ block copolymers in P3HT:PCBM blends.¹⁴⁰ More recently, ternary blends of P3HT, a perylene derivative and a diblock copolymer were found by Rajaram et al. to exhibit finer morphologies and higher photoluminescence quenching than a binary blend without the block copolymer.¹⁴¹ Further uses of block copolymers have utilised their self assembling nature and their use as sacrificial components in order to form templates for both organic photovoltaic and dye sensitised solar cell applications.¹⁴²⁻¹⁴⁵

As yet, there have been few reports of systematic studies into structure-function relationships in photoconductive block copolymers. Given the properties of block copolymers, their potential in the design of tailored bulk heterojunctions and the current lack of high efficiency block copolymer devices, experimental investigation in this area is obviously highly desirable.

2.4 Motivations and Layout of Thesis

As discussed in the introduction to this thesis, it is hoped that solar energy and specifically solar generated electricity will answer some of the questions about providing power for future generations. The result of this discussion is that a generic goal of those performing research in the area of photovoltaics is the advancement in understanding of basic science that will lead to cheaper and more efficient PV devices. This is no different for the author and this aim is one that underlies all the work presented in this report.

With new understanding of some of the working principles of OPVs and capabilities of block copolymers garnered in the previous sections, it is now possible to give the reader a more specific overview of the reasons for this project.

A key factor in determining short circuit current (J_{sc}), open circuit voltage (V_{oc}) and fill-factor (FF) of an organic bulk heterojunction PV device is morphology. As has been summarised in previous sections, the spatial arrangement of electron- and hole-conducting components in a device is important for a number of specific issues that affect photovoltaic performance. Morphological parameters such as domain size,

interfacial separation, domain crystallinity, preferential wetting of contacts and domain wiring to contacts will have a significant impact on almost all important processes in the solar-energy-to-electrical-energy conversion. These processes include:

- Absorption of light (formation of excitons) – Packing of molecules/crystallinity often affects the molecules absorption due to excitations that can delocalise over adjacent molecules. This will impact on the number of solar photons able to be absorbed and thus directly impact the J_{sc} .
- Exciton dissociation – Excitons have a finite lifetime and diffusion rate and are most likely to be separated at a donor-acceptor interface with appropriate energy level offset. These combined requirements mean that exciton dissociation is dependent on the average interfacial separation and those formed too far away from an interface cannot be harvested. This again directly impacts the J_{sc} .
- CT state dissociation – CT states formed by the dissociation of excitons at a donor acceptor interface will thermalise at a distance a from the interface. If this distance is not greater than the separation required to overcome the electron-hole mutual Coulombic attraction, the CT states will not be dissociated; therefore, if the average domain size prevents thermalisation at sufficient distance, CT states will not be dissociated. This will impact the J_{sc} .
- Charge conduction – Due to the requirement of inter-molecular hopping for efficient charge conduction, charge carrier transport in organic semiconductors is affected by the molecular packing/crystallinity. Poor charge carrier transport can lead to enhanced recombination of free charges and thus a higher series resistance leading to a worse FF and J_{sc} .
- Charge collection – In two component OPVs, one component will carry electrons and the other holes. As these must be collected at opposite sides of the device, the connectivity of domains to the appropriate electrodes will affect the charge collection in a device. Poor connectivity will result in enhanced recombination of free charges and thus a higher series resistance leading to a worse FF and J_{sc} .

All of these imply that controlling morphology in bulk heterojunction photovoltaics should be considered essential to efficient device performance. By utilising the concept of the block copolymer, a synthetic chemist can exert some degree of control over the morphology of a film made from the block copolymer created. As a direct result, there is also control over a select number of the design issues stated in the list above. This is a great leap forward in an aspect of PV device design that has, until now, been the subject of much experimentation by trial-and-error. However, there is still work to be done by the materials scientist and physicist using and understanding these materials and this is the subject of the following chapters.

One of the key ways in which to distinguish between the different effects seen above is to use spectroscopy to probe them individually. The physics of light and especially its interaction with matter is known as photophysics. Using spectroscopy to probe the photophysics of donor-acceptor block copolymer systems makes up a significant portion of this body of work and a description of the techniques used in these experiments is presented in, Chapter 3.

In Chapter 4, the photophysics of block copolymers in PV devices is for the first time systematically investigated. It has been the initial goal of the author to demonstrate that the morphological control obtained when using block copolymers is inherently useful when making organic solar cells. As such, a series of block copolymers are considered that are identical except for the polymerisation length of the chain, N . With no post-fabrication processing, it is found that smaller length chains exhibit finer domain structure and higher yields of photo-generated charged species than a longer length chain or polymer blend.

In Chapter 5, the effect of post-fabrication annealing and polymer crystallinity on morphology and interfacial charge transfer dynamics are investigated in nanostructured donor-acceptor block copolymer solar cells. In this chapter, a second series of block copolymers with a varying ratio of donor to acceptor component are used to determine the effect of chain packing and crystallinity on aspects of device photophysics and performance. Solvent vapour and thermal annealing are studied and compared and found to have significantly different effects on the photophysical properties of the series. Towards the end of the chapter, it is shown that block copolymers should rival and surpass the current state-of-the-art devices, but are limited by the orientation of their morphology.

In Chapter 6 a study is made for the first time on a semiconducting rod-rod type block copolymer. Specifically, the effects of finely mixed morphology on CT states using rod-rod type block copolymers are examined. An emissive CT state is probed to infer properties about the interface and the effects of morphology on the CT state decay pathways. Increased stability of the morphology generated using a block copolymer is found compared to a blend and this leads to higher device efficiencies.

In Chapter 7, the knowledge gained about the properties of the block copolymer in Chapter 6 is used in the development of a new apparatus that provides a set of tools to probe intermolecular interactions. Finally, in Chapter 8, a summary of the main conclusions is presented and ideas for further work are set out.

Chapter 3

Experimental Details

3.1 Fabricating Ultra-thin Polymer Films

There are a number of different methods for creating polymer films with thicknesses in the ranges necessary for optimal OPV performance. Some are only appropriate for lab sized, one off samples, where as others are applicable for scaling up and mass production. Methods include: drop casting, spin casting, screen printing, ink-jet printing and electrochemical deposition to name a few. The technique used to fabricate thin films for this report was spin coating, a non-scalable technique that can reliably produce ultra-flat films (to within a couple of nanometres) at thicknesses between 5 nm and 1 μm .

Spin coating has been used for deposition of thin films, most notably photo resist, for approximately fifty years and good theoretical and experimental treatment of the subject can be found in these references:^{146,147}. The process involves the spreading of a solute or melt on a flat substrate by rotation at high speed. Considering only the case of spin coating from solution, there are several factors that affect the thickness of the resulting film. Solution viscosity and therefore concentration is a key factor in determining final film depth, as are speed of rotation and (to some extent) substrate-solvent interface interaction and solvent vapour pressure. Only a few problems are encountered by the researcher using this technique: a) It is very wasteful and much of the solution is thrown off the side of the substrate; b) any small piece of contaminant on the substrate surface results in deformities that affect film smoothness. One further concern is that the technique is neither scalable, nor continuous. Therefore, for large scale production of organic solar cells, a different method of fabrication is necessary. Fortunately, this is a well investigated problem and has been overcome using both active (organic light emitting diodes) and inactive (news papers) organic inks.

In producing thin films for investigations collated in this report, a package spin coating system was used (Laurell, Spinner WS650S-6NPP LITE). Films were formed by dropping polymer solutions at 1-2 wt%, made up in a suitable solvent (often chloroform or toluene), onto a substrate (1.2 x 1.2 cm^2 glass or Indium Tin Oxide (ITO)/glass (Psiotec)) spinning at 1500-3000 rpm; films generated were generally between 70 and 300 nm thick. Substrates were all pre-cleaned by ultra-sonication in acetone and isopropyl alcohol for 20 minutes at room temperature in air.

3.2 Fabricating Devices

The basic architecture for devices is shown in Figure 3-1. Glass substrates with patterned ITO (Psiotec) were coated in conductive polymer (Baytron P), poly(3,4-ethylenedioxythiophene) doped with poly(4-styrene sulphonate) (PEDOT:PSS) by spin coating at 2000-5000 rpm for 60-300 s. Samples were then annealed at ~ 160 °C for > 30 minutes before an active layer was spin coated on top as described in section 3.1. Finally, patterned aluminium counter electrodes were evaporated on top of the active layer to a thickness of 100 nm in a vacuum of 5×10^{-6} mbar (custom design, Kurt J. Lesker). The active cell area is taken to be the area of the region of overlap between the ITO pattern and the Al pattern, shown as the hashed region in Figure 3-1. This is taken as 0.045 cm^2 in the case of devices made for this report.

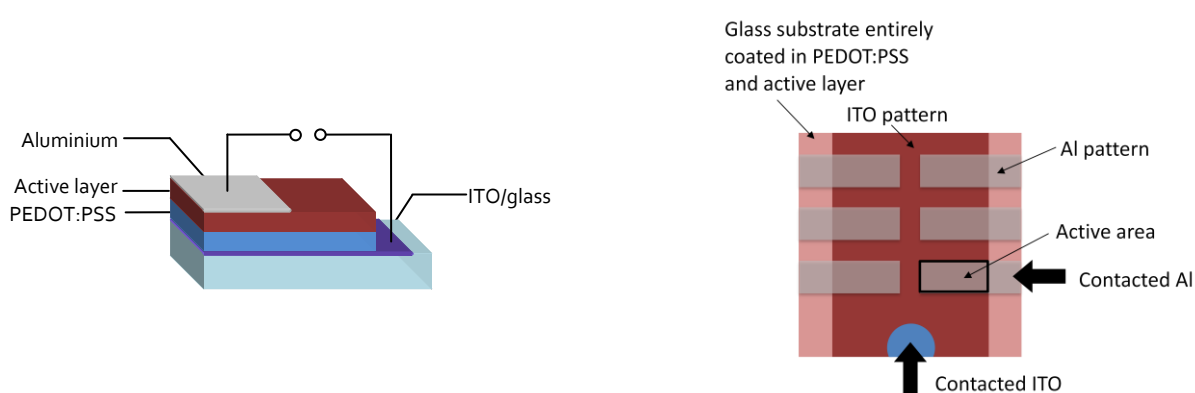


Figure 3-1 Schematic (left) showing polymer photovoltaic device architecture. Glass with a metal oxide conductive coating is layered with a conducting polymer and then the active layer; an aluminium contact is then evaporated on top to complete the device. The schematic on the right, shows both ITO and Al patterns in a top-down look at a device. The bottom right hand pixel is being tested and thus the active area of the cell is pictured in cross-hatch. For devices used in this report, this area was 0.045 cm^2 .

3.3 Experimental Techniques

3.3.1 Steady State UV/Vis Absorption Spectroscopy and Emission Spectroscopy

Absorption and photoluminescence (PL) spectra were measured at room temperature with a UV-visible spectrophotometer (Shimadzu, UV-1601) and a spectrofluorimeter (Horiba Jobin Yvon, Fluorolog-3), respectively.

3.3.2 Electrical Measurement of PV Devices under AM1.5 Solar Simulation

Due to atmospheric absorption of light, solar radiation at the earth's surface depends on the amount of atmosphere light has to travel through. Just outside the atmosphere, the solar spectrum is given the designation AM0. It is important for researchers from multiple institutions to be able to quote standard

device characteristics by testing under standard conditions similar to those under which the technology will eventually be used. To meet this requirement, standard solar simulation has been designated AM1.5 and corresponds to an incident angle of sunlight of 48°. Current-Voltage traces were obtained under AM1.5 solar spectral conditions using a ScienceTech solar simulator with solar spectral filter tuned using a calibrated silicon photodiode detector. Electrical measurement was conducted using a 2400 series source meter from Keithley.

3.3.3 Time Resolved Photoluminescence Spectroscopy

Transient photoluminescence data was collected by time-correlated single photon counting (TCSPC) (Horiba Jobin Yvon IBH, Fluorocube). This method for measuring transient luminescence lifetimes relies on excitation of the sample by a flash of light at such intensity (and with sufficient filtering) that the probability of detecting an emitted photon from a single flash is significantly less than unity. The time interval is then measured between the flash and arrival of a current pulse at the single photon transducer. A schematic of the setup used to perform such measurements is shown in Figure 3-2a.

Because (non-stimulated) emission is a random event, if an excited sample emits only a single photon then the probability of this emission at various times after excitation is proportional to the number of excited states at those times. This probability is exactly the same as the time-resolved decay for a large number of fluorophores. As a result, by measuring the time delays for a large number of single emission events, it is possible to build up a statistical picture of the sample time-resolved photoluminescence. In practice, the time delay between excitation and an emission event is measured using a time-to-amplitude converter (TAC) that outputs a voltage proportional to the time delay. The recorded pulses are discretised and a histogram of time delays is built up.¹⁴⁸ Such a histogram is shown in Figure 3-2b.

In our setup, excitation was by interchangeable LED laser diodes available at the following wavelengths: 282, 404, 467, 560 and 630 nm. Repetition rates were available upto 1 MHz with an average intensity of 80 $\mu\text{W cm}^{-2}$ and an instrument response of 250 ps (full width at half maximum, dependent on the specific laser diode used). Emission was measured at a selective wavelength controlled by grating monochromator.

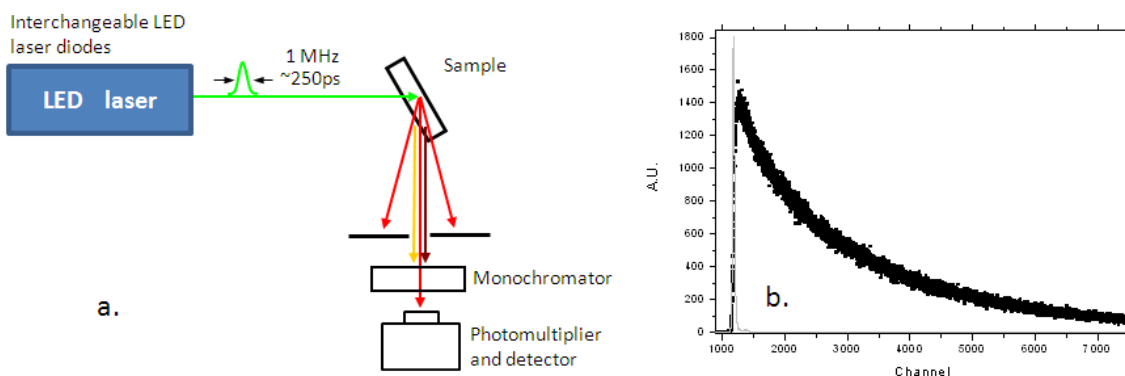


Figure 3-2

Figure a shows a schematic diagram of the set up for time correlated single photon counting method for measuring transient photoluminescence. The sample is mounted in such a way that specular reflection is out of the plane of the page. Figure b shows (in black squares) a histogram showing the photoluminescence lifetime for a thin film sample of poly(perylene bisimide acrylate). Excitation was at 467 nm, while emission was selectively measured at 630 nm. Each channel on the abscissa represents a time window of width 7 ps and excitation began at approximately channel 1200. The ordinate shows the actual number of emission events that occurred within each time window. The laser diode pulse is shown in grey.

3.3.4 Transient Absorption Spectroscopy

Transient absorption spectroscopy is a time-domain pump probe technique used to investigate photo-physical processes. A sample, either film or solution, is excited by a short laser pulse while a second, transmitted light source is monitored before and after excitation. A schematic of the experiment is shown in Figure 3-3. Any signal seen will be a tiny deviation in the background intensity of the probe source. At hundreds of nanosecond time scales and longer, species commonly investigated using this technique are triplet excited states and polarons.^{63,149-152}

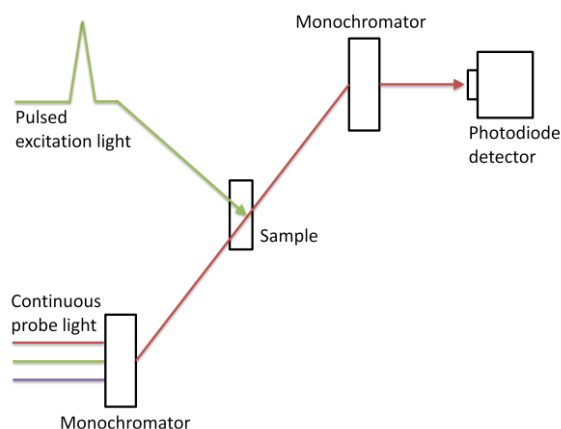


Figure 3-3

Schematic diagram showing the set up for transient absorption spectroscopy. A sample is illuminated with pulsed laser light while being continuously monitored by a second beam whose wavelength is selected by grating monochromator. This 'probe' light is compared before and after each excitation pulse in order to find the increase in absorption due to the presence of photo-generated free charge carriers.

When studying active organic layers for use in photovoltaics, photoexcitation leads to the formation of excited species that separate into dissociated charged states diffusing in the sample bulk. The charged

molecule has a ground state absorption that is often less energetic (more red shifted) than the neutral molecule absorption. So, by continuously monitoring the absorption of the sample at a wavelength far from the ground state absorption, and comparing transmission before and after excitation, the presence of charged states can be verified. The degree of absorption is related to the number of charged species present, which can be monitored as they decay with time after excitation. Using this technique, two pieces of information can easily be acquired: By changing the wavelength at which the sample is probed, a transient spectrum can be built, giving an indication of the absorption spectrum of the transient species; then by monitoring the decay of this spectrum, the decay dynamics can give an indication as to what decay processes are occurring. An example of each of these types of data is shown in Figure 3-4 for a film of poly[[[(2-ethylhexyl)oxy]methoxy-1,4-phenylene]-1,2-ethenediyl] (MEHPPV). The lower graph in the figure shows a transient spectrum (square symbols) taken at 1 μ s after excitation. The spectrum has been normalised and is shown overlaid on an absorption spectrum of a solution of MEHPPV chemically oxidised by an amine radical cation stabilised by a hexachloro antimonate counter ion (N(PhBr)₃ SbCl₆). In this way, the spectrum is assigned to absorption by MEHPPV cations. The spectra show negative change in absorption below 600 nm due to bleaching of the ground state absorption. Such bleaching is not permanent photo-degradation, but a transient feature whose decay mirrors the positive signals seen in the sample. As photo-excited states dissociate to form long-lived cations (and presumably anions too), the ground state MEHPPV molecules are depopulated. This leads to an increase in transmission at wavelengths at which MEHPPV absorbs in the ground state. This increase in transmission appears as a negative change in absorbance in TAS. The slight red shift in transient spectrum versus chemically oxidised spectrum is due to a small relaxation of the cation in the film. (A similar red shift is seen in the ground state absorption of MEHPPV in solution compared to film.) The decay of the cation is shown at 1000 nm in the upper graph of Figure 3-4. Often when polarons are seen in organic films at these time scales, the decay mechanism is bimolecular recombination; that is, charges undergo a random walk from molecule to molecule until they encounter an oppositely charged polaron, at which time they recombine. This type of decay is described by the rate equation is shown in Equation 3-1:

$$\frac{\partial p}{\partial t} = knp = kp^2 \quad \text{Equation 3-1}$$

in which n is the concentration of anions, p the concentration of cations and k is some constant. In the model it is assumed that all polarons are generated by the dissociation of excited states, or charge neutrality $n=p$; also it is implicit that opposite pair recombination is the sole loss process. TAS allows us to monitor the rate of change of the concentration of polarons — in the case above, cations. Thus, by integrating Equation 3-1, and assuming that sufficient time has passed so that there are a small fraction of the initially formed charges remaining, for pure bimolecular recombination there should be an inverse association between ΔOD and time. In fact, the decay in Figure 3-4 is closely fit by a power law decay with

exponent -0.393 ± 0.002 (not -1). Similar sub-linear decay dynamics are seen in many systems studied for use in organic photovoltaics, including those included in later chapters of this work, and are likely explained by the model of Nelson.¹⁵³ In this model, one charge is assumed to be essentially static while the other undergoes a random walk that is influenced by a varying hop rate due to a distribution of site energies. Thermally relaxed charges are said to be trapped and must overcome some energy barrier in order to continue their random walk. Such motion is stochastically dispersive and it is this dispersion that leads to the sub-linear recombination dynamics seen in the figure.

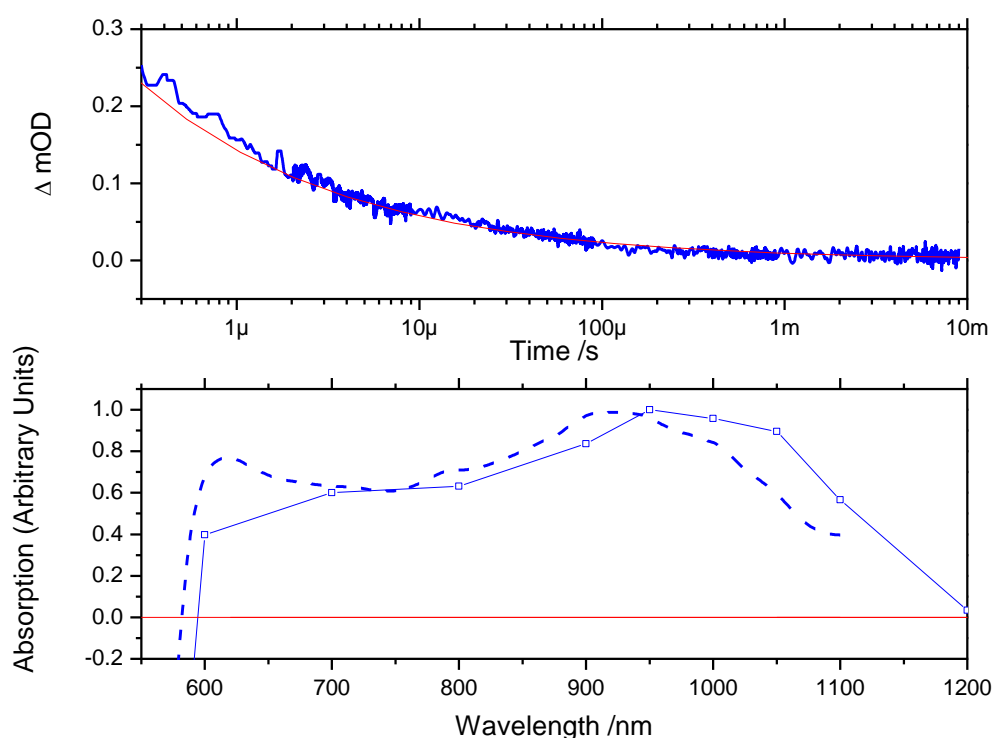


Figure 3-4 Showing two experiments performed by transient absorption spectroscopy. Shown in the lower plot is a transient spectrum (square symbol) and chemically oxidised spectrum (dashed line) of poly[[[(2-ethylhexyl)oxy)methoxy-1,4-phenylene]-1,2-ethenediyl] (MEHPPV). In the upper plot, the transient kinetic decay of the spectrum is measured at 1000nm; the fit is to a power law decay with exponent $\alpha = -0.393 \pm 0.002$. Excitation was at 500nm with fluence 60-80 $\mu\text{J cm}^{-2}$.

Further experiments such as dependence on pump intensity or on sample atmosphere can be very helpful in identifying species. For example, exposure to air/oxygen can help to determine whether a species is a triplet excited state or not. Singlet- \rightarrow triplet or triplet- \rightarrow singlet dipole transitions are symmetry forbidden; so, if a molecule has a singlet ground state, then a triplet excited state will decay very slowly back to ground. Molecular oxygen has a triplet ground state and so triplet excited states will undergo 'allowed' transitions to molecular oxygen. Using TAS, if an observed feature is suspected of being a triplet excited state, its decay

dynamics are observed under pure nitrogen and then again in air/oxygen. If the lifetime of the feature is shortened in the presence of oxygen, it is likely that the feature is a triplet excited state.

The set up used to take measurements for this body of work was home built with a time resolution of order 300 ns. Practically, samples were excited by laser with pulse width 0.6 ns and pulse energy density of 60-100 $\mu\text{J cm}^{-2}$ at 4 Hz repetition provided by a dye laser (Photon Technology International Inc. GL-301) pumped by a nitrogen laser (Photon Technology International Inc. GL-3300). Samples were probed using a quartz halogen lamp (Bentham, IL1) with a stabilized power supply (Bentham, 605). Probe light was detected by silicon or $\text{In}_x\text{Ga}_{1-x}\text{As}$ photodiode and the signal subsequently amplified and passed by electronic band-pass filters to improve signal to noise; using this setup it was possible to detect changes in absorption at wavelengths from 300-1700 nm of sub 10^{-5} . It is noted that excitation light intensities are far stronger than energy from one sun ($\sim 1 \mu\text{J cm}^{-2}$); this is necessary for reasons of signal-to-noise due to extremely low signal even at intense illumination. This is not the only concern when using this technique to analyse samples for use in photovoltaics. Samples must be transmissive in order to be probed by conventional TAS which means that fully functional devices can't be analysed under operation. This can and has been overcome by operating in a reflection mode; however, this requires far stronger probe light and is more involved than the technique used here.¹⁵⁴ It is still reasonable to use this experimental technique as an investigative tool for research into organic photovoltaics for several reasons. In the first case, if free charges are not present at microsecond timescales and high pump intensities, then it is unlikely that they will be available for collection in devices under lower light conditions. Secondly, TAS has been used frequently in the observation of excitonic triplet states that are generally parasitic to photocurrent. Finally, it has been observed for a number of materials systems, that the yield of free charges at $\sim 1 \mu\text{s}$ after excitation (as measured for non-contacted films by TAS) show a positive correlation with short circuit currents (measured in photovoltaic devices using the same material as the photoactive layer).¹⁵⁵

3.3.5 Atomic Force Microscopy

Atomic force microscopy (AFM) is a scanning force technique that uses a very fine tipped needle dragged across a sample surface. By monitoring the deflection of the needle, information is gathered about the topography of the surface. Often if the surface in question is soft, for example when examining polymers, the needle can move or scratch surface features. In this case, the needle can be vibrated vertically over the surface as it is dragged, gathering slightly less information than a needle in contact; this method is known as tapping mode. Due to the soft nature of the samples imaged in the studies presented here, topographical images were all obtained in tapping mode (Pacific Nanotechnology, Nano-R2).

Thickness measurements were also performed by AFM, using the same equipment, but in contact mode, by scanning across samples scratched with a needle.

3.3.6 Transmission Electron Microscopy

Transmission electron microscopy (TEM) uses a high energy beam of electrons to probe the structure of materials in an analogous way to transmission light microscopy. The resolution of this technique is far higher than that of light microscopy due to the small de Broglie wavelength of electrons. In this body of work, only simple bright field imaging is considered and so more complex imaging modes are not discussed further. For an in depth discussion of the technique, a good reference is found here: ¹⁵⁶.

When using bright field imaging, contrast results from variations in electron absorption due to differences in scattering cross section, concentration or thickness. One problem when imaging polymer blends using this technique is insufficient contrast between polymers as they are generally made up from similar atoms. This is overcome by selectively staining one of the components with a heavier element that has a larger cross section for the scattering of electrons. Commonly this has been done with osmium, ruthenium or iodine. For the purpose of this work, it was found that ruthenium staining gave sufficient contrast in the materials studied. Staining itself was performed for various times in an atmosphere of RuO₄ generated from the reaction between Ru [III] Cl hydrate and NaOCl. ¹⁵⁷⁻¹⁵⁹

Samples were investigated using this technique in either a cross sectional or top-down manner. Cross sections were fabricated on a water soluble sacrificial substrate (PEDOT:PSS) and subsequently embedded in low temperature curing epoxy resin and cut to ~50 nm thickness by ultra-microtome. Prior to embedding, samples were capped with a 60 nm layer of evaporated gold to prevent epoxy contamination of the sample surface. Samples for top-down images were fabricated on water soluble sacrificial substrates and both cross sections and free floating (non-embedded) films were transferred to copper grids for imaging cross-sectional and top-down images respectively. TEM was carried out using a JEOL 2000 MkII electron microscope operated at 200 kV.

3.4 Solvent Annealing

Solvent annealing is the term applied to the use of a solvent vapour atmosphere as a means for injecting or retaining solvent in a solid material at high concentrations. This allows for annealing because solvent intercalates in the solid material allowing for semi-fluid motion and thus structural rearrangement.

In order to perform certain experiments presented in this body of work, a rig was developed that allows for controlled solvent vapour annealing. A schematic of the set up is shown in Figure 3-5. Using the apparatus, a saturated vapour stream is generated by bubbling nitrogen through a chosen solvent in a temperature controlled environment. This saturated stream is then mixed with a dry stream to generate a flow with an accurately controlled fraction of saturation. The flow can then be passed over a sample to ensure constant exposure to the vapour stream. Clean dry nitrogen is driven through inert polymer and glass/pyrex tubing at specific mass flow rate by mass flow controller at up to 100 standard centimetres cubed per minute [scm]

(mks instruments). A back pressure is generated in the system by bubbling through silicone oil in order to ensure no leaks are present. Importantly, the rate of removal of solvent from a solid can be controlled using this set up by reducing the saturation of the atmosphere in a controlled fashion.

The saturation vapour pressure can be determined by an inexact, chemical engineer's version of the Clausius-Clapeyron equation called Antoine's equation (see Equation 3-2); in which p is the saturation vapour pressure (in mmHg) for a given temperature, T ($^{\circ}\text{C}$). The constants A , B and C are determined empirically and are generally quoted for a certain thermal range over which they are valid.

$$\log_{10} p = A - \frac{B}{C + T} \quad \text{Equation 3-2}$$

Two sample chambers were developed for the solvent annealing rig: one for thermally controlled solvent annealing in the dark and the second for studying samples spectroscopically during room temperature solvent annealing.

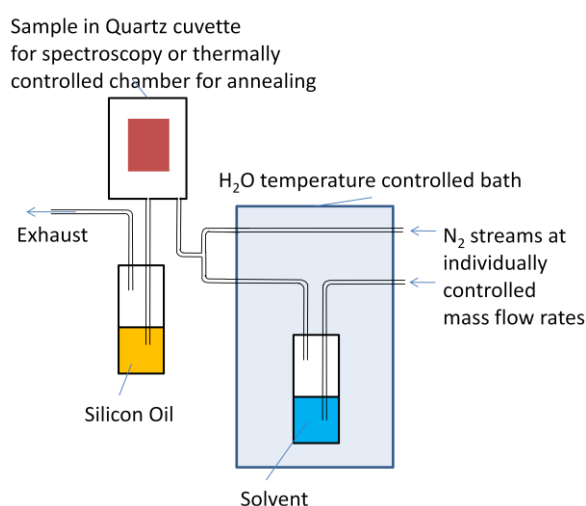


Figure 3-5
A schematic showing the experimental apparatus used for solvent annealing.

Chapter 4

Results: Charge separation and recombination in self-organizing nanostructured donor-acceptor block copolymer films

4.1 Abstract

In this chapter, a series of donor-acceptor diblock copolymers with varying molecular weight are studied in thin film format and compared with an 'equivalent' blend formed from donor and acceptor homopolymers. Steady-state and transient spectroscopies are used to demonstrate a correlation between low molecular weight block copolymers and increased photoluminescence quenching (upto 99%) leading to higher yields of long lived free charges. Such block copolymers are shown, by electron microscopy, to exhibit phase segregated microdomains whose size and periodicity are determined by their molecular weight. Photovoltaic devices made using these materials show a peak efficiency of 0.11% and correlate with our spectroscopic results, subject to a trade off between charge generation and transport/collection.

4.2 Introduction

As discussed in Chapter 2, new methods are urgently required to achieve better control of nanomorphology in donor-acceptor composites for the realization of efficient organic solar cells. One approach to is to use self-organizing and supramolecular materials to control nanomorphology of the photoactive layer in organic solar cells.^{63,160} For example, donor-acceptor block copolymers have recently attracted attention in the field of molecular electronic devices such as OPVs^{125,126,136,145,161} as they display several attractive properties including: phase separation of p-type and n-type block components restricted to length scales commensurate with exciton diffusion lengths in these materials and an ability to self-assemble into a range of different morphologies, one of which is hexagonally packed cylinders that, when aligned, bear a striking resemblance to 'optimised' nanostructures proposed in the literature.^{66,67,134} Construction of an all-in-one molecule can also include additional components for functional enhancement such as dyes for expanding visible absorption.^{162,163} Recent studies have addressed the use of block copolymers in organic solar cells.^{125,126,136,145} For example, Thelakkat and co-workers have reported donor-acceptor diblock copolymers carrying perylene bisimide and triphenyl amine as electron transporting and hole transporting groups respectively. Such

polymers have been shown to exhibit *bulk sample* microphase separated morphologies with domain spacings on the order of tens of nanometers, thereby rendering them desirable for OPV applications.^{125,127-129} More specifically, thin section transmission electron microscopy (TEM) images from these studies show triphenyl amine polymer blocks in a matrix of perylene bisimide with domain sizes of $\sim 0.5 \mu\text{m}$ for the blend compared to less than $\sim 50 \text{ nm}$ for the block copolymer. Devices fabricated from these materials were shown to exhibit an approximately one-order of magnitude improvement in short circuit photocurrent density and overall efficiency compared to control devices fabricated employing a random blend of the corresponding homopolymers. Furthermore, the improvement in device performance was tentatively attributed to an improved charge generation process due to a higher surface area donor-acceptor heterojunction in the block copolymer relative to the blend.¹³⁶ Many spectroscopic studies have recently addressed the charge separation and recombination reactions in random polymer-small molecule and polymer-polymer blend structures.^{52,152} To date, however spectroscopic studies focussing on charge generation and recombination in self-assembling materials such as block copolymers remain limited. A more detailed understanding of the parameters controlling charge transfer in self-organizing systems is now needed to facilitate the rational design and synthesis of new materials required for high efficiency OPV devices. In this chapter, the dynamics of charge separation and recombination is addressed in self organizing donor-acceptor block copolymers composed of poly(triphenylamine) PvTPA and poly(peryene bisimide acrylate) PPerAcr. In particular, an investigation is made into the influence of block copolymer molecular weight and phase separation length scale upon the dynamics of charge separation and recombination. It is shown that charge separation dynamics and yield are strongly dependent upon molecular weight with the lowest molecular weight block copolymer resulting in the most efficient charge separation yield. The recombination dynamics between the photogenerated charges are shown to be less strongly dependent upon block copolymer molecular weight. The present findings are discussed with relevance to the design and optimization of organic donor-acceptor solar cells.

4.3 Experimental

A number of block copolymers were synthesized as reported elsewhere.^{126,127} Blends were formed by 85% (wt.) of poly(peryene bisimide acrylate) (PPerAcr) with poly(vinyl triphenylamine) (PvTPA). Solutions were prepared in all cases in chloroform (all easily soluble) at a concentration of $\sim 1.5 \%$ by weight. Ultra thin polymer films for spectroscopic work were spin-coated onto glass substrates, pre-coated with conducting and transparent ITO, at a spin rate of 1500 rpm for 40 s from the chloroform solutions. Before spin-coating, substrates were pre-cleaned by sonication in acetone and isopropyl alcohol for 20 min before being dried in a stream of nitrogen.

Photovoltaic devices were fabricated by spin-casting PEDOT:PSS (Baytron P) onto substrates as used for thin films at a spin rate of 5000 rpm for 60 s. Substrates were pre-cleaned as before and additionally cleaned by sonication in de-ionized H₂O. Samples were then annealed at ~160 Celsius in air before a polymer film was spin-coated at 1500 rpm for 40s from solutions as above. Aluminium contacts were then evaporated to 100nm thick to give devices with active area of 0.045 cm².

Bulk samples for TEM were annealed for one hour at 210 °C in a nitrogen atmosphere, embedded into epoxy resin and microtomed. Staining was performed with vapor phase RuO₄ for 10 min.

4.4 Results and discussion

The chemical structure of the block copolymers studied herein are shown in Table 4-1. along with the corresponding schematic energy level diagram. A series of three block copolymers with varying molecular weights [hereafter referred to as polymer 1 ($M_n \sim 38 \text{ kg mol}^{-1}$), polymer 2 ($M_n \sim 28 \text{ kg mol}^{-1}$), and polymer 3 ($M_n \sim 9 \text{ kg mol}^{-1}$)] were compared to a blend formed from 85% PPerAcr and 15% PvTPA and pristine PPerAcr homopolymer ($M_n \sim 23 \text{ kg mol}^{-1}$). The molecular weight, polydispersity index (PDI) and PPerAcr weight percentage for all three polymers is summarised in Table 4-1. Thin films of the donor-acceptor block copolymers were spin-cast to thicknesses of between 150 and 200 nm. Steady state absorption spectroscopy (see Figure 4-1a) shows similar absorbance in each film due to similar numbers of absorbing species in each sample studied (since PPerAcr is the only species that absorbs in the visible in each sample); Figure 4-1a shows absorption spectra from a homopolymer PPerAcr and block copolymer 1 (all spectra are similar, only two are shown for clarity). The photoluminescence spectra of all films, excited at 470 nm, is presented in Figure 4-1a. Peak emission is observed at 650 nm and attributed to PPerAcr, as indicated by the PPerAcr homopolymer film. On addition of donor material, this emission is quenched by varying degrees. Block copolymer samples studied quench the emission in a trend related to their molecular weight, with the smallest polymer (3) having the largest degree of quenching; all emit less than the polymer blend film.

Table 4-1
Block copolymer series molecular characteristics

Polymer Short Hand	Polymer Designation	M_n/g mol ⁻¹	PDI	Percentage (by weight) PPerAcr	Degree of Polymerisation block n (PvTPA)	Degree of Polymerisation block m (PPerAcr)	Polymer Molecular Structure
Block copolymer 1	PvTPA-b-PPerAcr	40,000	1.97	79%	31	38	
Block copolymer 2	PvTPA-b-PPerAcr	27,800	1.47	64%	37	22	
Block copolymer 3	PvTPA-b-PPerAcr	9,200	1.43	73%	9	8	

Transient photoluminescence studies corroborate steady state quenching and are shown in Figure 4-1b. Under excitation at 467 nm, emission from perylene bisimide (630 nm) has a half time of 7 ± 1 ns (pristine PPerAcr) and is closely follows a monoexponential decay. It can be seen that addition of donor compound leads to successively shorter fluorescence lifetimes for polymer-blend followed by block copolymers 1, 2 and 3 (blue, orange and purple). Each trace is the result of the same exposure by each sample to a fixed number of incident photons; approximately the same number of photons is absorbed by each film (minor differences in absorbance are obviated by correcting for absorbance at the excitation wavelength). By comparing the integrated areas, the yield of fluorescence relative to pristine PPerAcr is estimated and the results are shown in Table 1. Further investigation of the transient luminescence from PPerAcr reveals a number of different emissive contributions to the photoluminescence spectrum with differing lifetimes (see Appendix C). It is not possible to spectrally resolve these contributions in time and it is very difficult to determine the effects of donor addition on the spread of lifetimes. However, on normalising the steady state emission spectra from Figure 4-1a, all are found to have an identical spectral shape; it would therefore seem unlikely that there is a changing contribution from the different emissive states for the different samples. In order to validate the relative emission yield found above, the relative fluorescence has also been estimated from steady-state photoluminescence measurements and are shown in Table 4-2. These values are in principal less accurate due to the imprecise correction of spectral defects caused by the monochromators and photomultiplier tube in the experimental set up. The good correlation between the two estimates confirms the order of photoluminescence quenching and the 0.01 relative yield of emission in copolymer 3.

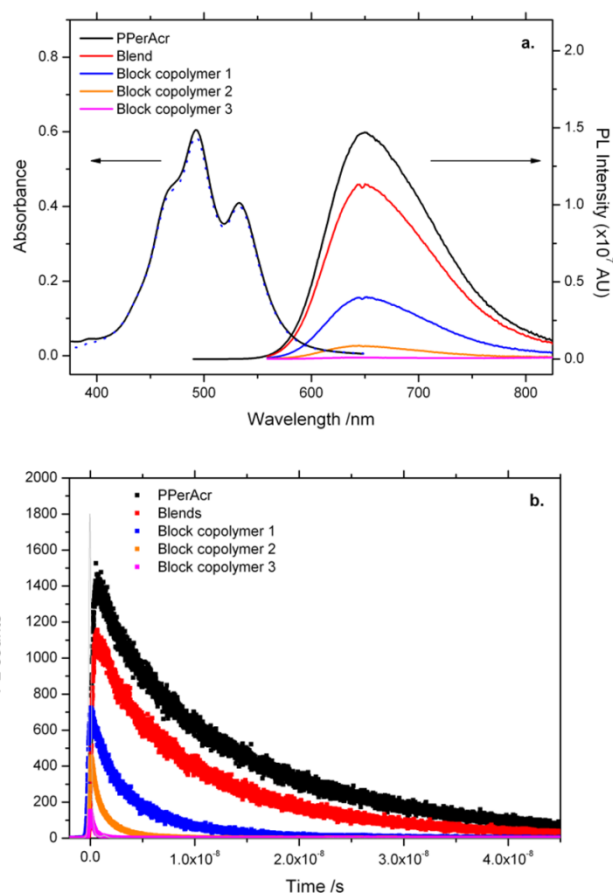


Figure 4-1

Figure 4-1a shows steady state absorption spectrum of homopolymer PPerAcr film (solid black line) and block copolymer 1 (dotted blue line), and photoluminescence spectra of homopolymer PPerAcr (solid black line), polymer blend (dashed red line) and block copolymers 1 (dotted blue line), 2 (dotted orange line) and 3 (dotted purple line) excited at 470 nm. Figure 4-1b shows transient photoluminescence data comparing pristine PPerAcr (black) with polymer blend (red) and varying molecular weight block copolymers (1, 2 and 3 in blue, orange and purple, respectively). Thin films were excited at 467 nm while emission from the perylene bisimide was measured at 630 nm. The photon counting was performed for the same amount of time in each experiment. The instrument response function is shown in grey (solid line) and has a full width at half maximum of 250 ps. Traces are corrected for minor differences in optical density at the wavelength of excitation.

Direct evidence for free charges in illuminated thin films of donor-acceptor material comes from observing changes in sample absorption in the red and near infra-red region of the visible spectrum. Films excited by a laser at 500 nm exhibit absorption features at 720, 800 and 950 nm; one such spectrum is shown in Figure 4-2a. Thin films of block copolymer, optically excited at 500 nm, were probed 2 μ s after excitation with light at varying wavelengths; the resultant change in absorption due to excitation is plotted and shows features we attribute to the presence of perylene bisimide anions. This is confirmed by the other two absorption spectra shown in the figure: the black squares are data taken by Gosztola et al. (reproduced from reference ¹⁶⁴) for an electrochemically reduced small molecule, substituted perylene diimide; the green squares are absorption data from a film of block copolymer 2 on ITO/glass in tetrahydrofuran with 0.01 M tetrabutylammonium perchlorate as a conducting electrolyte and held at -1.75 V relative to a platinum reference. Gosztola et al. assign their

spectrum to the radical anion of the perylene diimide derivative, which is unambiguously seen in our spectroelectrochemical data. Whilst the spectrum taken by TAS for a solid film of block copolymer 2 shows broadened features, the peak positions and relative intensities agree with the solution data to within the error of the experiment. The features seen in the block copolymer thin films are not present without excitation and are not present in pristine PPerAcr films.

Table 4-2
Relative fluorescence yields of blend and block copolymer series

Polymer	Quantum Yield of Fluorescence (relative to pristine PPerAcr) by TCSPC at 630 nm	Quantum Yield of Fluorescence (relative to pristine PPerAcr) by steady-state
Blend	0.63	0.78
Block Copolymer 1	0.19	0.27
Block Copolymer 2	0.04	0.06
Block copolymer 3	0.01	0.01

Figure 4-2b shows the transient of perylene bisimide anions, as observed at 720 nm, in thin films of polymer blend and block copolymers 1, 2 and 3. All samples show anion absorption with lifetimes on the order of microseconds. The amplitude of the signal (magnitude of change in optical density – $\Delta O.D.$) in this figure is directly related to the number of anions present (Beer-Lambert law); this implies that (for time scales before 10 μs) there is a trend of increasing charge carriers present with decreasing molecular weight of block copolymer, consistent with increased exciton dissociation seen in Figure 4-1. The inset in Figure 4-2b shows a log-log plot of selected transient absorption traces of block copolymer 3 from the main graph; a linear fit corresponding to a single power-law ($\Delta OD \sim t^{-\alpha}$) is indicative of a single decay mechanism with competing recombination versus transport dynamics.¹⁵³ We find that all traces shown in Figure 4-2 exhibit power-law decays with a single exponent in the range $\alpha = 0.3-0.5$, although only data and fit for block copolymer 3 is presented for clarity. The exponent taken from the inset graph, gives $\alpha = 0.49$ for polymer 3, suggesting the presence of thermal traps limiting the diffusion of charges, as has been reported in MDMO-PPV:PCBM ($\alpha = 0.3-0.4$)¹⁵² and P₃HT:PCBM ($\alpha = 0.3-0.7$)^{52,63} blends.

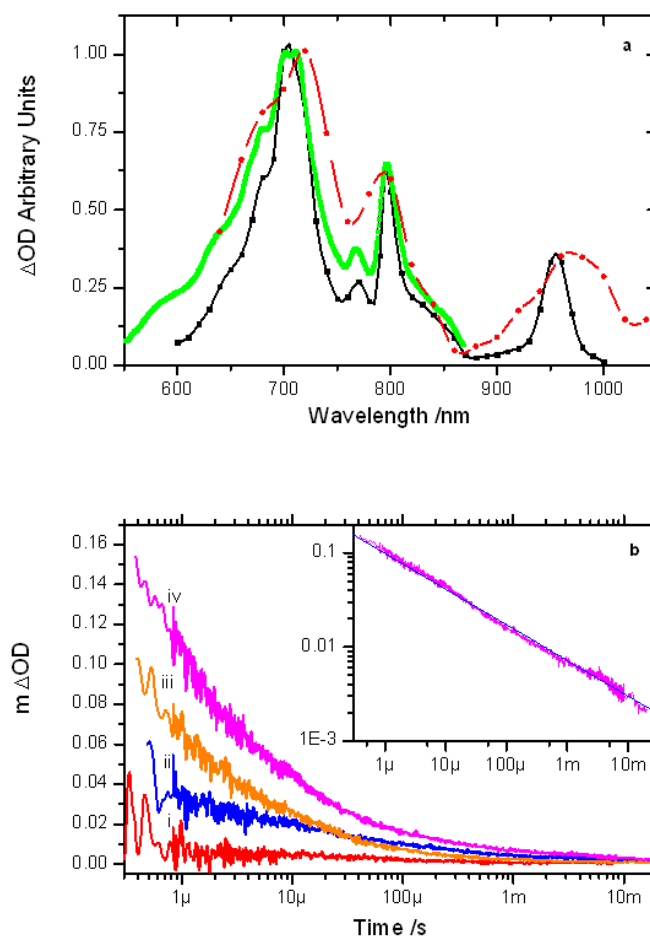


Figure 4-2

Figure 4-2a shows the transient absorption data for block copolymer 2 collected 2 μ s after an excitation pulse at 500 nm (red circles). Thin film samples were probed at varying wavelengths to form a transient spectrum. The figure also shows overlaid a spectroelectrochemical absorption trace of block copolymer 2 (green squares) and of a small molecule substituted perylene diimide reproduced from reference ¹⁶⁴ (black squares). Lines are shown as a guide to the eye. Figure 4-2b shows transient kinetic traces obtained when observing absorption due to perylene bisimide anions at 720 nm; polymer blend (red line,) and block copolymers with varying molecular weights, 1, 2 and 3 (blue, orange and purple lines) excited at 500 nm. The graph inset shows transient absorption data on log-log plot with linear fit for block copolymers 3. Samples are excited at 500 nm with energy densities of 60-80 μ J cm⁻².

Transmission electron microscopy was employed to determine the nanomorphology of the block copolymer samples. Microscopy images in Figure 4-3 a-c show phase separation in cross sections taken from bulk samples (5-6 μ m thick) of block copolymer. Bulk samples were utilised to observe equilibrium morphology that can be expressed without interference from effects seen in thin films such as confinement or free surface/substrate wetting effects. Dark regions denote perylene bisimide stained by RuO₄ and show ~25 nm wire-like domains in polymer 1 (Figure 4-3a) and ~12 nm wire-like domains in polymer 2 (Figure 4-3b). (Staining is most pronounced at the polymer interface). Polymer 3 does not show discernible phase separation (Figure 4-3c), this is most likely due to a low degree of polymerisation in this polymer which may reduce the segregation strength to a value below the order disorder transition (ODT), leaving the polymer in a disordered state where chains are intermixed. Figure 4-3d shows a 'top-down' TEM micrograph of a thin film composed of random blend of the two homopolymers PPerAcr and PvTPA. It is apparent that the phase separation of the donor-acceptor

domains is on the order of ~ 100-500 nm, considerably larger than the three block copolymer samples. It should be noted that block copolymer morphology in thin films may be different to that exhibited in bulk samples due to free-surface/substrate wetting effects and confinement effects. Different morphological structures may have different interfacial surface areas, however, interfacial separation (in at least one dimension) is limited by the physical length of each block in the copolymer. As such, microscopy images of bulk samples are still instructive for showing microphase separated length scales. For a cross sectional image of block copolymer 1 in thin film, the reader is directed to reference 125.

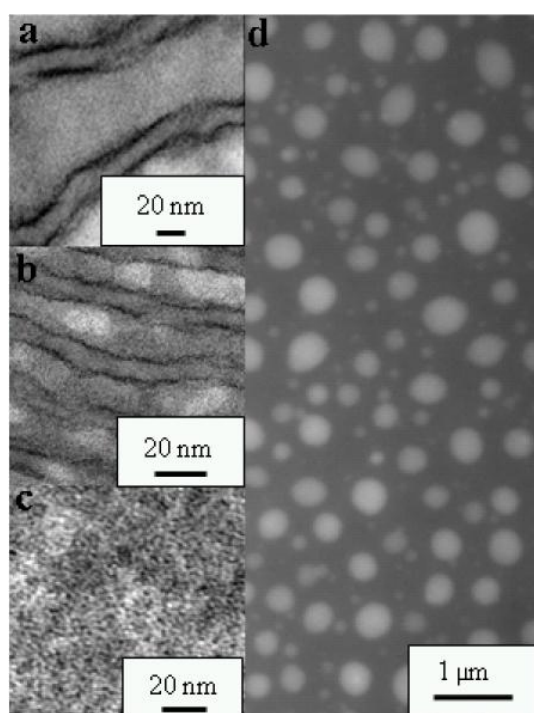


Figure 4-3
The figure shows TEM images of samples preferentially stained with RuO₄ to make PPerAc domains appear dark. Figure 4-3a, 4b, and 4c show thin sections cut from bulk samples of polymer 1, 2, and 3 respectively. Polymer 1 and 2 show nano-wires of perylene bisimide with diameter ~25 nm and ~10 nm respectively in a matrix of poly(vinyltriphenylamine). Polymer 3 exhibits no discernible phase segregation. Figure 4-3d shows a top down image of a thin film made from a blend of PPerAc and PvTPA with large domains of order 100-500 nm. Figures a-c were taken by researchers at Universität Bayreuth.

In a sample of non-conjugated block copolymer (coil-coil type), equilibrium morphology is generally determined by three factors: degree of polymerization (N), relative volume fraction (for a copolymer with A and B type monomers this would be $f_A = 1 - f_B$) and an enthalpic interaction parameter (χ) measuring the energetic penalty for contact between two dissimilar monomers. Both of the former variables are controlled through chemical synthesis whereas the latter is dependent on the choice of monomers making up the chain. Conjugated diblock copolymers by contrast are often rod-coil or rod-rod type and the stiffness of one or both chain components lead to additional interactions that alter the range and variety of possible microphase structures.^{117,118} The polymers with conjugated pendants under investigation in this article form a separate class to standard conjugated and non-conjugated

block copolymers. A flexible backbone should allow for coil-coil type interactions of traditional polymers, however π - π interactions have led to the observation of strong crystallisation in at least one block component (PPerAcr).¹²⁷ It is therefore necessary to rely on empirical techniques to probe segregated microdomain morphology in these polymers. However, from the chemical structure of these polymers it is possible to draw the following conclusions: block copolymers 1, 2, and 3 have similar block volume fractions and are composed of the same two monomer units. They differ significantly only in their degree of polymerization. This difference gives rise to differing size and periodicity of phase separated domain spacings, or in the case of polymer 3, a disordered state. Polymer 2 has a smaller degree of polymerization (corresponding to lower molecular weight) than 1 and has a shorter bulk sample inter-domain spacing, as seen in Figure 4-3. Smaller domains imply that on average, photo-induced excited states are generated closer to an interface where they are dissociated. This is evidenced by a correlation between higher degree of photoluminescence quenching, as illustrated in Table 1, and decreasing N in the block copolymer series and also an inverse correlation between yield of free charge carriers and decreasing N in the block copolymer series, seen in Figure 4-1 and Figure 4-2. Comparing a block copolymer sample with a corresponding weight-for-weight homopolymer blend, the above correlations are maintained when considering domain sizes and inter-domain spacing. In general, polymer blends will phase segregate to minimise component interfacial surface area; this gives rise to large domains compared to a block copolymer, in which phase segregation is constrained.¹²⁵ These large domains with low surface area to volume ratio are seen to give poor photoluminescence quenching and poor free charge carrier yields as compared to the block copolymer samples studied here.

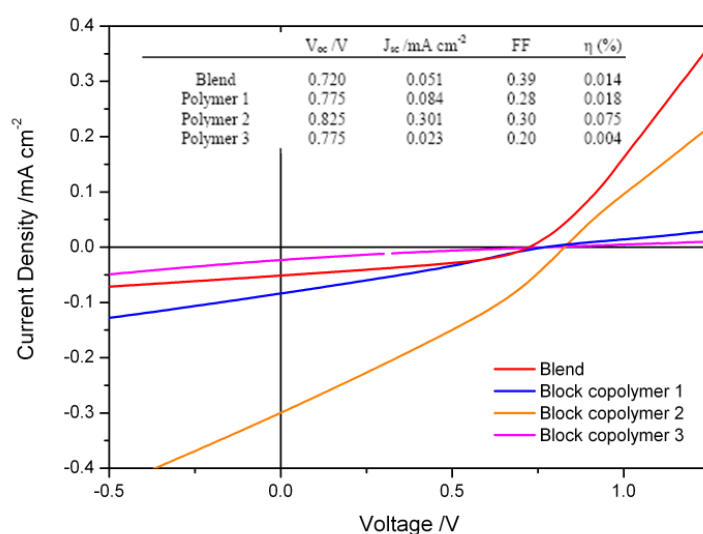


Figure 4-4
The figure shows Current-Voltage characteristics for blend (red line) and polymer 1-3 (blue, orange and purple lines) active layer devices (glass/ITO/PEDOT:PSS/active layer/Al electrode) under AM1.5 solar irradiation. Averaged cell properties are shown in the inset table.

It is apparent from Figure 4-2b that the charge recombination kinetics are less sensitive to modulation in molecular weight of the block copolymer than luminescence lifetime. However, it is interesting to note that the charge recombination dynamics for block copolymer 1 appear retarded, relative to polymers 2 and 3 (compare Figure 4-2b plot (ii) with Figure 4-2b plot (iii)). It is possible that the larger phase separated domains exhibited in block copolymer 1 relative to polymers 2 and 3 serve to move the photo-generated electrons and holes further apart after exciton dissociation (increasing spatial separation of electron and hole), thereby leading to a longer recombination lifetime. This assertion is supported by recent experimental and theoretical studies of charge transport and recombination in polymer blends where larger phase segregated domains were shown to reduce charge recombination and favour charge carrier transport.¹⁶⁵

Photovoltaic devices were fabricated from the materials studied using a standard architecture, glass/ITO/PEDOT:PSS/active layer/Al. Current-voltage traces, as well as key characteristics of these devices, illuminated under AM1.5 simulated solar irradiation, can be seen in Figure 4-4 and the inset table. The most efficient device was made from Polymer 2 (orange line) giving an average power conversion efficiency (PCE) of 0.075% and a maximum of 0.11%. The blend device (red line) shows an improved fill factor of 0.39 yet poor open circuit voltage and short circuit current contributing to a lower PCE of 0.014%. Polymer 1 (blue line) and polymer 3 (purple line) by contrast have poor fill factors with higher open circuit voltage. Polymer 3 exhibits the poorest performance due to a low fill factor and very small short circuit current, leading to a PCE of just 0.004%. This very low efficiency does not follow the trend of increasing open circuit voltage, short circuit current and PCE with decreasing molecular weight set by polymers 1 and 2. Indeed, the performance of a polymer 3 device is significantly worse than one made using the blend. The relatively poor device performance of polymer 3 (compared to polymers 1 and 2) can be rationalized by considering the lack of phase separation as is seen in in Figure 4-3c. Transport in such a homogenous blend will be poor as will contact selectivity at the aluminium electrode.

The inset table in Figure 4-4 shows a trend of increasing open circuit voltage, short circuit current and power conversion efficiency with decreasing domain size that correlates with our spectroscopic observations, but is broken by polymer 3. This suggests that a balance exists between domain sizes that encourage charge generation and those that aid transport and collection. This conclusion is directly supported by the work of Shah et al. who find that a similar balance must be struck in their numerical simulations on rod-coil block copolymers.¹³⁵

It should be noted here, that no post fabrication techniques were used for the data presented in this chapter. This was purposefully done in order to demonstrate the inherent properties of block

copolymers. The results were repeated under separate thermal annealing conditions (1 hr at 210° C or 15 hrs at 165° C in N₂ environment) and found to be qualitatively similar, correlations were maintained, although absolute values differ.

4.5 Conclusion

We have shown evidence that by using block copolymers as opposed to random blends, desirable interfacial phase separation can be achieved and controlled at the materials synthesis stage (degree of polymerization). A low molecular weight block copolymer studied herein (polymer 3) shows photoluminescence quenching of 99% compared to a control chromophore and 62% compared to an equivalent weight ratio random blend. This is attributed to the immediate proximity of excited states (excitons) to interfacial boundaries in block copolymers which also results in observable quantities of long-lived (order μ s) charge separated states in block copolymers and significantly fewer in a blend film. The present findings demonstrate that donor-acceptor block copolymers can be used to control both the nanomorphology and charge separation efficiency in organic solar cells. Finally, we use block copolymers to make OPVs with PCE of 0.11% that outperform a similar blend by a factor of four, but that are based on a degree of polymerization that constitutes a compromise between charge generation and transport/collection. This leads to the main conclusion that one should draw from this chapter: *by using donor-acceptor block copolymers, OPVs can be made whose performance can be affected, with minimal processing, by varying (at the materials fabrication stage) the intrinsic properties of the block copolymer.*

Chapter 5

Results: The influence of post-fabrication annealing and polymer crystallinity on the morphology and interfacial charge transfer dynamics in nanostructured donor-acceptor block copolymer solar cells

5.1 Abstract

In this chapter, we investigate the affects of post fabrication annealing on a series of block copolymers formed from a varying composition of poly-3-hexylthiophene (P₃HT) and poly(perylene bisimide acrylate) (PPerAcr). Two different annealing conditions have been considered: annealing in a chloroform solvent atmosphere and thermal annealing. We then employ spectroscopy and x-ray techniques to determine the differing nature of the annealed materials before performing further spectroscopic and devices studies. Spectroscopic studies on annealed samples lead to the conclusion that crystallinity in P₃HT plays a significant factor in the yields of long-lived charge carriers. Comparing charge yields in these polymers with those observed in P₃HT:PCBM blends, we determine that the degree of long-lived charge generation is comparable in the polymers studied here and P₃HT:PCBM. Both forms of annealing lead to increases in photovoltaic device performance over unannealed samples, although further control over active layer morphology is necessary for these materials to attain their potential.

5.2 Introduction

In the previous chapter, we have conducted a transient optical study addressing the charge separation and recombination in a series of pendant TPA-perylene bisimide block copolymers. More specifically, it was shown that by holding composition constant, and altering the molecular weight (and hence microdomain repetition length) of the donor-acceptor block copolymer, it is possible to control the degree of photoluminescence quenching and importantly, charge generation.¹⁶⁶ In particular, a small chain length block copolymer shows high photoluminescence quenching and an increased yield of long-lived charges compared to a longer chain length block copolymer or homopolymer blend of similar composition. These studies clearly reveal that one of the key parameters controlling charge photogeneration yield and lifetime in self-organizing donor-acceptor block copolymers is the molecular weight of the copolymer. In this

chapter, we build on our initial work and report a systematic study addressing the influence of polymer crystallinity and different modes of annealing (thermal and solvent vapour) on the structural and photophysical properties of a series of block copolymers based upon poly-3-hexylthiophene and perylene bisimide components. Herein it is shown that by annealing at room temperature in a solvent atmosphere, we are able to access morphologies that are not accessible by thermal annealing alone. Moreover, both post-fabrication thermal and solvent annealing are shown to provide an attractive approach to manipulate and control both the structure and morphology of the as-spun block copolymer films. Further to this, transient absorption spectroscopy is used to study the dynamics of charge recombination and show that the crystallinity of the poly-3-hexyl thiophene blocks plays a key role in controlling the charge photogeneration yield and lifetime in such block copolymer materials. These findings are discussed with relevance to the design of self-organizing block copolymer materials for high efficiency photovoltaic devices.

5.3 Experimental

Block copolymers were synthesized as reported elsewhere.¹³⁶ Solutions were prepared in all cases in chloroform (all easily soluble) at concentrations of between 0.5 - 1.5 % by weight. Ultra thin polymer films for spectroscopic work were spin-coated onto glass substrates at a spin rate of 1500 rpm for 40s from the chloroform solutions. Before spin-coating, substrates were pre-cleaned by sonication in acetone and isopropyl alcohol for 20 min.

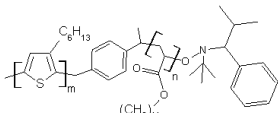
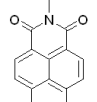
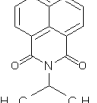
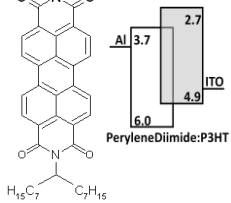
Photovoltaic devices were fabricated by spin-casting PEDOT:PSS (Baytron P) onto glass substrates pre-treated with a thin patterned layer of indium tin oxide (ITO) at a spin rate of 5000 rpm for 300 s. Substrates were pre-cleaned as before and additionally cleaned by sonication in de-ionized H₂O. Samples were then annealed at ~150 Celsius in air before a polymer film was spin-coated at 1500 rpm for 40s from polymer solutions in chloroform at ~0.5 % by weight. Samples were then annealed as below, before final contacts were applied. A lithium fluoride blocking layer was then deposited by evaporation to a thickness of 7 Å. Patterned aluminium contacts were then evaporated to 200nm thick to give devices with active area of 0.045 cm².

Samples for thermal annealing were held at 222 Celsius under Nitrogen for 10 minutes (the polymers melt at these temperatures). The hotplate was then switched off, and the samples allowed to cool with the hotplate over approximately 40 minutes. Solvent vapour annealing was performed using an apparatus similar to that described elsewhere and whose set up is found in Chapter 3.¹⁶⁷ Films were annealed in chloroform vapour for 30 minutes under a stream of vapour laden nitrogen moving at 50 sccm at 90% saturation. Vapour was removed by a stream of pure nitrogen flowing at 20 sccm for ~1 hour.

5.4 Results

The structure of the block copolymers studied herein can be found in Table 5-1. The polymers contain an acceptor block consisting of pendant perylene bisimide groups strung from a non-conjugated backbone (PPerAc) and a donor block of region-regular poly-3-hexylthiophene (P₃HT). In this block copolymer series, the chain length of P₃HT remains constant, while the number of monomer units of PPerAc is increased from 9 to 29 (an increase in percentage PPerAc by weight from 51% to 81%). For full information about the series, see Table 1.

Table 5-1
Block copolymer series molecular characteristics

Polymer Shorthand	Polymer Designation	Mn / g mol ⁻¹	Degree of polymerisation block m (P ₃ HT)	Degree of polymerisation block n (PPerAc)	Percentage (by weight) PPerAc	PDI	Polymer Molecular Structure
BCP-1	P ₃ HT-b-PPerAc	16000	29	9	51%	1.24	
BCP-2	P ₃ HT-b-PPerAc	16900	29	11	59%	1.25	
BCP-3	P ₃ HT-b-PPerAc	21000	29	19	72%	1.31	
BCP-4	P ₃ HT-b-PPerAc	24000	29	29	81%	1.51	

Thin films of block copolymers from the series of Table 1 are studied in three different conditions. The first condition represents films spin cast from chloroform. The second condition involves thermal annealing of the as-spun films whilst third condition involves solvent vapour annealing in chloroform of the as-spun films.

We first consider the steady-state UV/vis spectroscopy of the block copolymers under study. Absorption measurements on films spin cast from chloroform and subsequently subjected to post fabrication annealing can be seen in Figure 5-1. Pristine P₃HT and pristine PPerAc subject to identical conditions are included to help identify components in the block copolymer spectra. Comparing the block copolymer series in Figure 5-1a, we observe very similar peak positions with differing relative intensities. It is apparent that there is a small blue shift (~2 nm) in the peak at 494 nm with increasing perylene component as well as a decrease in absorption intensity of the peak at 535 nm and the bands at 400nm and 600nm; the trend is continued when comparing the block copolymers to pristine PPerAc (ie. 0% P₃HT component). In pristine PPerAc, there is structure in the absorption spectrum associated with interacting perylene moieties; the peaks at 493 nm and 534 nm are associated with the vibronic progression due to absorption of small molecule

perylene bisimide derivatives in solution. However the relative oscillator strengths of the progression and red absorption tail ($> 550\text{nm}$) are indicative of intermolecular transitions.¹⁶⁸⁻¹⁷⁰ The dashed line in Figure 5-1a, illustrates the absorption characteristics of a film of regio-random P₃HT, which exhibits a broad and featureless spectrum indicative of low intermolecular order. In P₃HT, additional order typically leads to an enhanced oscillator strength at the 550 nm and 600 nm transitions, leading to more structure in the absorption spectrum at these wavelengths.¹⁷¹ Such order is not observed in the block copolymer spectra at 600 nm where the absorption is almost exclusively due to P₃HT. From these observations, we conclude that the as spin cast films of block copolymer contain no significant amount of crystalline P₃HT. The differences in absorption spectra between polymers in the series are simply due to the changing ratios of non-crystalline P₃HT and 'as spun' PPerAcr.

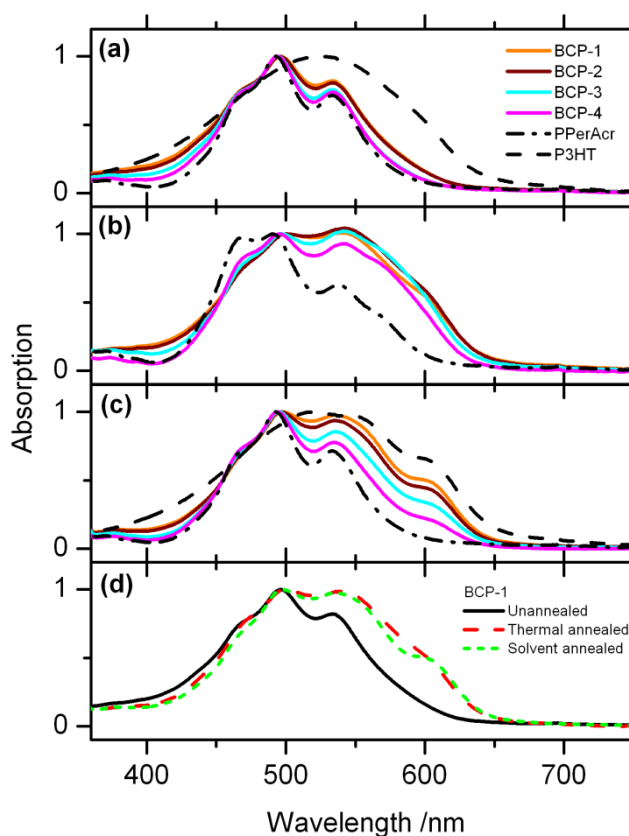


Figure 5-1

The figure shows normalised absorption for block copolymer and homopolymer thin films annealed under different conditions. Figure a shows as-spun films while figure b shows films subjected to thermal annealing at 220° for 10 minutes followed by a slow cool. Figure c shows films that have been solvent annealed in chloroform vapour (90% saturation) for 30 minutes followed by slow venting (in pure nitrogen). Polymers BCP-1, BCP-2, BCP-3 and BCP-4 are coloured orange, dark red, cyan and magenta respectively. Homopolymer films subject to the same treatment conditions are shown where appropriate; pristine P₃HT is shown as a dashed line while pristine PPerAcr is a dot-dashed line. Figure d shows the normalised absorption of a thin film of block copolymer BCP-1 after spin casting (solid line), thermal annealing (long dashes) and solvent vapour annealing (short dashes).

The absorption spectra for thermally annealed samples can be seen in Figure 5-1b along with a sample of homopolymer PPerAcr, annealed in a similar fashion. Thermally annealed pristine P₃HT is not included for

clarity, but the absorption after thermal annealing is well documented and is practically identical to that after solvent vapour annealing (shown in Figure 5-1c).^{171,172} Considering first the homopolymer PPerAcr film, there is a decrease in overall absorption (not shown) and a change in the ratio of peak heights, although not peak positions. The shoulder at 470 nm has become a separate peak whose strength has reduced least, whereas the peaks at ~493 nm and ~534 nm decay by 55% and 50% respectively. Additionally, the absorption tail is extended further into the red, though it is still negligible above 600 nm. Such changes are not due to thermal degradation as TGA shows weight loss only at much higher (>300° C) temperatures; additionally, the original spectrum may be recovered by annealing in chloroform vapour. The changes are in the same direction as those attributed to increasing aggregation of substituted molecular perylene bisimide in solution and it is concluded (*vide infra*) that changes upon thermal annealing are accompanied by an increase in intermolecular order. The decrease in absorption strength (as observed for the pristine homopolymer PPerAcr) is in contrast to absorption in a pristine film of P3HT in which absorption is seen to increase across the whole spectrum.^{63,78} There is also a much more defined structure in the spectrum of annealed P3HT due to increasing intermolecular order.¹⁷¹ The block copolymer series show a compounded absorption made up from annealed PPerAcr and annealed P3HT; this leaves the spectral waveforms looking remarkably similar.

The normalised absorption spectra for solvent vapour annealed samples are shown in Figure 5-1c. Annealing pristine PPerAcr films in a chloroform solvent vapour atmosphere alters the absorption spectra as demonstrated by Hüttner et al.¹⁶⁷ However, upon quenching with nitrogen (regardless of quenching rate we applied) the absorption spectra are rendered identical to those obtained immediately after spin casting (prior to any post-treatment). The block copolymer series however shows very distinct absorption features correlating with increasing percentage of PPerAcr component. All block copolymer films show a distinct shoulder at 610 nm, associated with crystalline P3HT. It is pertinent to note that the prominence of this shoulder decreases in a linear way with decreasing percentage P3HT component.

It is seen from Figure 5-1 that the absorption band of pristine PPerAcr at above 600nm is not greatly affected by thermal or solvent vapour annealing. Changes in the absorption spectra of the block copolymer series at such wavelengths can therefore be attributed to changes in the absorption due to P3HT. On spin casting, the degree of crystallinity in P3HT is small and the absorption of the block copolymer due to P3HT component is largely hidden by the features attributed to PPerAcr. Both thermal annealing and solvent vapour annealing induce changes in the crystalline nature of one or both components. As can be seen in Figure 5-1d, the absorption spectra of films of block copolymer BCP-1 with 51% by weight PPerAcr, the degree of order in the P3HT component determined purely by the absorption band at above 600 nm is very similar in each case.

In order to further analyse the features observed in our absorption data, we have performed wide angle x-ray diffraction (WAXD) on powder samples subjected to thermal and solvent vapour annealing. Results of these experiments are seen in Figure 5-2 and Figure 5-3. Figure 5-2a shows WAXD data for the block copolymer series as well as pristine P₃HT and pristine PPerAcr after thermal annealing. In thermally annealed pristine PPerAcr, we observe narrow peaks centred at 2.9°, 4.0° and 26°. These peaks are not yet assigned to specific reflections as they are still the subject of further investigation. In thermally annealed pristine P₃HT, reflections are seen at 5.4° and 23° assigned to (100) and a composite peak from the (002) and (020) reflections. These reflections are associated with the lamellar packing distance of 16Å and a π - π stacking distance of 7 Å respectively.^{15,173,174} The block copolymers show a combination of peaks from P₃HT and PPerAcr in varying degrees. Importantly, while all block copolymers show signs of PPerAcr peaks, BCP-3 and BCP-4 (which have the highest percentage component PPerAcr) show no peaks from P₃HT reflections. This is most clearly seen in Figure 5-2b, in which the intensities have been normalised and Figure 5-2c, in which wider angle reflections have been magnified.

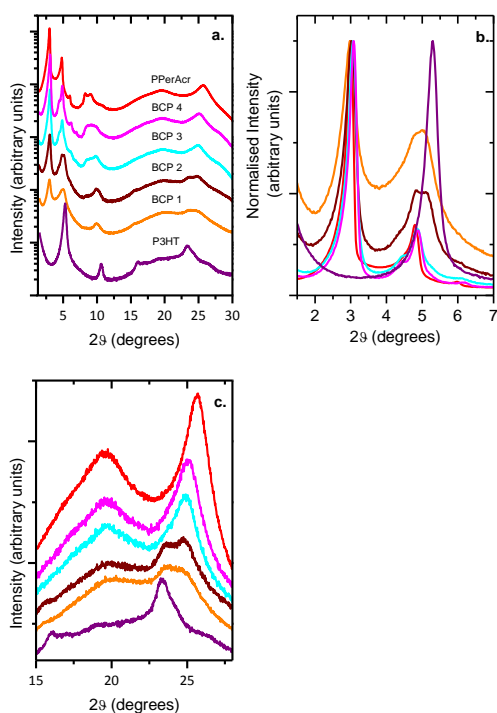


Figure 5-2
 Figure 5-2a shows WAXD data for samples of pristine PPerAcr, P₃HT and polymers BCP-1 – 4 that have been thermally annealed. Background levels have been offset for clarity. Figure 5-2b shows the same traces superposed after normalisation. Figure 5-2c shows a magnified portion of Figure 5-2a; the vertical ordering of samples in the image is the same as for Figure 5-2a. This data was recorded by researchers at Universität Bayreuth.

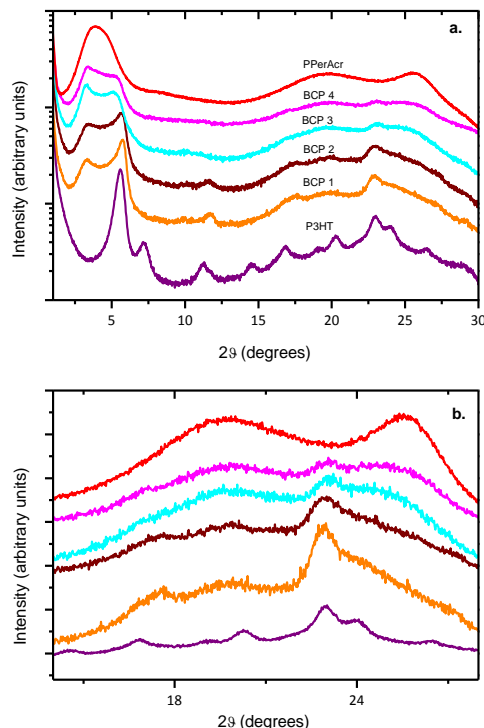


Figure 5-3
 Figure 5-3a shows WAXD data for samples of pristine PPerAcr and P₃HT as well as polymers BCP-1 – 4 that have been solvent annealed in a vapour of chloroform. Background levels have been offset for clarity. Figure 5-3b is a magnified image of a portion of Figure 5-3a; the vertical ordering of samples in the image is the same for both images. This data was recorded by researchers at Universität Bayreuth.

Figure 5-3a shows WAXD data for the series of polymers after solvent vapour annealing in chloroform. There are immediately apparent, differences between the solvent vapour annealed and thermally annealed homopolymers. Compared to a thermally annealed sample, the reflections in PPerAcr are now very much broader, and the two resolved peaks at 2.9° and 4.0° are now smothered by a single broad peak centred at $\sim 4^\circ$, although the peak at 26° remains as before. This broadening implies qualitatively that there is less order in the material than a thermally annealed sample. Solvent annealed P₃HT shows reflections at similar positions to thermally annealed P₃HT, although the signal is much stronger. Interestingly, all polymers in the block copolymer series show peaks from both PPerAcr and P₃HT. In addition, there is a correlation between enhanced P₃HT reflections and decreasing percentage PPerAcr component, seen at 5.4° and in Figure 5-3b at 23° .

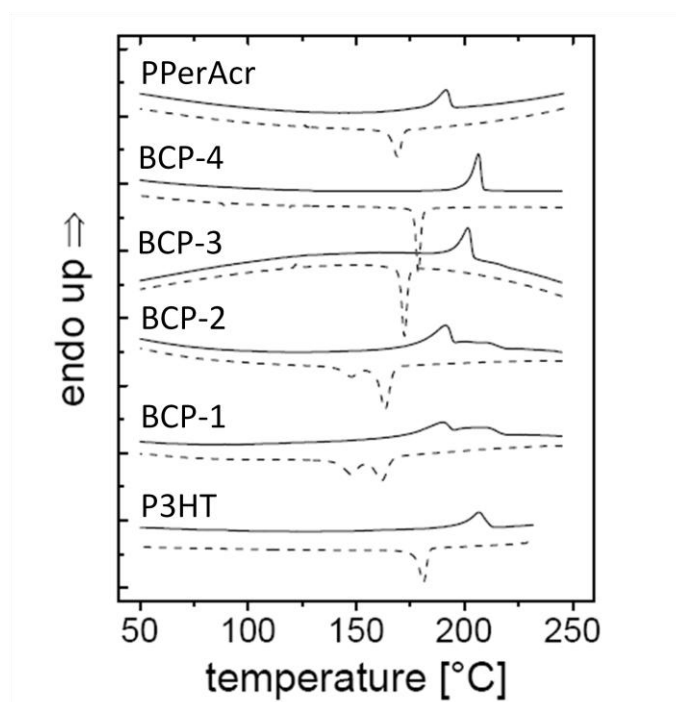


Figure 5-4

The figure shows differential scanning calorimetry of PPerAcr, P₃HT and polymers BCP-1 – 4; endothermal is up. Heating (solid lines) and cooling (dashed lines) were performed at 10 K per minute. Note the Double peaks in BCP-1 and BCP-2 corresponding to melting and crystallisation of both the P₃HT and PPerAcr compared to single peaks in BCP-3 and BCP-4 which correspond to PPerAcr transitions alone. This data was recorded by researchers at Universität Bayreuth.

Differential scanning calorimetry was carried out on each block copolymer and pristine polymer and the results are shown in Figure 5-4. Thermograms were measured three times at a rate of 10 K/minute and found to be stable. Polymers BCP-1 and BCP-2 display two endotherms on heating and two exotherms on cooling attributed to melting and crystallisation in each of the donor/acceptor constituents as is commonly observed in block copolymers. The lower temperature melting peaks and higher temperature peaks for crystallisation are found to be due to PPerAcr by temperature dependent x-ray measurements. In block copolymers with higher weight fraction PPerAcr, only a single transition (of the PPerAcr component) is easily observed on heating or cooling. Accompanying information can be found in Table 5-2 which shows

that the enthalpy for melting of the P₃HT component decreases with increasing percentage of PPerAcr down to the point where it is no longer seen in BCP-4. The reason for the larger undercooling of P₃HT compared to PPerAcr in polymers BCP-1 and BCP-2 and loss of P₃HT thermal transitions in polymers BCP-3 and BCP-4 is not clear, although we tentatively propose that crystallisation of the PPerAcr will be favoured due to its higher mobility as a side chain component. This occurs to such an extent in polymers BCP-3 and BCP-4 that crystallisation of the P₃HT component is almost entirely kinetically suppressed. Thermal annealing of thin film samples for spectroscopy was performed in a way that emulated the cooling curves of the DSC thermograms. In this way, films of polymer BCP-3 and BCP-4 were generated with little crystalline P₃HT in.

Table 5-2
Polymer melting and crystallization temperatures measured by DSC

* In block copolymer samples, melting enthalpy is for P₃HT component

Compound	T _{m1} [°C]	T _{m2} [°C]	T _{c1} [°C]	T _{c2} [°C]	ΔH _m [J/g]*
P ₃ HT	208	-	180	-	13.1
PPerAcr	191	-	169	-	9.8
BCP-1	190	211	148	162	10.3
BCP-2	191	211	148	163	8.8
BCP-3	202	-	172	-	-
BCP-4	206	-	179	-	-

Scanning electron microscopy (SEM) was employed to determine the surface morphologies present in block copolymer films. The results of such studies are presented in Figure 5-5. Figure 5-5a-d show SEM images of polymers BCP-1 – 4 respectively, with worm like light regions of PPerAcr in a matrix of darker P₃HT. These domains show no long range order, but are similar in size and appearance to those observed in bulk samples of other block copolymers containing PPerAcr component.^{128,129,137} Independent of composition, all four block copolymer samples show distinct phase segregation with similar surface morphology. There is no clear correlation between weight fraction of PPerAcr and the average PPerAcr domain width which is approximately 15 nm, however the fibrils enlarge in length from BCP 1-4.

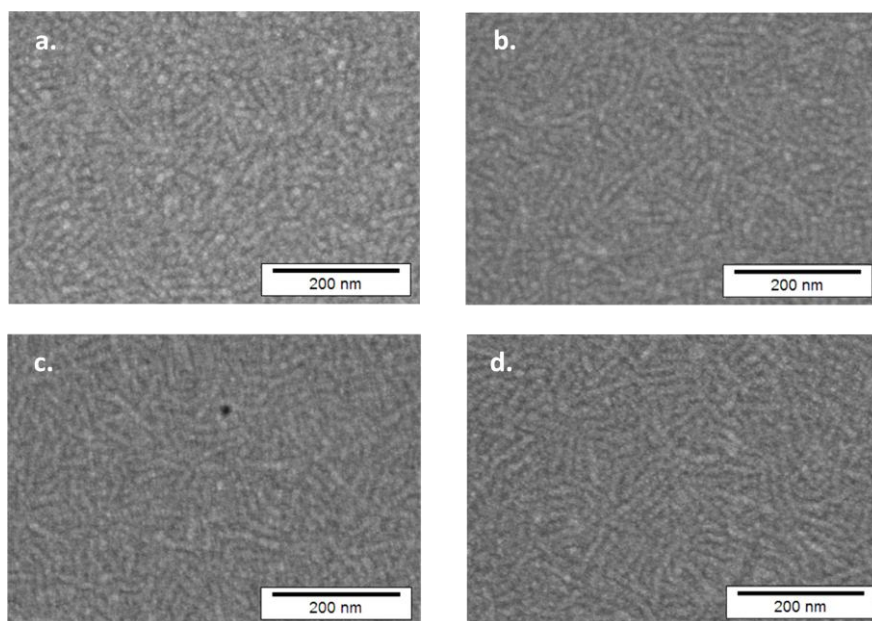


Figure 5-5
 Figures a, b, c and d show scanning electron micrographs of the surface of solvent vapour annealed thin films made from polymer BCP-1, BCP-2, BCP-3 and BCP-4 respectively. Before imaging, the film surfaces were sputtered with a small amount of Pt to prevent charge build up. Light regions are due to the PPerAcr component.

We consider next the photoinduced charge transfer processes occurring in the donor-acceptor block copolymer samples. Transient absorption spectroscopy (TAS) is a time domain pump-probe technique that has frequently been used to characterise the presence and nature of photo-generated species in polymer-small molecule and polymer-polymer blends.^{63,151,175,176} We have previously used TAS to identify and investigate long lived photo-generated anions in block copolymer samples with the same acceptor as is used in the current study (see Chapter 4).¹⁶⁶ The transient spectrum of photo-generated cations in P₃HT small molecule blends has similarly been reported and is well characterised.^{172,177} Figure 5-6 shows transient spectra taken at 1 μ s after excitation for polymer BCP-1, for a blend of P₃HT:PCBM and for a block copolymer PPerAcr-b-PvTPA. All block copolymers from this study (independent of annealing conditions) show identical transient spectra to that of polymer BCP-1 and are omitted for clarity. From this spectrum, we note the presence of PPerAcr anions and of P₃HT cations and that the ratio between them is independent of composition. The decay dynamics of the spectrum are independent of wavelength implying a single decay mechanism for both species. It is important to note that no signals are seen when investigating pristine homopolymer films.

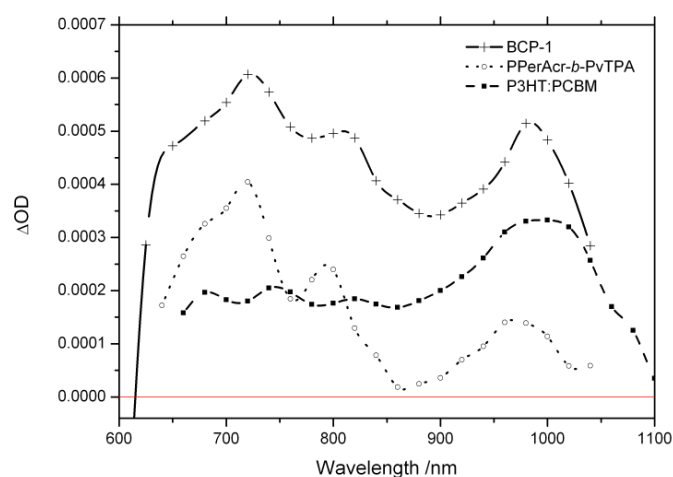


Figure 5-6

Figure 5-6 shows transient spectra for thin polymer films taken 1 μ s after excitation at 500nm (excitation density was 60-80 μ J cm⁻²). The solid black crosses show the transient spectra for polymer BCP-1 (solvent annealed). Also shown are the transient spectra for PPerAcr-b-PvTPA (open circles) and a blend of P₃HT:PCBM (open squares); both of these are scaled arbitrarily to allow clear observation of the all spectra. Lines are included as a guide to the eye.

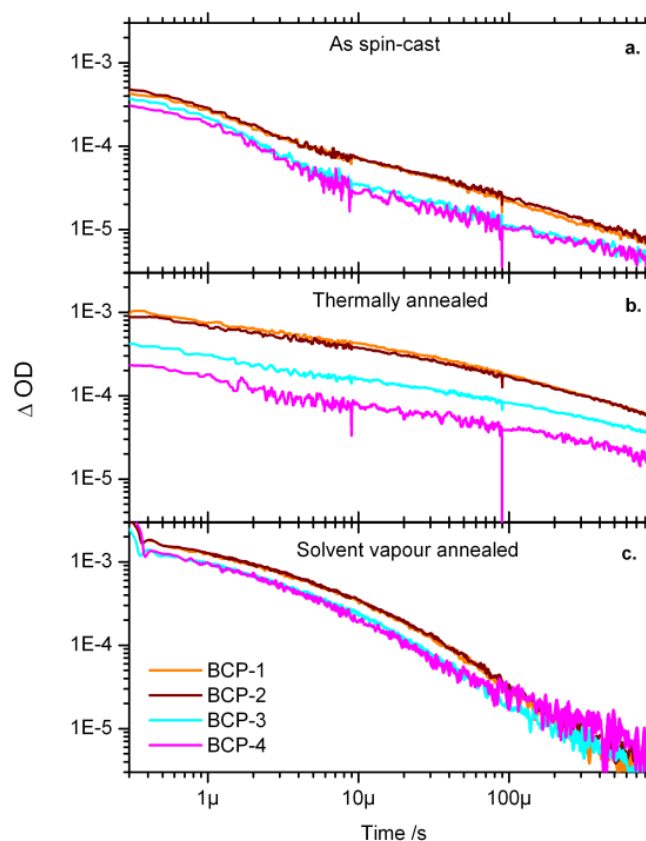


Figure 5-7

Figure 7 shows transient absorption kinetics at 720nm for polymers BCP-1 (orange), BCP-2 (brown), BCP-3 (light blue) and BCP-4 (pink). Excitation was at 500nm with fluence between 60-80 μ J cm⁻². Figure a shows the as spin cast (from chloroform) dynamics, whereas Figure b and c show the decay dynamics in thin films similarly spin cast, but then subjected to subsequent annealing steps. Films in Figure b underwent a thermal anneal at 220° for 10 minutes before slowly cooling with the hotplate for ~40mins. Films in Figure c were annealed in an N₂ atmosphere with 90% saturation of chloroform vapour for 30mins before being slowly purged with pure N₂.

The decay kinetics of the photo-generated polarons (at 720nm) are shown in Figure 5-7 for different annealing conditions; corrections have been made for differences in ground state absorption at the wavelength of excitation. Figure 5-7a shows transient absorption decays for 'as spin cast' polymer films. Increasing signal corresponds to a higher yield of charges and it is clear that there are more charges present in films of polymer BCP-1 and BCP-2 with lower weight fraction PPerAcr, although this small difference could also be due to a similar trend with decreasing overall chain length, as shown in the previous chapter.¹⁶⁶ The decay dynamics fit well with a model describing diffusion limited bimolecular recombination.¹⁵³ Of significantly more interest are the intensities of signals from films that have been thermally annealed, shown in Figure 5-7b. In this case, there is a clear correlation of increasing charge yield with decreasing weight fraction PPerAcr. Moreover, it is clear that the yield (at 1 μ s) in polymer BCP-4 has decreased slightly compared to its unannealed state; the yield in polymer BCP-3 has remained practically constant, while the yield in the other two block copolymers is increased by over double after thermal annealing. Figure 5-7c shows the decay dynamics at 720nm of transient features in block copolymer films subjected to solvent vapour annealing in chloroform. As with unannealed films, there is a small difference between films with varying block copolymer composition, however, in all cases, the charge yield (at 1 μ s) is increased three-fold relative to that observed for the unannealed films.

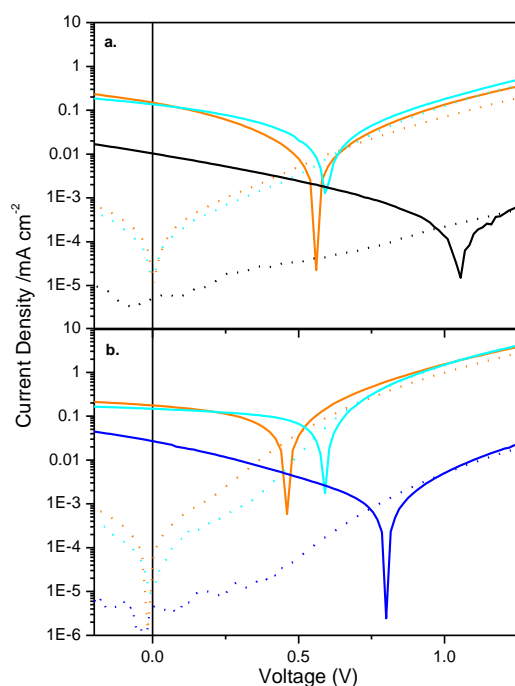


Figure 5-8

The figure shows current density-voltage traces for photovoltaics under AM1.5 solar simulation using polymer BCP-1 (Figure a) and polymer BCP-4 (Figure b) as active layers in an ITO/PEDOT:PSS/Active layer/LiF/Al device architecture. Black and dark blue trace corresponds to the unannealed devices; orange traces are the solvent annealed devices and light blue traces are thermally annealed devices, dashed lines are dark currents.

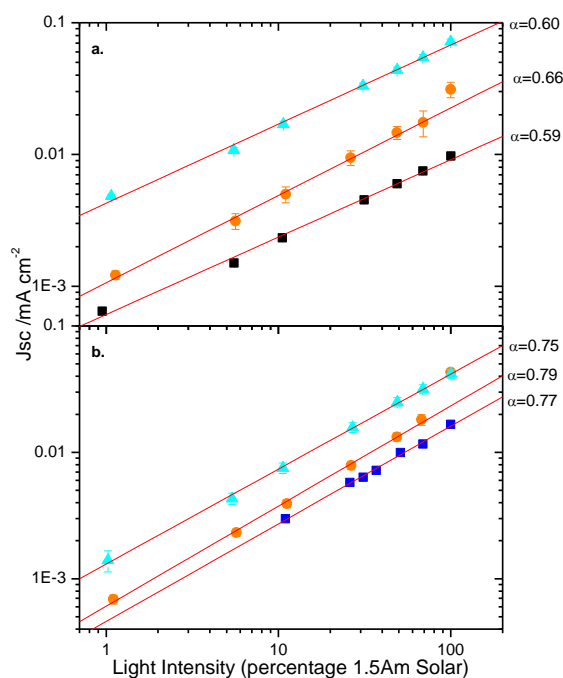


Figure 5-9

The figure shows plots of short circuit versus light intensity for polymer BCP-1 and BCP-4 in figures a and b respectively. As per Figure 5-8, orange traces correspond to solvent annealed devices and light blue traces are thermally annealed devices. The red lines are power law fits whose exponent is shown to the right of the figure. These data are averaged for a number of devices.

Photovoltaics were fabricated with block copolymers BCP-1 – 4 as active layers, sandwiched between Glass/ITO/PEDOT:PSS and LiF/Al. Figure 5-8 shows current density-voltage (JV) curves for photovoltaics fabricated using polymers BCP-1 and BCP-4 as an active layer in preannealed condition as well as after solvent vapour and thermal annealing. Both forms of annealing (thermal and solvent) have a significant and positive effect on the performance of the devices. While open circuit voltage (V_{oc}) drops, the short circuit current (J_{sc}) is significantly increased and the fill factor increases, which lead to enhanced power conversion efficiency. The increase in J_{sc} is broadly independent of annealing condition and active layer composition. Such an increase could be the result of polymer rearrangement from non-equilibrium morphology of highly intermixed chains (due to strain from spin casting) to phase segregated domains like those seen in Figure 5-5. The accompanying increase in fill factor is commonly related to an increase in mobility, thus this suggests that annealing may also result in improved mobility.^{13,178} Intensity dependence of the short circuit current was measured in each of the devices and is shown in Figure 5-9. The dependence in each case was found to be highly sub-linear and was quantified by fitting using a power law whose exponent is also shown in the figure.

5.5 Discussion

We begin our discussion by describing the effects of spin casting on film structure. By spin-casting from a low boiling point solvent at high angular velocities, it is possible to fabricate thin films of polymer in which there is little order. During spin casting of a polymer, solvent leaves the film at a rate that is in part dependent on the volatility of the solvent. As solvent is driven from the film, the thickness of the layer decreases as does the polymer mobility; at a certain concentration, the interplay between these effects can lead to the polymer being trapped in a glassy state (assuming that the polymer bulk glass transition temperature is well above room temperature).¹⁷⁹ If a blend of polymers is deposited, such a glassy state may be phase mixed and not phase segregated. By introducing solvent back into the film via solvent vapour annealing, or by thermal annealing, polymer mobility is sufficiently increased to allow further evolution towards a morphological equilibrium. However, during this annealing, other effects will play a role in the final morphologies observed. Such effects include: polymer-substrate and polymer-free surface interactions, polymer blend interactions (eg. de-mixing) and polymer self interactions, of both inter- and intramolecular nature (eg. π - π stacking and increasing chain linearity); additionally, during solvent vapour annealing, polymer-solvent interactions are important. The kinetics of annealing have also been shown to alter film morphologies, for example the rate of solvent quenching.^{180,181} Exercising control over this array of variables is no mean feat; but by using block copolymers and selecting certain fabrication and annealing

histories, we have reproducibly made thin films with the same material, but differing final morphologies that have subsequently been used in photophysical and device studies.

The annealing histories chosen are based on a common starting morphology showing little molecular order and no visible signs of phase segregation. Annealing in a vapour of chloroform and subsequent slow purging of the solvent leads to films containing aggregated PPerAcr and crystalline P₃HT component as seen in the absorption in Figure 5-1c and confirmed by WAXD, Figure 5-3. Independent of composition, this form of annealing leads to phase segregated morphology whose surface structure is seen by SEM, in Figure 5-5, to show nano-wires of PPerAcr embedded in a P₃HT matrix. An alternative path for increasing polymer mobility relies on thermal annealing by melting and slow cooling. Differential scanning calorimetry in shown in Figure 5-4 illustrates that as we cool from the melt, PPerAcr crystallises first. A second crystallisation peak (of the P₃HT component) is only seen in polymers BCP-1 and BCP-2. Wide angle x-ray diffraction in Figure 5-2 confirms that there is little crystalline P₃HT in block copolymers with a higher weight percentage of PPerAcr; the PPerAcr component becomes more ordered after thermal annealing in all polymers in the series. This leads to the conclusion that ordering of the PPerAcr component inhibits further crystallisation of P₃HT in these block copolymers. This maybe thought of in an analogous way to the solidification of liquid binary metallic alloys, in which composition has a strong effect on the size of crystal domains. A phase diagram was recently published for P₃HT:PCBM blends which are found to also follow this behaviour.¹⁸² In our system we suggest a similar mechanism, except that the two components are chemically bound and so solidification of one component will sterically hinder the mobility of the second. This is not uncommon and it has been observed in crystalline-crystalline block copolymers that the sequential order of phase segregation or crystallisation (often influenced by composition) can have a profound effect on final film morphology.^{122,183-185} However, by solvent vapour annealing in chloroform, we can encourage crystallisation of the P₃HT component, while leaving the PPerAcr component in its initial 'as-spun' state.

The transient absorption signal from a film made from polymer BCP-1 is seen in Figure 5-6 and can be compared to those of P₃HT:PCBM⁶³ and PPerAcr-b-PvTPA.¹⁶⁶ Doing so, we can isolate the signal from P₃HT cations alone and hence give an indication of the efficiency of free charge generation in the polymers studied herein compared to a standard 1:1 P₃HT:PCBM blend. The best match between the spectrum for polymer BCP-1 and a composite spectrum of PPerAcr anion and P₃HT cation is achieved for a composite ratio of ~1:1 (PPerAcr⁻:P₃HT⁺) and is shown in Figure 5-10. Such a fitting shows two problems: i) while the peak at 980 nm is fit well using this ratio, there is a small deviation in the accuracy of the fit between 750 and 900 nm; ii) the 1:1 ratio also implies an issues with regard to the reported values of the extinction coefficient of each of these radical species. By charge conservation, the number of charges in each film

should be the same. This means that comparing transient absorption is equivalent to comparing extinction coefficients, according to a modified Beer-Lambert law seen in Equation 5-1. In this equation: d is the film thickness (in cm^2), p is the concentration of absorbing species (cm^{-3}), N_A is Avagadro's number, ϵ is the extinction coefficient (and is a function of wavelength) and ΔOD is the change in optical density.

$$\Delta OD = \frac{1000d\epsilon(\lambda)p}{N_A} \quad \text{Equation 5-1}$$

Gosztola et al. have reported on the extinction coefficient for a perylene bisimide species similar to ours (and that, in the previous chapter, was shown to exhibit remarkably similar absorption) of $8 \times 10^4 \text{ M}^{-1} \text{ cm}^{-1}$ at the peak at 720 nm (in solution).¹⁶⁴ If there is no change in this coefficient on going from solution to the film, this would imply an extinction coefficient for P_3HT^+ of $8 \times 10^4 \text{ M}^{-1} \text{ cm}^{-1}$ at the peak at 980 nm. This value is four times that found by Clarke et al. and twice that found by Shuttle et al. using a charge extraction method to determine the number of absorbing species in a (solid state) sample.^{154,186} Addressing point one, the mismatch could be due to additional absorbing species in P_3HT , such as two-dimensional delocalised polarons as seen in $\text{P}_3\text{HT}:\text{PC}_{70}\text{BM}$ blends.^{177,186} Point two is however more worrying; the expected extinction coefficient ratio of 4:1 $\text{PPerAcr}^-(720 \text{ nm}):\text{P}_3\text{HT}^+(980 \text{ nm})$ (from Clarke and Gosztola) should result in a significantly lower peak in polymer BCP-1 at 980 nm as seen in Figure 5-10. One possible explanation is that the extinction coefficient of the perylene bisimide species is decreased on going from solution to solid state. Further work is ongoing to clarify this point.

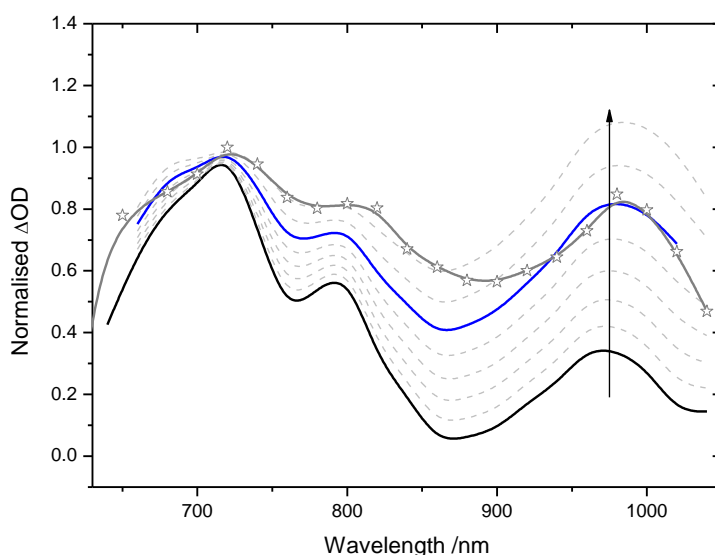


Figure 5-10
Shows the normalised transient spectrum of polymer BCP-1 (open stars) as well as the various ratios of $\text{P}_3\text{HT}^+ : \text{PPerAcr}^-$ spectra used in the fitting. The PPerAcr^- spectrum is shown (black solid line) as well as the summed spectra of $\text{PPerAcr}^- : \text{P}_3\text{HT}^+$ in the ratios 9:1, 8:2, 7:3 etc. up to 3:7 (dashed lines following arrow). The 1:1 fit is shown in solid blue.

We continue therefore with an extinction coefficient ratio of 1:1 at peak transient absorbance, bearing in mind the above discussion. Figure 5-11a shows the transient decay for a film of solvent annealed polymer BCP-3 excited by laser pulse of 500 nm at $65 \mu\text{J cm}^{-2}$ and probed at 980 nm. The decay has been corrected for the ground state absorption of the film at 500 nm and corrected to show the fraction of the absorption due solely to the P_3HT^+ cation based on the above considerations (ie. 74%). A film of annealed $\text{P}_3\text{HT}:\text{PCBM}$ (1:1 blend by weight) excited by $75 \mu\text{J cm}^{-2}$ laser pulse at 500 nm, probed at 980 nm and corrected for ground state absorption is also shown in Figure 5-11a. At 1 μs , it is clear that there is more charge in the block copolymer than the $\text{P}_3\text{HT}:\text{PCBM}$ blend (3 times more in fact). This seems rather unlikely, considering $\text{P}_3\text{HT}:\text{PCBM}$ devices have been prepared with external quantum efficiencies of $\sim 75\%$.¹⁸⁷ However, the above analysis does not take into account the fact that there is a non-linear response of the charge yield with excitation density. Figure 5-11b and c clarify the anomaly by showing the intensity dependence of the decays at 980 nm. In Figure 5-11b, the transient kinetics are shown for an excitation density of $\sim 3 \mu\text{J cm}^{-2}$ and there are seen to be more P_3HT polarons in $\text{P}_3\text{HT}:\text{PCBM}$ than the block copolymer. However, the yields are broadly comparable at these lower intensities.

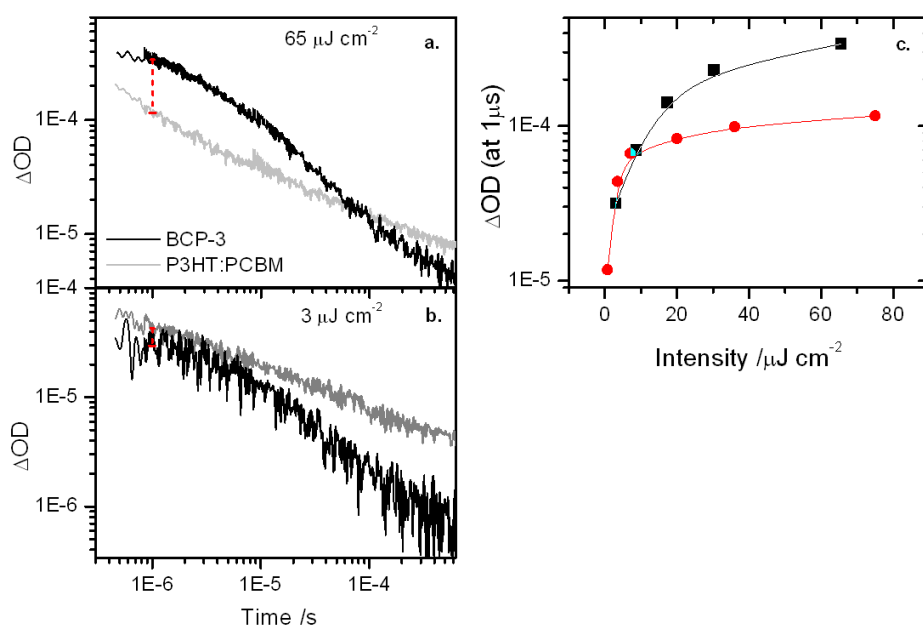


Figure 5-11

Figure a and b show the transient decays of solvent annealed polymer BCP-3 (black line) and thermally annealed $\text{P}_3\text{HT}:\text{PCBM}$ blend (grey line) probed at 980 nm after excitation by laser at $\sim 65 \mu\text{J cm}^{-2}$ and $\sim 3 \mu\text{J cm}^{-2}$ respectively. The red lines are a guide to the difference in absorption at 1 μs . Figure c shows the transient signal at 1 μs from solvent annealed polymer BCP-3 (black squares) and thermally annealed $\text{P}_3\text{HT}:\text{PCBM}$ blend (red circles) at various excitation densities. The lines are a guide to the eye. All traces have been corrected for minor differences in ground state absorption at the excitation wavelength of 500 nm. Additionally, the polymer BCP-3 data has been multiplied by 0.74, the fractional contribution of the P_3HT^+ cation to the transient absorption at 980 nm. The data for annealed $\text{P}_3\text{HT}:\text{PCBM}$ is reproduced from reference¹⁸⁶.

A comparable yield of cations might be expected on the basis of energetics, as PPerAcr has similar HOMO and LUMO values compared to those reported for PCBM. It is postulated that photoexcited states that find a donor-acceptor interface pass through a charge-transfer state before separating into charges in each

medium.^{49,51} By means of numerous possible decay pathways, the presence of this state significantly decreases the efficiency of dissociation. However, it was recently shown in polythiophene:PCBM blends that if the photoexcited singlet state energy is greater than the energy of the charge-transfer state by some excess, the degree of charge dissociation correlates with this surplus.⁵² The energy of the charge-transfer state was estimated to be the difference between the electron affinity of the acceptor and the ionisation potential of the donor (and some constant but unknown binding energy). As a result, if one were to consider a P₃HT:PCBM blend and replace PCBM with another acceptor with similar electron affinity (as long as there is no change in singlet excited state energy) one might expect little change in yield of long lived charges. Additionally, there is a broad positive correlation between transient absorption yields at 1 μ s after excitation and device short circuit current.¹⁵⁵ Based on the above analysis therefore, these polymers show the potential to reach record polymer-polymer organic photovoltaic device efficiencies.

The different forms of annealing that have been applied produce a strong variation in long lived charge yields as can be seen in Figure 5-7. Such variations are seen to correlate with crystallinity of the P₃HT component in the block copolymers. In thermally annealed films of polymers BCP-3 and BCP-4 where little crystalline P₃HT is observed, there is very little change in charge yield compared to the unannealed case. This is compared to the case of solvent annealing in chloroform in which both absorption and WAXD data show crystallisation in the P₃HT component in all polymer films and TAS data shows increased charge yields across the polymer range. These findings may be analysed by considering a similar effect, first observed by Clarke et al. for P₃HT:PCBM blends.¹⁷² In this study, an increase in charge photogeneration on annealing was attributed to a decrease in ionisation potential with increasingly crystalline P₃HT, leading to an increase in free energy for charge separation. Other researchers have also observed changes in the energy levels of P₃HT:PCBM charge-transfer state on annealing.¹⁸⁸ When taken in context with our results, the observed trends imply that a similar effect is likely occurring and that crystallinity in the P₃HT component plays a significant role in the yield of long lived charges for these polymers.

Despite the good relative charge yields seen in photo-physical studies of the block copolymer series, device performance is still limited, mainly by J_{sc} . Plotting J_{sc} versus light intensity (from 1% to 100% of 1 sun under AM1.5 solar irradiation) for these devices (shown in Figure 5-9) yielded sub-linear plots with exponents between 0.6-0.8. Such extreme non-linear behaviour (< 0.75) is beyond explanation by a space charge limited regime and is likely to be a result of a bimolecular recombination limited regime.¹⁸⁹ It is possible that if structures like those seen in Figure 5-5 are common morphologies for these films, there may be many non-wired or mixed domains acting as 'dead ends' in which bimolecular recombination is the only pathway available for charges. This conclusion is further indicated by the work of Tao et al. on photovoltaics made

using a block copolymer with semiconducting blocks similar to ours.¹³⁹ These authors find that devices exhibiting short range ordered nano-structures yield higher J_{sc} than those made with long range order. They attribute this to poorer transport due to a lack of directionality in the long range ordered morphologies.

5.6 Conclusion

A series of block copolymers have investigated that are formed from a varying composition of poly-3-hexylthiophene (P3HT) and poly(perylene bisimide acrylate) (PPerAcr). Two different annealing conditions have been considered: annealing in a chloroform solvent atmosphere and thermal annealing. By annealing in a vapour of chloroform, it is possible to induce morphologies that are not accessible by thermal annealing alone. Specifically, we can selectively affect the crystallinity of P3HT while leaving low intermolecular order in PPerAcr. Spectroscopic studies on annealed samples lead to the conclusion that crystallinity in P3HT plays a significant factor in the yields of long-lived charge carriers. Comparing charge yields in these polymers with those observed in P3HT:PCBM blends, we determine that the degree of long-lived charge generation is comparable in the polymers studied here and P3HT:PCBM. Both forms of annealing lead to increases in photovoltaic device performance over unannealed samples, although further control over active layer morphology is necessary for these materials to attain their potential.

The main conclusion from this chapter is therefore: the generation of long-lived (and thus free) charges in these block copolymers is not a limiting factor in device performance. Devices are limited by bimolecular recombination, although whether this is due to a high interfacial surface area or un-wired domains is a matter still under investigation.

Chapter 6

Results: A study of an all conjugated donor-acceptor-donor triblock copolymer

6.1 Abstract

In this chapter, we investigate an all conjugated donor-acceptor block copolymer that is the analogue of a well studied blend system. The photophysics and morphological differences between the block copolymer and blend are investigated. The block copolymer shows all the photo-physical and morphological characteristics of an intimately mixed system and displays a comparatively high yield of emission from an interfacially bound charge transfer state often known as an exciplex. We find that photo-induced charge yields in both the blend and the block copolymer are small and that these most likely account for the poor overall device efficiencies seen. However, block copolymer devices outperform blend devices by an order of magnitude in power conversion efficiency and this is probably due to better homogeneity in block copolymer film morphologies which leads to improved collection at the electrodes.

6.2 Introduction

In previous chapters, the block copolymers considered have employed donor-acceptor systems that have not been heavily studied in their constituent donor:acceptor blend form. We have included the blend system alongside the block copolymer in a previous investigation (found in Chapter 4) and been able to draw conclusions based on those experiments; however, detailed knowledge of the properties of a materials set have historically required concerted effort over many years using many complementary investigative techniques and often by many research groups. A good example of this is the blend between poly(3-hexylthiophene) (P3HT) and [6,6]-phenyl C₆₀-butyric acid methyl ester (PCBM). This blend was first used in photovoltaics in 2003 achieving ~3.5% efficiency,^{64,190} but since then there have been ~900 publications involving the pair (up to the start of 2010) and device efficiencies now stand at ~5%.¹⁸⁷ In this chapter, we investigate a block copolymer formed from a donor-acceptor materials set that is well studied and whose properties are thought to be well understood.

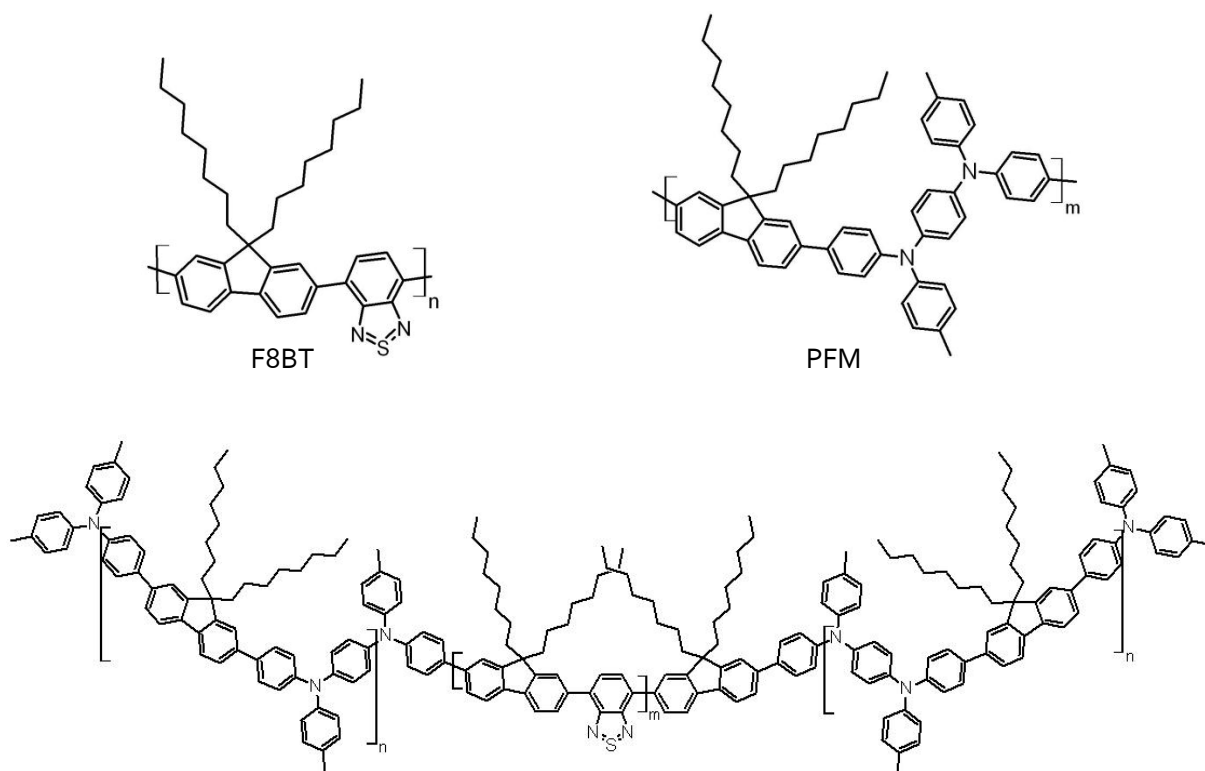


Figure 6-1
 Showing structures of polyfluorene copolymers poly(9,9'-dioctylfluorene-co-benzothiadiazole) (F8BT), poly(9,9'-dioctylfluorene-co-bis-N,N'-(4-tolyl)-bis-N,N'-phenyl-1,4-phenylenediamine) (PFM) and the ABA triblock copolymer formed from them.

The components for the block copolymer considered in this chapter are the polyfluorene copolymers poly(9,9'-dioctylfluorene-co-benzothiadiazole) (F8BT), as an electron transport material, and poly(9,9'-dioctylfluorene-co-bis-N,N'-(4-tolyl)-bis-N,N'-phenyl-1,4-phenylenediamine) (PFM), as a hole transport material; both of these may be seen in Figure 6-1. The block copolymer formed is an ABA triblock (also shown in Figure 6-1) with a polymer weight ratio of PFM to F8BT of 1:1 ($M_n = 43,500 \text{ kg mol}^{-1}$ and $\text{PDI} = 1.30$ ie. $A_{12}B_{40}A_{12}$). PFM is an analogue of poly(9,9'-dioctylfluorene-co-bis-N,N'-(4-butylphenyl)-bis-N,N'-phenyl-1,4-phenylenediamine) (PFB) with similar properties. PFB has been extensively studied in conjunction with F8BT to elucidate thin film structure and to relate morphology to photovoltaic performance.¹⁹¹⁻¹⁹⁹ The depth of knowledge about these materials in pristine and blend form makes the study of the block copolymer of great interest as more emphasis can be placed on the effects of the inherent structural properties of block copolymers. The following will introduce some of the key features that have been learnt about conjugated polyfluorenes over the past decade during which they have been studied.

Polyfluorene derivatives were well studied initially due to their performance in organic light emitting diodes (OLEDs) in which they were shown to have high charge-carrier mobility, good processability, thermal stability and high photoluminescence efficiencies.²⁰⁰⁻²⁰³ Among polyfluorene derivatives, most show strong, non-dispersive hole mobilities ($\sim 10^{-4} \text{ cm}^2 \text{ V}^{-1} \text{ s}^{-1}$) while electron transport is weak and highly dispersive;³¹

F8BT however is the exception and has been shown to display high ($\mu_{n \text{ max}} \sim 10^{-3} \text{ cm}^2 \text{ V}^{-1} \text{ s}^{-1}$, although still dispersive) electron mobilities.²⁰⁴ Blended polyfluorenes have received attention in OLEDs due to superior electronic properties, broadened emission spectra and improved device performance.^{39,205,206} In devices from these studies, charge injection occurs into an electron transporting polymer, F8BT, and a hole transporting polymer (often poly(9,9'-dioctylfluorene-co-N-(4-butylphenyl)diphenylamine) (TFB)); charges then travel to the donor-acceptor interface where they recombine to form excited states which then fluoresce. Blends of F8BT and PFB by comparison have relatively poor electroluminescence properties and have been shown to be more promising in photovoltaics applications.^{51,207} This is thought to be due to the energetic difference between charge separated states and parasitic localised excitations. A significant amount of work has gone into determining the energies and kinetics of processes in these blends and a brief description of these studies is presented below.

The presence of a neutral state localised at the blend heterojunction interface in F8BT:PFB and F8BT:TFB was first reported by Morteani et al. in 2003.³⁹ In this study, electroluminescence (EL) with very low threshold voltages was explained by a 'reverse photo-induced charge transfer' process in which electron-hole capture at the heterojunction proceeds (to the neutral state) without prior charge injection from one component. A schematic of this processes (adapted from ref: ²⁰⁸) is shown in Figure 6-2. The neutral state was observed to have significant charge-transfer character, be stabilised with respect to charge-separated states (due to conformational relaxation) and to have red shifted, long lived emission compared to individual component exciton emission. Such states have been termed exciplexes due to the similarity of their fluorescence properties to dimeric excited state complexes.

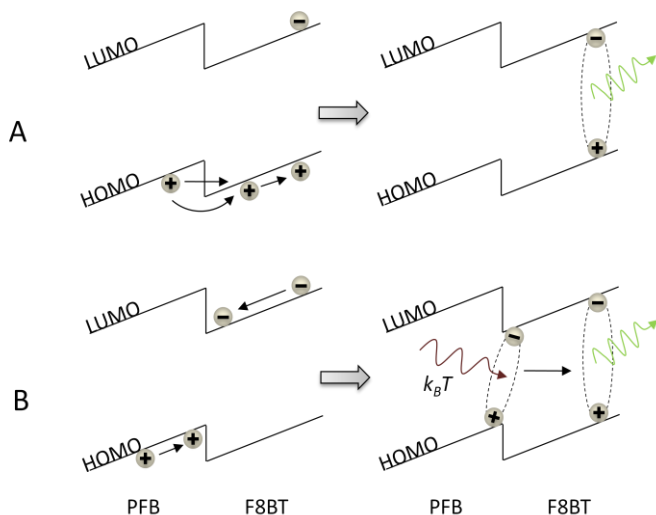


Figure 6-2

In the figure two schematics are shown for electroluminescence in blends of PFB:F8BT. In schematic A, an exciton is formed by injection of a hole across the energetic barrier at the blend interface. This is followed by exciton emission. In schematic B, the electron and hole are trapped at the interface without an injection step. The state formed is known as an 'exciplex'. This state is shown bound at the interface in the lower right hand schematic. This is found to generate excitons in a thermally activated process. The figure is adapted from reference ²⁰⁸.

Temperature dependent time resolved photoluminescence measurements in the study point toward a thermally activated promotion of the exciplex to excitons in F8BT, a feature further investigated by Morteani et al. in 2004.⁵¹ In the more recent investigation, a regeneration mechanism was postulated for the formation of 'secondary' bulk excitons after photoexcitation. Photoexcited states in this case form exciplexes at the interface and then are thermally regenerated to bulk excitons in a cyclical fashion. The

ratio of secondary excitons to exciplexes was found to follow an Arrhenius type dependence with activation energies 200 ± 50 meV (PFB:F8BT) and 100 ± 30 meV (TFB:F8BT). Additional studies on retrapping of secondary excitons at heterointerfaces indicate a strong dependence on blend morphology, an idea which is considered further later in the chapter.^{56,209}

Additionally, electric field dependent photoluminescence (PL) was used to demonstrate a strong positive dependence of exciplex generation on applied field. However, no correlation was found between applied field and exciplex decay rate, leading to the conclusion that the field dependence is due to a (dark) exciplex precursor; this was posited to be a geminate interfacial polaron pair. Estimating the relative dielectric of all polymers studied at 3.5, the authors then go on to successfully apply the Onsager model for field dependent dissociation of a weak electrolyte to determine the electron-hole separation of the geminate pair at ~ 3.1 nm (PFB:F8BT) and ~ 2.2 nm (TFB:F8BT). The higher energy for regeneration of bulk F8BT excitons coupled with the larger thermalised separation for the interfacial geminate pair in PFB:F8BT explain the higher degree of charge dissociation (and poor LED performance) seen in this blend compared to TFB:F8BT. The origins of these effects are due to differing energetics in the two blends leading to different stability of charge separated versus localised states.^{39,54,207}

Another feature of polyfluorenes has been the observance of triplet excited states (from here referred to simply as triplets). In poly(dioctyl fluorene), commonly known as PFO or F8, there is strong evidence for triplets seen in the glassy and crystalline β phase.^{210,211} Initial studies on F8BT by Dhoot et al. also demonstrated the presence of triplets.²¹² However, further work by Ford et al. on F8BT and F8BT:PFB blends showed that triplet formation in the blend is significantly enhanced compared to F8BT homopolymer.²¹³ In the same study, Ford and co-workers also showed a field dependence of the intersystem crossing quantum efficiency in F8BT:PFB blends, but no such dependence in pristine F8BT. The conclusion drawn is that intersystem crossing is enhanced at the interface in either the geminate charge pair or exciplex state due to the smaller electron-hole wave function overlap and thus small exchange energy. This idea has been taken further by Westenhoff et al. who have studied F8BT:PFB blends using ultra-fast transient absorption spectroscopy in order to estimate the rates of relevant decay pathways from an interfacial charge pair.⁵⁵ In doing so, the authors determine that intersystem crossing to form an F8BT triplet exciton outcompetes charge separation leading to only $\sim 10\%$ geminate pair dissociation.

In the following study, we first perform a spectroscopic study comparing the PFM-*b*-F8BT-*b*-PFM block copolymer to a 1:1 blend of F8BT:PFM. We find that the block copolymer exhibits comparatively small domain structure, confirmed by electron microscopy and scanning force microscopy. This information helps to demonstrate the dependence of photo-physical properties of the system on morphology. Photovoltaics formed from these materials are found to be poor, though block copolymer devices significantly

outperform those fabricated using the blend. Additional work looks at the effects of annealing on both block copolymer and blend systems, something that is taken even further in the following chapter.

6.3 Results

Thin films for UV-Vis absorption characterisation were spin coated onto glass slides from ~2% wt. solutions made with toluene. Films studied were made from the PFM-F8BT-PFM block copolymer, a 1:1 weight ratio of the homopolymer blend (PFM:F8BT) and individually from homopolymers PFM and F8BT; the absorption profiles may be seen in Figure 6-3. Peak absorption for homopolymer F8BT is at 470 nm while peak absorption for homopolymer PFM is measured at 380 nm. The similar absorption profiles for the block copolymer and blend support the formulation and 1:1 ratio of PFM and F8BT in the block copolymer.

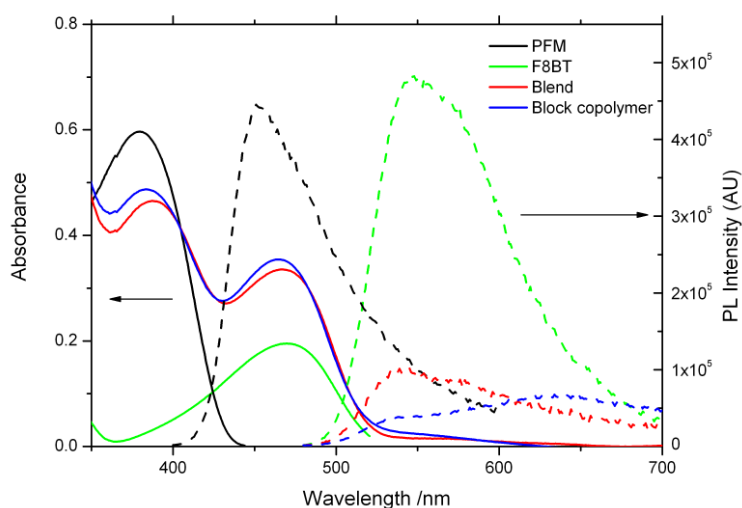


Figure 6-3

Figure 6-3 shows the steady state absorption spectra of homopolymer PFM film (solid black line), homopolymer F8BT film (solid green line), a 1:1 blend (by weight) F8BT:PFM film (solid red line) and a PFM:F8BT:PFM block copolymer film (solid blue line). Also shown is the photoluminescence spectra of homopolymer PFM (dashed black line) excited at 350 nm as well as homopolymer F8BT (dashed green line), polymer blend (dashed red line) and block copolymer (dashed blue line) excited at 465 nm.

Figure 6-3 also shows steady state emission from all samples after irradiation at 465 nm (with the exception of homopolymer PFM, which was excited using a wavelength of 380 nm). Pristine PFM exhibits an emission peak at 451 nm, whereas pristine F8BT has peak emission at 546 nm. By comparison with pristine F8BT we observe a large degree of quenching of emission in films comprising donor-acceptor materials, with a higher degree of quenching seen in the block copolymer compared to the blend (540 nm). A further interesting feature is seen in emission from the block copolymer material; a second (and more prominent) peak is observed that is bathochromically shifted (to 645 nm) from bulk F8BT emission. Such a peak has been observed in similar polymeric systems and is attributed to 'exciplex like' emission from excited states with part intramolecular and part charge transfer character localised at the donor-acceptor interface.^{39,51}

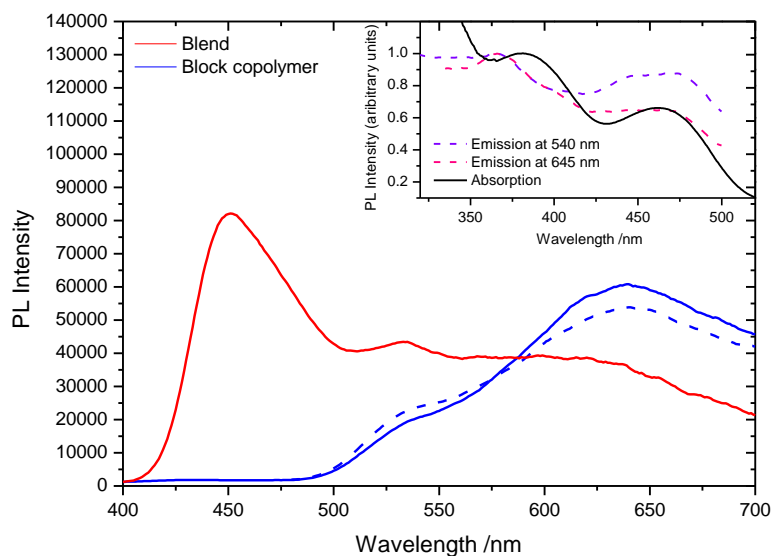


Figure 6-4

Figure 6-4 shows the emission spectra for a thin film of PFM-F8BT-PFM block copolymer excited at 381 nm (blue solid line) and 465 nm (blue dashed line). Also shown is the emission spectra for a thin film of PFM:F8BT 1:1 binary blend excited at 381 nm (red solid line). These traces have been adjusted to account for differences in the absorption strength of each film at the wavelength of excitation. The graph shown inset shows the excitation spectra for the block copolymer sample with emission at 540 nm (violet dashed) and 645 nm (pink dashed) as well as an overlaid absorption spectrum (black solid line). The excitation and absorption traces have been normalised to the peak at between 365-380 nm.

Of further interest is the relationship between excited states generated in each of the individual materials resulting from excitation at peak absorption of the PFM or F8BT component. As such, emission from the blend and block copolymer excited at 381 nm is shown in Figure 6-4. Also shown for comparison is the emission from the block copolymer excited at 465 nm. Considering just the block copolymer, it is clear that regardless of the wavelength of excitation a similar emission profile is observed. Most importantly, excitation at 381 nm results in very little emission from the PFM emission peak (~450 nm). Additionally, a shoulder in the emission is seen at ~540 nm under excitation at both wavelengths. This emission corresponds to radiative relaxation of excited states in F8BT as may be seen in Figure 6-3. Such emission implies that there is very fast energy transfer from the PFM to F8BT component. This could be via two plausible pathways: In the first, excited states of PFM migrate directly to F8BT via Förster energy transfer. The second possible pathway is that PFM excitons are captured at the interface to form exciplexes which then thermally regenerate to F8BT excited states. The stronger ratio of exciplex to excited state F8BT emission after excitation at 381 nm would seem to suggest the second process is more likely, though it is a problem considered further below. The graph inset in Figure 6-4 shows the excitation spectra for emission from the block copolymer at 540 nm (bulk F8BT emission) and 645 nm (exciplex emission) and confirms what is seen in the emission spectra: that exciting F8BT directly yields a higher ratio of F8BT:exciplex emission compared to excitation of PFM. The blue shift in the excitation peak at ~365 nm for both emission

wavelengths compared to the absorption peak (at ~380 nm) is likely due to an overlapping F8BT absorption at ~335 nm.

Also shown in Figure 6-4 is emission from a binary blend of F8BT and PFM excited at 381 nm. It is immediately apparent that in this case while there is some exciplex and bulk F8BT emission, there is also strong emission from the PFM component (at ~450 nm). In this case the coupling between PFM and either F8BT or the exciplex is insufficient to entirely suppress the excited states in PFM.

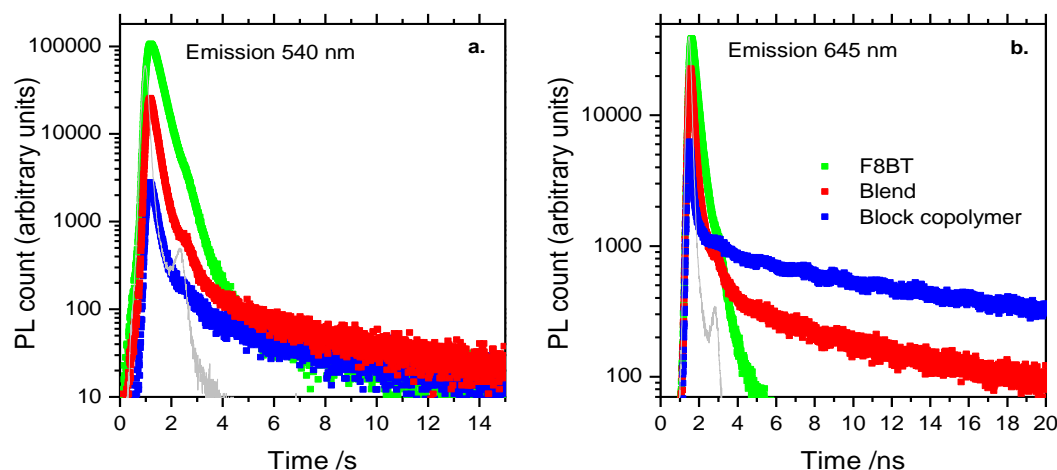


Figure 6-5

Figure 6-5a shows transient photoluminescence data comparing emission at 540nm from homopolymer F8BT (solid green squares), a 1:1 blend (by weight) F8BT:PFM (red crosses) and PFM:F8BT:PFM block copolymer (open blue circles) excited at 467nm. Figure 6-5b shows transient photoluminescence data comparing emission at 645nm from homopolymer F8BT (solid green squares), a 1:1 blend (by weight) F8BT:PFM (red crosses) and PFM:F8BT:PFM block copolymer (open blue circles) excited at 467nm. Single photon counting in each figure was performed for the same time per sample. In both figures, the instrument response function is shown in grey (solid line) and has full width at half maximum of 250ps.

Figure 6-5 shows transient photoluminescence studies on homopolymer F8BT, a PFM:F8BT binary blend and PFM-F8BT-PFM block copolymer performed using time correlated single photon counting after excitation at 467 nm. The emission time for PFM is faster than the instrument response and not shown. Emission was selectively measured at 540nm and 645 nm as shown in Figure 6-5a and Figure 6-5b respectively. Photoluminescence at 540nm is attributed to excited state relaxation in bulk F8BT and from pristine homopolymer F8BT we measure an excited state lifetime of 410 ± 90 ps. From Figure 6-5a the relative quantum yields for fluorescence are found to be 0.03 for PFM-F8BT-PFM block copolymer and 0.19 for the binary blend. For a similar number of chromophores, the block copolymer fluorescence is quenched by ~85% compared to the blend and ~97% compared to pristine F8BT. This confirms the results qualitatively analysed by steady state photoluminescence seen in Figure 6-3. A high degree of fluorescence quenching in the block copolymer is as a result of a higher yield of excited state dissociation at hetero-interfaces due to a smaller average distance between photogenerated excited states and donor-acceptor interfaces as has

been shown in Chapter 4.⁴⁴ Emission from the exciplex state is observed in block copolymer samples and more weakly in blend samples, shown in Figure 6-5b. Singlet emission is observed at this wavelength and retains a lifetime of 410 ps in pristine F8BT, but is shorter lived (within instrument response) in donor-acceptor materials due to the formation of other species. The exciplex decay is longer lived than excited state fluorescence and is found to have a monoexponential decay with time constant 27 ± 2 ns in a sample of block copolymer and 23 ± 2 ns in a blend sample (by fitting to a single exponential at times after singlet exciton emission has decayed). The longer lifetime for the exciplex in the block copolymer compared to the blend is expected based on the basis of more intimate mixing and therefore a higher probability for secondary exciton re-trapping, an effect commented on below. These values are in good agreement with the literature value found for exciplex lifetime for a 1:1 blend of F8BT:PFB spin cast from chloroform of 28 ns; although the value is highly dependent on film morphology.^{55,209}

Emission from the exciplex state is a parasitic loss mechanism to the generation of free charge carriers necessary for the efficient operation of photovoltaics. The exact nature of the exciplex state is largely unclear at present, though it is well known that it resides at the polymer-polymer interface.⁵¹ From both steady state and transient photoluminescence experiments conducted here, it is clear that there is a larger exciplex population in block copolymer films as compared to blend films; assuming that the population of exciplex states is proportional to the heterojunction area, this is then attributable to the larger interfacial surface area present in block copolymers as compared to blends. The assumption that exciplex state population is directly related to the interfacial surface area between n and p type components is reasonable when considering the mechanism for charge separation in conjugated polyfluorene blends proposed by Morteani et al. In the mechanism, photo-excited states may migrate to a heterojunction interface where they dissociate. The geminate charge pair formed either separates, or relaxes into its mutual coulombic potential well and forms a bound exciplex state. Elsewhere, we have shown that a larger interfacial surface area results in a greater number of excited states reaching an interface.¹⁶⁶ As long as the increase in heterojunction area does not affect the ratio of the rates of decay mechanisms for geminate charges at the interface,²⁰⁹ more excited states reaching an interface will result in a proportional increase in the exciplex population. It should be noted that an additional pathway for the decay of exciplex states has been observed in the form of thermal regeneration to bulk excitons in F8BT.^{39,51,208,209} However re-trapping of these singlet excitons and hence formation of exciplex states has been shown to be morphology dependent and will only act to further enhance exciplex emission in finely intermixed samples.²⁰⁹ This idea was investigated by time resolved emission spectroscopy and the results are seen in Figure 6-6.

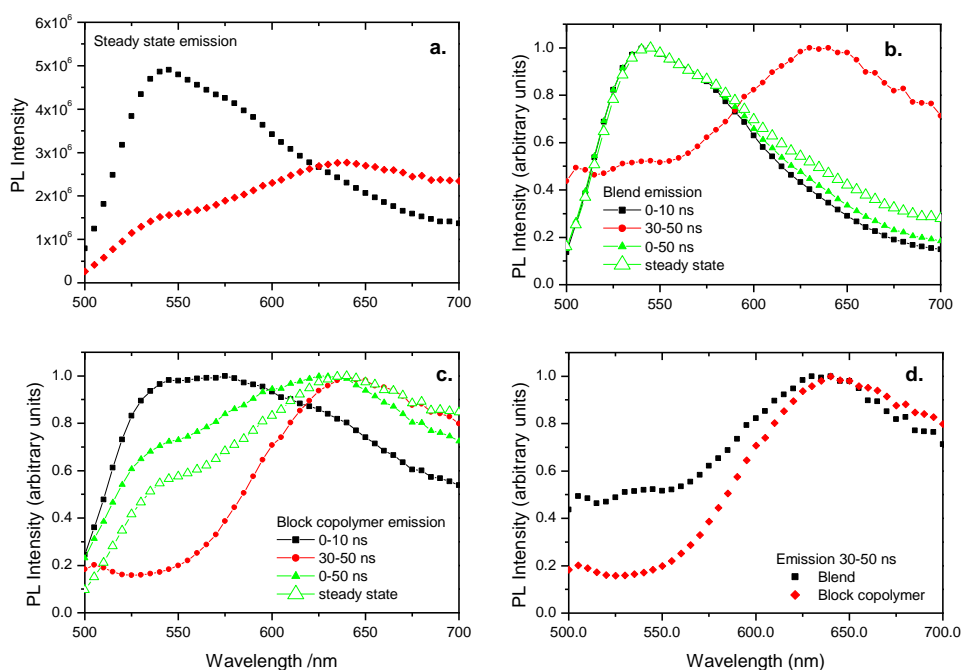


Figure 6-6

Figure 6-6 shows the results of transient photoluminescence studies performed varying the probed wavelength of emission. Excitation in all cases was at 467 nm with a pulse of width ~ 250 ps (FWHM). Figure 6-6a shows the steady state emission for a thin film of 1:1 blended F8BT:PfM (black squares) and for PFM-F8BT-PfM block copolymer (red diamonds). Figure 6-6b and c show normalised emission from the 1:1 blend film and block copolymer (respectively) as an average of the time resolved emission between 0-10 ns (black squares), 30-50 ns (red circles), 0-50 ns (green closed triangles) and steady state (green open triangles). Figure 6-6d shows emission averaged between 30-50 ns for the blend (black squares) and block copolymer (red diamonds) normalised and overlaid.

Figure 6-6b and c show emission from thin films of blended F8BT:PfM and PFM-F8BT-PfM block copolymer respectively. In each sub-figure, the spectra are built up by averaging the time resolved emission; doing so, the contribution of exciplex emission and F8BT bulk exciton emission can be resolved at late compared to early timescales. Figure 6-6d shows the normalised and overlaid emission from films of blend and block copolymer averaged between 30-50 ns; at these timescales, primary excitons in F8BT should have fully decayed and the emission must be due to longer lived species. In both spectra, there is a main peak at ~ 640 nm attributed to exciplex emission, however, there is an additional shoulder seen at ~ 540 nm that is present in both spectra, but significantly enhanced in the blend. In strong agreement with work done by Morteani et al., the additional feature is the result of thermal regeneration (back-transfer) of secondary bulk F8BT excitons from the exciplex state and the degree of phase segregation between the two components.²⁰⁹ While back-transfer is expected to occur in the block copolymer, the higher degree of intermixing means that secondary excitons are re-captured with high efficiency and hence delayed emission from F8BT is small. This is also in agreement with the longer lifetime observed for the exciplex in the block copolymer compared to the blend seen above (Figure 6-5); increasingly efficient re-trapping of short lived secondary excitons is expected to increase the observed lifetime of the exciplex. For near unity re-trapping, the exciplex lifetime should then approach the 'pure' exciplex lifetime; however, despite the high efficiency of re-trapping observed for the block copolymer, the exciplex lifetime (~ 27 ns) is significantly smaller than

the longest time found by Morteani et al. of ~ 54 ns (for a 97.5:2.5 by weight PFB:F8BT blend film spin cast from chloroform)²¹⁰. The reasons for this discrepancy are unclear, although it may be that differing sample preparation histories, leading to differing interchain conformations, in each body of work are to blame. This should be made the subject of further investigation.

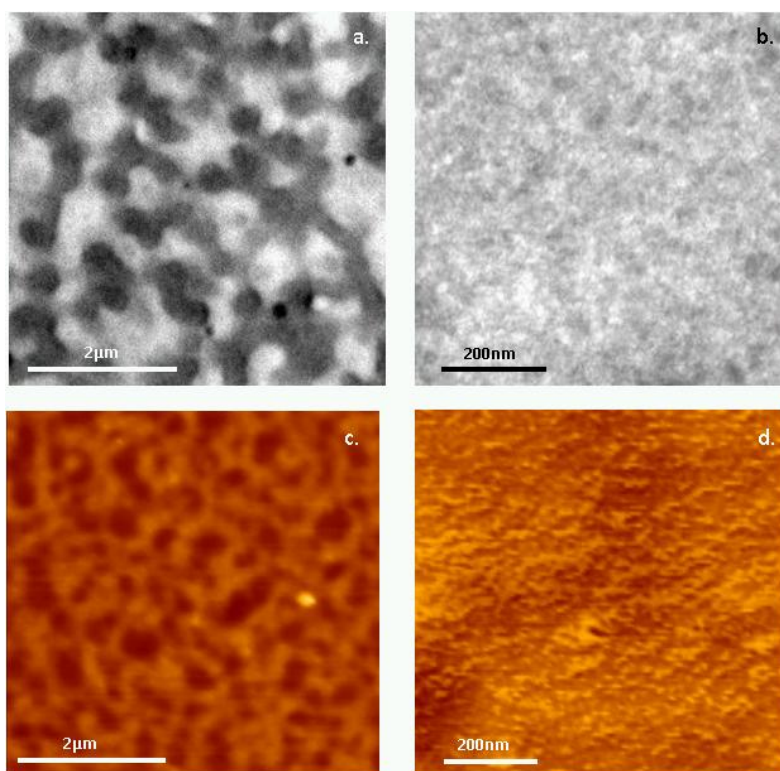


Figure 6-7

Figure 6-7a and b show transmission electron micrographs taken top-down through thin films of a PFM:F8BT blend and PFM-F8BT-PFM block copolymer respectively. Samples were stained with RuO_4 overnight causing the F8BT component to appear darker. Figure 6-7c and d show tapping mode atomic force micrographs of the surface of thin films of a PFM:F8BT blend and PFM-F8BT-PFM block copolymer respectively. The colour code in the AFM image give an indication of topographic height where lighter colour indicates protrusion from the sample surface; the scale is over 125 nm in Figure c and 15 nm in Figure d. Scale bars are included in each image.

Conformation of the degree of phase segregation between differing components in the block copolymer and blend is found by considering the images from Figure 6-7. Films of each sample were either prepared on a sacrificial substrate (PEDOT:PSS) and floated on water before being transferred to Cu grids for top-down imaging by transmission electron microscopy (Figure 6-7a and b), or were prepared on glass and investigated by tapping mode atomic force microscopy (Figure 6-7c and d). Films for TEM were stained overnight in a vapour of RuO_4 , which initial experiments have shown leave the F8BT component dark with Ru and hence appear dark under TEM. Both AFM and TEM images confirm the presence of apparent phase segregation on the order $0.5 \mu\text{m}$ for the blend film (Figure 6-7a and c). Films of block copolymer on the other hand display no such segregation and indeed it is difficult to unambiguously determine whether there is any phase segregation at all (Figure 6-7b and d).

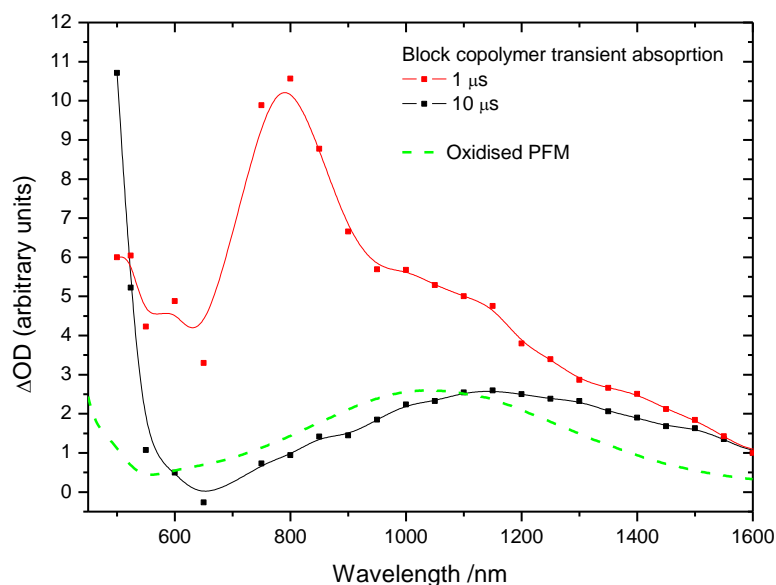


Figure 6-8

Figure 6-8 shows transient absorption data for a PFM-F8BT-PFM block copolymer collected $1\mu\text{s}$ (red squares) and $10\mu\text{s}$ (black squares) after excitation at 450nm . Films were excited at 450 nm by a 4Hz nitrogen pumped dye laser with fluence $50\text{--}70\mu\text{J cm}^{-2}$, while transient absorption was monitored by continuous monochromatic light. Also shown is an absorption spectrum of PFM homopolymer in toluene (green dashed line) that has been chemically oxidised by an amine radical cation stabilised by a hexachloro antimonate counter ion ($\text{N}(\text{PhBr})_3\text{ SbCl}_6$).

Quenching of the excited state in F8BT:PFM polymer blend and block copolymer is accompanied by the emergence of long lived transient absorption features shown for the block copolymer in Figure 6-8. Two features are seen in the block copolymer after excitation at 450 nm . The first is seen at the $1\mu\text{s}$ time scale and peaks at $\sim 800\text{ nm}$, while the second (peaking at $\sim 1150\text{ nm}$) is seen at longer time scales and is shown in the figure at $10\mu\text{s}$ after excitation. A binary blend of PFM and F8BT (1:1 blend by weight) exhibits a spectrum that includes only the feature peaking at $\sim 1150\text{ nm}$ at all time scales observed (not shown). Identification of the broad feature peaking at 1150 nm is confirmed by considering the absorption of a solution of PFM homopolymer in toluene (green dashed line) that has been chemically oxidised by an amine radical cation stabilised by a hexachloro antimonate counter ion ($\text{N}(\text{PhBr})_3\text{ SbCl}_6$). The transient spectrum is bathochromically shifted by $\sim 100\text{ nm}$ compared to the chemically oxidised solution; paralleling the energy shift observed in the ground state absorption peak on going from solution to the solid state. In this way, the broad feature is assigned to a cation (PFM^+) and confirms the presence of long lived charged species in both the blend and block copolymer. The feature seen in the block copolymer at $\sim 800\text{ nm}$ is attributed to F8BT triplets. This determination is made despite a lack of sensitivity to the presence of oxygen. Also, due to the overlap of this feature with the PFM^+ cation, it is very difficult to determine whether the decay is monomolecular (indicative of triplet intersystem crossing to ground). Despite these issues, it is possible to rule out the possibility that the signal is due to F8BT polarons. First and foremost is the differing timescale observed for the decay of this feature compared to PFM^+ ; as such, distinct mechanisms would be required for the decays of these species, which would seem unlikely given a lack of sources for charge beyond

photoexcitation. Moreover, a study of P₃HT:F8BT blends did not yield a peak at 800 nm indicating that it is unlikely that F8BT⁻ polarons are responsible for the feature. Similarly, F8BT⁺ cations are unlikely to be the source of the signal as they have been found (by chemical oxidation and pulse radiolysis) to reside at 680-720 nm, higher in energy than the observed feature.²¹⁴ Triplets of F8BT, on the other hand, have been well studied, and are known to peak at ~800 nm.^{212,213,215}

One minor aside of further interest is the change in the transient spectra observed for films of both blend and block copolymer on ITO/glass (not shown). In these cases, a single broad peak is observed at ~1300-1400 nm which smothers the triplet peak at 800 nm in the block copolymer. This peak is tentatively assigned to electro-reflectance in the ITO, which would imply either that hole injection is occurring from the ITO or there is direct photoexcitation of the ITO.²¹⁵

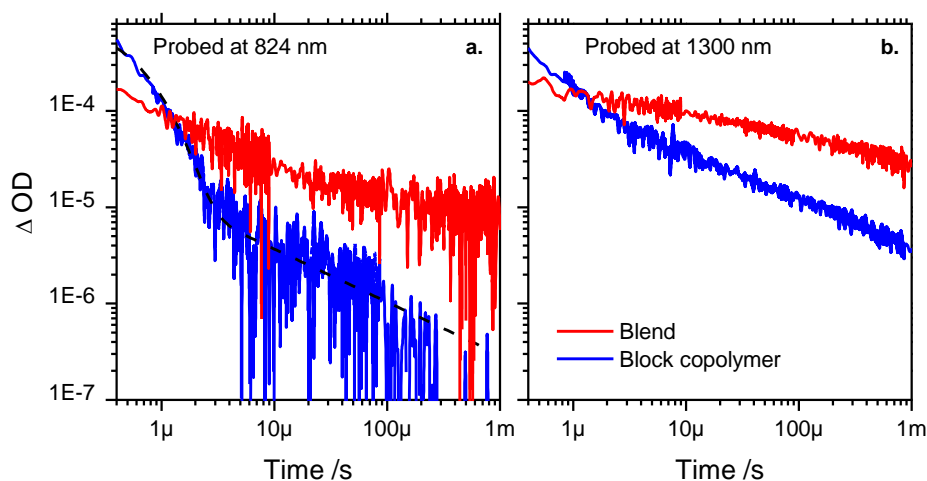


Figure 6-9

Figure 6-9a and b show transient absorption kinetics for PFM-F8BT-PFM block copolymer (blue line) and a PFM:F8BT blend (red line) at 824 nm and 1300 nm respectively. Minor differences in ground state absorption at the wavelength of excitation (450 nm) have been accounted for. The black dashed line in figure a is a fit to the sum of a monoexponential and power law decay with exponents $\tau_{\text{block copolymer}} = 6 \times 10^{-7}$ s and $\alpha_{\text{block copolymer}} = 0.55$.

The graphs shown in Figure 6-9a and b show transient kinetics from samples of F8BT:PFM binary blend and PFM-F8BT-PFM block copolymer at a probe wavelength of 824 nm and 1300 nm respectively. The decay at 1300 nm (Figure 6-9b) is far enough from the triplet peak at 800 nm to mainly represent the decay mechanism of PFM⁺ cations; at the time scales considered, this mechanism is the bimolecular recombination of PFM⁺ polarons (presumably with F8BT⁻ anions). Beyond 1 μ s at 1300 nm probe, both block copolymer and blend films are adequately described (over more than 3 orders of magnitude in time) by power laws with exponents $\alpha_{\text{block copolymer}}(1300 \text{ nm}) = 0.55 \pm 0.1$ and $\alpha_{\text{blend}}(1300 \text{ nm}) = 0.3 \pm 0.1$. The lifetime of free charge within a blend film is also seen to be longer than in a block copolymer sample. This could be due to differences in interfacial surface area between the electron transport and hole transport materials across

which recombination occurs. In well segregated blends, where average domain sizes are large (of order 1 μm and greater), the surface area for recombination is small compared to the block copolymer. The intensity of signal at a given time in the figure is directly related to the number of charges present in the film; this means that after $\sim 1 \mu\text{s}$ (the limit of resolution of the experiment) there are more charges present in the blend compared to the block copolymer. However, if one continues the decay trends back in time, at times before $\sim 1 \mu\text{s}$, there will be more charges in block copolymer compared to the blend.

In the decays at 824 nm, shown in Figure 6-9a, a biphasic nature of the block copolymer kinetics can clearly be observed. The fast component is the contributing factor in the difference between the transient spectra of the block copolymer at short and long time scales (and between the block copolymer and blend). The block copolymer kinetics are well fit by a sum of monoexponential and power law decay with monoexponential exponent $\tau_{\text{block copolymer}}(824 \text{ nm}) = 6 \times 10^{-7} \text{ s}$ (in good agreement with the values found in the literature of $3.5 \times 10^{-7} \text{ s}$ and 6.3×10^{-7}),^{55,150} while the power law exponent is held fixed with an exponent the same as seen at 1300 nm ($\alpha_{\text{block copolymer}} = 0.55$). A good fit using a monoexponential decay at early times acts as further confirmation of the identification of the fast component as a triplet; in addition, the agreement with literature values for the triplet decay constant, as well as an identical intensity dependence found for both fast and slow components suggests triplet-triplet annihilation is not the dominant decay mechanism. The blend film on the other hand shows only a power law decay at 824 nm, in keeping with the fact that the blend transient spectrum does not show a peak at $\sim 800 \text{ nm}$ at $1 \mu\text{s}$. The power law exponent is found to be $\alpha_{\text{blend}}(824 \text{ nm}) = 0.3 \pm 0.1$ and does not change across the spectrum probed (550 – 1600 nm), meaning that a single decay pathway leads to the decay of the observed transient features.

It should be noted that the biphasic decay is also seen at early time scales in the block copolymer at 1300 nm, but the ratio of triplet to charge at that wavelength is significantly smaller and so the polaron signal dominates. In addition, the blend decays also displays some biphasic character at early time scales, indicating that small quantities, or short lived triplets may also be present in these films.

The final piece of information to come from Figure 6-9 is an estimate of the quantum efficiency of charge generation for long lived charges (at $1 \mu\text{s}$). This relies on an estimate of the volume density of charged species, which can be determined from the change in absorption (ΔOD), but requires knowledge of the absorption cross section of the PFM^+ cation. An estimate of the extinction coefficient is made from work done by Dyer-Smith et al. on poly(9,9'-dioctylfluorene-co-bis-*N,N'*-(4-butylphenyl)-bis-*N,N'*-phenyl-1,4-phenylenediamine) (PFB) which is very similar in structure to PFM ,²¹⁶ from this the extinction coefficient is taken as $\epsilon_{\text{PFM}^+}(1300 \text{ nm}) \sim 5 \pm 2 \times 10^3 \text{ M}^{-1} \text{ cm}^{-1}$. With an excitation fluence of $70 \mu\text{J cm}^{-2}$ at 450 nm, approximately 1.6×10^{14} photons are incident on every square centimetre of sample. Given that the films were $90 \pm 15 \text{ nm}$ thick, there is the possibility to generate $\sim 1.8 \pm 0.2 \times 10^{19} \text{ cm}^{-3}$ excited states (absorption different from 100% is taken into account in the calculation of observed charge density). Using a modified

Beer-Lambert law, the charge density in the block copolymer and blend at $1 \mu\text{s}$ is found to be approximately the same and $2.2 \pm 1 \times 10^{18} \text{ cm}^{-3}$ yielding a charge generation quantum efficiency of $\sim 12 \pm 5\%$ which is in reasonable agreement with the predicted geminate pair dissociation yield ($\sim 10\%$ at 400 ns)⁵⁵ and the modest external quantum efficiency of a solar cell at short circuit (3.4%)⁴⁴ (nb. both of these studies were performed using F8BT:PFB blends). The calculated value is likely to be an overestimate as the triplet absorption while small, will contribute to the total signal at short time scales.

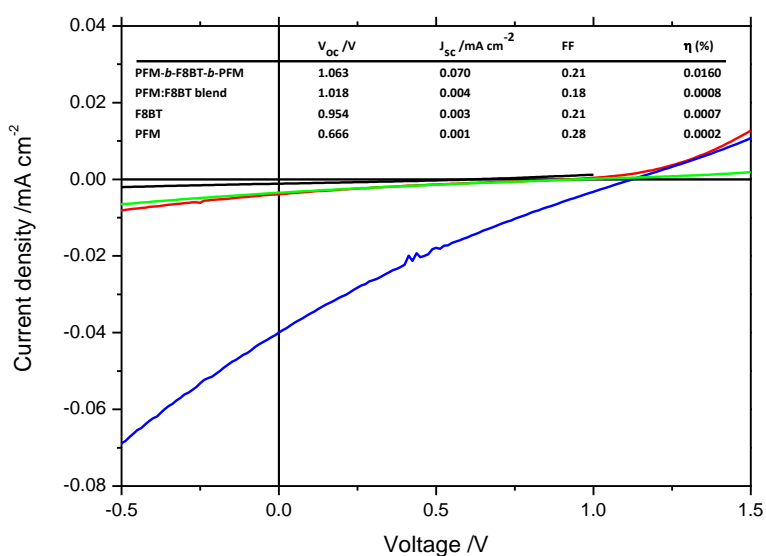


Figure 6-10

Figure 6-10 shows current density-voltage traces for photovoltaic devices formed in a glass/ITO/PEDOT:PSS/active layer/Al architecture exposed to AM1.5 solar simulation. The active layer was varied between PFM-F8BT-PFM block copolymer (blue), a PFM:F8BT blend (red), homopolymer F8BT (green) and homopolymer PFM (black). The inset table gives the relevant parameters for the devices shown.

Figure 6-10 shows the photovoltaic action of the materials studied in this chapter. Devices were formed in a glass/ITO/PEDOT:PSS/active layer/Al architecture and the summary of device properties is shown as a table inset to the figure. Immediately apparent is the significant increase in short circuit current available in a block copolymer device compared to a blend device. It is mainly this effect that causes an increase in the power conversion efficiency (η) of twenty times in the block copolymer compared to the blend. Additionally, the open circuit voltages are high in both block copolymer and blend due to the large energy gap between HOMO_{PFM} and $\text{LUMO}_{\text{F8BT}}$ ($\sim 1.48 \text{ eV}$). The observation that a more intimately mixed morphology yields better devices is consistent with work done by others on F8BT:PFB blends.^{75,217} Despite the increase from blend to block copolymer device short circuit current, all photovoltaics studied have relatively poor efficiencies compared to state-of-the-art all polymer devices (at 1.8%).²¹⁸ This is due to low short circuit currents and fill factors, suggestive of poor charge collection. This could be a result of little charge generated to begin with, or high free charge losses after generation and is likely to be a combination of both. In this case (as shown above), free charge generation is low at $\sim 10\text{-}20\%$, but higher at early time scales in the block copolymer. However, this difference (with no external electric field) cannot fully explain

the order of magnitude difference in short circuit current between block copolymer and blend. While low quantum efficiency for charge dissociation means poor devices in general, it is therefore likely that it is the loss of free charges that leads to the comparatively poor blend device efficiencies seen here. Whether this loss is a result of poor transport, high bimolecular recombination or poor collection at the electrodes is currently unknown, although it has been postulated (for F8BT mixed with PFB) that vertical ordering in well segregated blends is the cause of low collection efficiencies.⁷⁵ These results imply that, despite a high triplet yield, the block copolymer outperforms the blend in both generation of charge and device performance.

6.4 Results: Annealing studies

Now that the reader has gained an understanding of the photo-physical processes occurring in the F8BT-PFM blend or block copolymer system, we turn our attention to the effects of annealing on these processes. As demonstrated above, the morphology of these materials when spin cast from toluene plays an important role in the determining the degree of exciton quenching, exciplex emission, triplet and free charge generation. However, it is well known in F8BT:PFB blends that the solvent from which one spin casts will affect the phase segregation during spin casting.²¹⁷ Hence, the first investigation in this section is one of this nature.

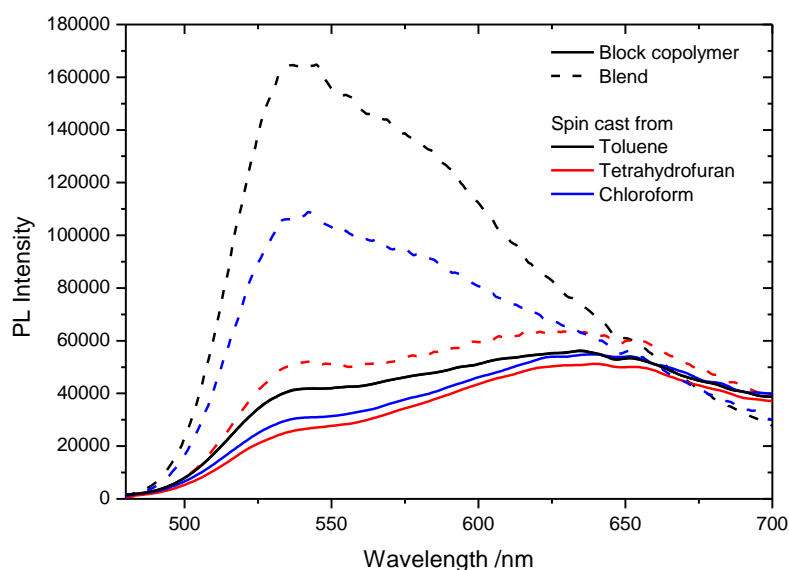


Figure 6-11

Figure 6-11 shows photoluminescence data for thin films of PFM-F8BT-PFM block copolymer (solid) and PFM:F8BT blend (dashed) spin cast from different solvents and excited at 465 nm. Films were spin cast from either toluene (black), tetrahydrofuran (blue) or chloroform (red). The emission has been corrected for minor differences in the ground state absorption at the wavelength of excitation.

Figure 6-11 shows steady state emission from samples of PFM:F8BT blend and PFM-F8BT-PFM block copolymer spin cast from toluene, THF and chloroform, excited at 465 nm. Block copolymer films spin cast from the three different solvents present similar emission profiles, with a peak at 645 nm corresponding to

exciplex emission and a smaller shoulder at 540 nm corresponding to radiative relaxation of singlet excited states in F8BT. There is a small change in the exciton quenching with chloroform showing the lowest 540 nm shoulder, but the spectra are broadly the same. By comparison, the blend films display markedly different emission, ranging from a profile similar to the block copolymer emission (for a film spin cast from chloroform) to a profile similar to pristine F8BT emission (for a film spin cast from toluene). If emission from the exciplex state (645 nm) as well as bulk singlet fluorescence quenching (540 nm) can be used qualitatively as a measure of interfacial surface area (as has been argued above), it can be seen that morphology in a blend sample is dependent on the solvent used in spin casting a film. These differences are due to both differing solubilities of the constituent components in each of the solvents and also the different boiling points of the solvents leading to faster drying and less time for phase segregation.²⁰⁵ For the case of blends spin cast from chloroform, our emission experiments are then consistent with a highly intermixed blend with domain sizes similar to those in the block copolymer.^{51,217}

It should be noted the same investigation was performed using chlorobenzene and p-xylene, both of which gave results qualitatively similar to toluene and THF and are not shown for clarity. In the following discussion, we examine some of the effects that this difference in morphology brings.

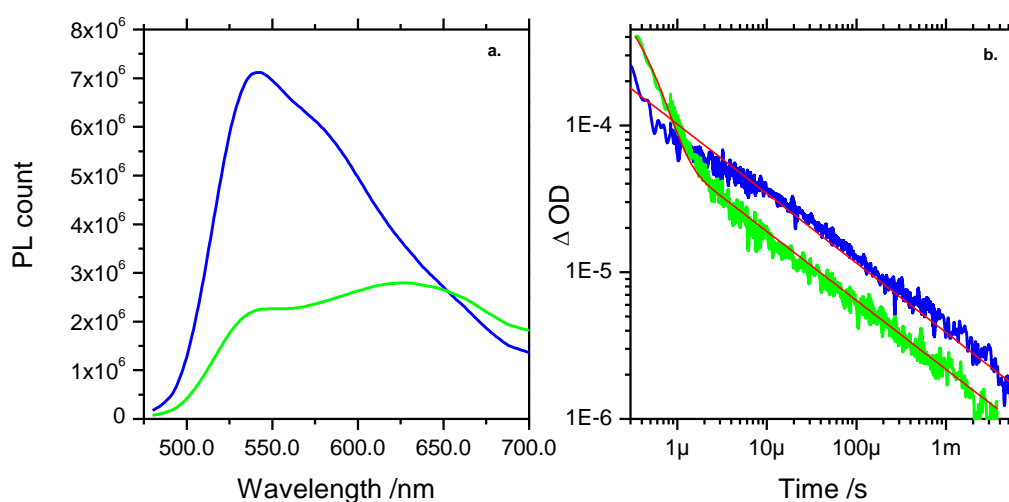


Figure 6-12

The figure shows emission spectra and transient absorption kinetics for a 1:1 blend of F8BT and PFM spin cast from either toluene (blue) or chloroform (green). Figure 6-12a shows the emission spectra for thin films on glass of 1:1 blends of F8BT and PFM excited at 465 nm. Figure 6-12b shows the transient kinetics for similar samples probed at 825 nm after excitation at 450 nm (with fluence $\sim 60 \mu\text{J cm}^{-2}$); the decays have been normalised for minor differences in the optical depth at the wavelength of excitation. The kinetics are fitted using either a single power law decay (for film spin cast from toluene (blue)) or sum of power law decay and exponential (for film spin cast from chloroform (green)).

Figure 6-12 shows emission spectra and transient absorption kinetics for 1:1 F8BT:PFM blend films spin cast from chloroform or toluene. The emission spectra of the films are similar to those seen in Figure 6-11 and are used as a reference when comparing the transient absorption kinetics seen in Figure 6-12b. The

transient absorption is observed at a probe wavelength of 825 nm (the peak of the F8BT triplet exciton absorption spectrum) after excitation at 450 nm. In the figure, the two sets of kinetics have been fit with appropriate models. For the film spin cast from toluene, a simple power law fit is used, similar to that observed in the previous section; this is indicative of pure dispersive bimolecular recombination decay and implies a single decay mechanism. However, the decay kinetics in a film spin cast from chloroform are not described well by a single power law decay; instead, there is a contribution at early time scales from F8BT triplet excitons whose decay is fit as an additional mono-exponential term with time constant $\tau = 2.9 \times 10^{-7}$ s. The similarities in photophysical properties between a blend film spin cast from chloroform and a block copolymer film are consistent with small domains in the chloroform spun blend.

A more detailed investigation into the morphology of the blend film spin cast from chloroform is shown in Figure 6-13a and c, compared with a film spin cast from toluene (Figure 6-13b and d). In Figure 6-13a and b, electron microscopy is used to see through the thickness of unsupported films that have been floated from a sacrificial substrate; selective staining with RuO_4 leaves F8BT dark in these images. Using this technique, the domains in both films appears to be large, on the order of hundreds of nanometres. In the chloroform spin cast film, domains of F8BT are apparently isolated (the white within these domains are burn sites where the film has suffered from the electron beam) whereas, in the toluene spin cast film, the domains are interconnected in at least two dimensions. These observations are further confirmed by mapping the topography of similarly prepared films using tapping mode AFM as seen in Figure 6-13c and d. The root mean squared roughness of the films is 1.25 nm for the chloroform spun film and 5.70 nm for the toluene spun film.

The large domains seen by TEM and AFM for the blend films spin cast from chloroform seem to be at odds with our spectroscopic data, which indicates that the blend is similar to the PFM-*b*-F8BT-*b*-PFM triblock copolymer whose domains are fine (see Figure 6-7). However, the correlation between large interfacial surface area and a strong photoluminescence quenching coupled with a high yield of exciplex emission is well studied and is commonly associated (in the case of F8BT:PFB blends) with spin casting from low boiling point solvents, especially chloroform.²¹⁷ This discrepancy has been explained previously by studies into the purity of individual phases on length scales that are difficult to probe even by TEM.^{72,75}

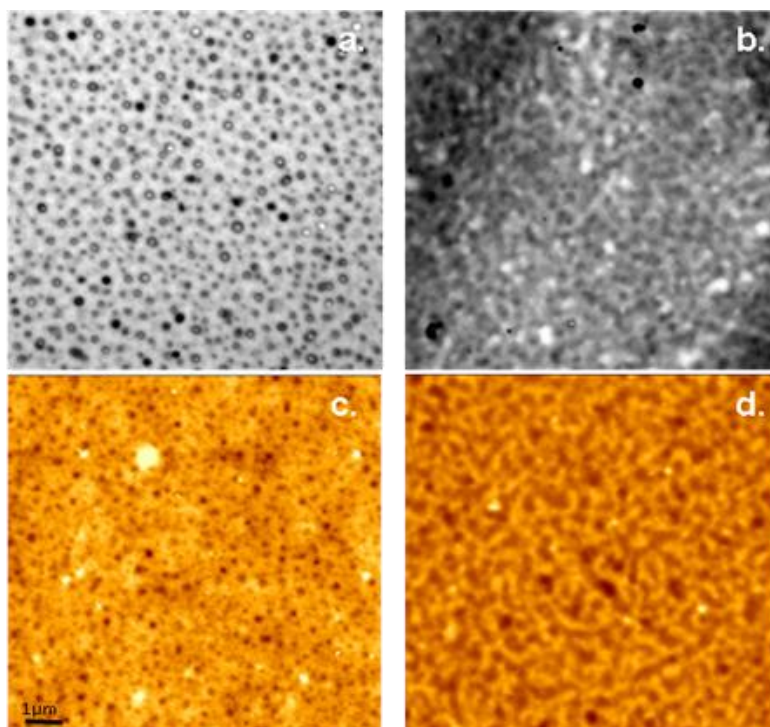


Figure 6-13

The figure shows transmission electron micrographs and atomic force micrographs of films of 1:1 blend F8BT:PFM spin cast from chloroform or toluene; the lateral scale of all figures is shown in Figure c. Figure 6-13a and b show TEM images of films spin cast from chloroform and toluene respectively taken through films that had been exposed to RuO₄ vapour overnight. As a result, F8BT is selectively stained and appears darker. Figure 6-13c and d show AFM tapping mode topography images of films spin cast from chloroform and toluene respectively. The vertical scale in each AFM figure is 12 nm and 65 nm for Figure c and d respectively where darker colours correspond to deeper troughs.

To sum this short section up: It is evident that by spin casting from chloroform, it's possible to make thin films from a blend of 1:1 F8BT:PFM, that show similar photo-physical properties to a thin film of PFM-*b*-F8BT-*b*-PFM block copolymer, but different macrophase domain structure.

In the following discussion, we will see that high exciplex emission yields, high triplet yields, and low charge yields are intrinsically linked by morphology, something that will be further pursued in the next chapter.

Figure 6-14 shows the main results of a long term annealing study performed over more than two hundred days. Thin films blend of 1:1 F8BT:PFM blend and PFM-*b*-F8BT-*b*-PFM block copolymer were prepared from solutions made with chloroform so that the photo-physical properties of the films was similar (as has been shown above). Evidence that this is the case is seen in Figure 6-14 in which the pre-annealed photoluminescence spectra in both materials peaks at 634 nm due to strong exciplex emission. The films were then put on a hot plate at 60°C in the dark for ~4,820 hours while control samples were held at room temperature in air and nitrogen and at 5°C. The glass transition temperature (T_g) in these materials is the subject of some debate and is seen to vary with the apparatus used in the measurement, molecular weight and in thin films depend on film thickness.²¹⁹ Reported values for F8BT range from 45-60°C, up to 122°C and 135-140°C for film thicknesses of between 30-300 nm and molecular weights from 9-255 kg mol⁻¹;²¹⁹⁻²²¹ and 76°C for PFM.²²² However, as the glass transition is a dynamic phenomenon, even substantially lower

temperatures than these can result in morphological change given sufficient time. The temperature chosen here was based on a value commonly expressed as in the range of device operating temperatures.²²³

The result of annealing for this extended period of time is in both cases a drastic change in photoluminescence spectral response. The emission after annealing, in both materials is primarily from the F8BT excitonic state peaking at ~555 nm and the peak due to exciplex emission (645 nm) is lost. A similar effect was observed by McNeil et al. on thermally annealing blends of F8BT:PFB spin cast from chloroform.⁴⁴

The control films showed a slight sensitivity of emission spectra to air exposure over the period of annealing. No such effect was observed in the absorption spectra and the final results are not consistent with significant degradation of one or both components.

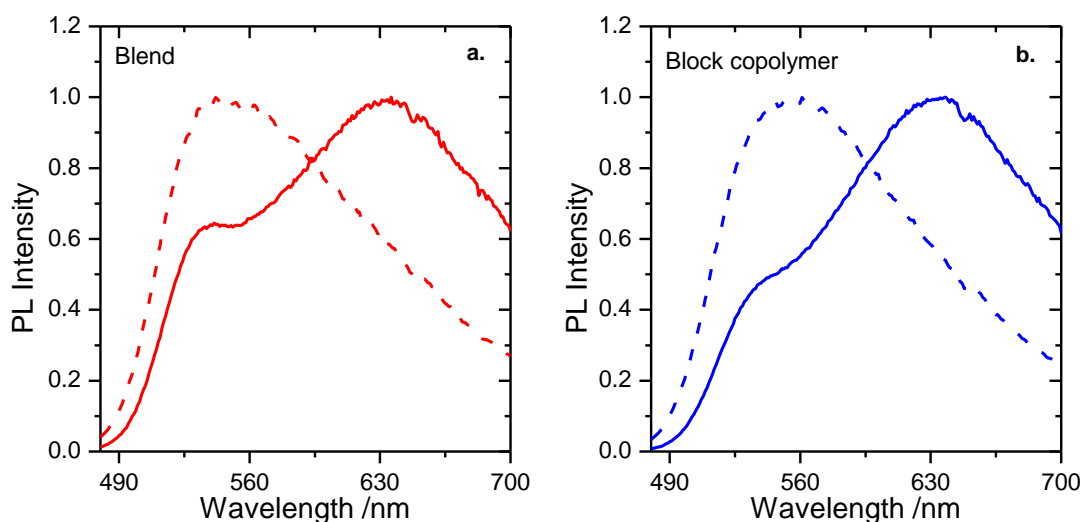


Figure 6-14

The figures show the effects of thermal annealing on films of PFM-*b*-F8BT-*b*-PFM block copolymer (blue) and PFM:F8BT blend (red) on photoluminescence after excitation at 465 nm. Figure a shows emission from a blend film spin cast from chloroform in its pre-annealed state (solid line) and after thermal annealing at 60° C for 4800 hrs (broken line). Figure b shows emission from a block copolymer film spin cast from chloroform in its pre-annealed state (solid line) and after thermal annealing at 60° C for 4800 hrs (broken line).

The changes in photoluminescence seen in Figure 6-14 are echoed by the transient absorption seen in Figure 6-15. Before annealing, strong transient absorption from the triplet exciton was seen in both block copolymer and blend films at 824 nm, seen in the darker lines of Figure 6-15. After annealing, the triplet signal has disappeared from both signals (the spectrum after annealing (not shown) contains no triplet peak, but only a PFM⁺ cation signal). The decrease in triplet signal also results in a higher yield of charges seen by the increase in signal after 1 μ s. The transient decay kinetics of the annealed block copolymer and blend, probed at 1300 nm are shown in Figure 6-15c and are very similar in intensity and decay dynamics, both being closely described by a single power law decay with the same exponent $\alpha=0.46$. The results of the annealing experiment are all consistent with the premise that more segregated domains and a smaller

interfacial surface area lead to a smaller exciplex and triplet yield. Such changes imply that the initial spin cast morphology did not satisfy a minimum free energy requirement and during annealing there was migration towards a morphological equilibrium in both materials sets. These results are also reproduced on solvent annealing in a chloroform atmosphere, something that will be considered more closely in the next chapter.

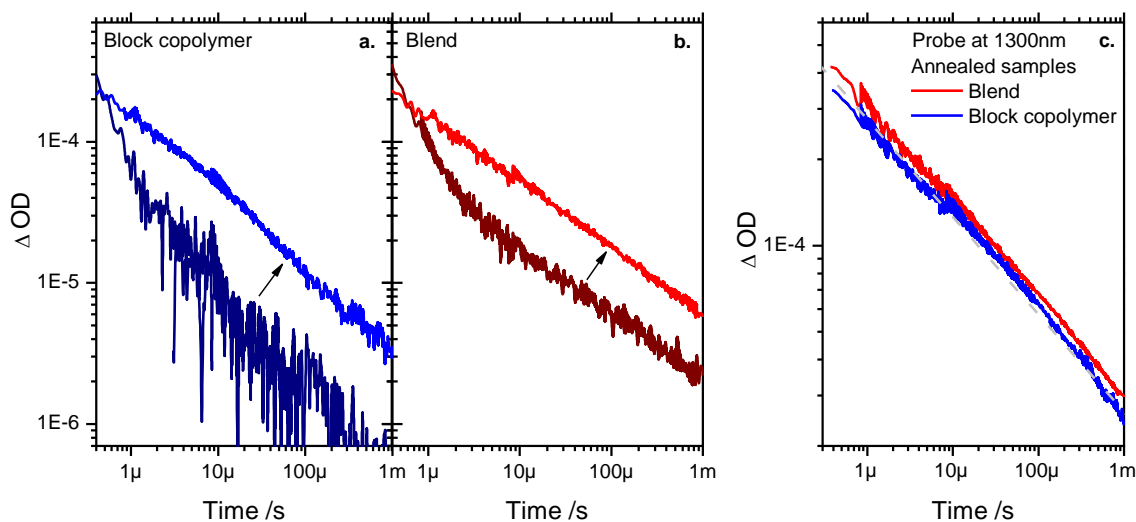


Figure 6-15

Figures a and b show the transient absorption decays for films of PFM-*b*-F8BT-*b*-PFM block copolymer (blues) and PFM:F8BT blend (reds) probed at 824 nm after excitation at 450 nm with fluence $\sim 75 \mu J cm^{-2}$. The decays are shown for the film in their initial (as spun from chloroform) state (darker) and after annealing at 60 °C for 4,800 hrs (lighter); arrows indicate the change in kinetics with annealing. Figure c shows the transient absorption kinetics for the annealed films probed at 1300 nm. All data is corrected for minor differences in ground state absorption at the wavelength of excitation.

6.5 Conclusions

In this chapter, we have investigated an ABA triblock copolymer based on well known materials, F8BT and PFM (an analogue of PFB). The results of this investigation are consistent with the large body of work on these similar materials and with the structural properties of block copolymers we have observed in the previous chapters.

In the first section of the chapter, as spun block copolymer and (equivalent composition) blend films were compared using spectroscopic and microscopic techniques. The block copolymer shows all the photo-physical and morphological characteristics of an intimately mixed system and displays a comparatively high yield of emission from an interfacially bound charge transfer state commonly associated with a large interfacial surface area. We find that photo-induced charge yields in both the blend and the block copolymer are small and that these most likely account for the poor overall device efficiencies seen. However, block copolymer devices still outperform blend devices by an order of magnitude and this is

probably due to better homogeneity in block copolymer film morphologies which leads to improved collection at the electrodes.

In the final section of the chapter, we investigate the effects of spin casting from different solvents and find that blend films can be produced (by spin casting from chloroform) with similar photo-physical and morphological traits to the block copolymer. Using such films, thermal annealing was performed to further demonstrate the inter-relation between photo-physics and morphology.

Chapter 7

Results: Spectroscopic studies on swollen block copolymer films

7.1 Abstract

In this chapter, a novel combination of solvent vapour annealing and spectroscopic techniques are introduced using the example of a block copolymer. In a solvent atmosphere, it is well known that polymers swell as they take up solvent. We have investigated the absorption, emission and transient absorption characteristics of films of block copolymer in a range of swollen states. The results of these measurements are then used to propose two mechanisms for the change in photophysics observed.

7.2 Introduction

As has been laid out in previous chapters, in organic bulk heterojunction photovoltaics, the interface between components plays an important role in the workings of devices. Probing the photo-physics at the interface is complex due to the reproducibility and length scales associated with the highly localised processes involved, for example electron transfer. Systematically investigating one such process for different molecular environments is extremely difficult and the bulk of data on the subject is from models and quantum chemical calculations.^{207,224} Typically, experimental techniques such as transient absorption spectroscopy and transient photoluminescence use optical probes that average over large interfacial surface areas (even in bilayer arrangements) and possibly a large number of interfacial molecular environments. Even in the event that a large proportion of these environments are similar, identifying said environment relies on techniques that are spatially sensitive to the length scales involved (often sub-nanometre), which are limited to high energy X-ray techniques requiring a synchrotron. While a similar argument could be made for the intermolecular interactions between different molecules in a single component system, adding a second component increases the complexity three-fold (two bulk components and an interface). One way of investigating interfacial photo-physical processes is to alter the environment at the interface in a controlled fashion and observe the effects. Block copolymers should go some way to helping us understand this problem as a large proportion of the interface will be made up from the joining units between the two components in the polymer. As a result, modifying the properties of the joining unit (for example a non-conjugated alkyl chain of varying length) at the synthesis stage should provide a

controllable method for investigating interfacial properties. However, this is the subject of further work and the fabrication of such polymers does not fall under the rubric of this thesis. Another method for altering the intermolecular and interfacial environment in solid state polymer systems has been the use of high compression hydrostatic loading in a diamond anvil press. A pertinent example is the spectroscopic work done by Schmidtke et al. on F8BT:PFB and F8BT:TFB blends in the pressure range 0-8 GPa.²²⁵ In this work, transient photoluminescence is performed at a range of pressures on both blend and homopolymer thin films in order to influence intermolecular proximity. The main conclusions drawn from the study are: that the photoluminescence spectrum of F8BT red shifts by 530 ± 60 meV whereas the charge-transfer exciton (exciplex) shifts by 270 - 370 meV (for the TFB or PFB blends respectively) over the pressure range 0.1 MPa – 8 GPa. This smaller shift in energy of the exciplex is accompanied by enhanced exciton charge-transfer rates at the interface and shorter exciplex lifetimes. All of these effects are postulated to be a direct result of smaller interfacial separation at increasing pressure. Studies on other polymers have confirmed that intermolecular compressibility is significantly higher than intramolecular compressibility at such pressures.²²⁶ While this technique provides one of the few methods available to reversibly alter local molecular morphologies, there are draw backs to the set up. First, the technique is neither simple nor cheap. Also, direct access to the sample is lacking under these conditions and mainly non-contact investigatory techniques must be used to probe samples under high pressures. Additionally, while compression can provide useful insight, increasing the intermolecular separation is obviously not possible in an anvil set up. In this chapter, a novel scientific tool is introduced that complements experiments that can be performed at high hydrostatic pressures. The technique is comprised of several optical investigatory experiments coupled with a set-up to provide a controlled solvent atmosphere (as described in Chapter 3). Polymers in solvent atmospheres absorb a certain amount of solvent dependent on the amount of solvent in the atmosphere, the energetic interaction between monomer and solvent molecules and the number of monomers making up the individual chains. Solvent uptake leads to swelling of the polymer as the volume fraction of solvent increases. The Flory-Huggins equation gives a quantitative description of the swelling of a polymer in a solvent atmosphere of partial vapour pressure p/p_{sat} (see Equation 7-1).²²⁷

$$\ln \frac{p}{p_{sat}} = \chi \cdot \varphi_p^2 + \ln(1 - \varphi_p) + \left(1 - \frac{1}{N}\right) \varphi_p \quad \text{Equation 7-1}$$

In this equation, p_{sat} is the saturation vapour pressure of the solvent at a given temperature; p is the vapour pressure of solvent in the atmosphere the polymer is exposed to; χ is a measure of the solvent-monomer energetic interaction known as the Flory-Huggins interaction parameter; N is the degree of polymerisation of the polymer in question and φ_p is the relative concentration of polymer, which in the case of swelling of films is the ratio of initial to swollen thickness d_0/d . This equation was used by Elbs et al. to determine the interaction parameter for various non-conjugated polymers and solvents using ellipsometry to determine the *in situ* thickness of swollen polymer films.¹⁰⁷ A similar technique was used by Hüttner et al. to investigate

poly(perylene bisimide acrylate) (PPerAcr), a similar polymer to that studied in chapters Chapter 4 and Chapter 5.¹⁶⁷ In this relevant study, ellipsometry, absorption and photoluminescence were used to observe the effects of solvent-annealing in a chloroform atmosphere. The authors determine that in the solvent chosen, the polymer is effectively immobile at a relative vapour pressure of less than 60% of saturation and only the alkyl chains are solvated; above this threshold, there is an increase in the degree of swelling with increasing solvent vapour pressure and there is an increase in the degree of perylene bisimide aggregation, leading to the supposition that the polymer becomes significantly more mobile. However, signs of aggregation at 100% saturation of vapour at room temperature indicate that at these concentrations, $\phi_p \sim 0.57$, the $\pi-\pi$ stacking is still significant (see Appendix C). While this demonstrates that solvent annealing (to induce changes in morphology) will be effective only above the saturation threshold, the technique holds far more potential for investigating intermolecular interactions in solvent-polymer binary and solvent-polymer-polymer ternary blends. The investigation of such interactions is the subject of this chapter in which, a controlled solvent vapour atmosphere is used to investigate aspects of the photo-physics of a triblock copolymer system, PFM-*b*-F8BT-*b*-PFM, first investigated in the previous chapter. The PFM-F8BT interaction is an interesting one to attempt to examine under swelling in a solvent atmosphere as it is possible to optically probe the interaction at the interface by observing the following: the charge transfer state by its emission, the degree of charge dissociation by observing PFM radical cations and the yield of F8BT triplet excitons. Also, since neither of these polymers is crystalline, it is likely that the monomer-monomer self interactions will be weaker than in the case of PPerAcr précised above. The use of block copolymers in such an environment is also advantageous due to the limit in separation achievable between the individual components that will provide an upper bound for the spatial proximity at an interface.

7.3 Experimental

For the purposes of the experiments in this chapter, thin films of triblock copolymer PFM-*b*-F8BT-*b*-PFM were spin cast on glass substrates. For the purposes of this investigation and to ensure reproducibility, films were all spin cast from chloroform and a new film was used for each experiment. The structure of the polymer can be seen in Figure 6-1 of Chapter 6. The experimental set-up used to maintain a solvent atmosphere is found in Chapter 3. The solvent used in the experiments was exclusively chloroform; this is for several reasons. The first has to do with the morphology found when spin casting from this solvent. In the previous chapter, it was found that spin casting from chloroform produces photo-physically similar blend and block copolymer films. Coupled with the fact that solvent annealing of these films in chloroform vapour leads to phase segregation, this leads to two conclusions: i) that chloroform is a relatively non-selective solvent for F8BT and PFM, and ii) that there is a positive interaction parameter between the two components, which indicates incompatibility. This is important for these experiments as it means that

swelling should be relatively homogenous in the two component system and that swelling will result in interspecies separation.²²⁸ Further experimental work is required to confirm these suppositions. Additionally, chloroform has a low boiling point and therefore a high vapour pressure at saturation. The saturation vapour pressure may be calculated using Antoine's equation (see Chapter 3) at 20° C with A (7.11), B (1233) and C (230) values from reference²²⁹ which are suitable for a range -63 - 263° C, yielding $p_{sat} = 21.04$ kPa. In the following section, the vapour pressure of chloroform is adjusted by mixing (by mass flow) a saturated nitrogen stream with a dry stream in different ratios. This gives rise to a vapour pressure which is quoted as a percentage of saturation. For example, a 40% vapour pressure of chloroform indicates a 20 sccm flow of saturated stream and 30 sccm of dry nitrogen mixed to a total of 50 sccm. A 100% saturated atmosphere was in general not used as condensation is likely at saturation and this renders the atmosphere susceptible to concentration variations.

7.4 Results

Figure 7-1 shows the results of steady state emission spectra taken at various relative vapour pressures. Figure 7-1a demonstrates the results of photoluminescence spectra taken from a film of block copolymer excited at 465 nm at 1 hour intervals in various concentrations of chloroform atmosphere. At the start of each hour, the relative vapour pressure of chloroform was increased by 10% from 0% (pure nitrogen) up to 90% of saturation. At the end of each hour, a PL spectrum was taken and the relative vapour pressure subsequently changed. By continuously monitoring the emission at a given wavelength throughout the experiment, it was determined that up to ~70% saturation, the changes in spectra occur within the first 5 minutes of being exposed to a new atmosphere. Above 60% of saturation, changes are continuous over the hour and well modelled as asymptotic. The arrow in the figure shows the change in main emission peak with increasing percentage saturation of vapour. As shown in the previous chapter and seen in Figure 7-1a in a pure nitrogen atmosphere, block copolymer films spin cast from chloroform have a high PL emission from the exciplex state at ~ 645 nm, although a shoulder at ~540 nm indicates that there is still some F8BT emission. As the vapour pressure of chloroform in the atmosphere is increased, the degree of exciplex emission decreases while the bulk F8BT emission remains roughly constant. At $0.7p_{sat}$ (yellow spectrum) the emission from F8BT begins to increase and above this vapour pressure, the F8BT emission begins to hide exciplex emission. The results of a second, higher resolution experiment are seen in Figure 7-1b and c. Here, the atmosphere was varied in steps of 5% at 10 minute intervals from 0% up to 40% of saturation. The spectra taken after dwelling for 10 minutes in a given atmosphere are shown in Figure 7-1b and an arrow indicates the trend with increasing relative vapour pressure. One other interesting piece of data from this graph is that the peak emission (ie. exciplex emission) red shifts in a linear fashion with increasing vapour

pressure from 635 nm in pure nitrogen to a maximum of 643 nm at 40% of saturation. The inset shows a ratio of the exciplex to F8BT exciton emission ($PL(\lambda = 645 \text{ nm})/PL(\lambda = 540 \text{ nm})$) at various atmospheric concentrations of chloroform and is fit by a straight line. Figure 7-1c shows the emission continuously monitored at 645 nm; at the beginning of each ten minute interval, the vapour pressure is changed and a new colour used in the graph to identify the emission during that period. To end both experiments, the solvent atmosphere was quenched by flowing pure nitrogen through the system at high pressure such that the volume of the sample chamber is replaced in a fraction of a second. Further PL spectra after quenching show that if the sample has been exposed to greater than 60% of saturation chloroform, the final PL spectrum shows no evidence of exciplex emission and resembles that of pristine F8BT; whereas for the experiment up to 40% of saturation only, the final PL spectrum is similar to the initial spectrum and the red shift of the exciplex peak recedes back to 635 nm.

These results point to a number of conclusions. Swelling of the block copolymer in chloroform at above 60% of saturation appears to have a permanent effect on the photo-physical properties of the film and hence, reptation can be assumed to occur due to sufficient polymer mobility at these concentrations. Below this threshold (ie. 0-40% of saturation), either the interaction parameter between the monomers making up the distinct blocks is negative (it is likely that the parameter is concentration dependent)²³⁰ or one or both of the polymers is insufficiently swollen as to be mobile (since this is a block copolymer, both components must be mobile for full chain reptation). However, in this range (0-40% saturation), something is occurring as a result of either the polymer-solvent or polymer-polymer interactions that does the following: a) reduces the yield of exciplex emission while leaving the emission from bulk F8BT excitons relatively unchanged, b) subtly decreases the energy of the exciplex emission by ~ 25 meV.

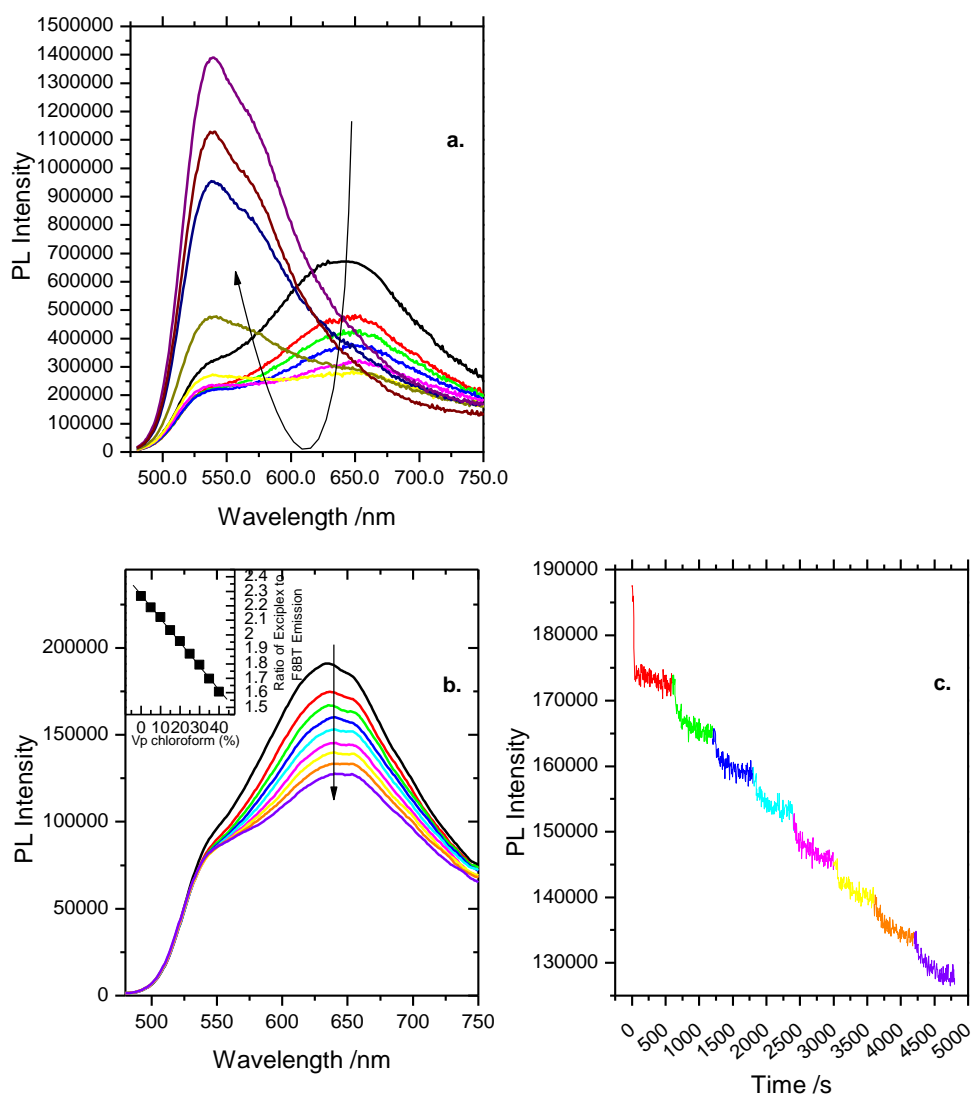


Figure 7-1

The figure shows the steady-state emission spectra collected for thin films of PFM-*b*-F8BT-*b*-PFM triblock copolymer exposed to various partial vapour pressures of chloroform. Figure 7-1a shows the emission spectra of a block copolymer film after successive exposure (for 1 hour intervals) to an increasingly concentrated atmosphere of chloroform vapour; at the start of each hour, the relative vapour pressure of chloroform was increased from pure nitrogen (black line) up to 90% of saturation (dark purple line) at intervals of 10% (missing out 40%). The arrow follows the main peak in each successive spectrum. Figure 7-1b shows the emission spectrum for a similar film at vapour pressures of 0% up to 40% of saturation at 5% intervals; increasing vapour pressure is indicated by the arrow. The inset in the figure shows the ratio of emission at 540 nm to that at 645 nm versus the relative vapour pressure of chloroform and is fit with a straight line. Figure 7-1c shows the emission at 645 nm continuously monitored over the experiment whose results are seen in Figure 7-1b; the atmosphere is changed at 600 s intervals by a 5% increase.

Absorption measurements under solvent atmosphere provide further evidence for permanent change in the film at high solvent vapour pressures. Absorption spectra were recorded for a thin film on glass in a nitrogen atmosphere and then at 40% saturation and at 10% intervals up to 90% of saturation. The various atmospheres were held for an hour before a spectrum was recorded. After quenching from 90% saturation with a fast stream of nitrogen, a further spectrum was recorded. The normalised spectra are shown in Figure 7-2. For low vapour pressures (40%) there is no change in the F8BT absorption peak at 463 nm,

however there is a 5 nm shift in the PFM absorption peak (see inset) from 382 to 387 nm. This shift is identical to that seen going from the block copolymer solution to solid; it is also entirely reversible on quenching. As the solvent concentration of the atmosphere increase, there is no further change in PFM peak position, but at ~70% saturation, the F8BT peak is seen to increase in relative intensity and hypsochromically shift to 460 nm. This shift is seen in solution, but to a much greater extent. Both the shift and relative increase in strength are irreversible on quenching. A permanent change in the absorption spectrum at solvent vapour pressure above 60% mirrors the observations from steady state emission above and provides further evidence for a morphological change at these polymer concentrations. In absolute values, the absorption does not change by more than 5% from the pure nitrogen case across the spectrum; at 450-470 nm where excitation occurs for the experiments studied in this chapter, the absorption at 40% saturation is changed by less than 2% from the nitrogen case.

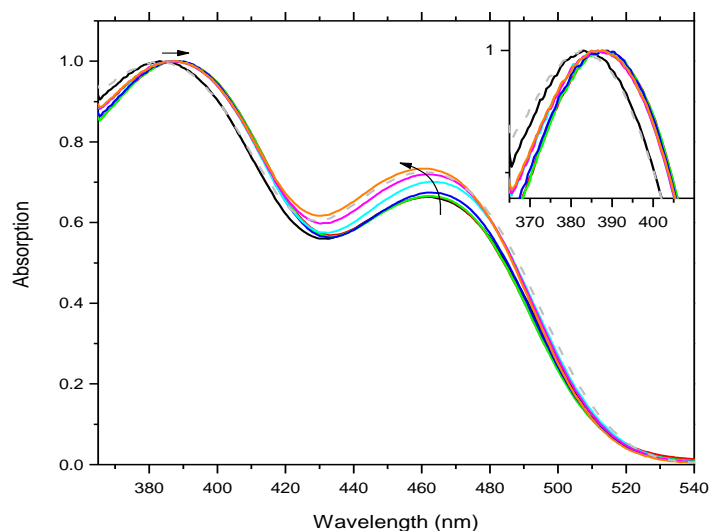


Figure 7-2

The figure shows the normalised absorption of a thin film of PFM-*b*-F8BT-*b*-PFM block copolymer in a nitrogen atmosphere (black line) and in chloroform/nitrogen atmospheres of progressively higher vapour pressure. The spectra were taken at 40% (red), 50% (green), 60% (blue), 70% (light blue), 80% (pink) and 90% (orange) of saturation. The grey dashed line shows the spectrum recorded after quenching from 90% saturation with high pressure nitrogen and was recorded in a pure nitrogen environment. The arrows depict the change in peak position with increasing solvent vapour pressure. The inset shows a higher resolution image of the PFM absorption peak.

Figure 7-3 shows the results of transient photoluminescence measurements performed on thin films of PFM-*b*-F8BT-*b*-PFM block copolymer in various concentrations of chloroform atmosphere upon excitation at 467 nm. Figure 7-3a shows the emission at 645 nm in chloroform vapour from 0% up to 40% of saturation in 5% intervals. On changing the atmospheric concentration, a ten minutes interval was left before starting an experiment in order to let the atmosphere equilibrate. The most obvious result from the graph builds on the observation from Figure 7-1 that emission is reduced at 645 nm; this reduction is in part due to a shorter exciplex lifetime. However, the decrease in lifetime alone cannot explain the reduction fully and so there must be a concurrent decrease in the initial exciplex yield. The lifetime of the exciplex is calculated by fitting a monoexponential decay at times after the bulk exciton emission has decayed (in this case after 20 ns). The

exciplex lifetime is plotted in Figure 7-3b as a function of the relative vapour pressure of chloroform in the atmosphere when the experiment was performed. (The graph also includes data for higher concentrations not shown in Figure 7-3a.) A linear fit has been applied to the lifetimes at vapour pressures up to 40%, although the fit is good up to ~60% of saturation. Assuming that there is no solvent induced change in F8BT exciton dynamics at 645 nm (there is little change observed at 550 nm monitored by upconversion with a resolution of 150 fs), the initial concentration of exciplexes may be determined by summing the contributions from exciton and exciplex emission in Figure 7-3a and normalising to the PL intensity at 645 nm from Figure 7-1b. Doing this (results not shown) shows that the initial yield of exciplexes also decreases in a linear fashion with solvent vapour concentration to 40% of saturation.

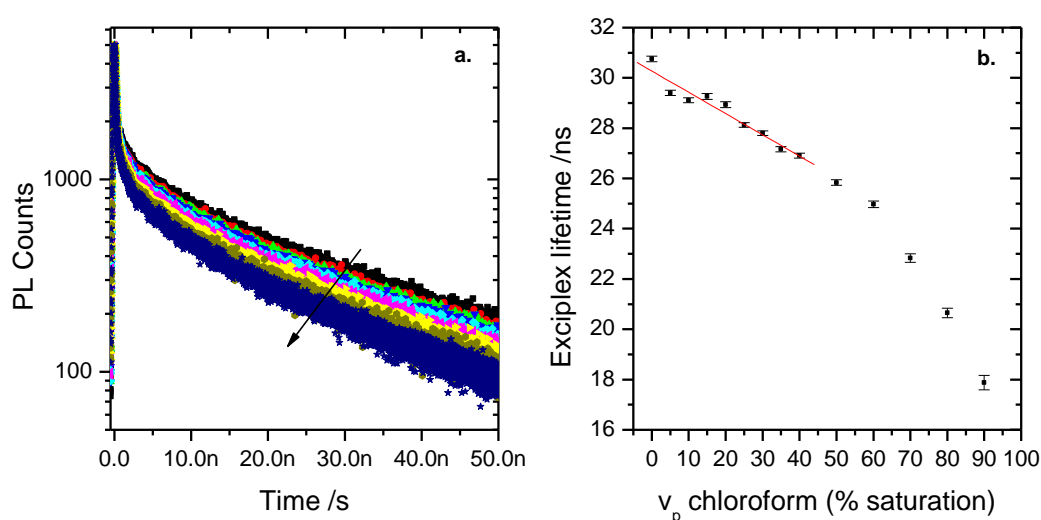


Figure 7-3

The figure shows the results of investigating the transient photoluminescence at 645 nm in films of PFM-*b*-F8BT-*b*-PFM block copolymer exposed to varying concentrations of chloroform vapour. Figure 7-3a shows the photoluminescence decays of the film after excitation at 467 nm in increasingly concentrated atmospheres, from pure nitrogen (black squares) in 5% intervals up to 40% of saturation (blue stars). The arrow shows the trend with increasing fraction of saturation. Figure 7-3b shows a graph of exciplex lifetimes measured at various vapour pressures of chloroform environment. A linear fit is applied to data points with vapour pressures below 40% of saturation.

Figure 7-4 shows the results of transient absorption spectroscopy from films of block copolymer exposed to different chloroform atmospheres. For a transient spectrum of the film under similar excitation conditions, see Figure 6-8 of Chapter 6.

Figure 7-4a shows the transient absorption kinetics probed at 825 nm after excitation at 450 nm with a fluence of $42 \mu\text{J cm}^{-2}$. Here again, the film has been subjected to chloroform atmospheres ranging from 0-40% of saturation at 5% intervals with a ten minute pause between an atmospheric change and the start of a measurement. Also included in the figure are fits to a sum of an exponential and power law; as in the previous chapter, these fits take into account the decay of the F8BT triplet exciton and PFM⁺ cation respectively. Both the lifetime of the exponential fit and the exponent for the power law decay were held constant in the fitting process and only the amplitude of each component varied. Holding the power law

constant across the range of solvent atmospheres is legitimate considering a separate experiment whose results are shown in Figure 7-4b. In this investigation, the same atmospheric conditions were applied to a similar sample and the decay kinetics probed at 1300 nm, well away from triplet exciton signal. Each of the traces measured is described well by a power law decay; the exponents of these decays are shown in the figure and found to have no trend with increasing vapour pressure. The exponent for the power law decay fit in Figure 7-4a was taken as the average of the values found in Figure 7-4b found to be $\alpha = 0.43(\pm 0.02)$. The exponential lifetime was found by fitting to the pure nitrogen case and then held constant in further curve fitting; the value was determined to be 3.75×10^{-7} s. The results from Figure 7-4a and b clearly indicate that the signal due to charges increases with increasing vapour pressure. Assuming that the extinction coefficient for PFM⁺ cations is unchanged in magnitude and spectral shape, this implies an increase in the yield of free charges. These are reasonable assumptions given that the ground state absorption changes only very slightly at these vapour pressures. Concurrently, there is a reduction in the yield of F8BT triplet excitons (again given similar assumptions about the exciton absorption cross section). Both of these are positive effects in the context of potential photovoltaic performance and a full understanding of the results would be of significant interest given the limited performance reported for this polymer system.^{44,55} Some explanation is proffered below, however an unambiguous model for these results requires further investigation and is the subject of ongoing work.

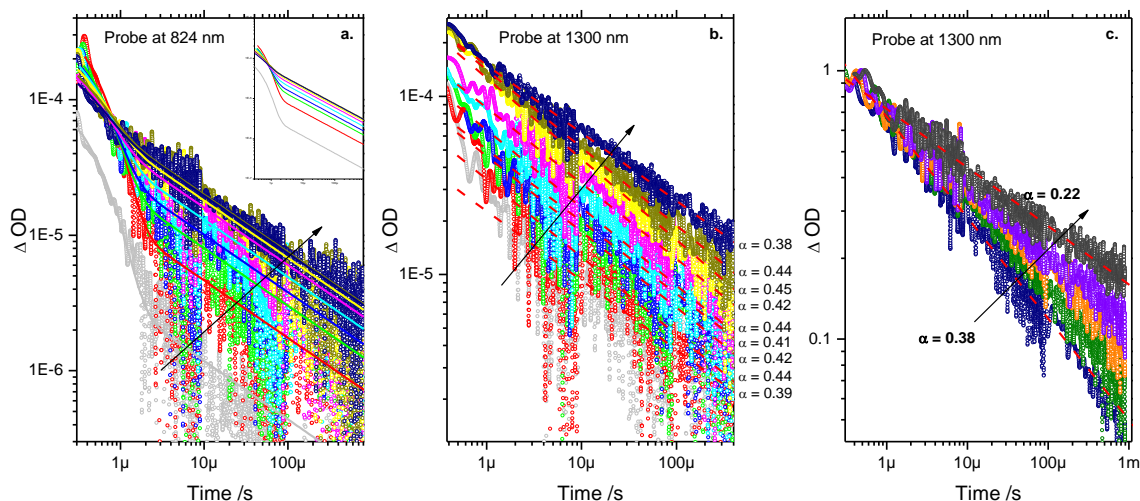


Figure 7-4

The figure shows transient absorption kinetics for a film of PFM-*b*-F8BT-*b*-PFM block copolymer after excitation at 450 nm in different chloroform atmospheres.

Figure 7-4a shows kinetics probed at 825 nm, taken in pure nitrogen (grey data) and at increasing concentrations of chloroform vapour at 5% relative vapour pressure intervals up to 40% of saturation. The arrow shows the trend with increasing concentration. Each of the traces was fit by a sum of a power law and monoexponential decay shown as solid lines in the same colour as the respective data. The inset figure shows the fits without the data. Figure 7-4b shows transient absorption kinetics for a similar film under similar conditions probed at 1300 nm. The traces are fit by power laws whose exponents are shown right of the figure.

Figure 7-4c shows the normalised kinetic traces probed at 1300 nm for vapour pressures at 40, 50, 60, 70 and 80% of saturation. The fits are power law decays whose exponents are shown in the figure. Again, the arrow shows the trend with increasing vapour concentration.

Figure 7-4c shows the normalised transient kinetics for the continuation of the experiment whose results are shown in Figure 7-4b. In the figure, the transient kinetics probed at 1300 nm are displayed for relative vapour pressures from 40% up to 80% of saturation in 10% intervals. A dwell time of one hour was left between adjusting the solvent atmosphere and recording the kinetics. With increasing solvent vapour pressure, the decay kinetics of the PFM⁺ cations are seen to become more dispersive; power law fits to the decays indicate a steady decrease in exponent to $\alpha=0.22$ at 80% saturation. This could be due to one or more of the following: i) morphological changes resulting in an increase in domain size such that the interfacial surface area to volume ratio is altered, ii) a change in the sub-transport density of states of either component leading to more dispersive bimolecular decay dynamics, iii) a change in the interfacial interaction such that the capture radius or driving force for recombination across the interface changes. It is tempting to speculate that the changes are due to morphological rearrangement to a more coarsely segregated structure in which the diffusion of free charges is less likely to result in recombination at an interface. In this way, the result would be similar to that found for solvent and thermal annealing of the PFM-*b*-F8BT-*b*-PFM block copolymer presented in Chapter 6. However, onset of the increase in power law exponent occurs at ~50% of saturation (and possibly even at 40%) which is not comparable with the results of the emission experiments above. The second argument is far more difficult to investigate and requires further work on the characteristics of the individual polymers in their swollen state. The third possibility has some merit given the generally low relative permittivity of polymers ($\epsilon_r \sim 3$ for conjugated polymers)⁶⁶ and the slightly higher permittivity of chloroform ($\epsilon_r \sim 4.8$). Dependent on where the solvent resides in the film, this would mean that attractive Coulomb forces could be more effectively screened leading to a smaller capture radius for the recombination event. However, in work by Nelson et al. modelling the decay characteristics of transient absorption measurements, Coulomb interactions are found to have a negligible effect on recombination compared to trapping-detraping mediated hopping; as such, smaller Coulomb interactions are unlikely to make a difference to the observed exponent.¹⁵³ These effects may have other implications for the photo-physics of the system and are discussed in more detail below.

Next we consider the possible effects of swelling that would lead to the observations in the PL and TAS experiments above. In summary, the observed effects include:

In chloroform solvent atmospheres with increasing solvent vapour pressure:

- a decrease in exciplex emission intensity
- a decrease in exciplex lifetime
- a small red shift in exciplex peak emission
- a decrease in triplet yield
- an increase in signal from long lived charges

In addition, these are all reversible at below 40% of a saturated vapour at room temperature.

One further piece of evidence is that these same effects are observed on thermal annealing films of PFM-*b*-F8BT-*b*-PFM block copolymer as seen in Chapter 6.

In determining an explanation for these effects, the first step is to qualify the local structural changes as a result of swelling at low (< 40% saturation) vapour pressures. Individually, F8BT and PFM will swell dependent on their solubility in chloroform. This is assumed to be similar in these components as explained above; in which case, the domains of each component will swell a similar amount. Given the lateral confinement in a thin film architecture, this has a non-trivial effect on the interfacial surface area to volume ratio between the components. As discussed above, the phase segregation observed in PFM-*b*-F8BT-*b*-PFM on thermal annealing (or solvent annealing in a saturated chloroform vapour) point toward a positive interaction parameter, $\chi_{\text{PFM-F8BT}}$. In general, repulsive or attractive interactions between the components of a copolymer lead to enhanced or reduced solubility of the copolymer in comparison to the average of the parental homopolymers.¹⁰⁷ A repulsive interaction between the monomers would lead to an increase in the solubility of the polymer. It has been suggested, that in copolymers, the origin of the increase in solubility is due to preferential solvation of the component interface.²³¹ Theoretical work by Fredrickson and Leibler, has shown that for block copolymers in non-selective, good solvents there is an inhomogeneity in polymer concentration; indeed, the solvent preferentially migrates to an interface where it can mediate unfavourable monomer interactions.²³² If the above conditions are met therefore, we might assume that with decreasing polymer concentration in a film, the interface swells preferentially leading to enhanced spatial segregation between blocks and an accumulation of solvent molecules at the interface. Testing this directly is the subject of ongoing work.

In looking for a hypothesis to explain the results above, the first point to consider is that both the absorption and overall PL quenching remain largely unchanged. This implies that ultra-fast generation of interfacial charge pairs (CPs)²³³ from primary F8BT excitons is unaffected by the presence of solvent at high polymer concentrations. Additional work by Reynolds et al. has probed the effects of solvent atmospheres on transient photoluminescence in films of PFM-*b*-F8BT-*b*-PFM with sub picoseconds resolution.²³⁴ The excited state lifetime at 550 nm is found to be 6 ± 1 ps and independent of solvent atmosphere below 40% saturation. According to Huang et al. in F8BT:PFB blends, the CP states may be either emissive exciplexes or non-radiative polaron pairs.²⁰⁷ The decay pathways then available to the CP include charge separation to dissociated charges (DC), recombination to F8BT triplet excitons (T) or decay to ground, all of which are summarised in Figure 7-5a.⁵⁵

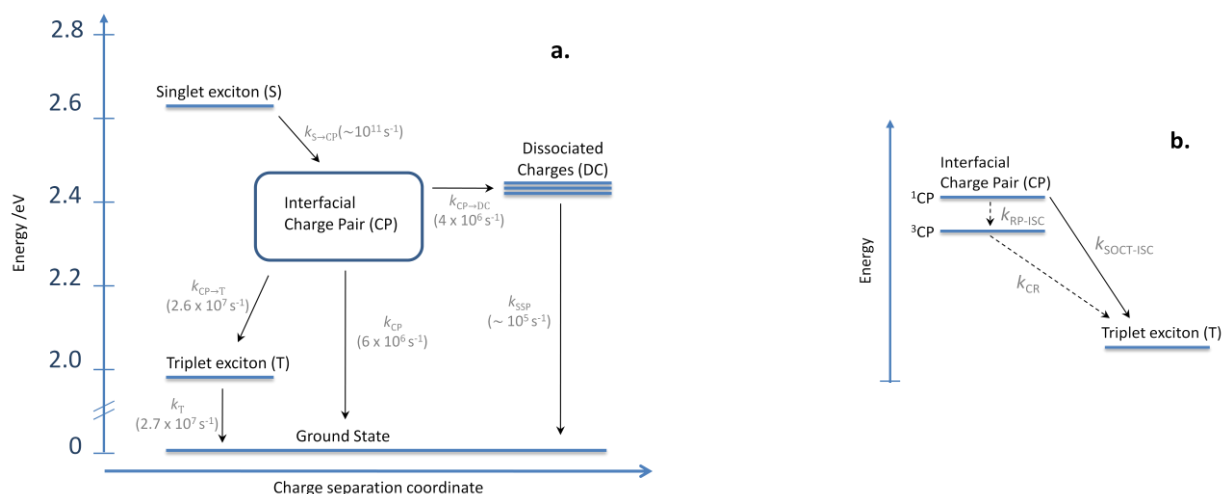


Figure 7-5
Figure a shows the charge recombination mechanism at the F8BT:PFM heterojunction. Adapted from ref. ⁵⁵. Figure 7-5b shows the different recombination pathways that enable intersystem crossing from a bound charge pair to a triplet exciton.

We will now consider in detail two possible explanations that satisfy the above observations. The first is based on the idea that swelling leads to a larger spatial gap at the interface, while the second is based on decreasing charge confinement due to the swelling of domains.

It is clear from the empirical evidence above that the presence of solvent in a PFM-*b*-F8BT-*b*-PFM thin film leads to significant changes in photo-physical properties. As the majority of these effects involve species that are either interfacially bound, or a result of processes that occur at the interface, it is reasonable to assume that solvent induced changes at the interface are partly responsible. The decrease in exciplex yield with increasing concentration of solvent atmosphere is consistent with the idea that swelling leads to a larger spatial gap at the interface. Such an increase would tend to reduce the (normally strong)⁵¹ exciplex binding energy due to a smaller Coulomb attraction as a result of a combination of increasing spatial separation and increased charge screening due to the higher solvent dielectric. Indeed, a small red shift in peak exciplex emission is observed. Coupled with this, the decrease in ionic character (and relative increase in covalent character) of the exciplex would lead to a shorter exciplex lifetime.^{207,225} A related possibility is that the decrease in exciplex lifetime is due to increasing thermal regeneration to secondary bulk excitons whose shorter lifetimes act to increase the rate of exciplex decay; however, this would appear unlikely as there is no absolute increase in emission from bulk F8BT excitons.

The decreases in triplet exciton yield and increases in charge yield (at 1 μs) may be explained in a similar fashion. There is still some ambiguity as to the mechanism for inter-system crossing (ISC) from the CP to triplet exciton. Two possibilities are that the CP directly recombines to the triplet exciton or that ISC occurs within the CP state and that a triplet bound charged pair recombines to form a triplet exciton (see Figure 7-5b). Both routes have been extensively studied in donor-acceptor dyads.^{54,235-240} As has been found by

others, it is difficult to distinguish which is the dominant process in such cases as ours;⁵³ but while there are methods to distinguish between them, both processes rely on a charge transfer step whose rate can be described by a golden-rule expression for radiationless transitions shown in Equation 7-2. In this equation: $V_{i \rightarrow f}$ is the matrix element of the perturbation \hat{H}' between initial and final states with wavefunctions ψ_i and ψ_f respectively (see Equation 7-3); λ is the Marcus reorganisation energy, which includes intra-molecular (λ_i) and solvent (λ_s) reorganisation components; ΔG is the free energy change in the reaction. It is worth noting that the equation may need to be modified for solid films due to the presence of a semi-continuous band of final states rather than a discrete molecular level; this requires integration of Equation 7-2 over the density of available states.²⁴¹

The main difference between spin-selective recombination and straight CP recombination to a triplet exciton is in the electronic coupling term that includes either a purely electronic or spin dependent matrix element.

$$k_{i \rightarrow f} = \left(\frac{4\pi^3}{h^2 \lambda k_B T} \right)^{\frac{1}{2}} V_{i \rightarrow f}^2 \exp \left(- \frac{(\Delta G + \lambda)^2}{4\lambda k_B T} \right) \quad \text{Equation 7-2}$$

$$V_{i \rightarrow f} = \langle \psi_i | \hat{H}' | \psi_f \rangle \quad \text{Equation 7-3}$$

If the rate of triplet decay is unchanged in a solvent atmosphere, a decrease in the observed yield of triplets corresponds to a decrease in the rate of triplet formation. As seen in the equations above, the rate of formation of triplets depends on i) the free energy change (ΔG) ii) the reorganisation energy (λ) and iii) the electronic coupling between initial and final states, $V_{i \rightarrow f}$. Assuming there is no change in the relevant energy levels with increasing solvent vapour concentration (there is no evidence for a shift in the singlet emission peak for example) then ΔG should remain unchanged. The intra-molecular reorganisation energy (λ_i) is mainly due to vibrational coupling and is unlikely to change; solvent and inter-molecular reorganisation (λ_s) however, will depend on the donor-acceptor separation (r) and the polarisability of the separating medium. In Marcus' formulism (see Equation 7-4), the medium is treated as a dielectric continuum with refractive index n and permittivity ϵ_r and the donor and acceptor treated as spheres of radius r^{\pm} ; if the donor and acceptor radii and refractive index are kept constant, it can be seen that λ_s will increase with increasing separation R and solvent polarity ϵ_r .^{242,243} This can either increase or decrease the rate of transfer dependent on the initial relationship between ΔG and λ_s and the magnitude of the change will be affected in a non-trivial way. As a result, this change can't be ruled out and further work is required to determine whether this has an impact on our results.

$$\lambda_s = \frac{e^2}{4\pi\epsilon_0} \left[\frac{1}{2r^+} + \frac{1}{2r^-} - \frac{1}{R} \right] \left(\frac{1}{n^2} - \frac{1}{\epsilon_r} \right) \quad \text{Equation 7-4}$$

The matrix term ($V_{i \rightarrow f}$) corresponds to electron tunnelling through a potential barrier and can be written as in equation Equation 7-5; here β is a function of the barrier height and R the spatial separation of initial and final states.

$$V_{i \rightarrow f}^2 = V_0^2 e^{-\beta R}$$

Equation 7-5

As has been seen in dye-sensitised nano-crystalline TiO_2 systems, varying the spatial separation of donor and acceptor sites can have a dramatic impact on electron transfer rates.^{244,245} If increasing solvent vapour pressure acts to increase the separation at the interface, this term would lead to an exponential decrease in the rate of triplet formation with separation. A similar argument can be applied to the decay of the CP directly to ground.

Charge separation on the other hand does not rely on a charge transfer step from the CP as dissociation can be achieved by intra-molecular charge diffusion which will be unaffected by swelling. The increase in observed charge can therefore be explained by a change in the branching ratio from the CP state due to a change in the relative decay rates. Using this argument, the decrease in signal of triplet and increase in signal of dissociated charge observed in the TAS experiment Figure 7-3a can be qualitatively explained.

Hence by this explanation we can account for the change in exciplex yield, lifetime and energy and the relative yields of triplets and charges and the reversibility of these processes (as solvent leaves the film, the interfacial spatial separation returns to near its initial value). However, the explanation fails to account for the similar (but permanent) effects observed in solvent annealed and thermally annealed samples. An argument could be made in which the rearrangement of molecules during annealing leads to permanent changes in the interfacial separation, although testing such a hypothesis is difficult.

A second plausible explanation for our results relies on the fact that the Onsager capture radius for these materials is of the same order as the domain spacing. As described in Chapter 2, excited states that are dissociated at the interface can lead directly to free charges if the electron transfer step results in a pair separation sufficient to overcome their mutual Coulomb attraction. However, if separation is not possible due to the confinement of charges within a small domain, then the pair must be caught and the chance for charge dissociation is diminished. In this case, the rate of dissociation is in competition with other decay pathways from the CP state (see Figure 7-5). On exposure to solvent, swelling may lead to higher volume domains in which charge confinement is reduced and dissociation of charge is more likely. A graphical representation of these changes is seen in Figure 7-6. Thus, in this description of our results, the exciplex and triplet yields are reduced due to competition from a faster rate for CP dissociation, which also obviously accounts for the increase in observed free charges. In addition, the rate of decay of the exciplex is linked to the rates of decay from the CP state which implies that the total sum of $k_{\text{CP-T}}$, k_{CP} , and $k_{\text{CP-DC}}$ is increased. This is consistent with an increased rate of charge dissociation ($k_{\text{CP-DC}}$). On solvent evaporation domains will shrink (deswelling) thus explaining the reversible nature of the effects at low relative vapour pressures. In

addition, the permanent photo-physical changes observed at higher vapour pressures (and on thermal annealing) are accounted for by a plastic rearrangement of molecules that leads to phase segregation and coarser domains. It is also possible that a changing dielectric within the materials, caused by either the presence of solvent or changes in local morphology, could be causing a decrease in the Onsager capture radius as shown by Equation 7-6. This is the subject of further work in this area.

$$r_c = \frac{e^2}{4\pi\epsilon_r\epsilon_0k_B T} \quad \text{Equation 7-6}$$

Consistent with the premise for this explanation, our previous results (see Chapter 6) suggest that the domain size in the as-spun block copolymer films is extremely fine, although exact values for domain sizes are unknown. In a donor-acceptor material set similar to that studied here (F8BT:PFB blends), Morteani et al. have found the Onsager capture radius of the CT state to be 3.1 nm.⁵¹

This explanation is more satisfying than the previous hypothesis given that it can explain the whole range of experimental observations.

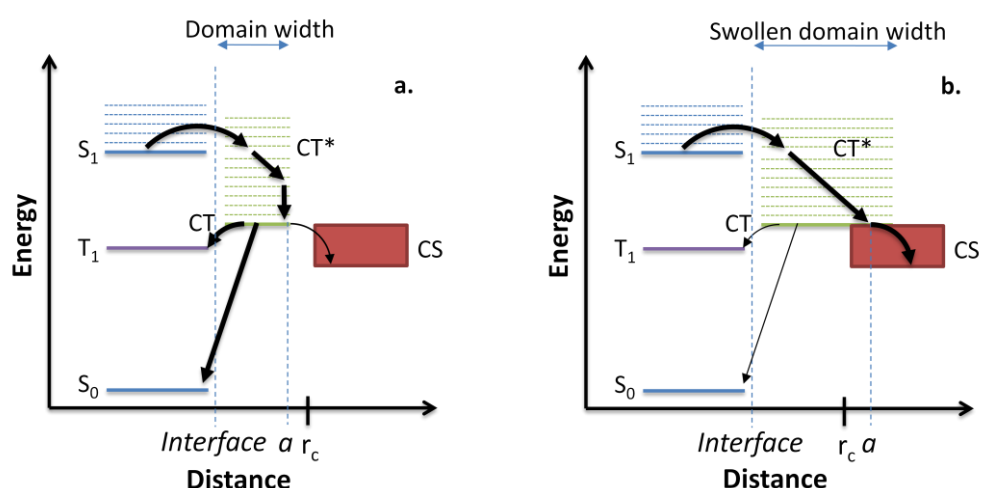


Figure 7-6 Schemes showing the pathways for an excited state near a donor-acceptor interface in a film of F8BT-*b*-PFM-*b*-F8BT block copolymer. The abscissa represents the separation distance between hole and electron. An initially excited state (S_1) that reaches an interface will undergo charge transfer. The fastest rate of transfer will be to an initially 'hot' charge transfer (CT^*) state. The excess energy will result in rapid thermalisation to a relaxed CT state at a thermalisation distance (charge pair separation) a . In Figure a, the representative domain width is small and thermalisation is limited to a separation less than the Onsager capture radius. As a result, dissociation to charge separated states (CS) is limited and the main decay pathways are to a triplet exciton state (T_1) or to ground (S_0) shown by thicker arrows. Figure b, represents the same film in a solvent atmosphere or after solvent or thermal annealing; the separation of bound charges in a CT state are no longer limited by domain size and thermalisation may result directly in separate charges.

Quantitative information is hard to garner from the data; this is not least because the actual degree of solvent uptake has not yet been measured, but also because of a lack of time resolution in the experiments performed. The formation of triplets and charges from the CP state are thought to occur on a ~10 ns and ~100 ns timescale respectively,⁵⁵ which are both too fast for the current transient absorption apparatus to measure. Further experiments are planned that should quantify the effects seen here and help to distinguish between the possible explanations presented.

7.5 Conclusions

In this chapter work has been presented on photo-physical studies of thin films of PFM-*b*-F8BT-*b*-PFM triblock copolymer undertaken in a controlled solvent atmosphere. The highly-concentrated polymer solution is intermediate between a solid film and a liquid solution and as such, the properties are also intermediate between them. Specifically, it was hoped that the use of the technique would help to elucidate the nature of interfacial interactions by controllably altering them. In the above experiments, we have found that by using an atmosphere of chloroform, the branching ratio for decay from a bound charge pair state can be altered in favour of free charges. This result is highly interesting considering that in the previous chapter, the limitations of using F8BT and PFM as materials for photovoltaics was made clear: namely, that triplet excitons in F8BT are lower in energy than the charge separated state necessary for efficient photoconduction; as a result, only on the order ~10% of absorbed photons are converted to generate extractable current (not considering current losses after generation). Any change in the branching ratio of CT state decay that favours charge dissociation will be of benefit to photovoltaics fabricated from these materials.

The tool-box thus presented is extremely versatile with a large parameter space for possible experiments. In comparison to high pressure hydrostatic loading, the set up for the experiments is relatively cheap and easy to build and maintain. In addition, modelling molecules in solvent is significantly easier than modelling them at high pressure.²⁴⁶ Further experiments are planned and/or in progress to both confirm the suppositions above in a quantitative fashion and expand the range of techniques available. These include: spectroscopic ellipsometry to determine the uptake of solvent and exact polymer concentrations at different vapour pressures; electronic techniques such as charge transport mobility measurements; altering the solvent used so that the effect of different dielectrics can be studied and so on.

In conclusion, a new technique has been tested to study interfacial interactions in a photo-conductive donor-acceptor block copolymer. Satisfactory qualitative conclusions have been drawn from a limited study and further investigations using the technique seem promising.

Chapter 8

Conclusions and Further Work

8.1 Conclusions

It has been the aim of this thesis to demonstrate the potential of block copolymers for the advancement of organic photovoltaics. With this goal in mind, we began by introducing both excitonic photovoltaics and block copolymers in Chapter 2. Given a better understanding of these two topics, a précis was made of the state of current research using block copolymers for photovoltaic applications. One of the conclusions of this section was a distinct lack of spectroscopic data and information in general on the photophysics of photoconductive block copolymers. This was deemed an important gap to try to bridge given the inherent structure-morphology relationship in these materials. Details of the techniques used to address this issue were then considered in Chapter 3.

The first results chapter (Chapter 4) provided a direct probe of the structure-function relationship in photoconductive block copolymers. We considered a pendant small molecule system in which triphenyl amine (donor) and perylene bisimide acrylate (acceptor) were strung from a saturated polymer backbone to form a block copolymer. Without post-fabrication processing, the photophysics of film samples of these materials were found to correlate with chain length: namely, shorter chains (that result in smaller domain spacings) show higher photoluminescence quenching (> 99%) and greater charge yields (~ a factor of four at $1\mu\text{s}$ in a short chain compared to the longest one studied). This correlation was found to extend to blends of the two homopolymers which have significantly larger domain spacing. The relationship between chain length and device performance was less clear, but shows that a balance must be met between structures for high charge generation and structures for better device efficiencies.

Further investigation into device performance was made in Chapter 5. In this chapter, use was made of a series of pendant acceptor (poly-(perylene bisimide acrylate)) and conjugated polymer (poly-3-hexylthiophene) block copolymer systems. Comparing the charge generation in these polymers with a well known blend system, the yield of long lived charges was found to be similar, leading to the hypothesis that device performance is not limited by charge generation, but by charge collection due to high recombination

losses. The exact reason for these losses is a matter for further investigation. A parallel study was made of the effects of annealing and domain crystallinity on photophysics and device performance. Solvent vapour annealing and thermal annealing were found to achieve different degrees of order in donor and acceptor materials. These results support the conclusion that strong ordering is important for charge generation as well as charge transport in polythiophenes.

In Chapter 6, the first example of an all conjugated block copolymer has been investigated. The polymer system is based on the heavily studied polyfluorene copolymers poly(9,9'-dioctylfluorene-co-benzothiadiazole) (F8BT) and an adapted version of poly(9,9'-dioctylfluorene-co-bis-*N,N'*-(4-butylphenyl)-bis-*N,N'*-phenyl-1,4-phenylenediamine) (PFB), of poly(9,9'-dioctylfluorene-co-bis-*N,N'*-(4-tolyl)-bis-*N,N'*-phenyl-1,4-phenylenediamine) (PFM). A comparative study was made between the block copolymer and a blend of homopolymers. The results of this study confirm the highly intermixed nature of the block copolymer and the insensitivity of the morphology formed to fabrication procedure. However, we have identified a strong, long-lived triplet exciton signature in the highly intermixed block copolymer that acts as a parasitic decay pathway for energy in the system. Charge yields at 1 μ s were used to determine the efficiency of long-lived charge generation, found to be $\sim 12 \pm 5\%$ in both the block copolymer and blend systems. This low yield is one of the reasons that efficiencies of devices fabricated from these materials are low (0.016% at best). Despite this, devices formed using block copolymer as the active layer outperform those formed from an equivalent blend of homopolymers by over an order of magnitude (in terms of power conversion efficiency). In the last part of the chapter, we discover that the photophysical properties of the block copolymer and blend are interchangeable dependent on annealing conditions, although the macroscopic phase segregation remains significantly different in each case. This raises an interesting question: what is the cause of the differences in photophysical properties between an annealed and unannealed F8BT-*b*-PFM-*b*-F8BT block copolymer film?

Finally, in Chapter 7 we aim to answer this question using a novel combination of techniques that allow for in-situ spectroscopy on films swollen in a solvent atmosphere. The trends with increasing solvent-atmosphere concentration provide evidence that point toward a confinement effect of small domains that inhibit free charge formation and lead to preferential inter system crossing or geminate recombination. Swelling the domains (or annealing to larger domain sizes) decreases the confinement effect and allows for a higher yield of charge generation. This is important in the context of organic photovoltaics given the limited charge yields calculated for these polymers in Chapter 6.

In general, the results from this thesis have been positive with regard to the application of block copolymers in organic photovoltaics. This mirrors the current research in this field, with state-of-the-art block

copolymer photovoltaics (0.5%)¹³⁸ swiftly encroaching on the polymer-polymer blend photovoltaic efficiency record (1.8%)²¹⁸. Using spectroscopic techniques, we have demonstrated the potential of the structure-morphology-function relationship in donor-acceptor block copolymers and in doing so filled a gap in existing research in this field.

8.2 Suggestions for Further Work

While suggestions have been made for specific additional work throughout the results chapters above, we feel it necessary to add this section to address the more pressing subject of how block copolymers can be utilised to further advance photovoltaics.

The evidence above has shown that the limited domain sizes of phase segregated photoactive block copolymers does not necessarily limit the charge generation in these materials. However, in all cases studied (and from browsing the relevant literature (see section 2.3)), it is short circuit currents (although poor fill factors also contribute) that are limiting device performance. We suggest some reasons for this apparent discrepancy:

- If there is a very strong dependence of the charge generation in these materials on externally applied electric field, then the spectroscopic results will not match up with the device results. In this case, free charge generation may be a potential limiting factor.
- Potentially high recombination losses due to large interfacial surface areas and therefore lower charge mean free paths.
- Potentially high recombination losses due to poor morphologies that result in unwired contacts and large numbers of dead ends.

These are problems that do not spell the end for block copolymer photovoltaics and are readily addressed by experiments on devices such as charge extraction, transient photovoltage measurements and mobility measurements.^{154,247} It is the suggestion of the author that measurements are carried out to determine which of these are the main contributors to low device currents. Armed with this knowledge, future research can then be directed towards improving mobilities, finding domain sizes and spacings that compromise between charge generation and recombination, or focussing on achieving structures in which all domains are wired to their respective contacts.

Appendix A

Hückel Molecular Orbital Theory and the Band Gap of Polymers

The Hückel model describes a qualitative and semi-empirical application of molecular orbital (MO) theory to conjugated and aromatic molecules.^{23,24} In the model, π MO energies can be approximated by employing a set of assumptions, the most important of which is that left over p_z orbitals can be treated as separate from the sp^2 hybridised σ carbon backbone; this is valid in most cases due to a large energetic difference between the hybridised orbitals and remaining p orbital. Then π orbitals are formed as a linear combination of the wave functions of each p_z orbital. For example in ethene:

$$\psi_{\pi} = c_1 \phi_{p_{za}} + c_2 \phi_{p_{zb}} \quad \text{Equation A-1}$$

Where ϕ are atomic orbitals and c are coefficients (to be found) that give the lowest energy MOs. The p_{za} and p_{zb} orbitals are labelled a and b in order to distinguish between them for ease of variable tracking; this is not strictly necessary as (in this case) the orbitals are indistinguishable. The expectation value for the energy of the π -orbital is:

$$\begin{aligned} \varepsilon &= \frac{\int \psi_{\pi}^* \hat{H} \psi_{\pi} d\tau}{\int \psi_{\pi}^* \psi_{\pi} d\tau} \quad \text{Equation A-2} \\ &= \frac{(c_1)^2 \int \phi_{p_{za}}^* \hat{H} \phi_{p_{za}} d\tau + (c_2)^2 \int \phi_{p_{zb}}^* \hat{H} \phi_{p_{zb}} d\tau + 2c_1 c_2 \int \phi_{p_{za}}^* \hat{H} \phi_{p_{zb}} d\tau}{(c_1)^2 \int \phi_{p_{za}}^* \phi_{p_{za}} d\tau + (c_2)^2 \int \phi_{p_{zb}}^* \phi_{p_{zb}} d\tau + 2c_1 c_2 \int \phi_{p_{za}}^* \phi_{p_{zb}} d\tau} \end{aligned}$$

Where \hat{H} is the Hamiltonian and the integral is over all space. After reducing this a little and introducing some notation for the Coulomb (H_{ii}), resonance (H_{ij}) and overlap (S_{ij}) integrals, Equation A-2 can be written as follows:

$$\varepsilon = \frac{(c_1)^2 H_{aa} + (c_2)^2 H_{bb} + 2c_1 c_2 H_{ab}}{(c_1)^2 + (c_2)^2 + 2c_1 c_2 S_{ab}} \quad \text{Equation A-3}$$

This is minimised by differentiating with respect to each of the coefficients in turn and setting the resulting expressions equal to zero.

$$c_1(H_{aa} - \varepsilon) + c_2(H_{ab} - \varepsilon S_{ab}) = 0 \quad \text{Equation A-4}$$

$$c_1(H_{ab} - \varepsilon S_{ab}) + c_2(H_{bb} - \varepsilon) = 0$$

These 'secular equations' are solvable only if the 'secular determinant' satisfies the condition:

$$\begin{vmatrix} H_{aa} - \varepsilon & H_{ab} - \varepsilon S_{ab} \\ H_{ab} - \varepsilon S_{ab} & H_{bb} - \varepsilon \end{vmatrix} = 0 \quad \text{Equation A-5}$$

Of course, this could be solved exactly using modern computational techniques, but in Hückel's model, further simplifications are made:

- All Coulomb integrals (of the form H_{ii}) are set equal to the ionization energy of the p orbital (in this case a $2p$ orbital) and denoted by α .

- Overlap integrals (of the form S_{ij}) are set to zero; this is a big assumption, because if there was no overlap between adjacent atoms, then no bonding would occur.
- All resonance integrals between non-neighbouring atoms (of the form H_{ij} where i and j are different and $i \neq j \pm 1$) are set to zero.
- All remaining resonance integrals are set equal (to an adjustable parameter β).

Thus, the determinant is reduced to:

$$\begin{vmatrix} \alpha - \varepsilon & \beta \\ \beta & \alpha - \varepsilon \end{vmatrix} = 0 \quad \text{Equation A-6}$$

Which is readily solved to find $\varepsilon = \alpha \pm \beta$. Each spare electron from the two carbon atoms can fill the π that is lowest in energy, leaving the other unfilled; this makes the HOMO-LUMO energy gap a value of 2β . An approximate value for the 2p orbital overlap between neighbouring carbons is $\sim -0.8\text{eV}$ giving an energy gap of $\sim -1.6\text{eV}$. This shows the level of accuracy of the model, as 1.6 eV is the energy of a photon with wavelength 775 nm , whereas the maximum absorption as measured is at 171 nm and ethene is transparent at visible wavelengths. By substituting these values into the two formula of Equation A-4, we can find the values of c_1 and c_2 for each energy and thus by Equation A-1 we find the molecular π -orbitals.

Considering a longer chain gives insight into the decreasing HOMO-LUMO energy offset with increasing conjugation, as can be seen in buta-1,3-diene.

Butadiene is solved in a similar way as above, but with a 4×4 determinant:

$$\begin{vmatrix} \alpha - \varepsilon & \beta & 0 & 0 \\ \beta & \alpha - \varepsilon & \beta & 0 \\ 0 & \beta & \alpha - \varepsilon & \beta \\ 0 & 0 & \beta & \alpha - \varepsilon \end{vmatrix} = 0 \quad \text{Equation A-7}$$

With solutions $\varepsilon = \alpha \pm 0.62\beta$, $\alpha \pm 1.62\beta$. The bottom two π orbitals are now filled and the HOMO-LUMO offset is 1.24β corresponding to $\sim -1\text{eV}$. With each successive addition of unsaturated carbon atoms to the chain, the determinant will be extended along the tridiagonal and the HOMO-LUMO offset energy decreases, leading to a progressively more red-shifted absorption peak.

The long chain case

The method above may be applied to longer and longer chains with higher and higher order determinants. The natural extension of the process for a chain of length n results in an $n \times n$ determinant. One way of analytically solving this case is to divide the determinant through by β and make the substitution:

$$2x = \frac{\alpha - \varepsilon}{\beta} \quad \text{Equation A-8}$$

such that the $n \times n$ determinant (U_n) becomes:

$$\begin{vmatrix} 2x & 1 & 0 & \cdots & 0 & 0 \\ 1 & 2x & 1 & \ddots & \vdots & 0 \\ 0 & 1 & 2x & \ddots & 0 & \vdots \\ \vdots & \ddots & \ddots & \ddots & 1 & 0 \\ 0 & \cdots & 0 & 1 & 2x & 1 \\ 0 & 0 & \cdots & 0 & 1 & 2x \end{vmatrix} = U_n \quad \text{Equation A-9}$$

This is recognised as one representation of a Chebyshev polynomial of the second type, defined by the relation:²⁴⁸

$$U_n(x) = \frac{\sin((n+1)\theta)}{\sin\theta} \quad \text{for } x = \cos\theta \quad \text{Equation A-10}$$

The solutions to the $n \times n$ case are now easily seen to be:

$$x = \cos\left(\frac{k\pi}{n+1}\right) = \frac{\alpha - \varepsilon}{2\beta} \quad \text{Equation A-11}$$

or

$$\varepsilon_k = \alpha + 2\beta\cos\left(\frac{k\pi}{n+1}\right) \quad \text{for } k = 1, 2, 3, \dots, n-1, n \quad \text{Equation A-12}$$

For increasingly long chain lengths, the difference between adjacent energy levels becomes increasingly small. This is graphically represented in Figure A-1 for chain lengths of 4, 40 and 100. As the bottom half of these orbitals will be filled, the HOMO-LUMO energy offset will also decrease.

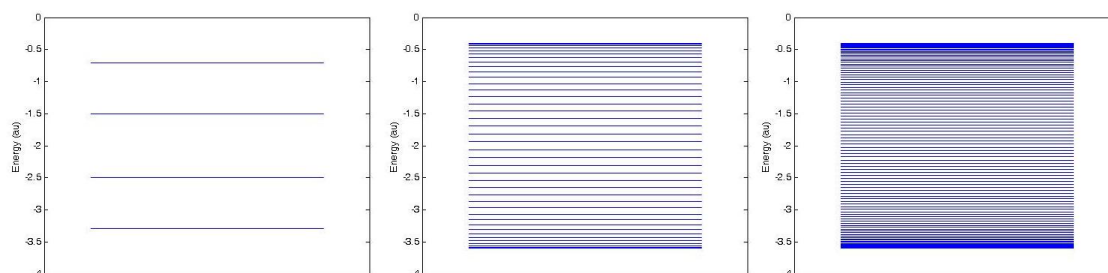


Figure A-1
The figure shows the results of Equation A-12 using $\alpha=-2$ and $\beta=-0.8$ and for three different values of chain length, n : 4, 40 and 100 from left to right.

Once the energy offset becomes less than $k_B T$ (the approximate energy available at the ambient temperature T), electrons can hop between unoccupied states and the polymer will show metallic conductivity. However, it is well known that this does not occur due to a deformation of the polymer skeleton that leads to an energetic stabilisation known as Peierls' distortion which introduces a HOMO-LUMO gap as will be shown below.

Peierls' distortion and Band Gaps

In certain polymer chains, a geometric distortion in the monomer-monomer bonds leads to energetic stabilisation. Such an asymmetric conformation is known as an alternant structure and is shown in Figure A-2. In the following discussion, we will show that this stabilising effect leads to an energy gap (in an example of a polyene) between the filled and non-filled molecular orbitals and hence a metal-insulator

transition. Figure A-2 gives an indication of why this occurs for a hexatriene molecule. In this picture, alternant structure leads to orbitals that have greater or less overlap with neighbouring orbitals than in the regular structure. In-phase p-orbitals with greater overlap and out-of-phase p-orbitals with less overlap will stabilise the π -molecular orbital; the inverse is also true, for example if in-phase orbitals are further apart with less overlap, then the energy of the π -molecular orbital will be destabilised. It is easily shown then, that this will have the greatest stabilising effect for the HOMO, while the greatest destabilising effect is felt by the LUMO.

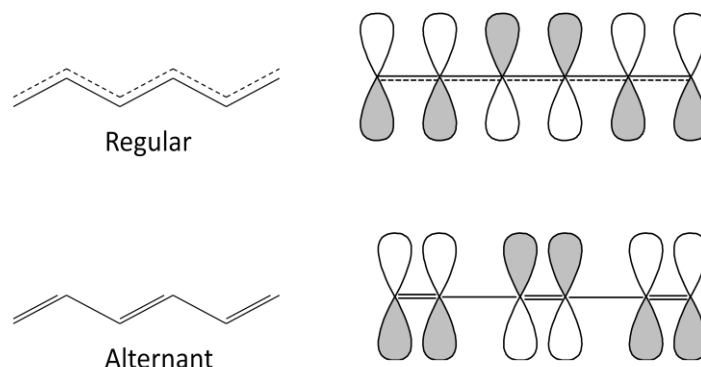


Figure A-2
The figure shows the difference between regular and alternant structures in hexatriene. On the right, the HOMO π -orbital is shown for both structures. In the alternant structure, when two 'in-phase' p orbitals are close together or two 'out-of-phase' orbitals are far apart, the energy level is stabilised. Adapted from reference 249.

In the discussion of Hückel's model above, the nearest neighbour p-orbital interaction was set equal to β . Now we see that this value will be split in the alternant structure to $\beta+d\beta$ and $\beta-d\beta$ dependent on a greater or lesser overlap between adjacent p-orbitals. This will lead to a secular determinant of the form:

$$\begin{vmatrix} \alpha - \varepsilon & \beta + d\beta & 0 & 0 & \dots & 0 \\ \beta + d\beta & \alpha - \varepsilon & \beta - d\beta & 0 & \ddots & 0 \\ 0 & \beta - d\beta & \alpha - \varepsilon & \beta + d\beta & \ddots & 0 \\ 0 & 0 & \beta + d\beta & \alpha - \varepsilon & \ddots & 0 \\ \vdots & \ddots & \ddots & \ddots & \ddots & \beta + d\beta \\ 0 & 0 & 0 & 0 & \beta + d\beta & \alpha - \varepsilon \end{vmatrix} = Q_n \quad \text{Equation A-13}$$

Finding the values of ε this (for $Q_n=0$) requires a little more work than in the case above. We follow the method of Coulson.²⁵⁰ For simplicity, we make the substitutions:

$$\alpha - \varepsilon = A, \quad \beta + d\beta = s \quad \text{and} \quad \beta - d\beta = d$$

This gives the determinant Q_n (with $2n$ rows and columns) as:

$$\begin{vmatrix} A & s & 0 & 0 & \dots & 0 \\ s & A & d & 0 & \ddots & 0 \\ 0 & d & A & s & \ddots & 0 \\ 0 & 0 & s & A & \ddots & 0 \\ \vdots & \ddots & \ddots & \ddots & \ddots & s \\ 0 & 0 & 0 & 0 & s & A \end{vmatrix} = Q_n \quad \text{Equation A-14}$$

Now we consider a second determinant with $2n-1$ rows and columns of the form:

$$\begin{vmatrix} A & d & 0 & 0 & \dots & 0 \\ d & A & s & 0 & \ddots & 0 \\ 0 & s & A & d & \ddots & 0 \\ 0 & 0 & d & A & \ddots & 0 \\ \vdots & \ddots & \ddots & \ddots & \ddots & s \\ 0 & 0 & 0 & 0 & s & A \end{vmatrix} = R_n \quad \text{Equation A-15}$$

Then we expand both determinants in the top row to find:

$$Q_n = AR_n - s^2Q_{n-1} \quad \text{Equation A-16}$$

$$R_n = AQ_{n-1} - d^2R_{n-1} \quad \text{Equation A-17}$$

Elimination of R_n then gives the recurrence relationship:

$$Q_{j+1} = (A^2 - s^2 - d^2)Q_j - s^2d^2Q_{j-1} \quad \text{for } j = 1, 2, 3, \dots, n \quad \text{Equation A-18}$$

Using the conditions $Q_0=0$ and $Q_{n+1}=0$ we can use Equation A-18 to define the characteristic polynomial $P(x)$:

$$P(x) = -x^2 + (A^2 - s^2 - d^2)x - s^2d^2 \quad \text{Equation A-19}$$

This equation has roots r_1 and r_2 and we use the exponent of x to track the solution to Q_j :

$$Q_j = D_1r_1^j + D_2r_2^j \quad \text{Equation A-20}$$

Using the conditions above, we find that $D_1 = -D_2$ and (since $D \neq 0$):

$$\left(\frac{r_1}{r_2}\right)^{n+1} = 1$$

By using the following identity:

$$r_1r_2 = \left(\frac{(A^2 - s^2 - d^2) + \sqrt{(A^2 - s^2 - d^2)^2 - 4s^2d^2}}{2}\right) \left(\frac{(A^2 - s^2 - d^2) - \sqrt{(A^2 - s^2 - d^2)^2 - 4s^2d^2}}{2}\right) = s^2d^2$$

This becomes:

$$\left(\frac{r_1^2}{s^2d^2}\right)^{n+1} = 1 \quad \text{Equation A-21}$$

Since the roots of a quadratic are often complex, this can be written using $1 = e^{2ki\pi}$ for integer values of k , yielding the roots:

$$r_{1,k} = sde^{i\pi\left(\frac{k}{n+1}\right)} \quad \text{Equation A-22}$$

$$r_{2,k} = sde^{-i\pi\left(\frac{k}{n+1}\right)} \quad \text{for } k = 1, 2, 3 \dots, n$$

Then, by the identity:

$$\begin{aligned} r_1 + r_2 &= \left(\frac{(A^2 - s^2 - d^2) + \sqrt{(A^2 - s^2 - d^2)^2 - 4s^2d^2}}{2}\right) \\ &\quad + \left(\frac{(A^2 - s^2 - d^2) - \sqrt{(A^2 - s^2 - d^2)^2 - 4s^2d^2}}{2}\right) = A^2 - s^2 - d^2 \end{aligned}$$

We obtain:

$$sd\left(e^{i\pi\left(\frac{k}{n+1}\right)} + e^{-i\pi\left(\frac{k}{n+1}\right)}\right) = 2sdc\cos\varphi = A^2 - s^2 - d^2 \quad \text{Equation A-23}$$

or

$$(\varepsilon - \alpha)^2 = (\beta - d\beta)^2 + (\beta + d\beta)^2 + 2(\beta + d\beta)(\beta - d\beta)\cos\varphi \quad \text{Equation A-24}$$

Solving the quadratic in ε gives:

$$\varepsilon_k = \alpha \pm \sqrt{(\beta - d\beta)^2 + (\beta + d\beta)^2 - 2(\beta + d\beta)(\beta - d\beta)\cos\left(\frac{k\pi}{n+1}\right)} \quad \text{Equation A-25}$$

for $k = 2, 4, 6, \dots, n$

The k values are only even integers because of the nature of the determinant Q_n , which must be of even size. For an odd integer value of n , the determinant to be solved is R_n , which will have the same solution as Equation A-25, but odd integer values for k . A simple check of Equation A-25 is performed by setting $d\beta=0$; in this case, we return to the non-distorted (regular structure) case (Equation A-12) for $\varphi/2=\vartheta$. The effects of Equation A-25 on the energy levels are most easily seen by replotting Figure A-1 using this new equation as can be seen in Figure A-3.

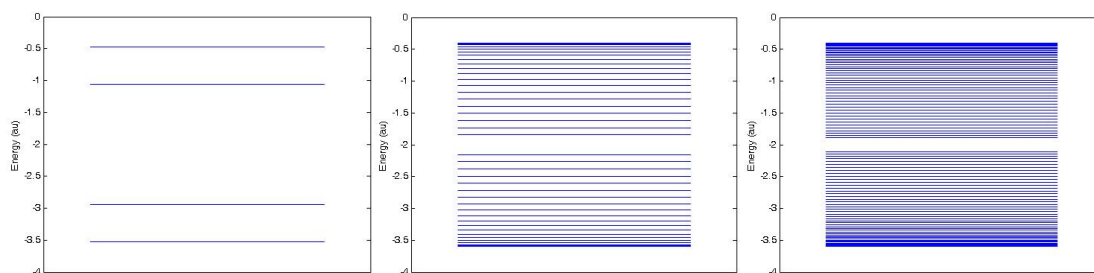


Figure A-3
The figure shows the results of

Equation A-25 using $\alpha=-2$, $\beta=-0.8$, $d\beta=0.05$ and for three different values of chain length, n : 4, 40 and 100 from left to right.

Since all levels up to $n/2$ will be filled (ie. the lower half of the orbitals seen in the figure), there is now a gap between the HOMO and LUMO levels. In addition, the sum of the energies of the occupied orbitals is seen to be lower in the structurally distorted case showing that alternant structure is favoured.

Appendix B

Flory-Huggins Theory of Polymer-Solution and Polymer-Polymer Demixing

In order to discuss phase segregation in polymer-polymer blends, we must first determine the free energy of the system and then see if it is minimised by segregation. This is achieved most simply by considering a straight forward extension of a polymer-solvent system first approached by Flory and Huggins. A simple way to do this is to begin with the lattice model.

The 'lattice model' is based on viewing a polymer as a connected series of cells each containing a polymer segment; all surrounding cells contain solvent molecules, see Figure B-1. Two significant assumptions that are normally made are: i) that polymer end effects are neglected – this can only be made as long as the polymer is long enough; ii) that all polymer segments are the same, and there is no energetic difference between placing one segment or another in contact with the solvent.

Such a system, represented by a flat lattice in Figure B-1, has a free energy made up of two components: an entropy term describing the number of ways of arranging the chain on the lattice, and an energy term describing the interactions between adjacent molecules. We now consider how these two components relate to the mixing of the polymer and solution.

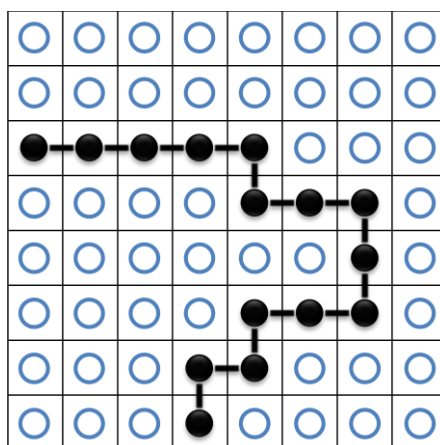


Figure B-1

The figure demonstrates the lattice model for a polymer solution. One polymer chain (black closed circles) is shown on a lattice with some solution around it (blue open circles). Each filled connected circle represents a polymer segment (not necessarily monomer) that is about the same size as a solvent molecule.

Enthalpy term

On a lattice with Ω sites, we define the fraction of lattice sites occupied by the polymer as φ . Each occupied cell has an energy that depends on the interaction energies between itself and the constituents in its nearest neighbour cells (co-ordination number 'z'). These interaction energies may be: ϵ_{pp} , $\epsilon_{ps} = \epsilon_{sp}$ and ϵ_{ss}

where the subscript denotes polymer and solvent. On the lattice, the total number of interactions of this sort will be:

polymer segment - polymer segment interactions $z \Omega \varphi^2/2$

polymer segment - solvent molecule interactions $z \Omega (1-\varphi)\varphi$

solvent molecule - solvent molecule interactions $z \Omega (1-\varphi)^2/2$

This yields a total energy, U , of:

$$\frac{U}{k_B T} = \frac{z\Omega}{k_B T} \left[\left(\frac{\varepsilon_{pp} + \varepsilon_{ss}}{2} - \varepsilon_{ps} \right) \varphi^2 + (\varepsilon_{ps} - \varepsilon_{ss}) \varphi + \frac{\varepsilon_{ss}}{2} \right] \quad \text{Equation B-1}$$

$$= \chi_{ps} \Omega \varphi (1 - \varphi) + \text{const.} + \text{terms linear in } \varphi$$

In which we have defined χ_{ps} , known as the Flory-Huggins interaction parameter according to:

$$\chi_{ps} = \frac{z}{k_B T} \left[\varepsilon_{ps} - \frac{1}{2} (\varepsilon_{pp} + \varepsilon_{ss}) \right] \quad \text{Equation B-2}$$

For most cases, χ is found to be positive. A nice description for why this should be is described by de Gennes:⁹¹

The interaction energies, ε_j are predominantly due to van der Waals attractions that are essentially proportional to the product of electronic polarisabilities (α) for both molecules. Since these interactions are attractive, the energy describing the interaction will be negative. Thus for some positive k :

$$\begin{aligned} \varepsilon_{pp} &= -k\alpha_p^2 \\ \varepsilon_{ss} &= -k\alpha_s^2 \\ \varepsilon_{ps} &= -k\alpha_p\alpha_s \end{aligned}$$

Which implies that:

$$\chi_{ps} \propto \frac{k}{2} (\alpha_s - \alpha_p)^2$$

will be positive. Of course, this is a simple estimate and other effects such as hydrogen bonding, steric effects etc. will alter the outcome; but positive χ_{ps} is a general observation.

Entropy term

In order to consider the number of configurations of the system (W), we start by laying one segment at a time on the lattice. The first segment can go anywhere on the Ω sites of the lattice; the second one must go on one of z adjacent sites. The next and the all subsequent segments must go on $z-1$ sites.

So for the first polymer of length N (noting there are two ends to the chain):

$$w_1 = \Omega z (z-1)^{N-2} \approx \Omega (z-1)^{N-1} \quad \text{Equation B-3}$$

in which the approximation is for large chain lengths. Now, for the $(j+1)^{\text{th}}$ polymer, there will already be Nj sites occupied, so the first segment can go anywhere on $\Omega - Nj$ sites, and the next on one of z adjacent sites, the fraction of which are empty is $1 - Nj/\Omega$ and so on as before. With the same approximation as in Equation B-3 and one step further, this yields:

$$w_{j+1} \approx (\Omega - N_j) \left[(z-1) \left(1 - \frac{N_j}{\Omega} \right) \right]^{N-1} \approx w_1 \left(1 - \frac{N_j}{\Omega} \right)^N \quad \text{Equation B-4}$$

The total number of configurations is the product of Equation B-3 and Equation B-4 over all j up to the total number of polymer chains, n_p . Assuming the chains are indistinguishable, this is written as:

$$W = \frac{1}{n_p!} \prod_{j=1}^{n_p} w_j \quad \text{Equation B-5}$$

Now according to Boltzmann, the entropy will be proportional to the logarithm of this term. Taking the logarithm and converting the sum to an integral gives:

$$\begin{aligned} \ln W &= \int_0^{n_p} \left[\ln \left(\Omega (z-1)^{N-1} \left(1 - \frac{Nj}{\Omega} \right)^N \right) - \ln(j) \right] dj \\ &= \Omega \left[\frac{\varphi}{N} \ln \varphi - (1-\varphi) \ln(1-\varphi) \right] + \text{linear terms in } \varphi \end{aligned} \quad \text{Equation B-6}$$

Using $\phi = n_p N / \Omega$.

Summing up

The free energy of the system is given by:

$$F = -k_B T \ln W + U \quad \text{Equation B-7}$$

However, it is most convenient now to consider the free energy of mixing $F_m(\Omega, \varphi)$ instead of the free energy of the overall system $F(\Omega, \varphi)$. This will justify our exclusion of linear terms in φ . The free energy of mixing is defined as the difference between the free energy of the mixed system, and the free energy of the pure polymer and pure solvent. This gives:

$$F_m(\Omega, \varphi) = F(\Omega, \varphi) - F(\Omega\varphi, 1) - F(\Omega(1-\varphi), 0) \quad \text{Equation B-8}$$

The second term on the right of Equation B-8 corresponds to the free energy of a pure polymer state, while the last term corresponds to the free energy of the pure solvent. Substituting Equation B-1 and Equation B-6 into this equation yields the free energy for mixing in the system Equation B-9:

$$F_m = \Omega k_B T f_m(\varphi) \quad \text{Equation B-9}$$

$$\text{for } f_m(\varphi) = \frac{\varphi}{N} \ln \varphi + (1-\varphi) \ln(1-\varphi) + \chi_{ps} \varphi(1-\varphi) \quad \text{Equation B-10}$$

Extension to polymers

Let us now consider the case of two polymers. This is a natural extension of the scenario above in which Equation B-10 becomes:

$$f_m(\varphi) = \frac{\varphi_A}{N_A} \ln \varphi_A + \frac{\varphi_B}{N_B} \ln \varphi_B + \chi_{AB} \varphi_A \varphi_B \quad \text{Equation B-11}$$

For polymers A and B, with chain lengths N_A and N_B , respectively, and whose volume fractions satisfy the relation $\varphi_A + \varphi_B = 1$. This can be rewritten using the notation $\varphi_A = \varphi$ and $\varphi_B = (1-\varphi)$ and dropping the subscript from χ to get:

$$F_m = \Omega k_B T \left[\frac{\varphi}{N_A} \ln \varphi + \frac{(1-\varphi)}{N_B} \ln(1-\varphi) + \chi \varphi(1-\varphi) \right]$$

Equation B-12

Will it segregate?

We want to know whether the two polymer homogeneous blend (denoted by H) will phase segregate to two phases. Ignoring kinetic effects, the condition for phase segregation will be that the decomposition is energetically favourable. This means that the system in two phases, labelled p and q , must have a lower free energy than the mixed system H .

Let us be explicit about what we mean by phase p and q . In phase p , a fraction of the lattice sites (say Ω_p/Ω) will be made up of polymer A and B with volume fraction φ_p ; that is φ_p sites in phase p will be segments of polymer A, and $1-\varphi_p$ sites will be segments of polymer B. Similarly for phase q but with Ω_q/Ω sites made up of volume fraction φ_q . One might assume that the two phases will be pure polymer A and polymer B; however, we will find that this is not the case.

The free energy of mixing for the system segregated to phases p and q will be a weighted sum of the free energies of each phase:

$$F_m = k_B T [\Omega_p f_m(\varphi_p) + \Omega_q f_m(\varphi_q)]$$

Equation B-13

A good way of visualising this energy is seen in Figure B-2, in which the blue curve has been drawn using Equation B-12. Here we have arbitrarily assigned volume fractions to the three phases: p , q and H (although due to mass conservation, phase H must be between phase q and p). The free energy of each phase is the height of the curve at the relevant volume fraction; however, determining the free energy of the two phase system is not as straight forward.

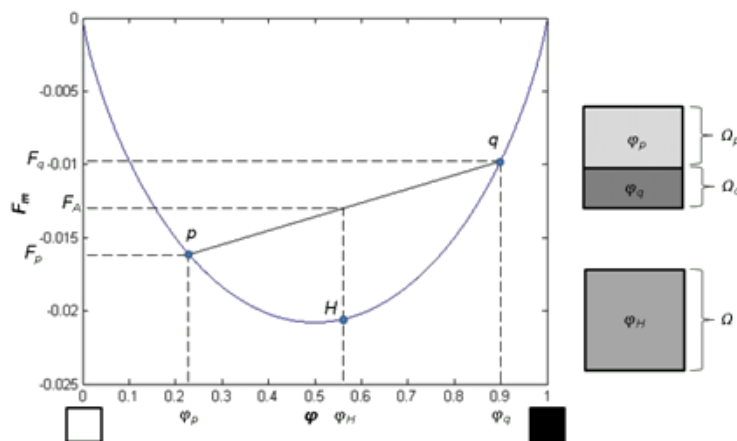


Figure B-2

The figure shows a free energy of mixing versus volume fraction plot based on Equation B-12 with parameters: $N_A = N_B = 10,000$, $\chi = 0$ and $T=300$; in addition, Ωk_B is set to unity. For a description of the various points drawn on the graph, see text. The graphical representations on the right demonstrate the one phase and two phase conditions; pure polymer A is shown by black and pure polymer B is shown by white.

We can simplify this by using the following identities. By mass and volume conservation: $\Omega_p + \Omega_q = \Omega$ and $\Omega_p \varphi_p + \Omega_q \varphi_q = \Omega \varphi_H$ both of which imply that Ω_p and Ω_q can be written as: $\Omega_p = \Omega \frac{\varphi_q - \varphi_H}{\varphi_q - \varphi_p}$ and $\Omega_q = \Omega \frac{\varphi_H - \varphi_p}{\varphi_q - \varphi_p}$

We can then rewrite Equation B-13 as:

$$F_m = k_B T \Omega \left[f_m(\varphi_p) \frac{\varphi_q - \varphi_H}{\varphi_q - \varphi_p} + f_m(\varphi_q) \frac{\varphi_H - \varphi_p}{\varphi_q - \varphi_p} \right] \quad \text{Equation B-14}$$

This corresponds to the point on the intersection of the line joining p and q with a free energy, F_A . This is obviously at greater energy than the non-segregated blend, and so demixing will not occur in this case.

It should now be apparent that whatever two phases we choose for p and q , the free energy will never be minimised by segregation. In fact, phase segregation will not occur unless the curve is inverted from the shape in Figure B-2. This requires that Equation B-12 contains a maximum in free energy at some intermediate value of φ . A maximum point will be a stationary point with negative curvature or mathematically $\delta F_m / \delta \varphi = 0$ and $\delta^2 F_m / \delta \varphi^2 < 0$. Making the simplification $N = N_A = N_B$ for demonstrative purposes, the derivatives of F_M are:

$$\frac{\delta F_M}{\delta \varphi} = k_B T \Omega \left[\chi(1 - 2\varphi) + \frac{1}{N} \ln \left(\frac{\varphi}{1 - \varphi} \right) \right] \quad \text{Equation B-15}$$

$$\frac{\delta^2 F_M}{\delta \varphi^2} = k_B T \Omega \left[\frac{1}{N\varphi(1 - \varphi)} - 2\chi \right] \quad \text{Equation B-16}$$

Setting Equation B-15 to zero and rearranging gives:

$$\chi N = \frac{(-1)}{1 - 2\varphi} \ln \left(\frac{\varphi}{1 - \varphi} \right) \quad \text{Equation B-17}$$

Equation B-17 defines the boundary between a single phase and double phase system. A graph of χN against φ can be seen in the left-hand plot from Figure B-3 and using Equation B-16 we see that the region above the curve will satisfy the condition $\delta^2 F_m / \delta \varphi^2 < 0$ and thus two phases are energetically favourable. The line on this graph demarcates the coexistence curve. Below a critical value, $\chi = \chi_c$, only one phase will exist, regardless of the starting phase. This value is found easily as the minimum point on the coexistence curve and is given by $\chi_c = 2/N$. In order to demonstrate these effects, a graph is drawn (right-hand plot of Figure B-3) in which χN has been varied across the critical value of χ_c . Above this value, the free energy plot displays a maximum and two minima; whereas below the critical value, there is only a single minimum. This has important implications for polymer blends. As polymers normally have large chain length N , the value of χ_c is often found to be very small; this is the main reason that strong incompatibility between polymers is often observed.

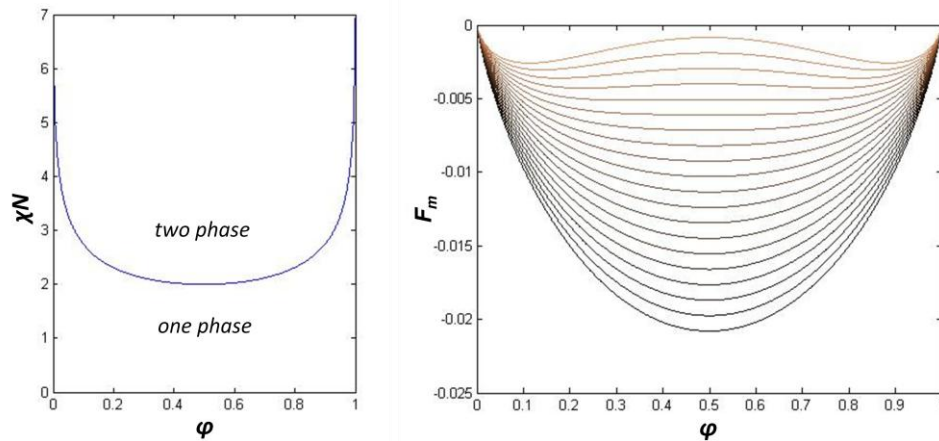


Figure B-3

The plot left shows a graphical representation of Equation B-15 and Equation B-16. On the right, the plot is similar to that in Figure B-2, based on Equation B-12 with parameters: $N_A = N_B = 10,000$, $T=300$ and Ωk_B is set to unity; however, χ is varied from $0-2.7 \times 10^{-3}$ which means that χN varies from $0-2.7$. This leads to the different plots, with lighter colour indicating a higher value of χN . Above $\chi N=2$, a maxima and two minima can be seen in the plots, corresponding to the point at which two phases are energetically more favourable than one phase.

There are now two further points to discuss given a free energy curve in which segregation can occur: i) What values of initial volume fraction (ϕ_H) will spontaneously dissociate to form two phases? ii) If segregation occurs, what are the volume fractions of the two phases?

First we consider point i: outside the minima, we have a region of positive curvature that means that the mix is stable in one phase (see Figure B-4a). Between the minima however, there is also a region that has negative curvature. This region is between the minimum and inflection point. In this region, there are phases p and q that we can choose that can either decrease or increase the free energy of the system (as seen in Figure B-4a). However, the phases that result in a decrease in free energy also require a large change in composition that is unlikely to occur spontaneously. As a result, segregation will only occur by nucleation of one phase (eg. p' in Figure B-4a) inside the other. Small changes in composition are always energetically unfavourable; hence this region is metastable with regard to segregation. Between the two inflection points however, the curvature of the free energy is negative and a homogeneous blend is unstable against infinitesimal fluctuations in density or composition. This means that segregation will spontaneously occur. The threshold that defines the boundary of this region is known as the spinodal curve and is shown in Figure B-4b. It is determined by equating the second derivative of F_m in Equation B-16 to zero.

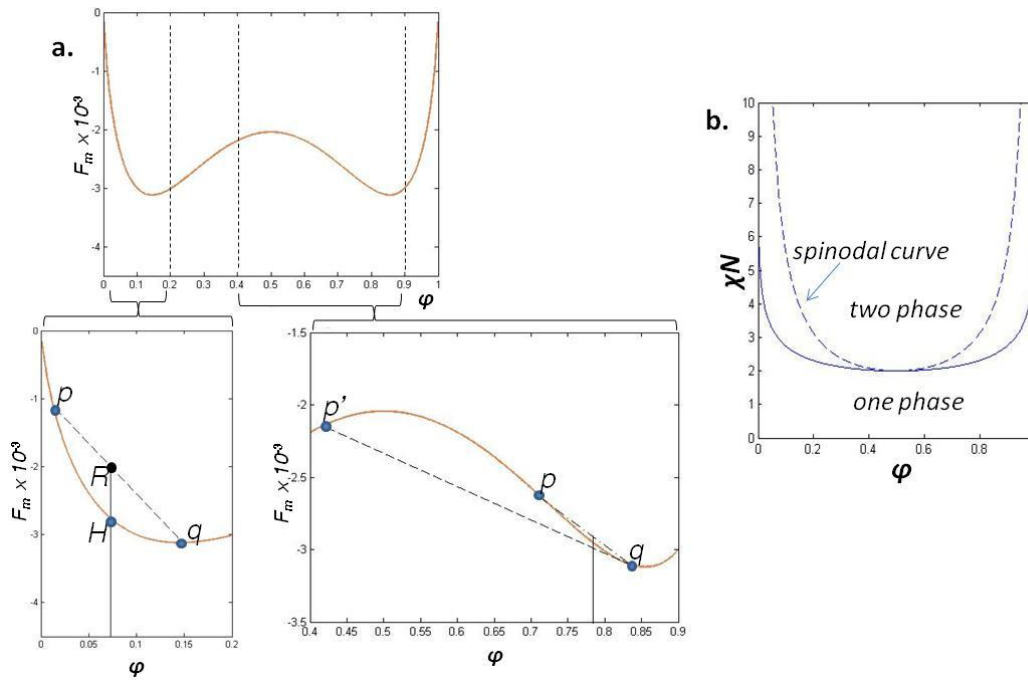


Figure B-4

Figure a shows a free energy plot with parameters: $N_A=N_B=10,000$, $T=300$, Ωk_B is set to unity and $\chi=2.5 \times 10^{-3}$. Two sections have been enlarged to show the energetic change due to segregation for different initial concentrations. The first, lower left, is stable in the homogenous state; whereas the second, lower middle, is metastable as the system is stable with regard to small fluctuations in composition, but not larger ones. Figure b shows a plot similar to Figure B-3, except that the spinodal curve has been drawn on demarcating the region in which segregation will occur spontaneously.

Now turning to point ii: if segregation does spontaneously occur, the system will naturally move to the state with the lowest free energy of mixing. The choice for phases p and q that cause this to be the case is most easily explained using a graphical representation. From Figure B-5, it is clear that choosing phases to be p' and q' does not result in the lowest free energy for an arbitrarily chosen initial phase H . The lowest free energy obtainable (at point R) is achieved by having phases p and q on the common tangent between the two minima. These concentrations are known as equilibrium phases. Mathematically, this is expressed by the condition:

$$\left. \frac{\delta f_m}{\delta \phi} \right|_{\phi_p} = \left. \frac{\delta f_m}{\delta \phi} \right|_{\phi_q} = \frac{f_m(\phi_q) - f_m(\phi_p)}{\phi_q - \phi_p} \quad \text{Equation B-18}$$

One direct implication of this is that the two phases are not pure polymer A and polymer B, but mixtures themselves that are either rich in polymer A or rich in polymer B. Although, as is clear from the right-hand plot of Figure B-3, as χN is increased (the system is more strongly segregated), the two minima become closer to pure A and B.

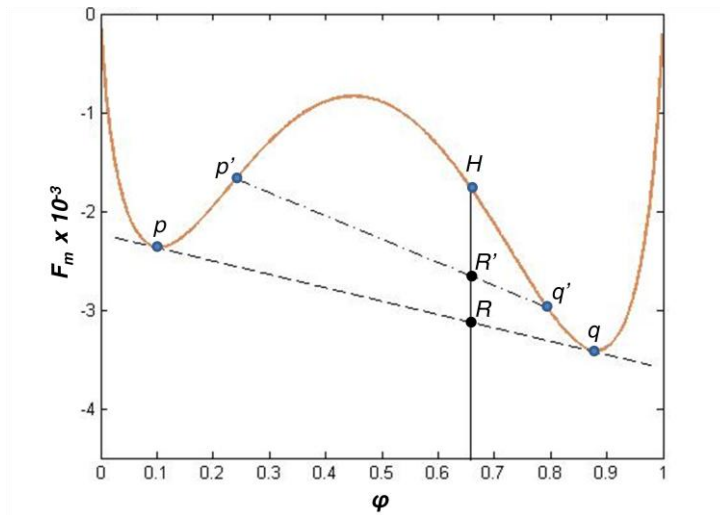


Figure B-5

The figure shows a free energy plot with parameters: $N_A=10,000$, $N_B=8,000$, $T=300$, Ωk_B is set to unity and $\chi=3 \times 10^{-3}$. The asymmetric shape is as a consequence of differing values of N_A and N_B . An arbitrary initial homogenous phase (H) has been put on the plot and the free energy of mixing is shown for two sets of possible segregated phases (p, q) and (p', q'). Both are lower in energy than the initial phase, so demixing will occur. However, phase segregation to p and q is preferable as R is lower in energy than R' .

Appendix C

Additional Research on Perylene Diimide

Substituted perylene diimides (PDI also known as perylene bisimides) are stable, organic semiconducting dyes. They have been intensely studied and used in electronic and optical devices such as field-effect transistors,^{251,252} and photovoltaic devices.^{141,160,253,254} Interaction between the chromophores can have a dramatic effect on the ensemble optical and electronic properties. For example by altering the substituents on the nitrogens, or in the so called 'bay area' (that is positions 1, 6, 7 and 12 eg. hexabenzocoronene), the stacking can be altered and optical absorption and luminescence can be tuned across nearly the entire visible spectrum.^{169,255-257} Such interaction is a result of spatial organisation due to self-assembly via one or more of the following: liquid crystals,^{160,258} hydrogen bonding,²⁵⁹ metal complexation,²⁶⁰ as well as π - π stacking.^{170,261,262} Additionally, structural control has been achieved by building large multichromophoric dye assemblies²⁶³ and by incorporating PDI moieties in polymers either by a saturated tether along the long axis²⁶⁴ or across the bay-area with continuity in conjugation.^{254,265} Another feature of well ordered PDI based crystals is n-type mobility comparable to the highest achieved in organic semiconductors (of the order $0.1 \text{ V cm}^{-1} \text{ s}^{-1}$)²⁵¹; although it has been postulated that hole mobilities should be of similar magnitude.^{261,262} Highly conducting, stable, n-type organic chromophores are uncommon and hence PDI and its derivatives are an interesting alternative to C_{60} derivatives commonly used as the electron conducting material in organic photovoltaics.^{16,17}

The aim of this appendix is to provide some insight into the properties of the polymeric acceptor used in

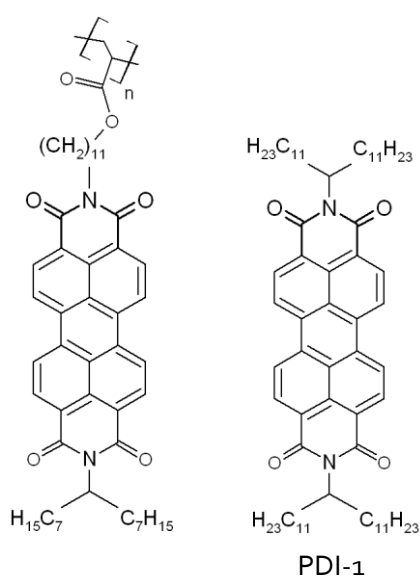


Figure C-1
Structure of polymer (left) and small molecule (right) based on perylene diimide (PDI) referred to as PPerAcr and PDI-1 respectively.

both Chapter 4 and Chapter 5. It is not meant to be a self-sufficient presentation of results, but merely a collection of pertinent experiments that are relevant to other chapters which would otherwise be made clumsy by their incorporation.

The polymer used as an electron transport material in chapters Chapter 4 and Chapter 5 is poly (perylene diimide acrylate) shortened to PPerAcr synthesised at the University of Bayreuth in the group of M. Thelakkat; it is a comb type polymer (dissimilar to those mentioned above) whose fundamental properties have been studied to a minimal extent. Hüttner et al. have demonstrated electron mobilities of $1.2 \times 10^{-3} \text{ V cm}^{-1} \text{ s}^{-1}$ in organic field effect transistors as well as investigated the effect of solvent annealing on *in situ* solid-state optical properties.^{167,252} In the following

analyses, some basic optical studies are performed on PPerAcr as well as a reference small molecule termed PDI-1; the structures of both of these compounds are shown in Figure C-1. Following these, a study of annealing effects on PPerAcr optical and structural properties is made which are important for the conclusions drawn in Chapter 5.

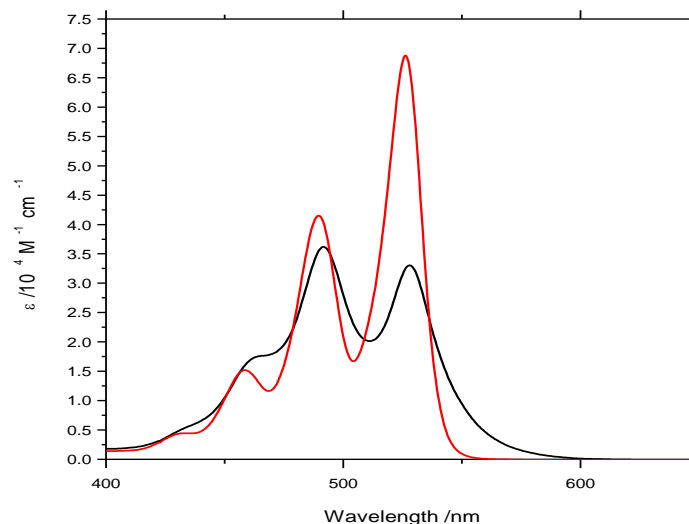
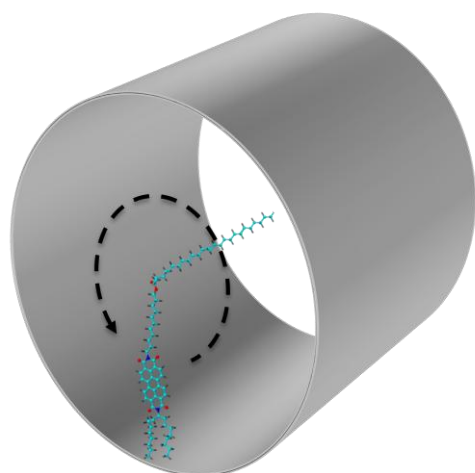


Figure C-2
The figure shows the absorption strength of PPerAcr (black line) and PDI-1 (red line) in dilute solutions made up in chloroform.

Figure C-2 shows the absorption spectra for PPerAcr and PDI-1 in dilute chloroform solution. PDI-1 was made to a concentration of $\sim 1.0 \times 10^{-4} \text{ mol dm}^{-3}$ and exhibits three absorption maxima at 458.5, 489.5 and 526 nm characteristic of perylene diimide fine structure. The absorption of PPerAcr is also shown in the figure and was taken from a solution made to a concentration of $3.9 \times 10^{-6} \text{ mol dm}^{-3}$ (which equates to an isotropic monomer concentration of $\sim 1.1 \times 10^{-4} \text{ mol dm}^{-3}$).

Figure C-3
The grey cylindrical surface encloses the volume that the PDI moieties can occupy when strung along a saturated carbon backbone. Only one monomer and the backbone are shown. For PPerAcr with 28 repeat units, the volume is $1.7 \times 10^{-22} \text{ dm}^3$.



The polymer absorption still displays some vibronic fine structure, although the peaks at 491.5 and 528 nm are red shifted with respect to PDI-1. Most significantly however are the apparent changes in absorption cross section of the different vibronic transitions and the tail extending beyond 550 nm. These spectral shifts are highly indicative of the formation of face-to-face dye aggregates and PDI-PDI interactions.^{168,258,266} The results suggest that the chaining effect of being strung to a polymer backbone increases the local concentration of PDI moieties and increases the degree of aggregation. In order to get an idea of the increase in concentration, the maximum volume the polymer can fill is estimated as a cylinder and is shown in

Figure C-3. The PPerAcr has 28 repeat units and the volume the cylinder occupies is $\sim 1.7 \times 10^{-22} \text{ dm}^3$ assuming a length of $\sim 1.7 \text{ nm}$ for the long axis of the PDI.²⁶⁷ If the PDI moieties are evenly distributed in this volume, the monomer concentration becomes 0.28 mol dm^{-3} , which is significantly higher than if the monomers are considered to be free throughout the solution volume. Of course, this will be a lower limit to the local monomer concentration and in increasingly concentrated solutions it is likely that the monomers from different polymer chains will interact.

Confirmation of this increased local concentration comes from a study of the degree of aggregation in PDI-1. Figure C-4a shows the changes in extinction coefficient of PDI-1 dissolved in methylcyclohexane (MCH). It is easily seen that such changes would lead to a spectrum similar to that of the polymer. Such stacking is ascribed to strong π - π interactions in discotic molecules and in general leads (reversibly) to polydisperse, linear aggregates. The formation of similar aggregates has been described by isodesmic chemical equilibria, in which a constant equilibrium value (K) is assumed for all binding and unbinding processes.^{170,268} Fitting the UV/Vis spectral data to such a model in Figure C-4b (using the shoulder at 540 nm) shows that the behaviour is described well by the model, which yields a room temperature equilibrium constant of $K = 127 \pm 4 \text{ dm}^3 \text{ mol}^{-1}$. This value is between two and four orders of magnitude smaller than those observed for PDIs with different N-group and bay-area substituents, indicating that stacking in 'swallow tail' perylene diimide is not favourable.^{170,269} The vertical line represents the local concentration of PDI moieties in a single polymer chain of PPerAcr calculated above. However, PPerAcr is insoluble in MCH.

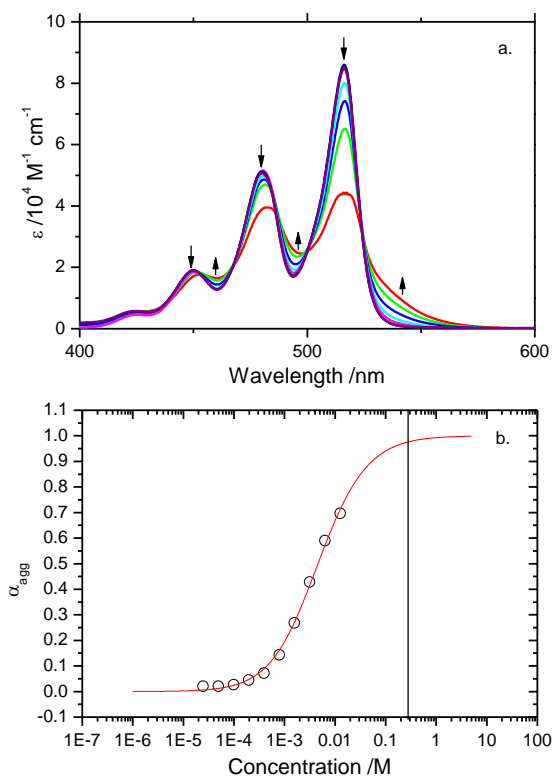


Figure C-4

Figure a shows the effects of increasing concentration (and hence aggregation) on the absorption strength of PDI-1 in MC H. Figure b shows the fraction of aggregated π -faces (α_{agg}) fit using the isodesmic model given the absorption in Figure a; the isodesmic chemical equilibrium constant is found to be $K=128 \pm 4 \text{ dm}^3 \text{ mol}^{-1}$. The vertical line in the figure represents the approximate local concentration of monomers in PPerAcr.

On deposition in a film, PPerAcr displays a further tendency to aggregation as seen by the absorption shown in Figure C-5a. The trends in absorptivity seen in the increasingly concentrated small molecule from Figure C-4a continue on moving from polymer in solution to film; this is to be expected given the increasing concentration of a solution during spin casting.

Figure C-5b shows the absorption spectra for a film of PPerAcr subjected to two annealing steps. The first step was to heat the film in a nitrogen atmosphere to above melting (at 220°C) for ten minutes before switching off the hot plate and allowing the film to cool slowly over ~ 40 minutes. The overall absorption of the film is substantially decreased as can be seen in the figure inset. Further, the same trend in peak variation is seen as for increasingly aggregated stacks in solution; namely the shoulder at 458.5 nm has increased in relative strength and now forms a distinct peak, while the o-o peak at ~ 526 nm has decreased in intensity and is bathochromically shifted to 538 nm; additionally, the red tail has grown and displays a shoulder at ~ 565 nm. Upon exposing this film to a saturated chloroform atmosphere for 30 minutes and then quenching with high pressure nitrogen, the original absorption is recovered in both strength and form. Interestingly, during solvent annealing in this fashion, Hüttner et al. have shown that films of this material show *in situ* aggregation effects like those observed in the thermally annealed sample.¹⁶⁷ This would imply

that it is the removal of solvent from the film that leads to the shape of the absorption spectrum and degree of aggregation seen in spin cast films.

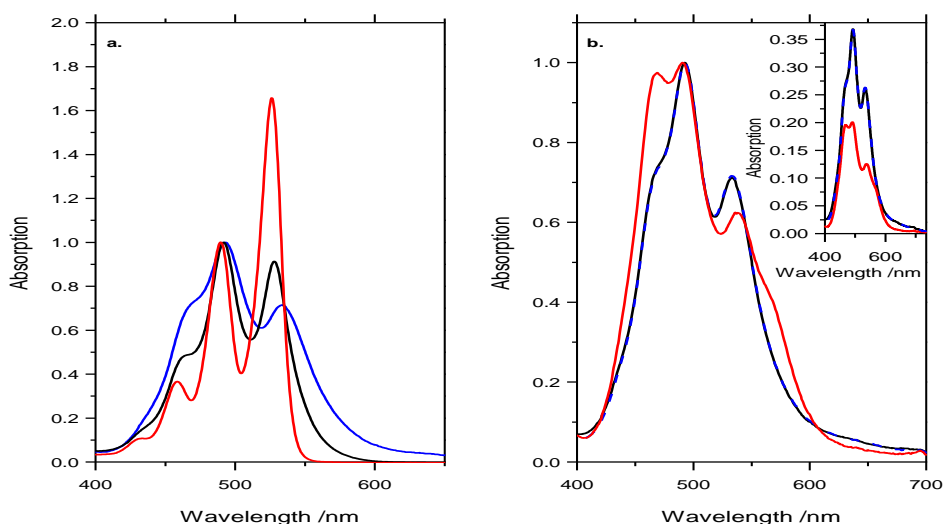


Figure C-5

Figure a shows the normalised absorption spectra of PDI-1 in solution (red), PPerAcr in solution (black) and a film of PPerAcr (blue). Figure b shows normalised absorption spectra (and absolute spectra inset) of a single PPerAcr film taken after different annealing conditions. A film 'as spin cast from chloroform' (black line) was thermally annealed to melt at 220° C for 10 minutes before being allowed to cool with the hot plate (red line). This same film was then subsequently annealed in a chloroform vapour at 100% saturation for 30 minutes before being quenched with a high flow rate dry N₂ stream (blue dashed line).

The emission properties of an unannealed film of PPerAcr are shown in Figure C-6. From the figure, it can be seen that across the emission spectrum there is an increasing photoluminescence lifetime at progressively lower energies. This emission has been attributed (in small molecule PDIs) to a complex admixture of Frenkel excitons and relaxed excited states, although the lengthening lifetime at longer emission wavelengths is consistent with a dominant low-energy excimer emission.^{168,266}

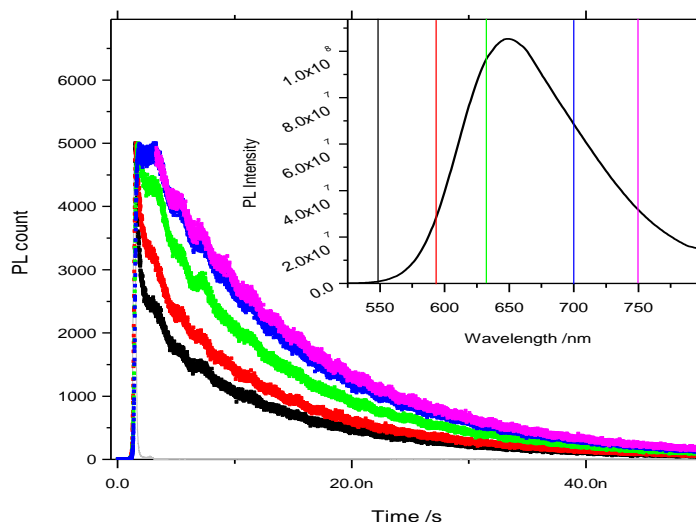


Figure C-6

The figure shows the transient photoluminescence of a film of PPerAc at various wavelengths after excitation at 467 nm. Emission at 550 nm (black), 590 nm (red), 630 nm (green), 700 nm (blue) and 750 nm (purple) are shown as well as the instrument response function (grey). The inset shows steady state emission from the film after excitation at 465 nm; also on the inset are shown the wavelengths at which time resolved traces were taken.

Packing conformation in small molecule PDIs has been the subject of much debate in recent years. Numerous crystal structures have been reported for PDI derivatives with stacked cofacial packing at distances of between 3.34 and 3.55 Å.^{256,257} In these studies, a substantial crystallochromy was found, with crystals ranging from orange to black dependent on their imide substituents and attributed to the degree of π overlap between adjacent molecules in the stack.²⁷⁰ Detailed molecular dynamics calculations and x-ray scattering experiments have also identified a spiralled stacking motif in swallow-tail PDI derivatives (very similar to PDI-1) with an angle of $\sim 45^\circ$ between adjacent molecules in the stack.^{261,262,271,272} Primarily, this is due to the secondary carbons next to the imide nitrogens, which force the alkyl chains out of the plane of the molecule and thereby hamper π - π stacking. The low equilibrium constant for aggregation found in Figure C-4b above confirms this supposition. As yet, it is unclear what packing conformation the PPerAc aggregates are in and further work is required to identify the crystal structure. Speculation at this point would suggest that it is possible for a spiral stacking motif to be present in PPerAc as well. This is vindicated to some extent by the similarity between the x-ray diffraction pattern measured for thermally annealed PPerAc (see Figure 5-2 from Chapter 5) and that observed for a small molecule PDI in reference¹⁷⁰, whose π - π stacking is thought to have rotational character.

In this appendix, some of the more fundamental properties of perylene diimide molecules have been discussed with a view to providing additional information for the results chapters dealing with poly (perylene diimide acrylate) as an acceptor material.

Appendix D

Table of Collaborators

Chapter	Collaborators	Contribution
Chapter 4	Prof. M. Thelakkat, Dr. M. Sommer, Dr. S. Lindner (Universität Bayreuth)	Providing materials, TEM images
Chapter 5	Prof. M. Thelakkat, Dr. M. Sommer, Mr. S. Hüttner (Universität Bayreuth)	Providing materials, SEM images, WAXD x-ray diffraction images, complementary annealing studies
Chapter 6	Prof. A. Holmes, Dr. D. Jones (University of Melbourne), Mr. L. Reynolds (Imperial College London)	Providing materials, sample prep
Chapter 7	Prof. A. Holmes, Dr. D. Jones (University of Melbourne)	Providing materials

Bibliography

- (1) BP *Statistical Review of World Energy*, 2007.
- (2) Council, W. E. *Survey of Energy Resources*, 2007.
- (3) Lewis, N.; Nocera, D. *Proceedings of the National Academy of Sciences of the United States of America* **2006**, *103*, 6.
- (4) Mackay, D. J. C. *Sustainable Energy - without the hot air*; UIT Cambridge (available free online from www.withouthotair.com), 2008.
- (5) Neftel, A.; Moor, E.; Oeschger, H.; Stauffer, B. *Nature* **1985**, *315*, 45-47.
- (6) IPCC *Fourth Assessment Report: Climate Change*, 2007.
- (7) Henson, R. *The Rough Guide to Climate Change*; First edition ed.; Rough Guides Ltd., 2006.
- (8) Chapin, D. M.; Fuller, C. S.; Pearson, G. L. *Journal of Applied Physics* **1954**, *25*, 676-677.
- (9) Shockley, W.; Queisser, H. *Journal of Applied Physics* **1960**, *32*.
- (10) Green, M. A. *Third Generation Photovoltaics: Advanced Solar Energy Conversion*; Springer-Verlag, 2004.
- (11) Sarasin *Sustainability Report - Solar Energy*, 2005.
- (12) Pray et al., L. *White Paper - Chemical Sciences and Society Symposium* **2009**.
- (13) Reyes-Reyes, M.; Kim, K.; Carroll, D. L. *Applied Physics Letters* **2005**, *87*, 083506.
- (14) Kim, K.; Liu, J.; Namboothiry, M. A. G.; Carroll, D. L. *Applied Physics Letters*. **2007**, *90*, 163511.
- (15) Ma, W.; Yang, C.; Gong, X.; Lee, K.; Heeger, A. J. *Advanced Functional Materials* **2005**, *15*, 1617-1622.
- (16) Kim, J. Y.; Lee, K.; Coates, N. E.; Moses, D.; Nguyen, T.-Q.; Dante, M.; Heeger, A. J. *Science* **2007**, *317*, 222-225.
- (17) Park, S. H.; Roy, A.; Beaupre, S.; Cho, S.; Coates, N.; Moon, J. S.; Moses, D.; Leclerc, M.; Lee, K.; Heeger, A. J. *Nature Photonics* **2009**, *3*, 297-302.
- (18) IUPAC.
- (19) Kittel, C. *Introduction to Solid State Physics*; Wiley, 1996.
- (20) Riordan, M.; Hoddeson, L. *Spectrum, IEEE* **1997**, *34*, 46-51.
- (21) Kip, A. F. *Fundamentals of Electricity and Magnetism*; McGraw-Hill Book Company 1962.
- (22) Atkins, P.; de Paula, J. *Atkins' Physical Chemistry*; Oxford University Press, 2002.
- (23) Hückel, E. *Zeitschrift für Physik. A, Hadrons and nuclei* **1931**, *70*, 204-286.
- (24) Hückel, E. *Zeitschrift für Physik. A, Hadrons and nuclei* **1931**, *72*, 310-337.
- (25) Kroon, R.; Lenes, M.; Hummelen, J. C.; Blom, P. W. M.; de Boer, B. *Polymer Review* **2008**, *48*, 531 - 582.
- (26) Coropceanu, V.; Cornil, J. r. m.; da Silva Filho, D. A.; Olivier, Y.; Silbey, R.; Brédas, J.-L. *Chemical Reviews* **2007**, *107*, 926-952.
- (27) Lee, J. Y.; Roth, S.; Park, Y. W. *Applied Physics Letters* **2006**, *88*, 252106.
- (28) Karl, N. *Synthetic Metals* **2003**, *133-134*, 649-657.
- (29) Karl, N.; Marktanner, J. r. *Molecular Crystals and Liquid Crystals Science and Technology. Section A. Molecular Crystals and Liquid Crystals* **2001**, *355*, 149 - 173.
- (30) Geens, W.; Shaheen, S. E.; Wessling, B.; Brabec, C. J.; Poortmans, J.; Sariciftci, N. S. *Organic Electronics* **2002**, *3*, 105.

- (31) Redecker, M.; Bradley, D. D. C.; Inbasekaran, M.; Woo, E. P. *Applied Physics Letters* **1998**, *73*, 1565-1567.
- (32) Bässler, H. *Physica Status Solidi b* **1981**, *107*, 9-54.
- (33) Hoppe, H.; Sariciftci, N. S. *Journal of Materials Research* **2004**, *19*, 1924-1945.
- (34) Haugeneder, A.; Neges, M.; Kallinger, C.; Spirkl, W.; Lemmer, U.; Feldmann, J.; Scherf, U.; Harth, E.; Gügel, A.; Müllen, K. *Physical Review B* **1999**, *59*, 15346.
- (35) Marks, R. N.; Halls, J. J. M.; Bradley, D. D. C.; Friend, R. H.; Holmes, A. B. *Journal of Physics: Condensed Matter* **1994**, 1379.
- (36) Sariciftci, N. S.; Smilowitz, L.; Heeger, A. J.; Wudl, F. *Science* **1992**, *258*, 1474-1476.
- (37) Kraabel, B.; Hummelen, J. C.; Vacar, D.; Moses, D.; Sariciftci, N. S.; Heeger, A. J.; Wudl, F. *The Journal of Chemical Physics* **1996**, *104*, 4267-4273.
- (38) Tvingstedt, K.; Vandewal, K.; Gadisa, A.; Zhang, F.; Manca, J.; Inganäl's, O. *Journal of the American Chemical Society* **2009**, *131*, 11819-11824.
- (39) Morteani, A. C.; Dhoot, A. S.; Kim, J. S.; Silva, C.; Greenham, N. C.; Murphy, C.; Moons, E.; Ciná, S.; Burroughes, J. H.; Friend, R. H. *Advanced Materials* **2003**, *15*, 1708-1712.
- (40) Veldman, D.; Meskers, S. C. J.; Janssen, R., A. J. *Advanced Functional Materials* **2009**, *19*, 1939-1948.
- (41) Benson-Smith, J. J.; Goris, L.; Vandewal, K.; Haenen, K.; Manca, J. V.; Vanderzande, D.; Bradley, D. D. C.; Nelson, J. *Advanced Functional Materials* **2007**, *17*, 451-457.
- (42) Yin, C.; Kietzke, T.; Neher, D.; Horhold, H.-H. *Applied Physics Letters* **2007**, *90*, 092117-3.
- (43) Offermans, T.; Meskers, S. C. J.; Janssen, R. A. J. *Chemical Physics* **2005**, *308*, 125-133.
- (44) McNeill, C. R.; Westenhoff, S.; Groves, C.; Friend, R. H.; Greenham, N. C. *The Journal of Physical Chemistry C* **2007**, *111*, 19153-19160.
- (45) Onsager, L. *The Journal of Chemical Physics* **1934**, *2*, 599-615.
- (46) Onsager, L. *Physical Review* **1938**, *54*, 554.
- (47) Braun, C. L. *The Journal of Chemical Physics* **1984**, *80*, 4157-4161.
- (48) Tachiya, M. *The Journal of Chemical Physics* **1988**, *89*, 6929-6935.
- (49) Wojcik, M.; Tachiya, M. *Radiation Physics and Chemistry* **2005**, *74*, 132-138.
- (50) Peumans, P.; Forrest, S. R. *Chemical Physics Letters* **2004**, *398*, 27-31.
- (51) Morteani, A. C.; Sreearunothai, P.; Herz, L. M.; Friend, R. H.; Silva, C. *Physical Review Letters* **2004**, *92*, 247402.
- (52) Ohkita, H.; Cook, S.; Astuti, Y.; Duffy, W.; Tierney, S.; Zhang, W.; Heeney, M.; McCulloch, I.; Nelson, J.; Bradley, D. D. C.; Durrant, J. R. *Journal of the American Chemical Society* **2008**, *130*, 3030-3042.
- (53) Veldman, D.; Chopin, S. p. M. A.; Meskers, S. C. J.; Janssen, R. A. J. *The Journal of Physical Chemistry A* **2008**, *112*, 8617-8632.
- (54) Dance, Z. E. X.; Mickley, S. M.; Wilson, T. M.; Ricks, A. B.; Scott, A. M.; Ratner, M. A.; Wasielewski, M. R. *The Journal of Physical Chemistry A* **2008**, *112*, 4194-4201.
- (55) Westenhoff, S.; Howard, I. A.; Hodgkiss, J. M.; Kirov, K. R.; Bronstein, H. A.; Williams, C. K.; Greenham, N. C.; Friend, R. H. *Journal of the American Chemical Society* **2008**, *130*, 13653-13658.
- (56) Benson-Smith, J. J.; Wilson, J.; Dyer-Smith, C.; Mouri, K.; Yamaguchi, S.; Murata, H.; Nelson, J. *The Journal of Physical Chemistry B* **2009**, *113*, 7794-7799.
- (57) Halls, J. J. M.; Pichler, K.; Friend, R. H.; Moratti, S. C.; Holmes, A. B. *Applied Physics Letters* **1996**, *68*, 3120-3122.
- (58) Halls, J. J. M.; Walsh, C. A.; Greenham, N. C.; Marseglia, E. A.; Friend, R. H.; Moratti, S. C.; Holmes, A. B. *Nature* **1995**, *376*, 498-500.
- (59) Walheim, S.; Boltau, M.; Mlynek, J.; Krausch, G.; Steiner, U. *Macromolecules* **1997**, *30*, 4995-5003.
- (60) Liu, J.; Shi, Y.; Yang, Y. *Advanced Functional Materials* **2001**, *11*, 420.
- (61) Rispens, M. T.; Meetsma, A.; Rittberger, R.; Brabec, C. J.; Sariciftci, N. S.; Hummelen, J. C. *Chemical Communications* **2003**, 2116-8.

- (62) Li, G.; Shrotriya, V.; Huang, J.; Yao, Y.; Moriarty, T.; Emery, K.; Yang, Y. *Nature Materials* **2005**, *4*, 864-868.
- (63) Kim, Y.; Cook, S.; Tuladhar, S. M.; Choulis, S. A.; Nelson, J.; Durrant, J. R.; Bradley, D. D. C.; Giles, M.; McCulloch, I.; Ha, C.-S.; Ree, M. *Nature Materials* **2006**, *5*, 197-203.
- (64) Padinger, F.; Rittberger, R. S.; Sariciftci, N. S. *Advanced Functional Materials* **2003**, *13*, 85-88.
- (65) Sivula, K.; Ball, Z. T.; Watanabe, N.; Fréchet, J. M. J. *Advanced Functional Materials* **2006**, *18*, 206-210.
- (66) Coakley, K. M.; McGehee, M. D. *Chemistry of Materials* **2004**, *16*, 4533-4542.
- (67) Buxton, G.; Clarke, N. *Physical Review B* **2006**, *74*.
- (68) Nedelcu, M.; Ducati, C.; Ludwigs, S.; Hillmyer, M.; Steiner, U.; Snaith, H. *Nano Letters* **2009**, *9*, 2813-9.
- (69) Sun, B.; Snaith, H. J.; Dhoot, A. S.; Westenhoff, S.; Greenham, N. C. *Journal of Applied Physics* **2005**, *97*, 014914-6.
- (70) Coakley, K. M.; Liu, Y.; Goh, C.; McGehee, M. *MRS bulletin* **2005**, *30*, 37.
- (71) Campoy-Quiles, M.; Ferenczi, T.; Agostinelli, T.; Etchegoin, P. G.; Kim, Y.; Anthopoulos, T. D.; Stavrinou, P. N.; Bradley, D. D. C.; Nelson, J. *Nature Materials* **2008**, *7*, 158-164.
- (72) McNeill, C.; Watts, B.; Thomsen, L.; Belcher, W.; Greenham, N.; Dastoor, P.; Ade, H. *Macromolecules* **2009**, *42*, 3347-3352.
- (73) Bavel, S. S. v.; Sourty, E.; With, G. d.; Loos, J. *Nano Letters* **2008**, *9*, 507-513.
- (74) Oosterhout, S. D.; Wienk, M. M.; van Bavel, S. S.; Thiedmann, R.; Jan Anton Koster, L.; Gilot, J.; Loos, J.; Schmidt, V.; Janssen, R. A. J. *Nature Materials* **2009**, *8*, 818-824.
- (75) McNeill, C. R.; Watts, B.; Thomsen, L.; Ade, H.; Greenham, N. C.; Dastoor, P. C. *Macromolecules* **2007**, *40*, 3263-3270.
- (76) Sirringhaus, H.; Brown, P. J.; Friend, R. H.; Nielsen, M. M.; Bechgaard, K.; Langeveld-Voss, B. M. W.; Spiering, A. J. H.; Janssen, R. A. J.; Meijer, E. W. *Synthetic Metals* **2000**, *111-112*, 129-132.
- (77) Chang, J.-F.; Sun, B.; Breiby, D. W.; Nielsen, M. M.; Solling, T. I.; Giles, M.; McCulloch, I.; Sirringhaus, H. *Chemistry of Materials* **2004**, *16*, 4772-4776.
- (78) Erb, T.; Zhokhavets, U.; Gobsch, G.; Raleva, S.; Stühn, B.; Schilinsky, P.; Waldauf, C.; Brabec, C. J. *Advanced Functional Materials* **2005**, *15*, 1193-1196.
- (79) Joshi, S.; Grigorian, S.; Pietsch, U. *Physica Status Solidi a* **2008**, *205*, 488-496.
- (80) Moulé, A. J.; Meerholz, K. *Advanced Functional Materials* **2009**, *19*, 3028-36.
- (81) Lodge, T. P. *Macromolecular Chemistry and Physics* **2003**, *204*, 265-273.
- (82) Förster, S. S.; Plantenberg, T. T. *Angewandte Chemie* **2002**, *41*, 689-714.
- (83) Bates, F. S.; Fredrickson, G. H. *Physics Today* **1999**, *52*, 32-38.
- (84) Szwarc, M.; Levy, M.; Milkovich, R. *Journal of the American Chemical Society* **1956**, *78*, 2656.
- (85) Khandpur, A. K.; Förster, S.; Bates, F. S.; Hamley, I. W.; Ryan, A. J.; Bras, W.; Almdal, K.; Mortensen, K. *Macromolecules* **1995**, *28*, 8796-8806.
- (86) Matsen, M. W.; Bates, F. S. *Macromolecules* **1996**, *29*, 1091.
- (87) Ryan, A. J.; Mai, S.-M.; Faircough, J. P. A.; Hamely, I. W.; Booth, C. *Physical Chemistry Chemical Physics* **2001**, *3*, 2961.
- (88) Meier, D. J. *Journal of Polymer Science. Part C* **1969**, *26*, 81.
- (89) Helfand, E.; Tagami, Y. *The Journal of Chemical Physics* **1972**, *56*, 3592-3601.
- (90) Helfand, E.; Wasserman, Z. R. *Macromolecules* **1976**, *9*, 879-888.
- (91) de Gennes, P. G. *Scaling Concepts in Polymer Physics*; Cornell University Press: Ithaca, 1979.
- (92) Leibler, L. *Macromolecules* **1980**, *13*, 1602-1617.
- (93) Fredrickson, G. H.; Bates, F. S. *Annual Review of Materials Research* **1996**, *26*, 501.
- (94) Bates, F. S.; Fredrickson, G. H. *Annual review of Physical Chemistry* **1990**, *41*, 525.
- (95) Matsuyama, T. *Japanese Journal of Applied Physics. Part 1* **2006**, *45*, L20.
- (96) Thurn-Albrecht, T.; Schotter, J.; Kästle, G. A.; Emley, N.; Shibauchi, T.; Krusin-Elbaum, L.; Guarini, K.; Black, C. T.; Tuominen, M. T.; Russell, T. P. *Science* **2000**, *290*, 2126-9.

- (97) Tsarkova, L.; Knoll, A.; Krausch, G.; Magerle, R. *Macromolecules* **2006**, *39*, 3608.
- (98) Fasolka, M. J.; Mayes, A. M. *Annual Review of Materials Research* **2001**, *31*, 323.
- (99) Ludwigs, S.; Schmidt, K.; Stafford, C. M.; Amis, E. J.; Fasolka, M. J.; Karim, A.; Magerle, R.; Krausch, G. *Macromolecules* **2005**, *38*, 1850.
- (100) Radzilowski, L. H. *Journal of Polymer Science. Part B* **1996**, *34*, 3081.
- (101) Knoll, A. A.; Horvat, A. A.; Lyakhova, K. K. S.; Krausch, G. G.; Sevink, G. G. J. A.; Zvelindovsky, A. A. V.; Magerle, R. R. *Physical Review Letters* **2002**, *89*, 035501.
- (102) Huinink, H. P.; Brokken-Zijp, J. C. M.; van Dijk, M. A.; Sevink, G. J. A. *The Journal of Chemical Physics* **2000**, *112*, 2452-2462.
- (103) Huinink, H. P.; van Dijk, M. A.; Brokken-Zijp, J. C. M.; Sevink, G. J. A. *Macromolecules* **2001**, *34*, 5325-5330.
- (104) Xuan, Y.; Peng, J.; Cui, L.; Wang, H.; Li, B.; Han, Y. *Macromolecules* **2004**, *37*, 7301.
- (105) Peng, J.; Wei, Y.; Wang, H.; Li, B.; Han, Y. *Macromolecular Rapid Communications* **2005**, *26*, 738.
- (106) Matsuyama, T. *Japanese Journal of Applied Physics. Part 1* **2005**, *44*, 3524.
- (107) Elbs, H.; Krausch, G. *Polymer* **2004**, *45*, 7935.
- (108) Peng, J. J.; Xuan, Y. Y.; Wang, H. H.; Yang, Y. Y.; Li, B. B.; Han, Y. Y. *The Journal of Chemical Physics* **2004**, *120*, 11163-70.
- (109) Harant, A. W. *The Journal of Vacuum Science and Technology* **2005**, *23*, 1615.
- (110) Flory, P. J. *Proceedings of the Royal Society of London. Series A, Mathematical and Physical Sciences* **1956**, *234*, 73-89.
- (111) Heiser, T.; Adamopoulos, G.; Brinkmann, M.; Giovanella, U.; Ould-Saad, S.; Brochon, C.; Van de Wetering, K.; Hadziioannou, G. *Thin Solid Films* **2006**, *511*, 219-223.
- (112) Matsen, M. W.; Barrett, C. J. *The Journal of Chemical Physics* **1998**, *109*, 4108.
- (113) Lee, M.; Cho, B.; Kang, Y.; Zin, W. *Macromolecules* **1999**, *32*, 7688-7691.
- (114) Hayakawa, T. T.; Horiuchi, S. S. *Angewandte Chemie* **2003**, *42*, 2285-9.
- (115) Olsen, B. D.; Segalman, R. A. *Macromolecules* **2005**, *38*, 10127-10137.
- (116) Ho, C.; Lee, Y.; Dai, C.; Segalman, R.; Su, W. *Macromolecules* **2009**, *42*, 4208-4219.
- (117) Chen, J. T.; Thomas, E. L.; Ober, C. K.; Hwang, S. S. *Macromolecules* **1995**, *28*, 1688-1697.
- (118) Chen, J. T.; Thomas, E. L.; Ober, C. K.; Mao, G. *Science* **1996**, *273*, 343-6.
- (119) Semenov, A. N.; Vasilenko, S. V. *Soviet Physics - JETP* **1986**, *63*, 70-79.
- (120) Reenders, M.; Brinke, G. t. *Macromolecules* **2002**, *35*, 3266.
- (121) Pryamitsyn, V.; Ganesan, V. *The Journal of Chemical Physics* **2004**, *120*, 5824-5838.
- (122) Müller, A. J.; Arnal, M. L.; Balsamo, V. In *Progress in Understanding of Polymer Crystallization*; Springer: 2007.
- (123) Olsen, B.; Shah, M.; Ganesan, V.; Segalman, R. *Macromolecules* **2008**, *41*, 6809-6817.
- (124) Gratt, J. A. *Journal of applied polymer science* **2004**, *91*, 3362-3368.
- (125) Lindner, S. M.; Hüttner, S. S.; Chiche, A. A.; Thelakkat, M. M.; Krausch, G. G. *Angewandte Chemie* **2006**, *45*, 3364-8.
- (126) Lindner, S.; Thelakkat, M. *Macromolecules* **2004**, *37*, 8832.
- (127) Lindner, S.; Kaufmann, N.; Thelakkat, M. *Organic Electronics* **2007**, *8*, 69-75.
- (128) Sommer, M.; Thelakkat, M. *The European Physical Journal - Applied Physics* **2006**, *36*, 245-249.
- (129) Sommer, M.; Lindner, S.; Thelakkat, M. *Advanced Functional Materials* **2007**, *17*, 1493-1500.
- (130) Sun, S. S.; Zhang, C.; Ledbetter, A.; Choi, S.; Seo, K.; Bonner, C. E.; Drees, M.; Sariciftci, N. S. *Applied Physics Letters* **2007**, *90*.
- (131) Sun, S. *Journal of Materials Science* **2005**, *40*, 1429-1443.
- (132) Sun, S. S. *Solar Energy Materials and Solar Cells* **2003**, *79*, 257-264.
- (133) de Boer, B.; Stalmach, U.; van Hutten, P. F.; Melzer, C.; Krasnikov, V. V.; Hadziioannou, G. *Polymer* **2001**, *42*, 9097-9109.
- (134) Sylvester-Hvid, K. O.; Rettrup, S. *The Journal of Physical Chemistry B* **2004**, *108*, 4296-4307.

- (135) Shah, M.; Ganesan, V. *Macromolecules* **2009**, *43*, 543-552.
- (136) Sommer, M.; Lang, A.; Thelakkat, M. *Angewandte Chemie International Edition* **2008**, *47*, 7901-7904.
- (137) Sommer, M.; Huttner, S.; Wunder, S.; Thelakkat, M. *Advanced materials* **2008**, *20*, 2523.
- (138) Zhang, Q.; Cirpan, A.; Russell, T. P.; Emrick, T. *Macromolecules* **2009**, *42*, 1079-1082.
- (139) Tao, Y.; McCulloch, B.; Kim, S.; Segalman, R. A. *Soft matter* **2009**, *5*, 4219.
- (140) Yang, C.; Lee, J.; Heeger, A.; Wudl, F. *Journal of Materials Chemistry* **2009**, *19*, 5416-5423.
- (141) Rajaram, S.; Armstrong, P. B.; Kim, B. J.; Frechet, J. M. J. *Chemistry of Materials* **2009**, *21*, 1775.
- (142) Botiz, I.; Darling, S. B. *Macromolecules* **2009**.
- (143) Nedelcu, M.; Ducati, C.; Ludwigs, S.; Hillmyer, M.; Steiner, U.; Steiner, U.; Nedelcu, M.; Ducati, C.; Ludwigs, S.; Hillmyer, M.; Snaith, H. *Nano letters* **2009**, *9*, 2813-9.
- (144) Gratt, J. A.; Cohen, R. E. *Journal of Applied Polymer Science* **2003**, *88*, 177.
- (145) Gratt, J. A.; Cohen, R. E. *Journal of Applied Polymer Science* **2004**, *91*, 3362-3368.
- (146) Emslie, A. G.; Bonner, F. T.; Peck, L. G. *Journal of Applied Physics* **1958**, *29*, 858-862.
- (147) Meyerhofer, D. *Journal of Applied Physics* **1978**, *49*, 3993-3997.
- (148) Lakowicz, J. R. *Principles of Fluorescence Spectroscopy*; Plenum Press, 1983.
- (149) Wong, W.; Jones, D.; Yan, C.; Watkins, S.; King, S.; Haque, S. *Organic Letters* **2009**, *11*, 975-978.
- (150) Ohkita, H.; Cook, S.; Ford, T. A.; Greenham, N.; Durrant, J. R. *Journal of Photochemistry and Photobiology A: Chemistry* **2006**, *182*, 225.
- (151) Montanari, I.; Nogueira, A. F.; Nelson, J.; Durrant, J. R.; Winder, C.; Loi, M. A.; Sariciftci, N. S.; Brabec, C. *Applied Physics Letters* **2002**, *81*, 3001-3003.
- (152) Nogueira, A. F.; Montanari, I.; Nelson, J.; Durrant, J. R.; Winder, C.; Sariciftci, N. S.; Brabec, C. *The Journal of Physical Chemistry B* **2003**, *107*, 1567-1573.
- (153) Nelson, J. *Physical Review B* **2003**, *67*, 155209.
- (154) Shuttle, C. G.; O'Regan, B.; Ballantyne, A. M.; Nelson, J.; Bradley, D. D. C.; Durrant, J. R. *Physical Review B* **2008**, *78*, 113201-4.
- (155) Clarke, T. M. *Personal Communication*
- (156) Williams, D. B.; Carter, C. B. *Transmission electron microscopy: A textbook for materials science*; Plenum Press: New York, 1996.
- (157) Brown, G. M.; Butler, J. H. *Polymer* **1997**, *38*, 3937.
- (158) Haubruge, H. G.; Jonas, A. M.; Legras, R. *Polymer* **2003**, *44*, 3229.
- (159) Wang, Y.; Coombs, N.; Turak, A.; Lu, Z.; Manners, I.; Winnik, M. A. *Macromolecules* **2007**, *40*, 1594.
- (160) Schmidt-Mende, L.; Fechtenkotter, A.; Mullen, K.; Moons, E.; Friend, R. H.; MacKenzie, J. D. *Science* **2001**, *293*, 1119-1122.
- (161) Barrau, S.; Heiser, T.; Richard, F.; Brochon, C.; Ngov, C.; van de Wetering, K.; Hadziioannou, G.; Anokhin, D. V.; Ivanov, D. A. *Macromolecules* **2008**, *41*, 2701-2710.
- (162) Krebs, F. C.; Hagemann, O.; Jørgensen, M. *Solar Energy Materials and Solar Cells* **2004**, *83*, 211-228.
- (163) Hagemann, O.; Jørgensen, M.; Krebs, F. C. *Journal of Organic Chemistry* **2006**, *71*, 5546-5559.
- (164) Gosztola, D.; Niemczyk, M. P.; Svec, W.; Lukas, A. S.; Wasielewski, M. R. *The Journal of Physical Chemistry A* **2000**, *104*, 6545-6551.
- (165) Frost, J. M.; Cheynis, F.; Tuladhar, S. M.; Nelson, J. *Nano Letters* **2006**, *6*, 1674-1681.
- (166) King, S.; Sommer, M.; Huttner, S.; Thelakkat, M.; Haque, S. *Journal of Materials Chemistry* **2009**, *19*, 5436-5441.
- (167) Huttner, S.; Sommer, M.; Chiche, A.; Krausch, G.; Steiner, U.; Thelakkat, M. *Soft Matter* **2009**, *5*, 4206-4211.

- (168) Ferguson, A. J.; Jones, T. S. *The Journal of Physical Chemistry B* **2006**, *110*, 6891-6898.
- (169) Würthner, F. *Chemical Communications* **2004**, 1564-1579.
- (170) Chen, Z.; Stepanenko, V.; Dehm, V.; Prins, P.; Siebbeles, L. D. A.; Seibt, J.; Marquetand, P.; Engel, V.; Würthner, F. *Chemistry - A European Journal* **2007**, *13*, 436-449.
- (171) Brown, P. J.; Thomas, D. S.; Köhler, A.; Wilson, J. S.; Kim, J.-S.; Ramsdale, C. M.; Sirringhaus, H.; Friend, R. H. *Physical Review B* **2003**, *67*, 064203.
- (172) Clarke, T. M.; Ballantyne, A. M.; Nelson, J.; Bradley, D. D. C.; Durrant, J. R. *Advanced Functional Materials* **2008**, *18*, 4029-4035.
- (173) Chen, T.-A.; Wu, X.; Rieke, R. D. *Journal of the American Chemical Society* **1995**, *117*, 233-244.
- (174) Wu, Z.; Petzold, A.; Henze, T.; Thurn-Albrecht, T.; Lohwasser, R. H.; Sommer, M.; Thelakkat, M. *Macromolecules*.
- (175) Nogueira, A. F.; Montanari, I.; Nelson, J.; Winder, C.; Sariciftci, N. S.; Brabec, C.; Durrant, J. R. *Synthetic metals* **2003**, *137*, 1505.
- (176) Ford, T. A.; Ohkita, H.; Cook, S.; Durrant, J. R.; Greenham, N. C. *Chemical Physics Letters* **2008**, *454*, 237-241.
- (177) Korovyanko, O. J.; Österbacka, R.; Jiang, X. M.; Vardeny, Z. V.; Janssen, R. A. J. *Physical Review B* **2001**, *64*, 235122.
- (178) Zen, A.; Saphiannikova, M.; Neher, D.; Grenzer, J.; Grigorian, S.; Pietsch, U.; Asawapirom, U.; Janietz, S.; Scherf, U.; Lieberwirth, I.; Wegner, G. *Macromolecules* **2006**, *39*, 2162-2171.
- (179) McKenna, G. B. *Journal de Physique IV* **2000**, *10*, 53-57.
- (180) Lin, Z. Q.; Kim, D. H.; Wu, X. D.; Boosahda, L.; Stone, D.; LaRose, L.; Russell, T. P. *Advanced Materials* **2002**, *14*, 1373.
- (181) Li, G.; Yao, Y.; Yang, H.; Shrotriya, V.; Yang, G.; Yang, Y. *Advanced Functional Materials* **2007**, *17*, 1636-1644.
- (182) Müller, C.; Ferenczi, T. A. M.; Campoy-Quiles, M.; Frost, J. M.; Bradley, D. D. C.; Smith, P.; Stingelin-Stutzmann, N.; Nelson, J. *Advanced Materials* **2008**, *20*, 3510-3515.
- (183) Albuerne, J.; Marquez, L.; Muller, A. J.; Raquez, J. M.; Degee, P.; Dubois, P.; Castelletto, V.; Hamley, I. W. *Macromolecules* **2003**, *36*, 1633-1644.
- (184) He, C.; Sun, J.; Deng, C.; Zhao, T.; Deng, M.; Chen, X.; Jing, X. *Biomacromolecules* **2004**, *5*, 2042-2047.
- (185) Radano, C. P.; Scherman, O. A.; Stingelin-Stutzmann, N.; Muller, C.; Breiby, D. W.; Smith, P.; Janssen, R. A. J.; Meijer, E. W. *Journal of the American Chemical Society* **2005**, *127*, 12502-12503.
- (186) Clarke, T. M.; Jamieson, F. C.; Durrant, J. R. *The Journal of Physical Chemistry C* **2009**, *113*, 20934-20941.
- (187) Gunes, S.; Neugebauer, H.; Sariciftci, N. S. *Chemical Reviews* **2007**, *107*, 1324-1338.
- (188) Goris, L.; Poruba, A.; Hod'akova, L.; Vanecek, M.; Haenen, K.; Nesladek, M.; Wagner, P.; Vanderzande, D.; De Schepper, L.; Manca, J. V. *Applied Physics Letters* **2006**, *88*, 052113-3.
- (189) Mihailetchi, V. D.; Wildeman, J.; Blom, P. W. M. *Physical Review Letters* **2005**, *94*, 126602-4.
- (190) Chirvase, D.; Chiguvare, Z.; Knipper, M.; Parisi, J.; Dyakonov, V.; Hummelen, J. C. *Synthetic Metals* **2003**, *138*, 299-304.
- (191) McNeill, C. R.; Frohne, H.; Holdsworth, J. L.; Dastoor, P. C. *Nano Letters* **2004**, *4*, 2503-2507.
- (192) Chiesa, M.; Burgi, L.; Kim, J. S.; Shikler, R.; Friend, R. H.; Sirringhaus, H. *Nano Letters* **2005**, *5*, 559-563.
- (193) Shikler, R.; Chiesa, M.; Friend, R. H. *Macromolecules* **2006**, *39*, 5393-5399.
- (194) McNeill, C. R.; Watts, B.; Thomsen, L.; Belcher, W. J.; Greenham, N. C.; Dastoor, P. C. *Nano Letters* **2006**, *6*, 1202-1206.
- (195) Milner, R. G.; Arias, A. C.; Stevenson, R.; Mackenzie, J. D.; Richards, D.; Friend, R. H.; Kang, D. J.; Blamire, M. *Materials Science and Technology* **2002**, *18*, 759-762.
- (196) Chappell, J.; Lidzey, D. G.; Jukes, P. C.; Higgins, A. M.; Thompson, R. L.; O'Connor, S.; Grizzi, I.; Fletcher, R.; O'Brien, J.; Geoghegan, M.; Jones, R. A. L. *Nature Materials* **2003**, *2*, 616-621.

- (197) Stevenson, R.; Arias, A. C.; Ramsdale, C.; MacKenzie, J. D.; Richards, D. *Applied Physics Letters* **2001**, *79*, 2178-2180.
- (198) Snaith, H. J.; Friend, R. H. *Thin Solid Films* **2004**, *451-52*, 567-571.
- (199) Xia, Y. J.; Friend, R. H. *Advanced Materials* **2006**, *18*, 1371-1376.
- (200) Tang, W.; Ke, L.; Tan, L.; Lin, T.; Kietzke, T.; Chen, Z. K. *Macromolecules* **2007**, *40*, 6164-6171.
- (201) Kraft, A.; Grimsdale, A. C.; Holmes, A. B. *Angewandte Chemie International Edition* **1998**, *37*, 402-428.
- (202) Moons, E. *Journal of Physics: Condensed Matter* **2002**, *14*, 12235-12260.
- (203) Liu, B.; Yu, W. L.; Lai, Y. H.; Huang, W. *Chemistry of Materials* **2001**, *13*, 1984-1991.
- (204) Campbell, A. J.; Bradley, D. D. C.; Antoniadis, H. *Applied Physics Letters* **2001**, *79*, 2133-2135.
- (205) Yimsiri, P.; Mackley, M. R. *Thin Solid Films* **2007**, *515*, 3787-3796.
- (206) Kim, J.-S.; Friend, R. H.; Grizzi, I.; Burroughes, J. H. *Applied Physics Letters* **2005**, *87*, 023506-3.
- (207) Huang, Y.-s.; Westenhoff, S.; Avilov, I.; Sreearunothai, P.; Hodgkiss, J. M.; Deleener, C.; Friend, R. H.; Beljonne, D. *Nature Materials* **2008**, *7*, 483-489.
- (208) Morteani, A. C.; Ho, P. K. H.; Friend, R. H.; Silva, C. *Applied Physics Letters* **2005**, *86*, 163501-3.
- (209) Morteani, A. C.; Friend, R. H.; Silva, C. *The Journal of Chemical Physics* **2005**, *122*, 244906.
- (210) Cadby, A. J.; Lane, P. A.; Mellor, H.; Martin, S. J.; Grell, M.; Giebeler, C.; Bradley, D. D. C.; Wohlgenannt, M.; An, C.; Vardeny, Z. V. *Physical Review B* **2000**, *62*, 15604.
- (211) Cadby, A. J.; Lane, P. A.; Wohlgenannt, M.; An, C.; Vardeny, Z. V.; Bradley, D. D. C. *Synthetic Metals* **2000**, *111-112*, 515-518.
- (212) Dhoot, A. S.; Greenham, N. C. *Advanced Materials* **2002**, *14*, 1834-1837.
- (213) Ford, T. A.; Avilov, I.; Beljonne, D.; Greenham, N. C. *Physical Review B* **2005**, *71*, 125212.
- (214) Fratiloiu, S.; Fonseca, S. M.; Grozema, F. C.; Burrows, H. D.; Costa, M. L.; Charas, A.; Morgado, J.; Siebbeles, L. D. A. *The Journal of Physical Chemistry C* **2007**, *111*, 5812-5820.
- (215) Dhoot, A. S.; Ginger, D. S.; Beljonne, D.; Shuai, Z.; Greenham, N. C. *Chemical Physics Letters* **2002**, *360*, 195-201.
- (216) Dyer-Smith, C.; Benson-Smith, J. J.; Bradley, D. D. C.; Murata, H.; Mitchell, W. J.; Shaheen, S. E.; Haque, S. A.; Nelson, J. *The Journal of Physical Chemistry C* **2009**, *113*, 14533.
- (217) Arias, A. C.; MacKenzie, J. D.; Stevenson, R.; Halls, J. J. M.; Inbasekaran, M.; Woo, E. P.; Richards, D.; Friend, R. H. *Macromolecules* **2001**, *34*, 6005-6013.
- (218) McNeill, C. R.; Abrusci, A.; Zaumseil, J.; Wilson, R.; McKiernan, M. J.; Burroughes, J. H.; Halls, J. J. M.; Greenham, N. C.; Friend, R. H. *Applied Physics Letters* **2007**, *90*, 193506-3.
- (219) Campoy-Quiles, M.; Sims, M.; Etchegoin, P. G.; Bradley, D. D. C. *Macromolecules* **2006**, *39*, 7673-7680.
- (220) Yang, Z.; Huck, W. T. S.; Clarke, S. M.; Tajbakhsh, A. R.; Terentjev, E. M. *Nature Materials* **2005**, *4*, 486-490.
- (221) Donley, C. L.; Zaumseil, J.; Andreasen, J. W.; Nielsen, M. M.; Sirringhaus, H.; Friend, R. H.; Kim, J.-S. *Journal of the American Chemical Society* **2005**, *127*, 12890-12899.
- (222) Bernius, M.; Inbasekaran, M.; Woo, E.; Wu, W.; Wujkowski, L. *Journal of Materials Science* **2000**, *11*, 111-116.
- (223) Katz, E. A.; Faiman, D.; Tuladhar, S. M.; Kroon, J. M.; Wienk, M. M.; Fromherz, T.; Padinger, F.; Brabec, C. J.; Sariciftci, N. S. *Journal of Applied Physics* **2001**, *90*, 5343-5350.
- (224) Sreearunothai, P.; Morteani, A. C.; Avilov, I.; Cornil, J.; Beljonne, D.; Friend, R. H.; Phillips, R. T.; Silva, C.; Herz, L. M. *Physical Review Letters* **2006**, *96*, 117403-4.
- (225) Schmidtke, J. P.; Friend, R. H.; Silva, C. *Physical Review Letters* **2008**, *100*, 157401-4.
- (226) Mardalen, J.; Samuelsen, E. J.; Konestabo, O. R.; Hanfland, M.; Lorenzen, M. *Journal of Physics: Condensed Matter* **1998**, *10*, 7145-7154.
- (227) Flory, P. J. *Principles of polymer chemistry*; Cornell University Press: Ithaca, 1975.

- (228) Guo, Y.; Gu, B.; Lu, Z.; Du, Q. *Journal of Applied Polymer Science* **1999**, *71*, 693-698.
- (229) Yaws, C. L. *The Yaws Handbook of Vapour Pressure: Antoine Coefficients*, 2007.
- (230) Barton (editor), A. F. M. *CRC-handbook of polymer-liquid interaction parameters and solubility parameters*; CRC Press, 1990.
- (231) Knoll, A.; Magerle, R.; Krausch, G. *The Journal of Chemical Physics* **2004**, *120*, 1105.
- (232) Fredrickson, G. H.; Leibler, L. *Macromolecules* **1989**, *22*, 1238-1250.
- (233) Westenhoff, S.; Howard, I. A.; Friend, R. H. *Physical Review Letters* **2008**, *101*, 016102.
- (234) Reynolds, L. X. *Personal Communication*.
- (235) Turro, N. J.; Kraeutler, B. *Accounts of Chemical Research* **1980**, *13*, 369-377.
- (236) Schulten, K.; Wolynes, P. G. *The Journal of Chemical Physics* **1978**, *68*, 3292-3297.
- (237) Dance, Z. E. X.; Mi, Q.; McCamant, D. W.; Ahrens, M. J.; Ratner, M. A.; Wasielewski, M. R. *The Journal of Physical Chemistry B* **2006**, *110*, 25163-25173.
- (238) Steiner, U. E.; Ulrich, T. *Chemical Reviews* **1989**, *89*, 51-147.
- (239) Weller, A.; Staerk, H.; Treichel, R. *Faraday discussions of the Chemical Society* **1984**, *78*, 271.
- (240) Till, U.; Hore, P. J. *Journal of Molecular Physics* **1997**, *90*, 289 - 296.
- (241) Schmickler, W. *Interfacial Electrochemistry*; Oxford University Press: Oxford, 1996.
- (242) Marcus, R. A. *The Journal of Chemical Physics* **1965**, *43*, 679-701.
- (243) Peeters, E.; van Hal, P. A.; Knol, J.; Brabec, C. J.; Sariciftci, N. S.; Hummelen, J. C.; Janssen, R. A. J. *The Journal of Physical Chemistry B* **2000**, *104*, 10174-10190.
- (244) Saif, A. H.; Samantha, H.; Katja, P.; Emilio, P.; Mukundan, T.; James, R. D. *Angewandte Chemie International Edition* **2005**, *44*, 5740-5744.
- (245) Clifford, J. N.; Palomares, E.; Nazeeruddin, M. K.; Gratzel, M.; Nelson, J.; Li, X.; Long, N. J.; Durrant, J. R. *Journal of the American Chemical Society* **2004**, *126*, 5225-5233.
- (246) Kirkpatrick, J. *Personal Communication*.
- (247) Shuttle, C. G.; Maurano, A.; Hamilton, R.; O'Regan, B.; de Mello, J. C.; Durrant, J. R. *Applied Physics Letters* **2008**, *93*, 183501-3.
- (248) Mason, J. C.; Handscomb, D. C. *Chebyshev Polynomials*; Chapman and Hall.
- (249) Aoki, Y.; Imamura, A. *The Journal of Chemical Physics* **1995**, *103*, 9726-9737.
- (250) Coulson, C. A. *Proceedings of the Royal Society of London. Series A - Mathematical and Physical Sciences* **1938**, *164*, 383-396.
- (251) Malenfant, P. R. L.; Dimitrakopoulos, C. D.; Gelorme, J. D.; Kosbar, L. L.; Graham, T. O.; Curioni, A.; Andreoni, W. *Applied Physics Letters* **2002**, *80*, 2517-2519.
- (252) Huttner, S.; Sommer, M.; Thelakkat, M. *Applied Physics Letters* **2008**, *92*, 093302-3.
- (253) Tang, C. W. *Applied Physics Letters* **1986**, *48*, 183-185.
- (254) Zhan, X. W.; Tan, Z.; Domercq, B.; An, Z.; Zhang, X.; Barlow, S.; Li, Y.; Zhu, D.; Kippelen, B.; Marder, S. *Journal of the American Chemical Society* **2007**, *129*, 7246.
- (255) He, X.; Zhou, W.; Li, Y.; Liu, X.; Li, C.; Liu, H. *Journal of Nanoscience and Nanotechnology* **2008**, *8*, 2005-2010.
- (256) Hadicke, E.; Graser, F. *Acta Crystallographica Section C* **1986**, *42*, 189-195.
- (257) Hadicke, E.; Graser, F. *Acta Crystallographica Section C* **1986**, *42*, 195-198.
- (258) Struijk, C. W.; Sieval, A. B.; Dakhorst, J. E. J.; van Dijk, M.; Kimkes, P.; Koehorst, R. B. M.; Donker, H.; Schaafsma, T. J.; Picken, S. J.; van de Craats, A. M.; Warman, J. M.; Zuilhof, H.; Sudholter, E. J. R. *Journal of the American Chemical Society* **2000**, *122*, 11057-11066.
- (259) Neuteboom, E. E.; Beckers, E. H. A.; Meskers, S. C. J.; Meijer, E. W.; Janssen, R. A. J. *Organic & Biomolecular Chemistry* **2003**, *1*, 198.
- (260) You, C.-C.; Wurthner, F. *Journal of the American Chemical Society* **2003**, *125*, 9716-9725.
- (261) Marcon, V.; Kirkpatrick, J.; Pisula, W.; Andrienko, D. *Physica Status Solidi b* **2008**, *245*, 820-824.
- (262) Marcon, V.; Breiby, D. W.; Pisula, W.; Dahl, J.; Kirkpatrick, J.; Patwardhan, S.; Grozema, F.; Andrienko, D. *Journal of the American Chemical Society* **2009**, *131*, 11426-11432.
- (263) Chen, L. X.; Xiao, S.; Yu, L. *The Journal of Physical Chemistry B* **2006**, *110*, 11730-11738.

- (264) Neuteboom, E. E.; Meskers, S. C. J.; Meijer, E. W.; Janssen, R. A. J. *Macromolecular Chemistry and Physics* **2004**, *205*, 217-222.
- (265) Huo, L.; Zhou, Y.; Li, Y. *Macromolecular Rapid Communications* **2008**, *29*, 1444-1448.
- (266) Scholz, R.; Kobitski, A. Y.; Vragovic, I.; Wagner, H. P.; Zahn, D. R. T. *Organic Electronics* **2004**, *5*, 99-105.
- (267) Rybak, A.; Pisula, W.; Jung, J.; Ulanski, J. *Thin Solid Films* **2008**, *516*, 4201-4207.
- (268) Martin, R. B. *Chemical Reviews* **1996**, *96*, 3043-3064.
- (269) Würthner, F.; Thalacker, C.; Diele, S.; Tschierske, C. *Chemistry* **2001**, *7*, 2245-2253.
- (270) Klebe, G.; Graser, F.; Hadicke, E.; Berndt, J. *Acta Crystallographica Section B* **1989**, *45*, 69-77.
- (271) Nolde, F.; Pisula, W.; Muller, S.; Kohl, C.; Mullen, K. *Chemistry of Materials* **2006**, *18*, 3715-3725.
- (272) Hansen, M. R.; Graf, R.; Sekharan, S.; Sebastiani, D. *Journal of the American Chemical Society* **2009**, *131*, 5251-5256.